General Disclaimer

One or more of the Following Statements may affect this Document

- This document has been reproduced from the best copy furnished by the organizational source. It is being released in the interest of making available as much information as possible.

- This document may contain data, which exceeds the sheet parameters. It was furnished in this condition by the organizational source and is the best copy available.

- This document may contain tone-on-tone or color graphs, charts and/or pictures, which have been reproduced in black and white.

- This document is paginated as submitted by the original source.

- Portions of this document are not fully legible due to the historical nature of some of the material. However, it is the best reproduction available from the original submission.

NATIONAL AERONAUTICS AND SPACE ADMINISTRATION

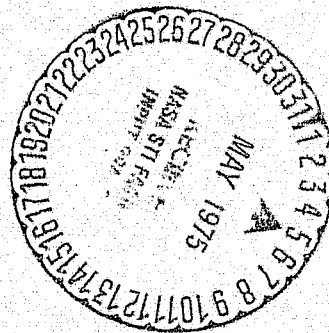# *The Deep Space Network*
Progress Report 42-26

January and February 1975

JET PROPULSION LABORATORY

CALIFORNIA INSTITUTE OF TECHNOLOGY

PASADENA, CALIFORNIA

April 15, 1975

Preface

Beginning with Volume XX, the Deep Space Network Progress Report changed from the Technical Report 32- series to the Progress Report 42- series. The volume number continues the sequence of the preceding issues. Thus, Progress Report 42-20 is the twentieth volume of the Deep Space Network series, and is an uninterrupted follow-on to Technical Report 32-1526, Volume XIX.

This report presents DSN progress in flight project support, tracking and data acquisition (TDA) research and technology, network engineering, hardware and software implementation, and operations. Each issue presents material in some, but not all, of the following categories in the order indicated:

Description of the DSN

Mission Support
  Ongoing Planetary/Interplanetary Flight Projects
  Advanced Flight Projects

Radio Science
  Radio Science Support
  Special Projects

Supporting Research and Technology
  Tracking and Ground-Based Navigation
  Communications—Spacecraft/Ground
  Station Control and Operations Technology
  Network Control and Data Processing

Network Engineering and Implementation
  Network Control System
  Ground Communications
  Deep Space Stations

Operations
  Network Operations
  Network Control System Operations
  Ground Communications
  Deep Space Stations

Planning and Facilities
  TDA Planning
  Facility Engineering

In each issue, the part entitled "Description of the DSN" describes the functions and facilities of the DSN and may report the current configuration of one of the five DSN systems (Tracking, Telemetry, Command, Monitor and Control, and Test and Training).

The work described in this report series is either performed or managed by the Tracking and Data Acquisition organization of JPL for NASA.

Contents

DESCRIPTION OF THE DSN

MISSION SUPPORT

Ongoing Planetary/Interplanetary Flight Projects

RADIO SCIENCE

Special Projects

SUPPORTING RESEARCH AND TECHNOLOGY

Tracking and Ground-Based Navigation

PRECEDING PAGE BLANK NOT FILMED

Communications—Spacecraft/Ground

Station Control and Operations Technology

Network Control and Data Processing

NETWORK ENGINEERING AND IMPLEMENTATION

Deep Space Stations

OPERATIONS

Network Operations

PLANNING AND FACILITIES

TDA Planning

Facility Engineering

DSN Functions and Facilities

N. A. Renzetti
Office of Tracking and Data Acquisition

The objectives, functions, and organization of the Deep Space Network are summarized. Deep space station, ground communication, and network operations control capabilities are described.

The Deep Space Network (DSN), established by the National Aeronautics and Space Administration (NASA) Office of Tracking and Data Acquisition (OTDA) under the system management and technical direction of the Jet Propulsion Laboratory (JPL), is designed for two-way communications with unmanned spacecraft traveling approximately 16,000 km (10,000 mi) from Earth to the farthest planets of our solar system. It has provided tracking and data acquisition support for the following NASA deep space exploration projects, for which JPL has been responsible for the project management, development of the spacecraft, and conduct of mission operations:

(1) Ranger.

(2) Surveyor.

(3) Mariner Venus 1962.

(4) Mariner Mars 1964.

(5) Mariner Venus 1967.

(6) Mariner Mars 1969.

(7) Mariner Mars 1971.

(8) Mariner Venus/Mercury 1973.

The DSN has also provided tracking and data acquisition support for the following projects:

(1) Lunar Orbiter, for which the Langley Research Center carried out the project management, spacecraft development, and mission operations functions.

(2) Pioneer, for which the Ames Research Center carried out the project management, spacecraft development, and mission operations functions.

(3) Apollo, for which the Lyndon B. Johnson Space Center was the project center and the Deep Space Network supplemented the Spaceflight Tracking and Data Network (STDN), which is managed by the Goddard Space Flight Center (GSFC).

(4) Helios, a joint United States/West Germany project.

(5) Viking, for which the Langley Research Center provides the project management and Lander spacecraft, and conducts mission operations, and for which JPL provides the Orbiter spacecraft.

The Deep Space Network is one of two NASA networks. The other, the Spaceflight Tracking and Data Network, is under the system management and technical direction of the Goddard Space Flight Center. Its function is to support manned and unmanned Earth-orbiting and lunar scientific and advanced technology satellites. Although the DSN was concerned with unmanned lunar spacecraft in its early years, its primary objective now and into the future is to continue its support of planetary and interplanetary flight projects.

A development objective has been to keep the network capability at the state of the art of telecommunications and data handling and to support as many flight projects as possible with a minimum of mission-dependent hardware and software. The DSN provides direct support to each flight project through that project's tracking and data systems. This management element is responsible for the design and operation of the hardware and software in the DSN which are required for the conduct of flight operations.

As of July 1972, NASA undertook a change in the interface between the network and the flight projects. Since January 1, 1964, the network, in addition to consisting of the Deep Space Stations and the Ground Communications Facility, had also included the Mission Control and Computing Facility and had provided the equipment in the mission support areas for the conduct of mission operations. The latter facilities were housed in a building at JPL known as the Space Flight Operations Facility (SFOF). The interface change was to accommodate a hardware interface between the network operations control functions and the mission control and computing functions. This resulted in the flight project's picking up

the cognizance of the large general-purpose digital computers, which were used for network processing as well as mission data processing. It also assumed cognizance of all of the equipment in the flight operations facility for display and communications necessary for the conduct of mission operations. The network has already undertaken the development of hardware and computer software necessary to do its network operations control and monitor functions in separate computers. This activity became known as the Network Control System implementation. A characteristic of the new interface is that the network provides direct data flow to and from the stations via appropriate ground communications equipment to Mission Operations Centers, wherever they may be; namely, metric data, science and engineering telemetry, and such network monitor data as are useful to the flight project. It accepts command data from the flight project directly into the ground communications equipment for transmission to the station and thence to the spacecraft in a standardized format.

In carrying out its functions, the network activities can be divided into two general areas. The first includes those functions which are associated with the in-flight support and in tracking the spacecraft; its configuration can be characterized as follows:

(1) *DSN Tracking System.* Generates radio metric data; i.e., angles, one- and two-way doppler and range, and transmits raw data to mission control.

(2) *DSN Telemetry System.* Receives, decodes, records, and retransmits engineering and scientific data generated in the spacecraft to Mission Control.

(3) *DSN Command System.* Accepts coded signals from Mission Control via the Ground Communications Facility (GCF) and transmits them to the spacecraft in order to initiate spacecraft functions in flight.

The second category of activity supports testing, training, and network operations control functions and is configured as follows:

(1) *DSN Monitor and Control System.* Instruments, transmits, records, and displays those parameters of the DSN necessary to verify configuration and validate the network. Provides operational direction and configuration control of the network and primary interface with flight project mission control personnel.

(2) *DSN Test and Training System.* Generates and controls simulated data to support development, test, training, and fault isolation within the DSN. Participates in mission simulation with flight projects.

The capabilities needed to carry out the above functions have evolved in three technical areas:

(1) The Deep Space Stations that are distributed around Earth and which, prior to 1964, formed part of the Deep Space Instrumentation Facility. The technology involved in equipping these stations is strongly related to the state of the art of telecommunications and flight/ground design considerations and is almost completely multimission in character. Table 1 gives a description of the Deep Space Stations and the Deep Space Communications Complexes (DSCCs) they comprise.

(2) Ground communications. This technology supports the Earth-based point-to-point voice and data communications from the stations to the Network Operations Control Area at JPL, Pasadena, and to the Mission Operations Centers, wherever they may be. It is based largely on the capabilities of the common carriers throughout the world which are engineered into an integrated system by the Goddard Space Flight Center for support of all NASA programs. The term "Ground Communications Facility" is used for the sets of hardware and software needed to carry out the functions.

The Network Operations Control Center is the functional entity for centralized operational control of the network and interfaces with the users. It has two separable functional elements; namely, Network Operations Control and Network Data Processing.

The functions of the Network Operations Control Center are:

(1) Control and coordination of network support to meet commitments to network users.

(2) Utilization of the network data processing computing capability to generate all standards and limits required for network operations.

(3) Utilization of network data processing computing capability to analyze and validate the performance of all network systems.

The personnel who carry out the above functions are on the first floor of Building 230, wherein mission operations functions are carried out by certain flight projects. Network personnel are directed by an Operations Control Chief. The functions of the Network Data Processing are:

(1) Processing of data used by Network Operations Control for the control and analysis of the network.

(2) Display in Network Operations Control Area of data processed in Network Data Processing Area.

(3) Interface with communications circuits for input to and output from Network Data Processing Area.

(4) Data logging and production of the intermediate data records.

The personnel who carry out these functions are located in Building 202, which is approximately 200 m from Building 230. The equipment consists of minicomputers for real-time data system monitoring, two XDS Sigma 5's, display, magnetic tape recorders, and appropriate interface equipment with the ground data communications.

Table 1. Tracking and data acquisition stations of the DSN

DSCC	Location	DSS	DSS serial designation	Antenna Diameter, m (ft)	Antenna Type of mounting	Year of initial operation
Goldstone	California	Pioneer	11	26(85)	Polar	1958
		Echo	12	26(85)	Polar	1962
		(Venus)[a]	13	26(85)	Az-El	1962
		Mars	14	64(210)	Az-El	1966
Tidbinbilla	Australia	Weemala	42	26(85)	Polar	1965
		Ballima	43	64(210)	Az-El	1973
—	Australia	Honeysuckle Creek	44	26(85)	X-Y	1973
Madrid	Spain	Robledo	61	26(85)	Polar	1965
		Cebreros	62	26(85)	Polar	1967
		Robledo	63	64(210)	Az-El	1973

[a]A maintenance facility. Besides the 26-m (85-ft) diam Az-El mounted antenna, DSS 13 has a 9-m (30-ft) diam Az-El mounted antenna that is used for interstation time correlation using lunar reflection techniques, for testing the design of new equipment, and for support of ground-based radio science.

Mariner 10 Mission Support

E. K. Davis

DSN Systems Engineering Office

This report covers the period from October 15, 1974 through February 15, 1975. The primary objectives during this portion of the extended mission were to assure survival of the spacecraft for a third Mercury encounter through conservation of attitude control gas and to conduct trajectory correction maneuvers (TCMs) as necessary to target the spacecraft for a solar occultation zone pass. Special support activities included TCMs 6 and 7 conducted on October 30, 1974 and on February 12–13, 1975, respectively. This period also saw the DSN interface organization involved in (1) the allocation of sufficient coverage to assure accurate orbit determination solutions, (2) monitoring of DSN implementation for Viking to assure maintenance of compatible interfaces and capabilities required for Mariner 10, and (3) the development of encounter coverage, sequences, and readiness test plans.

I. Planning and Operations

During October 1974, the DSN participated with the Project in planning and preparing for TCM 6. A major effort went into obtaining sufficient tracking coverage for Mariner 10 in the face of higher priority tasks: Pioneers 10 and 11, Helios A pre-launch tests, Viking implementation, and Deep Space Station (DSS) upgrades. This period saw DSS 44 down for conversion from the Spaceflight Tracking and Data Network (STDN) to DSN configuration; DSS 14 down for Viking implementation; and DSS 63 down for gear box repairs. Limited but adequate coverage was provided for Mariner 10. TCM 6 was accurately performed on October 30, 1974, and there were no DSN support problems.

Due to spacecraft attitude control problems and high usage of attitude control gas in October, Project placed the spacecraft in a roll-drift mode with the high-gain antenna and solar panels positioned to produce torques in the pitch, yaw, and roll axes that would minimize gas consumption. This required communications to be conducted over the spacecraft low-gain antenna and lowering of the data rate to 8-1/3 bps. Furthermore, the spacecraft roll mode seriously impacted the navigation accuracy achievable with the previously negotiated DSN tracking time. Project requested additional radio metric data, particularly three-way doppler data to understand roll signatures in the doppler data and additional ranging points. Special efforts were required to resolve the tracking coverage conflicts among the various users.

Planning for TCM 7 continued through November and early December 1974. In order to allow for a single maneuver strategy and to avoid coverage conflicts during the Helios A launch and Pioneer 11 encounter periods, TCM 7 was rescheduled from early January 1975 to February 12, 1975. This permitted allocation of adequate coverage for Mariner 10 pre- and post-maneuver orbit determination activities. During this time the spacecraft continued its flight in the solar torque, roll-control mode. Following resolution of the December 1974–February 1975 tracking allocations, full attention was given to development of a compromise plan for the March 1975 period.

On December 16, 1974, the DSN met with the Mariner 10 Project to develop an understanding of essential encounter requirements, as well as the requirements of other flight projects during the March 1975 period. This meeting resulted in a significant reduction of Mariner 10's initial requirement for 8 days of continuous 64-meter subnet coverage at encounter. This reduction was a key factor in permitting the DSN to draft a recommended solution to the problem. In summary, the problem was as follows:

(1) Helios and Mariner view periods are almost entirely overlapping during March 1975.

(2) Helios A perihelion, an event of prime interest, would occur March 15, 1975, requiring 64-meter subnet coverage during the period March 5–25, 1975.

(3) Mariner 10's Mercury encounter would occur on March 16, 1975, requiring 64-meter subnet coverage during the period March 12–20, 1975.

(4) Pioneer 11 and 10 solar conjunction would occur on March 24, 1975 and April 4, 1975, respectively, requiring 64-meter subnet coverage during the period March 19–April 4, 1975.

The problem was significantly reduced by the following:

(1) Helios A would not use DSS 63 since coverage in this longitude is provided by the German tracking station.

(2) Mariner 10 agreed to schedule pre-encounter critical events to occur over DSS 63. These included: (a) central computer and sequencer load for encounter (March 11, 1975), (b) Canopus reacquisition (March 13, 1975), and (c) far encounter TV calibrations and tests (March 14–15, 1975), thus leaving DSSs 14 and 43 free to support other projects.

(3) Mariner 10 reduced the encounter 64-meter subnet coverage requirements to the minimum essential to recover near-encounter imaging and non-imaging data, three consecutive passes on March 16–17 (GMT).

Meetings and negotiations continued between the flight projects throughout January 1975 to reach agreements on detailed tracking schedules based on the proposed compromises.

By early February 1975, plans for TCM 7 were completed, and the required DSS coverage was allocated. Since the spacecraft continued in the roll-drift mode, timing of the roll by monitoring Canopus and other star crossings was critical to proper execution of the maneuver. Coverage from 64-meter stations was required to acquire these data at 33-1/3 bps since link conditions were inadequate for communications via the 26-meter stations. However, shortly before start of the maneuver sequence on February 12, 1975, a change in time of the Canopus crossing was noted and the TCM was postponed until February 13.

Excellent support was provided by DSS 63. Recovery of data was continuous throughout the TCM even though a dropout had been expected due to the planned adverse pitch angle. DSS 63 accomplished two post-TCM replays of telemetry data acquired during the burn to fill gaps caused by difficulties at the data processing facility. As evidenced by greater than planned changes in the doppler data, TCM 7 was other than planned. Early indications indicated a 20 percent error as a result of either engine overburn, roll error, pitch error, or a combination of all of these error sources. Effect on the required Mercury aim point is uncertain at this time. It will be necessary for the Project to negotiate for additional DSS tracking passes to obtain sufficient doppler and ranging data to rapidly redefine the orbit.

Planning for support at Mercury's third encounter is in the final stages. Requirements have been defined, and the DSN has developed a minimum, but adequate, test plan to revalidate DSS 64-meter subnet data systems and verify readiness to support special data rates and sequences at encounter. In many respects, third encounter will be similar to the first encounter. The primary objective is to obtain non-imaging science data at 2450 bps, particularly from the solar occultation zone. A secondary objective is to recover imaging data during near encounter, except when passing the dark portion of the planet in the solar occultation zone. Unlike the first encounter, the spacecraft will not pass through the Earth occultation zone during

this third pass. This targeting provides an opportunity to acquire data for support of celestial mechanics experiments which was not available on the previous encounters: first encounter had a tracking gap due to Earth occultation giving a break in continuous two-way doppler near the planet; the second encounter was targeted to optimize television on a bright-side pass, but was too far from the planet to provide precise results.

A number of engineering tests with the spacecraft have been planned for the immediate post-encounter period including propulsion subsystem burn to depletion. The spacecraft will be programmed to command its transmitter off on April 1, 1975. DSS coverage will be scheduled to confirm this event, which will mark the end of a very dynamic and productive mission.

II. Program Control

The DSN continued to provide monthly inputs to the Project Management Report throughout this period. The interface organization kept the Project informed of changes in the network status due to Viking implementation activities and negotiated changes to capabilities that occurred during this period. The DSN will conduct an encounter readiness review in early March 1975 following completion of planned tests.

III. Implementation Activities

Very little implementation was planned or required for Mariner 10 during this period. Primary attention was given to maintaining required capabilities and interface compatibility in the face of extensive network implementation for the Viking mission.

As planned, the Project was committed to transfer operations to the redesigned command system by mid-January 1975. After resolution of initial minor difficulties on January 16, 1975, the change-over took place smoothly and commanding has continued in this mode.

The low-noise ultra cone has been maintained at DSS 43 for third encounter support. This required negotiation of the DSS 43 RF cone reconfiguration work scheduled in preparation for Viking 75. However, maintaining the low-noise S-Band Megawatt Transmit (SMT) cone in place at DSS 14 could not be accommodated through a delay of cone reconfiguration work. During January 1975, the SMT cone was replaced with the S-Band Polarization Diversity (SPD) cone. The DSN will, however, install the SMT maser in the SPD cone to improve system performance.

With Project agreement, it was necessary to terminate the Block III planetary ranging capability at DSS 14 in order to meet the Viking schedule for completing the Block IV configuration. Connection of the ranging assembly to the Block IV receiver–exciter is in process. If this configuration is not verified and operational by early March 1975, the Block III configuration will be restored for Mariner 10 encounter support.

The 230-kbps super group communications service between DSS 14 and JPL is in the process of reactivation. The circuit had been deactivated during cruise to avoid lease costs.

Viking Mission Support

D. J. Mudgway
DSN Systems Engineering Office

D. W. Johnston
Network Operations Office

The previous article in this series covered the initial phases of the Network Implementation for Viking. This article briefly outlines the background on the establishment of the DSN/Viking test schedule and describes the progress that has been made in accomplishing the engineering tests and operational training and testing required to prepare the DSN for support of the Viking Project tests, training, and flight operations.

I. Background

The Deep Space Network (DSN) preparations for Viking 1975 (VK'75) have followed the same general pattern applied to previous missions. Briefly, the milestone dates for DSN support of Project tests were established jointly by the DSN, Viking Mission Control and Computing Center (VMCCC), and the Viking Project Office (VPO), in the Level 3 Schedule. These dates were then utilized by the DSN Manager and Network Operations Project Engineer (NOPE) as DSN target completion dates, and to establish the start dates reflected on the Level 5 Schedule for DSN Operations testing and training.

Agreements were then negotiated between the DSN Manager and the implementing organization (Division 33) concerning budgets and the design, procurement, proto-

type testing, and implementation of the new Viking equipment to meet the operations test start dates. The schedules detailed in the last DSN Progress Report (Ref. 1) varied for the different stations and consisted of five major blocks of time sequentially covering: (1) preparations at Compatibility Test Area 21 (CTA 21) and STDN (MIL-71) to support compatibility tests, (2) DSSs 11 and 14 to support Planetary Operations Tests, (3) DSSs 42, 43, 44, 61, and 63 to support launch and cruise tests, (4) DSS 12/62 to support cruise tests, and eventually (5) all DSSs to support planetary tests.

Previous articles have covered CTA 21 and STDN (MIL-71) activities. This article deals mainly with DSSs 11 and 14 in detail, with minor references to the other stations, and covers activities that had occurred as of February 21, 1975.

II. Mission Preparation Status Summary

There have been the usual technical and operational problems in preparing the DSN to support the VK'75 mission, but the biggest single problem with DSS 11 and 14 preparations has been the slip in the implementation completion milestone at DSS 14.

The 26-m stations require relatively minor hardware additions for Viking, but the 64-m stations require extensive equipment installations. The overseas 64-m stations (DSSs 43 and 63) are not scheduled to be fully implemented for Viking until after launch. DSS 14, however, was scheduled to be fully implemented to support the VK'75 Project pre-launch planetary tests.

The implementation completion milestone for DSS 14 was originally scheduled for September 15, 1974. It first moved to mid-October, then mid-November, early December, and finally to January 4, 1975. This total slip of 3-1/2 months can be attributed to the problems described in the last DSN Progress Report (Ref. 1).

The generation of procedures for DSN System Performance Tests (SPTs) and Mission Configuration Tests (MCTs), and actual test accomplishment, had originally been scheduled to take place between September 15 and mid-November; time was also scheduled during this period for on-site mission-independent training (MIT) and mission-dependent training (MDT). Then followed a six-week period to January 1, 1975, during which time the station "freeze" for DSN support of Pioneer 11 Jupiter encounter precluded accomplishment of SPT/MCTs at DSS 14. DSS Operational Verification Tests (OVTs) were to commence in mid-November and be completed on March 1, 1975, overlapping with DSN/VMCCC System Integration Tests (SITs) during February 1975.

Because of the lack of hardware, the on-site MIT and MDT activities were moved to January and the multimission SPTs had to be cancelled. The mission-dependent MCTs, which provide for adequate testing of the DSN systems to Viking specifications, started on December 21, 1974. The OVTs were then compressed and rescheduled to start the first week in February 1975; the length of each test and number of tests were reduced, but more tests per week had to be scheduled.

On-site training programs are well underway at DSSs 11 and 14. MCTs have almost been completed and OVTs are nearing completion. Details of these activities are provided in succeeding paragraphs of this article. Table 1 summarizes the current test and training status of those DSN stations that are committed for support of the launch and cruise phase of the mission.

III. DSN Training

A. Mission-Independent Training

Network mission-independent training, though normally not a part of a Mission Test and Training Plan, is an essential prerequisite to VK'75-oriented training and testing. The majority of the subsystems to be used during the VK'75 mission remain unchanged from previous missions, although the VK'75 configurations require up to six full telemetry streams and two command streams at a single 64-m station in place of the total of four telemetry streams and one command stream as for previous missions.

Training data and documentation for new equipment are supplied to the DSN Training Unit Supervisor of Section 422 by the Cognizant Operations Engineers of the affected subsystems. The DSN Training Unit prepares a training package to be sent along with the new equipment to the affected locations. It is the responsibility of the Facility Managers to see that personnel training on mission-independent equipment is carried out.

New Network equipment required as part of the VK'75 mission 64-m configurations consists of:

(1) 100-kW transmitter and exciter selector (400 kW at DSS 14).

(2) Six-channel Simulation Conversion Assembly (SCA).

(3) Block IV Receiver/Exciter and Subcarrier Demodulator Assemblies (SDAs).

(4) Faraday rotation equipment.

(5) Automated weather station.

(6) Planetary Ranging Assembly and Range Demodulator Assembly.

(7) SDA/Symbol Synchronizer Assembly (SSA)/Data Decoder Assembly (DDA)/Block Decoder Assembly (BDA)/Telemetry and Command Processor (TCP)/Command Modulator Assembly (CMA) switching modifications.

(8) Simulated time switching.

(9) Dual Doppler Counter.

(10) S/X-band antenna modifications.

(11) Antenna Pointing Conical Scan System.

Mission-independent training has to be completed at all locations prior to the start of System Performance Tests.

B. Network Mission-Dependent Training

1. General. The Network mission-oriented training consists of classroom instruction and training exercises conducted at each facility for the facility staff. It includes any "in-house" operational tests designed by the Facility Director to exercise the VK'75 configuration.

All mission-oriented operator training carried out at a facility is the direct responsibility of the Facility Director, who is the Training Controller for the "in-house" training at his location.

A comprehensive training package was delivered to each station by the VK'75 Network Operations Project Engineer (NOPE) to assist the facility directors in this phase of training. The package includes lists of Viking Lander and Orbiter commands from which the stations produce Mylar command tapes for their use, and use for operator training in manual command exercises. All Viking unique computer "type-ins" for standard operations, plus those used for troubleshooting and failure isolation and recovery, were also included for use in conjunction with the Standard Operations Procedures and the procedures in the Network Operations Plan for Viking 1975.

2. Objective. The objective of this training is to ensure that all Network operational personnel are adequately trained to support the VK'75 pre-launch and mission activities.

3. Training Requirements. Each Facility Director, acting as Training Controller at his facility, considers the following list in determining training needs and preparing plans:

(1) Operations personnel proficiency in mission-independent tasks.

(2) Knowledge of mission design and sequences.

(3) Spacecraft radio frequency (RF) modes and data formats.

(4) DSN configurations corresponding to spacecraft modes.

(5) DSN commitments for data acquisition, ground transmission, and real-time and nonreal-time data handling.

(6) Ground system performance requirements, standards and limits, and alarm conditions.

(7) Priorities and constraints.

(8) Spacecraft commands that affect DSN configurations and procedures.

(9) Reaction times for system initialization, configuration, reconfiguration, acquisition, etc.

(10) Failure detection, analysis, and recovery.

(11) Backup modes and alternate procedures.

(12) Flight Operations System (FOS) interface and procedures for mission direction, planning, sequence of events, schedules, operational parameters, etc.

(13) Problem and failure reporting procedures.

(14) Configuration and change procedures.

Information on these subjects is found in the Network Operations Plan (NOP) for Viking 1975 and other project documents supplied to each facility by the NOPE.

4. Operational Procedures. Every endeavor is made during the training tests to exercise the procedures contained in the NOP, with particular emphasis on the voice backup command procedures and manual TCD configuration and initialization.

5. Sequence of Events. The sequence of events (SOE) given in NOP Table 4-1 may be adapted or modified by the station for the training exercises. Copies of the Operational Verification Test SOE produced by the NOPE is now available at the stations.

6. Simulation. DSS On-Site Training Tests are accomplished using the SCA as a self-contained VK'75 spacecraft telemetry simulator, using the fixed pattern data tapes supplied by the NOPE.

7. Reporting. A problem on previous missions has been for the NOPE, and DSN Operations Management, to obtain a clear understanding of a facility's current training status. An instance is where a four-shift station would report 75% trained prior to supporting a project test, and, when queried on their poor performance, would reply that the shift involved was completely untrained on the project in question (implying that the other three shifts were 100% trained).

To avoid situations where "75% trained" could mean four shifts three-quarters trained, or three shifts fully trained and one shift untrained, or any number of combinations, the reporting format illustrated by Table 2 has been adopted.

The percentage of "training complete" is the Facility Director's estimate of a shift's ability to support any phase

of the VK'75 mission. The fractional number is to represent the number of shift personnel (including the Shift Supervisor) who are fully trained, over the total number of operators on the shift. This includes those operators who are fully experienced with their particular subsystem and who require little or no reorientation to support the new mission, e.g., Digital Instrumentation Subsystem (DIS), Analog Instrumentation Subsystem (AIS), and Antenna Mechanical Subsystem (ANT). The remarks should cover pertinent items such as "New Transmitter Subsystem (TXR) Operator," "New Command System Analyst," etc.

IV. DSN Testing

The DSN testing falls in the two specific categories of engineering and operational tests described below.

A. Engineering Tests

1. System Performance Tests

a. Purpose. The purpose of the Telemetry Command, Monitor, or Tracking Facility SPT is to demonstrate that each system meets the specified level of performance when tested simultaneously with operational software. The tests normally are conducted with hardware that has been transferred from the development to the operations organization and software that has been transferred to the DSN Program Library. The test procedures are contained in DSN 850-series documents. They make use of all elements of the Deep Space Station subsystems within a given station and provide a basis for DSS system-level maintenance, performance verification, and prepass testing. The successful completion of an SPT verifies that the system meets documented specifications and qualifies it for Network-level support on a mission-independent basis.

b. Prerequisites. The main prerequisites to running an SPT are:

(1) Implementation of DSS/GCF and NOCC complete.

(2) Hardware and software transferred to Operations.

(3) Facility mission-independent training complete.

c. Personnel. The SPTs are supported by the following individuals:

(1) Test Conductor: Section 421 System Cognizant Operations Engineer (SCOE).

(2) DSS, GCF, and NOCC personnel as required.

d. Comment. SPTs have been successfully completed at DSS 11, but late equipment implementation precluded their accomplishment at DSS 14 (see Section II, above).

2. Mission Configuration Tests

a. Purpose. The purpose of the Telemetry, Command, Monitor, or Tracking MCT is to demonstrate that the Network system(s) meets the specified level of performance when tested singly or simultaneously in the Viking configurations specified in the Network Operations Plan. The tests utilize software and hardware that have been transferred to Operations and are run with all elements of the DSN, DSS, GCF, and NOCC. Test procedures are contained in DSN 850-series documents, which provide the basis for system-level maintenance, performance verification, and prepass testing. Successful completion of the MCTs verifies the Network's capability to support VK'75.

b. Prerequisites. The following should be accomplished before MCTs are run:

(1) Completion of SOTs.

(2) Configuration of the DSN for VK'75 operations completed.

c. Personnel. MCTs are supported by the following individuals:

(1) Test Conductor: SCOEs at direction of VK'75 NOPE (or his designate).

(2) DSS, GCF, and NOCC personnel as required.

d. DSS 14 MCT status. Table 3 provides a summary of DSS 14 Configuration/Interface (C/I) MCTs and Performance Test (PT) MCTs, the results of which are described below.

(1) MCT periods 1 through 6 (from December 21, 1974 to January 5, 1975) consisted solely of isolating and rectifying hardware failures and interface problems mostly related to the newly implemented Viking telemetry and command configurations. No meaningful test results were obtained, but numerous necessary minor modifications to the hardware and streamlining of MCT procedures were accomplished.

(2) MCT period 7 (January 8, 1975) resulted in achievement of the objectives of C/I tests 1, 2, and 3 (strong signal) with data passing successfully through the three telemetry channels of Telemetry

and Command Data Subsystem (TCD) 1. Subsequent tests through February 3, 1975 resulted in completion of all TLM strong signal VK'75 MCTs and completion of Command System tests 1, 2, and 3 on the alpha Block III Receiver/Exciter (BLK III RCV/EXR) Subsystem string.

(3) The completion of these tests qualified DSS 14 to support the DSN Operational Verification Tests (OVTs) and DSN/VMCCC System Integration Tests (SITs). Final transfer of the BLK IV RCV/EXR and some associated equipment from engineering to operations will permit completion of weak signal telemetry system MCTs and the remainder of the Command and Tracking System MCTs prior to the Viking Project Ground Data System (GDS) tests and Planetary Verification Tests (PVTs).

(4) The extra time required for this testing that was necessitated by the equipment failures and debugging activities was obtained by reducing Pioneer, Mariner, and Helios tracking coverage.

3. DSN/VMCCC System Integration Tests

a. Purpose. These tests verify the interface between elements of the DSN and the VMCCC. All data flow interfaces are verified at data rates expected during mission operations. These tests also verify hardware interfaces in a multiple-mission environment.

b. Prerequisites. Successful completion of the DSN SPTs and MCTs and some DSN Operational Verification Tests (OVTs) are prerequisites to the SITs. However, while OVT completion is desirable, it is not mandatory as operational procedures are not necessarily followed during these tests.

c. Personnel. The following individuals support the SITs:

(1) Test Supervisor: VMCCC Facility Engineer.

(2) Test Conductor: VMCCC Integration Test Supervisor.

(3) DSN Test Support: VK'75 NOPE, SCOEs, and Network Operations Analysts (NOAs), plus DSS, GCF, and NOCC personnel as required.

(4) Performance Evaluation: VK'75 Ground Data System Engineer.

d. Comments. The first SITs, which are scheduled for February 25 at DSSs 11 and 14, were slipped to February 28 and March 2, respectively, to allow interfacing of the Planetary Ranging Assembly (PRA) with the BLK IV

RCV/EXC to be accomplished so that ranging support could be provided to the Pioneer 10/11 and Helios Projects.

B. Operational Verification Tests

1. Purpose. The purpose of these tests is to verify the operational readiness of the Network to support the Project Test and Training and Operational Phases. They demonstrate the operational proficiency of Network personnel in the use of operating procedures, interfaces, and equipment. They demonstrate that Network personnel are adequately trained and, in addition, provide valuable training. OVTs follow a time-compressed SOE designed to exercise all DSN operational procedures and confirm the ability of the stations to send manual commands and carry out telemetry bit rate changes in the time specified.

2. General. The first OVTs with any facility are considered to be a phase of training coupled with performance demonstration. The training aspect diminishes progressively as the tests proceed. Since all DSS, GCF, and NOCC operational shifts of personnel must be adequately exercised, it will be necessary for the Viking NOPE to initiate the scheduling of extra OVTs at specified times.

3. Prerequisites. Satisfactory completion of the following tests is a prerequisite to running OVTs with a facility:

(a) Software Acceptance Tests for all systems.

(b) System Performance Tests for all systems.

(c) Mission Configurations Tests.

4. Personnel. The following DSN Operations personnel are required:

(a) Test Conductor: VK'75 NOPE (or his designate).

(b) Normal shift complement at each of the supporting facilities required for each test, unless otherwise specified.

5. DSS 11 OVT status. Three OVTs have been conducted with DSS 11. The station was configured for VK'75 cruise/planetary operations and was cycled through simulated events with two Orbiters and a Lander. The tests are proceeding very well, and, as indicated by the following, the station is fully qualified to support the forthcoming SITs and Project tests:

a. OVT 1, February 5, 1975. This was the first Viking OVT with any station and was considered 80% successful despite the occurrence of numerous minor problems.

b. OVT 2, February 11, 1975. Some simulation problems; 85% success.

c. OVT 3, February 17, 1975. Some new problems; 75% success.

6. DSS 14 OVT status. To date, the three OVTs described below have been conducted with DSS 14. The station was configured for planetary, three-spacecraft operations (two Orbiters and one Lander) with the DSS Simulation Conversion Assembly (SCA) operating in a six-channel, fixed-pattern mode, remotely controlled from the Network Operations Control Center (NOCC). Each test was supported by a different DSS crew.

a. OVT 1, February 12, 1975. Used NOP backup configuration because of Symbol Synchronizer Assembly and Data Decoder Assembly failure (SSA and DDA). Initial problems setting up the SCA caused a late test start. The test progressed through the sequence of events (SOE) completing 74 out of the total 146 events. It was partially successful, and excellent training was obtained.

b. OVT 2, February 14, 1975. Used backup configuration (two DDA failures). Initial SCA setting up problems used substantial portion of the test time. Approximately 30% successful.

c. OVT 3, February 16, 1975. Again used backup configuration (DDA failure). Approximately 90% successful.

As anticipated with such a complex DSS configuration, numerous minor procedural problems and difficulties have become apparent and are being corrected. The DSS and NOCC operations personnel are adapting more quickly than expected to this complex mode of operations, and should be fully qualified to support the project tests and flight mission. The hardware failures are a source of concern; however, the first three tests have demonstrated that the backup configurations documented in the NOP have been a valuable investment of time and effort.

V. Conclusion

Based on the experience gained to date, and barring any serious slippages in implementation completion dates at the overseas 64-m stations, no problems are anticipated in completing the DSN test and training programs for VK'75. Successful completion of these programs will assure a high level of DSN performance in support of the subsequent VK'75 Ground Data System (GDS) tests, Project test and training exercises, and actual flight operations.

A total of 26 VK'75 GDS tests will be supported by the DSN. Initially, single system telemetry, command, and tracking tests are conducted with DSSs 11 and 14, followed by combined system/combined DSS tests with the same stations. Combined system tests are then conducted with each DSS, with some combined DSS tests simulating specific mission sequences.

DSSs 11, 14, 42, 43, 61, and 63 will have completed all GDS tests by June 15, 1975 (this includes the Planetary Verification Tests (PVTs) scheduled for DSSs 11 and 14 on April 21 and 28). On completion of the GDS tests, the DSN is committed to support the Project Flight Operations Personnel Tests (FOPTs) including Personnel Test/Training Tests (TTs), Verification Tests (VTs), Demonstration Tests (DTs) and finally the Operational Readiness Tests (ORTs), as specified in the VK'75 Flight Operations Test on Training Plan.

Reference

1. Mudgway, D. J., "Viking Mission Support," in *The Deep Space Network Progress Report 42-25*, pp. 37–42, Jet Propulsion Laboratory, Pasadena, Calif., Feb. 15, 1975.

Table 1. Completion of DSN training/testing for VK '75

DSS	Training		Testing	
	MIT, %	MDT, %	MCT,ᵃ %	OVT, %
11	77	25	100	50
14	75	20	85	45
42/43	40	10	75	0
61/63	45	12	80	0

ᵃPercentages are for Telemetry and Command System testing
required prior to first DSN/VMCCC System Integration Tests.

**Table 2. Example of a VK '75 operational
training status report**

Facility	Total number of shifts	Report date		
DSS 14	4	5-15-75		

Shift	% Training complete	Total number 100% trained / Total number on shift	Remarks
A	50	5/10	New RCVR/EXC operator
B	70	7/10	
C	66	6/9	
D	37	3/8	Two on vacation

Average training status of station = 223/4 = 55%.

Table 3. DSS 14 MCT status

Period	Test	Purpose	Time required, hours
1	Configuration Interface Test 1 on TCD String 1	Verify primary interfaces with one TCD (data flow, lock indicators, AGC voltage) with DDA-1 and SSA-1 in use.	7
	Configuration Interface Test 3 on TCD String 1	Same as Test 1 but with DDA-2 and SSA-2 in use.	5
		Period 1 total	12
2	Configuration Test 3 on TCD String 1	Same as Test 1 but interfacing secondary receiver and SDA combinations.	7
	Configuration Interface Test 4 on both TCD strings	Tests interface between all SDAs and each TCD internal bit sync loop.	3
		Period 2 total	10
3	Configuration Interface Test 1 on TCD String 2	Same as Period 1.	7
	Configuration Interface Test 2 on TCD String 2	Same as Period 1.	5
		Period 3 total	12
4	Configuration Interface Test 3 on TCD String 2	Same as Period 2.	8
		Period 4 total	8
5	Performance Test 1 (12 hours required due to strong signal system verification test and learning curve; note that subsequent test times are reduced)	Configure both TCD strings; simulating 2 Orbiters, 1 Lander at the following data rates: ORB = 16.0 kbps coded 33⅓ bps uncoded LDR = 1.0 kbps coded 8⅓ bps uncoded	8
		Period 5 total	8
6	Performance Test 2	Same as previous Performance Test (PT) but with data rates: ORB = 8.0 kbps coded 33⅓ bps uncoded LDR = 500.0 bps coded 8⅓ bps uncoded	5
	Performance Test 3	Same as previous PT but with data rates: ORB = 4.0 kbps coded 33⅓ bps uncoded LDR = 250.0 bps coded 8⅓ bps uncoded	5
		Period 6 total	10
7	Performance Test 4	Same as previous PT but with data rates: ORB = 2.0 kbps coded 33⅓ bps uncoded LDR = 250.0 bps coded 8⅓ bps uncoded	5
	Performance Test 5	Same as previous PT but with data rates: ORB = 1.0 kbps coded 8⅓ bps uncoded LDR = 250.0 bps coded 8⅓ bps uncoded	5
		Period 7 total	10

Table 3 (contd)

Period	Test	Purpose	Time required, hours
8	Performance Test 6	Same as previous PT but with data rates: ORB = 16.0 kbps uncoded 33⅓ bps uncoded LDR = 1.0 kbps coded 8⅓ bps uncoded	5
	Performance Test 7	Same as previous PT but with data rates: ORB = 8.0 kbps uncoded 33⅓ bps uncoded LDR = 500.0 bps coded 8⅓ bps uncoded	5
		Period 8 total	10
9	Performance Test 8	Same as previous PT but with data rates: ORB = 4.0 kbps uncoded 33⅓ bps uncoded LDR = 250.0 bps uncoded 8⅓ bps uncoded	5
	Performance Test 9	Same as previous PT but with data rates: ORB = 4.0 kbps uncoded 33⅓ bps uncoded LDR = 250.0 bps coded 8⅓ bps uncoded	5
		Period 9 total	10
10	Performance Test 10	Same as previous PT but with data rates: ORB = 1.0 kbps uncoded 8⅓ bps uncoded LDR = 250.0 bps coded 8⅓ bps uncoded	5
	Performance Test 11	Tests 8⅓ bps uncoded data utilizing both the internal bit sync loop (IBS) and the SSA.	5
		Period 10 total	10
11	Performance Test 11	Repeat for remaining TCD string.	5
	Performance Test 12	Same as Test 11 but 33⅓ bps uncoded data rate.	5
		Period 11 total	10
12	Performance Test 12	Same as previous but on remaining TCD string.	5
	ODR record/playback demonstration	Self explanatory.	7
		Period 12 total	12
13	Command Test 1	Manual mode test for Viking Orbiter.	4
	Command Test 2	Manual mode test for Viking Lander.	4
		Period 13 total	8
14	Command Test 3	Automatic tests.	7
	Command Test 4	Reliability Tests (with telemetry).	4
		Period 14 total	11
		Period 1 through 14 total	141

Pioneer 11 Mission Support

R. B. Miller

DSN Systems Engineering Office

The cursory scientific results of the Pioneer 11 Jupiter encounter are described.
The DSN performance during the 60-day encounter is described with emphasis
on the Command System performance.

I. Pioneer 11 Jupiter Encounter Cursory Scientific Results

The principal differences between the Pioneer 10 and 11 encounters important to the science observations are: First, Pioneer 11 went much closer to the planet; second, the outbound leg of the trajectory occurred at a different local time, that is, at a different phase relative to the Sun and out in a much higher magnetic latitude than Pioneer 10; and, third, repeat observations at a different epic in time which will help differentiate between spatial and temporal fluctuations in the observed phenomenon.

As with the Pioneer 10 Jupiter encounter, Pioneer 11 detected multiple-bowshock crossings as it approached the planet Jupiter. It is therefore indicated that extensive fluctuations in the magnetosphere of Jupiter are most likely a common occurrence. Jupiter has very large moons, which are very close to the planet compared to the planet's radius. For this reason, there was considerable interest before the Pioneer 11 encounter as to whether there were interactions between the moons and the magnetosphere. The spacecraft trajectory carried Pioneer 11 very close to the flux tube of the satellite Io. An interaction of the magnetosphere with the orbit of Io was not immediately apparent in the helium vector magnetometer data; however, there did appear to be noticeable effects due to Ganymede and Callisto. Since the Pioneer 11 trajectory swept out a much wider range of longitude than Pioneer 10, it is expected to have a much better map of the magnetic field, in particular the dipole component of the magnetic fields orientation, location, and magnitude, than was possible with Pioneer 10 data alone. There were indications from the measurements by the dual flux-gate magnetometer that the magnetic field of the planet closer than 3 Jupiter radii could not be successfully represented by an offset dipole but was more complex, and that tentative modeling of the more complex field could help explain the decimetric radio emissions from Jupiter which are observed on Earth.

The inner core or dipole region is where there is strong trapping of particles. For high-energy protons in the region greater than 35 million electron volts, Pioneer 10 measured a peak at about 3-1/2 Jovian radii, and the Pioneer 10 data ended with the downward slope after this peak. Pioneer 11 went much closer and measured the same peak as Pioneer 10, and there are indications of a

second peak closer in to the planet. Similar peaks were observed on the way in and the way out, thus indicating that the peaks are caused by a contained group of particles in the magnetic field which form a shell-like structure around the planet. These protons are the same kind of energy as is produced in a cyclotron on Earth, but produce no radio emission and are therefore undetectable except by *in situ* measurements. The inner peak for low-energy protons had an intensity of approximately 150,000,-000 protons per square centimeter per second. This core structure of charged particles appears to be one of the more stable features of the planet Jupiter.

Measurements of the electrons in the core region around Jupiter in the energy spectrum of those electrons capable of producing radio emissions indicate perhaps 10 times the abundance as was expected based on Earth observations of radio emissions. Proper modeling of this electron content versus the radio emissions is very important to astrophysics since ground-based measurements of radio emissions are used to deduce electron content in distant objects.

Concentration of high-energy protons and electrons around the plasma sheath discovered by Pioneer 10 was confirmed by Pioneer 11. It appears that there is an acceleration mechanism in effect around the plasma sheath region. The 10-hour periodicity in the radiation intensity, which was assumed to be tied more closely with the equatorial plane passage of Pioneer 10, was also evident in the higher latitude data received by Pioneer 11. A sweeping effect of the inner moons indicated by Pioneer 10 was reconfirmed by Pioneer 11. There is also confirming evidence that bursts of electrons and protons seemed to escape Jupiter's magnetosphere. This is implied by the observation of the 10-hour periodicity in particle count as the spacecraft approached the magnetosphere as early as 6 months before closest approach to the planet.

The two-month long imaging of the planet Jupiter enabled viewing changes in the visible features of that time scale, and the year-spacing between Pioneers 10 and 11 enabled seeing longer-term changes in the visible features. Pioneer 11 appeared to show a little more structure in the red spot and crisper definition of flow around the red spot. The convective plumes of rising gas about the equator were still present in the Pioneer 11 pictures.

Because of the change of Pioneer 11 to a Saturn trajectory, the ultraviolet photometer was not able to view the planet Jupiter during this flyby. However, it did view the Galilean satellites of Jupiter, and preliminary indica-tions are that the hydrogen cloud observed associated with Io during Pioneer 10 was confirmed as still existing, whereas it appears that Ganymede and Callisto do not have a hydrogen cloud associated with them.

The meteoroid detector measured a higher concentration of small particles in the Jupiter environment than in interplanetary space, and comparison of the Pioneer 10 and 11 data indicates that these particles are being focused into Jupiter from their solar orbits and are not in orbit around the planet.

The occultation experiment seemed to be highly successful again, with all open- and closed-loop data successfully recovered. The experimenter expected to see less multipath due to layering in the Pioneer 11 data than in the Pioneer 10 data because of the different trajectory. Rather surprisingly, though, the Pioneer 11 data seemed to be even more complex than the Pioneer 10 and will require extensive analysis in order to draw firm conclusions.

The celestial mechanics experiment received very good data. The nature of the Pioneer 11 trajectory meant that the possible gravitational effects of the planet Jupiter were observed over much wider latitudes, and indications are that, from a gravitational standpoint, Jupiter is a very smooth body in hydrostatic equilibrium; that is to say, no evidence of mass concentrations was observed. The perturbations of the trajectory due to the large satellites of the planet Jupiter will enable accurate determination of the masses and estimates of the densities of the four Galilean satellites. Preliminary results indicate that the two inner satellites, Io and Europa, appear to be denser than the two outer Galilean satellites, Ganymede and Callisto. This will have implications as to what their formation process may have been.

II. DSN Performance During the Pioneer 11 Jupiter Encounter

The overall DSN performance during the Pioneer 11 Jupiter encounter was at the same high level of reliability as was demonstrated during the Pioneer 10 Jupiter encounter despite the fact that launch of the Helios-A mission occurred only 7 days after the closest approach of Pioneer 11 to the planet Jupiter.

The most significant non-command problem experienced by the DSN was noise at DSSs 63 and 43 a few weeks prior to the periapsis passage. The problem at both

stations is referred to as "noise spikes," which is the term used for an increase in receiver noise due to some kind of return of the transmitted signal. The usual real-time method around the problem is to reduce the transmitter power and therefore the power of the returned noise. This workaround was acceptable during the Pioneer far encounter because of the large uplink margin that the spacecraft enjoys at the Jupiter distance. This problem was, however, a concern for the near-encounter period when possible radiation effects on the spacecraft could require high transmitter power. Noise spikes can be caused either by problems internal to the microwave system or by external reflections or arcing on the actual antenna structure. The problem at both stations was reduced to an acceptable level before near encounter. The problem at DSS 43 was isolated to a section of waveguide, which was replaced. The corresponding section of waveguide had been replaced at DSS 43 previously due to noise spiking problems. (As a consequence, a structural design change is in process for this section of waveguide.) The noise-spiking problem at DSS 63 was reduced to an acceptable level by removing the dichroic plate and ellipsoid from the top of the cones. There were no noise-spiking problems during the rest of the encounter after the above action was taken.

As with Pioneer 10, the biggest concern for the total Ground Data System was command reliability. This is the case with the Pioneer 10 and 11 missions because of the fact that both missions involve flying an extremely complex planetary encounter sequence without the aid of an on-board programmer. A tremendous number of commands are required to operate the encounter sequence, with the majority of the command requirement due to a single instrument, the Imaging Photo Polarimeter (IPP) (the details of the IPP instrument's operation and the resulting large number of commands required are described in Ref. 1). Pioneer 11 required 28% fewer commands than Pioneer 10, mostly due to better performance of the IPP instrument, where problems with gain control and stepping which existed on Pioneer 10 were corrected on the Pioneer 11 instrument prior to launch.

The overall command reliability of Pioneer 11 is compared to Pioneer 10 in Table 1. In this table, the reliability is compared using the total number of DSN aborts, where an abort is defined as a failure of a command to transmit in real time due to a DSN-caused failure or operator error. Of the 17,286 commands transmitted during the Pioneer 10 60-day encounter

period, there were seven DSN aborts, resulting in a total command reliability of 99.96%. The figure for Pioneer 11 is comparable in that there were 12,358 commands transmitted during the 60-day encounter period of which eight were aborted due to a DSN problem, resulting in a total command reliability of 99.94%. Of those eight failures, four were caused by the same type of anomaly at DSS 63, which resulted in elapsed timed commands. This failure occurred during several DSS 63 passes in November until the problem was finally isolated to a timing problem in a particular Telemetry and Command Processor.

The total number of real-time aborts is not a complete measure of the Command System reliability and its effect on the Project execution of the encounter sequence. This is because once the failure has occurred, the Project ceases trying to transmit commands until the Command System is restored. In order to get a picture of this aspect of the Command System reliability, the total number of failures (whether they caused an abort or not), along with the mean-time between failure and the mean-time to recover from the failure, is listed in Table 2. This table lists the statistics for four different levels of support. Levels of support are defined in advance as the means of committing to the Project the amount of redundancy and the amount of effort that will go into a particular track. Level 1 is the highest level of redundancy the DSN can provide, where the redundant telemetry and command strings are loaded and are processing simultaneously with the string that is supporting the track, and a maximum effort is made by station personnel to recover rapidly in the event of a failure in the real-time string. A 6-minute recovery from a failure in redundant equipment is committed during Level 1 support. As the table shows, Level 1 support was committed for just the three passes surrounding periapsis, and there were no Command System failures during that period. Level 2 support is essentially the same equipment configuration as Level 1 support, but the recovery requirement is relaxed to less than or equal to 20 minutes. From Table 2 one can see that there were 144 passes where the committed Level 2 support was provided, and during those passes there were 11 failures in the Command System with a mean-time to restore of only 6.45 minutes, well within the 20-minute requirement. There were also 26 passes labeled as Level 2-F in Table 2, where the Level 2 redundant configuration could not be completely provided because of failures in the redundant equipment. Fortunately, during none of these passes was there a failure in the prime on-line equipment. Level 3 support does not require that the backup string be loaded and running during the pass and

relaxes the recovery time requirement to 30 minutes or less. The table shows that there were 36 passes with Level 3 support in which only 2 failures occurred, and the mean-time to recover was 22 minutes, which also meets the recovery requirement. (Statistical data were extracted from Refs. 2, 3, and 4.)

As was the case for the Pioneer 10 encounter, during the Pioneer 11 encounter the overall performance of the Ground Data System, and in particular the DSN portion of the Ground Data System, was such that there was no compromise in the science return during the 60 days of encounter due to a Ground Data System or DSN problem.

References

1. Miller, R. B., "Pioneer 10 and 11 Mission Support," in *The Deep Space Network Progress Report*, Technical Report 32-1526, Vol. XVI, pp. 15–21, Jet Propulsion Laboratory, Pasadena, California, Aug. 15, 1973.

2. Hoffman, B., *Command System Reliability During Pioneer 11 Encounter*, 421-PF-CMD-050, Jan. 21, 1975 (JPL internal report).

3. Frampton, R., Hoffman, B., and Tucker, W., *Command System Monthly Report for November 1974*, 421-PF-CMD-048, Dec. 10, 1974 (JPL internal report).

4. Frampton, R., Hoffman, B., and Tucker, W., *Command System Monthly Report for December 1974*, 421-PF-CMD-049, Jan. 9, 1975 (JPL internal report).

Table 1. Command reliability during Pioneer 10 and 11 Jupiter encounter

Mission	Total commands transmitted during 60-day encounter	Total number of DSN aborts[a]	Total command reliability,[b] %
Pioneer 10	17,286	7	99.96
Pioneer 11	12,358	8	99.94

[a]Defined as failure of a command to transmit in real time due to a DSN-caused failure or error.

[b](Total commands − number of aborts)/total commands.

Table 2. Command system reliability during Pioneer 11 Jupiter encounter

Support level	Number of passes	Number of failures	Mean time between failures, h	Mean time to recover, min	Reliability,[a] %
1	3	0	—	—	100.00
2	144	11	93.8	6.45	99.89
2-F[b]	26	0	—	—	100.00
3	36	2	153.9	22	99.76

[a](Track time − total time failed)/track time.

[b]Failure to provide committed Level 2 configuration.

Helios Mission Support

P. S. Goodwin
DSN Systems Engineering Office
W. G. Meeks
Network Operations Office

Helios-A, the cooperative U.S./West German space flight, is now successfully enroute to its 0.31-astronomical unit (AU) perihelion passage of the Sun in mid-March 1975. This article describes the DSN performance to date, along with a few minor problem areas that have developed but do not jeopardize mission objectives.

I. Introduction

The previous article (Ref. 1) discussed the successful launch of Helios-1 (previously denoted Helios-A) on December 10, 1974, and the support provided by the DSN through the completion of the critical Step II maneuver sequence of the spacecraft which oriented its spin axis towards the ecliptic pole. The final sequence of the Step II maneuver oriented the spacecraft's despun high-gain antenna (HGA) towards Earth. Early science instrument telemetry data indicated a possible problem with one of the experiment packages; however, that article closed before the extent of the problem was fully diagnosed.

II. Mission Status and Operations

A. Scientific Data Versus Spacecraft High-Gain Antenna Operation

With a successful conclusion to the critical Step I and II spacecraft maneuver sequences and the subsequent orientation of its high-gain antenna, the equally critical checkout of the scientific experiment package was initiated by the Flight Team and Project Scientists. Ten mutually complementary experiments are carried by Helios-1. These experiments are designed to achieve, as a package, the science portion of the Helios mission. The experiment package checkout using the spacecraft high-gain antenna proceeded nominally through the first four experiments. Experiment 5 (the Plasma and Radio Wave Experiment) telemetry data contained an excessive level of noise. The experimenter, Dr. Gurnett of the University of Iowa, requested that the spacecraft's operational antenna be switched to the medium-gain antenna to isolate the noise source. This request was honored, but on a later pass over Deep Space Station (DSS) 42. After the initial delay caused by the Experiment 5 anomaly, final verification and configuration of the scientific experiment data package continued using the spacecraft high-gain antenna.

With the exception of Experiment 5, the checkout and analysis of the scientific experiments established the

integrity of the package. At this juncture, Experiment 5 underwent intensive analysis. The experimenter recommended spacecraft medium-gain antenna operations which would result in substantially lower, and therefore unacceptable, spacecraft telemetry data rates during the early phase of the mission. Thus, the high-gain antenna mode was selected, at the expense of Experiment 5 data, to allow operation at a higher data rate using the 26-meter deep space stations.

As Mission Operations Phase I came to a close in early January 1975, noise on Experiment 1 telemetry data was detected. Analysis of Experiment 1 (the Plasma Detectors Experiment by Dr. Rosenbauer of the Max Planck Institute) telemetry data revealed that noise generated during high-gain antenna mode operation was also affecting its data. With Experiment 5 data being essentially worthless and an important part of Experiment 1 data being lost due to high-gain antenna operation, the consensus was to increase operations on the spacecraft medium-gain antenna by using the 64-meter deep space stations.

This mutual German–NASA decision was made to maximize scientific data return of the total scientific experiment package. Medium-gain antenna operations required schedule reallocation of the 64-meter stations at Goldstone and Australia, in conjunction with the 100-meter German Effelsberg station, to maximize scientific data return during January and February, when only DSN 26-meter station support had been originally scheduled. To minimize the amount of switching between high-gain and medium-gain antenna modes, a Helios antenna switching plan was implemented.

This plan, which was agreed upon by both Flight Operations and Project Scientists, resulted in maximum medium-gain antenna operations by providing extended coverage by the large aperture antennas. The defined tracking schedule in this plan required 14 switching operations during the period January 30 to February 28, 1975, for a total of 28 switches between medium-gain and high-gain antenna modes. The DSN 26-meter stations did provide support during several of the extended medium-gain antenna mode operations, but usually only provided scheduled coverage during spacecraft high-gain antenna operating modes, which enabled maximum telemetry data rate.

The first Helios perihelion occurs March 15, 1975 with the attendant critical period coverage; the total Helios perihelion period is March 3 through March 27, 1975. During Helios perihelion coverage, when the large aperture antennas provide almost total coverage, the plan is to operate in the medium-gain antenna mode during one pass every other day.

B. Mission Phase I/II Handover

Mission Phase I was defined as that time period wherein Mission Operations were conducted by the German Operations Team, but from the JPL Mission Support Area (MSA). It encompassed pre-launch operations activities, launch, Step I and II maneuvers, and subsequent operations up to four weeks following launch—at which time Mission Operations personnel were transferred to the German Space and Operations Center (GSOC) at Oberpfaffenhofen, West Germany. Mission Phase II is defined as that time period starting with the completion of Phase I and continuing through the spacecraft entry into first solar occultation.

Transfer of Mission Control Area responsibility from JPL to GSOC was accomplished, as planned, on January 10, 1975 at 1400 GMT. Two of the three German Flight Operations Teams departed JPL on January 7, 1975 for the GSOC. To provide for a smooth handover, one operations team remained at JPL until January 14, 1975. A DSN Operations representative also accompanied the German Flight Operations Teams to GSOC to provide real-time interface and problem analysis pertaining to DSN Operations support.

Data comparison between JPL and GSOC real-time computer programs showed full agreement regarding Helios flight data. Calibration and limit values were adjusted, where needed. GSOC successfully recorded and processed data from the Effelsberg station while in a multimission configuration with West Germany's AEROS-B and Symphonie Projects, which were active simultaneously with Helios-1.

Mission control responsibility had been with the German Flight Operations Teams at JPL since the successful launch of the Helios spacecraft on December 10, 1974; however, the German Space Operations Center had actively participated since the initial spacecraft acquisition over DSS 42 (Australia). The German Effelsberg Station (GES) first tracked the spacecraft on December 13, 1974, and the German Telecommand Station (GTS) first transmitted to the spacecraft on December 15, 1974.

The continuity of mission operations during this handover verified the soundness of the Mission Phase I/II

handover plan. Interface problems and/or questions that arose were addressed as they happened by those cognizant personnel involved. Internetwork operating procedures are continuing to be refined to further enhance mission operations.

C. Operational Interface Change

With the departure of the German Flight Operations Teams, the JPL Helios mission support at JPL consisted only of the remaining JPL Mission Operations Support (MOS) teams. This JPL staffing remained at the Phase I level of support until February 1, 1975, 1530 GMT. At that time, a new operational support mode was implemented.

The new operational mode for Mission Phase II involves a German/JPL real-time voice interface between the German Network Operations Control Chief (NOCC) and the DSN Operations Chief (OPSCHIEF)/Mission Control and Computing Center Operations Controller (MCCC OPSCON), rather than via the JPL Chief of Mission Operations Support (CMOS) which was the case for Phase I. The CMOS and the JPL Command Operator will continue to support all critical Phase II operations on a shift-by-shift basis, as appropriately scheduled in advance; otherwise, support will be on a call-up basis. Within three hours of a request by GSOC to the DSN OPSCHIEF/ MCCC OPSCON, preparations for commanding in the backup mode (command initiated from JPL) will commence. This applies 24 hours a day, 7 days a week, throughout the remainder of the mission.

During all noncritical periods, including periods of commanding in the backup mode, the operational interface with JPL exists through the DSN OPSCHIEF and MCCC OPSCON. All MCCC-related coordination is handled by the OPSCON. DSN-related (including DSN Ground Communications Facility (GCF)) coordination is handled by the OPSCHIEF.

The "CMOS Call-Up" has been exercised only once since February 1, 1975. On February 4, 1975, at 2025 GMT, GSOC requested backup mode commanding from JPL because of an inoperative computer at the German Center. Within 10 minutes, the first of 9 backup commands was sent and verified. Backup command support was successful and terminated at 2225 GMT, when control was transferred back to GSOC.

The present operational mode, with its critical-period coverage and call-up provision, has proven capable of providing adequate support for the Helios-1 Mission Phases II and III. Future adjustments to this coverage, if required, will be negotiated between JPL and GSOC Mission Operations.

D. Scheduled Versus Actual Coverage

From Helios-1 launch until February 13, 1975, a total of 199 station tracks of the requested 202 tracks have been completed. Only seven 64-meter station tracks (DSS 14) were originally requested by the long-range schedule. However, the problems encountered with Experiments 1 and 5, plus a downlink signal level anomaly, caused real-time schedule changes. This involved successful negotiations with other projects to secure additional 64-meter coverage substantially greater than the original requirement for investigation of these problems. Multiple-mission tracking and Helios Project data requirements have necessitated schedule changes that have caused Helios to lose three complete passes, one over Australia and two at Goldstone. Considering the varied spacecraft tracking requirements of the DSN and similar viewperiods between Helios and Pioneer, spacecraft coverage has been very good to date.

Helios-1 will be entering a critical perihelion mission period during mid-March 1975. DSN resources will be extremely scarce because of the Mariner 10 and Pioneer Projects' critical activities also planned for mid-March. A Network Allocation Plan has been formulated by all affected projects to meet multiproject requirements. Results will be covered in the next report.

E. Helios Downlink Signal Level Variation

DSS 62 (Spain) reported on January 8, 1975 that since Helios-1 had been switched back to high-gain antenna mode on December 20, 1974, random transient phenomena had been observed on the system noise temperature chart recordings. These transients, which were noted as small but sudden changes in system temperature, could be detected in both two-way (one station) and three-way (two station) tracking configurations. This observation eliminated the possibility that the noise was being generated by the station transmitter. Occasional variations of 1 to 2 dB in the downlink signal level had also been detected.

The variation in the received signal level was one aspect of the anomaly that was not as readily observable as was the system temperature chart recording. This is due to the sample rate of the station monitoring device, the Digital Instrumentation Subsystem (DIS), and the DSS receivers being configured in narrow AGC bandwidths. The DIS algorithm uses several points to calculate the receiver AGC. With the receivers in the narrow bandwidth position, a smoothing action resulted in the

observed downlink signal level fluctuations. Therefore, only the occasional large variations of 1 to 2 dB were observable.

As a result of their astute observations, DSS 62 (Spain) initiated a thorough investigation of the Helios downlink signal during pass 27 on January 5, 1975. The variations in the downlink signal level were directly correlated to the transients on the system noise temperature chart recording during this test, but no definite trend or periodicity of the variations could be established.

The Helios downlink investigation was expanded by the DSN throughout the 26-meter network that was supporting Helios. The analysis efforts were concentrated at DSS 12 (Goldstone). DSS 62's initial experiences were duplicated at DSS 12 on passes 32 through 35. No attempt was made to isolate the problem within the spacecraft during the DSN investigation, inasmuch as it was a Helios Project responsibility. The investigation provided detailed information on the characteristics of the shape, duration, and recovery time of the variations. This phenomenon has only been observed with data associated with spacecraft high-gain antenna operation. One typical 3-1/2-hour period that was analyzed had 22 randomly occurring variations. The magnitude of the majority of these variations was 0.3 to 0.6 dB, with an average duration of approximately 5 seconds; but some had a magnitude of as much as 2 dB. The DSN has provided the above information to the German Operations Team, and is continuing to assist and provide support to GSOC, as required, in their efforts to isolate and correct the variations in Helios-1 downlink transmission.

F. Telecommunication Constraints Caused by Grayout/ Blackout

The Helios orbit, relative to the Sun–Earth line, at various times during the mission crosses either in front of or behind the Sun. As the spacecraft approaches the Sun–Earth line, telecommunication is disrupted, either by solar-generated noise or by total occultation of the spacecraft, thus causing a grayout or a blackout, respectively. The critical angular range is expected to be plus and minus 3 degrees around the Sun–Earth line.

The first grayout has occurred and data are being compiled for analysis. Results should be available for the next DSN Progress Report. DSS 62 (Spain) first observed the grayout effects during pass 70, February 17, 1975. The grayout period lasted through pass 72, and again DSS 62 was tracking the spacecraft as it exited the region of solar grayout. The most severe solar effects were observed by DSS 62 and DSS 12 (Goldstone) during pass 71, February

18, 1975. The receiver out-of-lock times were so extensive that no useful telemetry data were observable.

III. DSN System Performance for Helios

A. Telemetry System

The Helios Telemetry System performance analysis has shown that a constant improvement in the Helios telecommunications link performance versus predicted performance has occurred. This improvement has been noted in the actual residual calculations of the downlink signal level and signal-to-noise ratio (SNR). The improvement of telecommunications link performance is still being analyzed and has not yet been satisfactorily explained. Link analysis of actual performance has resulted in minor changes to the predicted pre-flight nominal predictions. These parameter adjustments are incorporated into the DSN Link Analysis and Prediction (computer) Program (LAPP) for refinements to the telemetry predictions for real-time operations.

The investigation of the aforementioned variations in the downlink signal level was one area of major analysis activities during this reporting period. Other significant analytical studies were made on the Helios telemetry threshold and the Helios performance at solar conjunction. Both of these studies will be relevant for Helios perihelion which occurs March 15, 1975. The only Helios telemetry discrepancy reports opened during this period concerned anomalous SNR residuals and were not considered significant.

B. Tracking System

The DSN Tracking System performance for Helios-1 from launch through January 31, 1975 has been nominal. Predicted spacecraft frequencies, both transmitted and received, have been extremely accurate and reliable. Trend analysis of 160 Helios tracks indicates the doppler noise for Helios-1 averaged 0.003 Hz, which is well within specification. The two-way doppler residual averaged -0.1 Hz, indicating a high reliability in the Helios Project-supplied ephemeris tapes. Several tracking discrepancy reports were opened during this period but none was considered significant.

C. Command System

During the months of December 1974 and January 1975, 6890 commands were transmitted to the Helios spacecraft. No DSN Command System aborts occurred; however, two Project command aborts have happened. A system abort is an abort due to a Command System

failure. A Project abort is a command aborted by Project, i.e., disabled while being transmitted.

Although minor command equipment anomalies have occurred throughout the network, they have caused no significant impact to the Helios Project's Command System performance.

IV. Conclusions

The Helios-1 spacecraft has now passed in front of the Sun (first syzygy) enroute to an 0.31-AU perihelion passage, which will be well into the unexplored region of the solar system inside the orbit of the planet Mercury. DSN coverage support to date has not been completely as planned before launch, due to both spacecraft anomalies and schedule difficulties with other flight project support; however, mission objectives have not been jeopardized. The scheduling difficulties are expected to increase during March 1975, especially with respect to 64-meter station coverage, due to a severe peaking of flight project activity: Mariner 10 will re-encounter the planet Mercury a day after the Helios-1 perihelion point, and Viking pre-launch implementation within the DSN will necessitate some selected station downtime. The impact on Helios-1 will be a lower science telemetry bit rate return when coverage is provided by 26-meter DSSs instead of 64-meter DSSs. Nonetheless, near-continuous coverage of the Helios-1 perihelion region is still planned for this important mission event.

Reference

1. Goodwin, P. S., "Helios Mission Support," in *The Deep Space Network Progress Report 42-25*, pp. 43–46, Jet Propulsion Laboratory, Pasadena, Calif., Feb. 15, 1975.

Helios Flight 1 Spacecraft/Deep Space Network Compatibility Test Summary

A. I. Bryan
DSN Systems Engineering Office

The Helios flight 1 spacecraft/DSN compatibility testing followed a very successful three-phase compatibility test program for the Helios prototype spacecraft. This article covers the tests from arrival of the flight 1 spacecraft at Cape Canaveral, Florida through launch. The compatibility tests consisted of (1) DSN/spacecraft radio frequency tests at both weak and strong signal levels, and (2) verification of radio frequency compatibility with the Helios flight 1 spacecraft mated to the launch vehicle at Launch Complex 41.

I. Introduction

This report covers the DSN/Helios flight 1 (F-1) spacecraft compatibility testing that extended over 56 hours from October 25 through 28, 1974, and for 8 hours on November 26, 1974. The compatibility tests performed during these periods were divided as follows:

(1) DSN/spacecraft radio frequency (RF) tests at both weak and strong signal levels during October 25–28, 1974.

(2) Verification of RF compatibility performed on November 26, 1974 with the Helios F-1 spacecraft mated to the launch vehicle at Launch Complex 41.

The DSN/Helios F-1 spacecraft compatibility testing followed a very successful three-phase program of compatibility testing between the DSN and the Helios prototype spacecraft (Ref. 1).

II. Test Report

The DSN/Helios F-1 spacecraft telecommunications compatibility testing utilized a test system that was operationally representative of a standard DSN station. The test system was under control of a computer to provide appropriate test conditions in an automatic mode of operation.

The spacecraft configurations during all of the tests were agreed upon by the Flight Project and the DSN. Spacecraft modes were selected to exercise a representative subset of all possible configurations, and to minimize the time required for completion of an adequate test program.

A. Telecommunications Compatibility Tests

These tests provided an assessment of telecommunications compatibility status between the Helios F-1 spacecraft and the Network based upon the results obtained between the DSN equipment in the STDN (MIL 71) station and the Helios F-1 spacecraft. These tests, conducted within the scheduled time period of October 25 through 28, 1974, were the final phase of the documented three-phase plan for establishing telecommunications compatibility between the Network and the Flight Project.

Procedures for conducting these tests were prepared by the Network. Test parameters and spacecraft design criteria were provided by the Helios spacecraft telecommunications engineers. The final procedures and test plans were reviewed and approved during a joint meeting of the DSN/Helios Project telecommunications representatives at Cape Canaveral. In particular, the Helios telecommunications representatives provided extensive support during the test procedure preparation and test planning phases.

The total time to accomplish the Helios F-1 spacecraft/ STDN (MIL 71) compatibility tests was 56 hours. The successful completion of the tests during this time period was due in large measure to the excellent support provided by the JPL and Goddard STDN (MIL 71) management and operating personnel.

1. Test objectives. The objectives of the tests were to verify telecommunications design compatibility between the Network and the Helios F-1 spacecraft. The design compatibility was previously established between the DSN and the Helios prototype spacecraft in testing at the JPL Compatibility Test Area at Pasadena.

A selected set of standard tests, as specified in the Deep Space Network/Flight Project Interface Compatibility Test Design Handbook, for verifying transponder RF, command, telemetry, and metric data compatibility were performed. In addition, telemetry erasure rate tests were extended in response to Project requests, to include Data Decoder Assembly (DDA) statistical data. All tests were accomplished in accordance with the Network Test and Training Plan for Helios Project.

2. Test description. The Helios F-1 spacecraft was configured for flight operations and STDN (MIL 71) was configured to simulate a DSN station. The spacecraft was located in the clean room of Building AO, Cape Canaveral AFS, Florida, and STDN (MIL 71) was located at the MILA-STDN Station, Kennedy Space Center, Florida. An S-band RF air link of approximately 16 km (10 miles) was

utilized between a 1.85-meter antenna at Building AO and a 1.2-meter antenna at the STDN station. RF link amplitude variations were 0.5 dB peak-to-peak for the critical tests in telemetry and command.

The STDN station software utilized in performing these tests was supplied by the DSN and was a subset of software officially released to the station for Helios Project support. The programs consisted of:

(1) Telemetry and Command Data Handling Program. This program provides independent control of the commanding and telemetry handling functions. Commands may be controlled manually from the station or automatically from the Mission Control and Computing Center. Telemetry may be decoded, formatted, and transmitted to the Mission Control and Computing Center for decommutation and display.

(2) Planetary Ranging Assembly Program. This program provides either continuous spectrum or discrete spectrum operation for determining very accurate range estimates of a spacecraft at planetary distances.

(3) Helios Decommutation and Data Validation Program. This program provides the capability of decommutating spacecraft engineering data and display at the station for verifying spacecraft parameters during compatibility testing.

(4) Multiple-Mission Test Program. This program provides a flexible test capability for performing bit error rate, word error rate, and signal-to-noise estimates.

3. Test results. Table 1 provides a summary of the test results. Significant events and data in the areas of RF, telemetry, command and metric data are described below:

a. Radio frequency acquisition and tracking. The criteria established for acquisition and sweep rates, spectrums, threshold, carrier, and subcarrier phase jitter measurements were either successfully met or exceeded. Special RF spectrum data required for the launch and first Goldstone pass modes were performed and provided to the DSN Network Operations Project Engineer for initial spacecraft acquisition procedures.

b. Telemetry. Bit error rate (BER) measurements at 8 and 32 bps uncoded were very successful with respect to test criteria. The spacecraft was configured for all experiments during these two tests in order to provide maximum data density to the Symbol Synchronizer

Assembly. ST_B/N_0 levels corresponding to an expected BER of 10^{-4} were established for both tests.

Frame deletion rate measurements at 256, 1024, and 2048 sps were equally successful. A special overfill program to the Helios Decommutation and Data Validation Program, provided by Office 420, was utilized to output Data Decoder Assembly statistical data. The data included number of frames counted, number of computations per frame, erased frames counted, and a distribution table of these data. The ST_s/N_0 levels established for these tests simulated 0.418 AU for 256 sps, 0.202 AU for 1024 sps, and 0.705 AU for 2048 sps. Additionally, the utilization of the special overfill to the Helios Decommutation and Data Validation Program provided the means of extending these tests to obtain the distribution of computations per frame. Therefore, the system telemetry performance was more critically determined.

c. Command. Command performance was performed on a functional basis due to limited test time. Command performance was successfully simulated for 2.0-AU conditions from a 26-meter antenna station at 10 kW (uplink −142.1 dBm, without ranging) and a 64-meter antenna station at 20 kW (uplink −136.6 dBm, with ranging). Both spacecraft command detectors (512 and 448 Hz) were tested.

d. Metric. The polarity of the spacecraft "ranging channel" was found to be INVERTED. This condition, different from the prototype spacecraft, represented no major impact as provisions for correcting phase reversal was resident in the Planetary Ranging Assembly software. With the exception of phase reversal, both continuous and discrete ranging measurements were well within expected values.

No differenced range versus integrated doppler (DRVID) testing was performed due to limited test time and higher priority items.

B. RF and Data Verification Tests

These tests provided an assessment of telecommunications compatibility status between the DSN, represented by DSN equipment in the STDN (MIL 71) station, and the Helios F-1 spacecraft after encapsulation and mating to the launch vehicle. These tests conducted on November 26, 1974, were a subset of tests performed previously between the F-1 and the DSN equipment in the STDN (MIL 71) station at Merritt Island, Florida, in October 1974.

Procedures for conducting these tests were prepared by the DSN, and spacecraft test parameters and design criteria were provided by the Helios Telecommunications Project. The final procedures were reviewed and approved during a joint meeting of the DSN/Helios Project Test Team at Cape Canaveral.

The total time to accomplish the Helios F-1 spacecraft STDN (MIL 71) compatibility tests was 8 hours.

1. Test objectives. The objective of the tests was to verify continued compatibility between the DSN and the Helios F-1 spacecraft after the spacecraft had been configured for launch operations. All tests were accomplished in accordance with the Network Test and Training Plan for Helios Project.

2. Test description. The Helios F-1 spacecraft was in launch configuration and STDN (MIL 71) was configured to simulate a DSN station. The spacecraft was located at Launch Complex 41, Cape Canaveral AFS, Florida and STDN (MIL 71) was located at the STDN (MIL Station, Kennedy Space Center, Florida). An S-band RF air link of approximately 16 km (10 miles) was utilized to establish the spacecraft/ground station interface. The spacecraft transmit/receive function was performed by connecting a test point at the shroud to a 1.2-meter antenna connected to the launch service tower.

The ground station software utilized in performing these tests was supplied by the DSN and was a subset of software officially released to the station for Helios Project support. The programs consisted of:

(1) Telemetry and Command Data Handling Program. This program provides independent control of the commanding and telemetry handling functions. Commands may be controlled manually from the station or automatically from the Mission Control and Computing Center. Telemetry may be decoded, formatted, and transmitted to the Mission Control and Computing Center for decommutation and display.

(2) Planetary Ranging Assembly Program. This program provides either continuous spectrum or discrete spectrum operation for determining very accurate range estimates of a spacecraft at planetary distances.

(3) Helios Decommutation and Data Validation Program. This program provides the capability of decommutating spacecraft engineering data and display at the station for verifying spacecraft parameters during compatibility testing.

3. Test results. Table 2 provides in summary form the test results. Significant events and/or items in the areas of RF, telemetry, command, and metric data are described below:

a. Radio frequency. Short-term RF link fluctuations throughout the test period were observed to ±1.5 dB on the link between Launch Complex 41 and MIL 71. All phases of the RF tests were successfully completed.

b. Telemetry. Short-term RF link variations during subtest 1 were observed to be ±1.5 dB. However, variations during subtest 3 were observed to be ±7.5 dB and resulted in the Telemetry and Command Subsystem (TCD) dropping lock occasionally. (This same situation was experienced during the Helios prototype spacecraft/ Launch Complex 41 test.) In view of the adverse conditions under which subtest 3 was conducted, it was an "engineering judgement" that both telemetry tests performed satisfactorily.

c. Command. Short-term RF link variations during command subtest 1 were observed to be ±6 dB. Variations during subtest 3 were ±2 dB. During subtest 1, 114 commands were sent successfully, and during subtest 3, 118 commands were sent successfully.

d. Metric. Ranging system acquisition time was successfully completed with no problems experienced.

III. Conclusions

The successful conclusion of the formal DSN/Helios compatibility program enabled the establishment of telecommunications compatibility and was evidenced by the successful launch of the Helios F-1 spacecraft on December 10, 1974.

The importance of a formal compatibility test program is clearly demonstrated by the problem areas uncovered, verified, and resolved during the DSN/Helios testing. Prominent problem areas discovered and resolved during this test program were:

(1) Deficiencies in the engineering model transponder. The transponder exhibited lag in sensitivity, pushing effects at strong uplink signal levels, instability of the voltage-controlled crystal oscillator, and improper shielding.

(2) Polarity of the ranging channel in the F-1 spacecraft was inverted. This condition was different from the prototype spacecraft.

(3) Many hundreds of hours of test time were used at the DSN station (DSS 71) to determine optimum modulation indices for the Helios Mission. A full description of this testing was published in Ref. 2.

(4) An elaborate test system to simulate uplink and downlink amplitude, phase, and frequency modulation conditions during the spacecraft Step II maneuver was performed. This simulation demonstrated that the spacecraft could be successfully commanded during this very critical phase of flight.

These problems, undetected and unresolved prior to launch, would have presented serious operational problems to the Network with the spacecraft in flight.

References

1. Bryan, A. I., "Helios Prototype Spacecraft Deep Space Network Compatibility Test Summary," in *The Deep Space Network Progress Report 42-23*, pp. 22–36, Jet Propulsion Laboratory, Pasadena, California, Oct. 15, 1974.

2. Layland, J. W., "DSS Tests of Sequential Decoding Performance," in *The Deep Space Network Progress Report 42-20*, pp. 69-77, Jet Propulsion Laboratory, Pasadena, California, Apr. 15, 1974.

Test date (1974)	Test title	Test No.	Deep Space Network								CAR SUP	Bit rate	EXC
			BLK III RCV	BLK III EXC	PRA RNG	CMD	Uplink doppler, Hz/s	Uplink offset, kHz	CMA SUBC offset	SDA SUBC offset			
10/25	Spacecraft maximum sweep and acquisition rate	I. 1	1	1	OFF	OFF	500	—30	NA	NA	HI	2048	1
			1	1	OFF	OFF	500	+30	NA	NA	HI	2048	1
			1	1	OFF	OFF	80	—9.7	NA	NA	HI	2048	1
			1	1	OFF	OFF	80	+9.9	NA	NA	HI	2048	1
10/26	Downlink spectrum analysis	II. 1	1	1	OFF	OFF	NA	NA	NA	NA	HI	2048	1
		II. 2	1	1	OFF	OFF	NA	NA	NA	NA	HI	128	1
		II. 3	1	1	OFF	OFF	NA	NA	NA	NA	LO	32	1
		II. 7	1	1	ON (Idle seq.)	NA	NA	NA	NA	NA	HI	2048	1
		II. 10	1	1	ON	ON	NA	NA	NA	NA	HI	128	1
10/25	Uplink threshold	III. 1	1	1	OFF	OFF	NA	NA	NA	NA	HI	128	1
		III. 2	1	1	ON	OFF	NA	NA	NA	NA	HI	128	1
		III. 3	1	1	OFF	OFF	NA	NA	NA	NA	HI	128	1
10/25	Carrier residual phase jitter	IV. 1	1	1	OFF	OFF	NA	NA	NA	NA	HI	2048	1
		IV. 2	1	1	OFF	OFF	NA	NA	NA	NA	HI	2048	2
		IV. 3	1	1	OFF	OFF	NA	NA	NA	NA	HI	2048	1
			1	1	OFF	OFF	NA	NA	NA	NA	HI	2048	1
		IV. 4	1	1	OFF	OFF	NA	NA	NA	NA	HI	2048	1
			1	1	OFF	OFF	NA	NA	NA	NA	HI	2048	1

Table 1. DSN/Helios F-1 spacecraft telecommunication test summary

Spacecraft							Test data		Test Time, min	Test comments
RCV	PWR	ANT	TWT	RNG	S/C DM	S/C FM	Performance	Criteria		
1	HP	MGA	2	OFF	0	4	Acquired @ −100.0 dBm; tracked to +32.5 kHz	Acquire @ −100.0 dBm; track to +32.5 kHz	125	Acquired U/L @ best lock (VCXO 1) 2115.679152 MHz
1	HP	MGA	2	OFF	0	4	Acquired @ −100.0 dBm; tracked to −32.5 kHz	Acquire @ −100.0 dBm; track to −32.5 kHz		Acquired U/L @ best lock (VCXO 1) 2115.679152 MHz
1	HP	MGA	2	OFF	0	4	Acquired @ −141.0 dBm; tracked to +32.5 kHz	Acquire @ −141.0 dBm; track to −32.5 kHz		Acquired U/L @ best lock (VCXO 1) 2115.679152 MHz
1	HP	MGA	2	OFF	0	4	Acquired @ −141.0 dBm; tracked to −32.5 kHz	Acquire @ −141.0 dBm; track to −32.5 kHz		Acquired U/L @ best lock (VCXO 1) 2115.679152 MHz
1	HP	MGA	1	OFF	0	4	No spurs observed	No spurious signal within 30 dB of carrier	17	Subcarrier OSC No. 2 noncoherent mode
1	LP	LGA	NA	OFF	0	4	No spurs observed	No spurious signal within 30 dB of carrier	15	Subcarrier OSC No. 1 noncoherent mode
1	LP	LGA	NA	OFF	0	4	No spurs observed	No spurious signal within 30 dB of carrier	20	Subcarrier OSC No. 1 noncoherent mode
1	LP	LGA	1	OFF	0	4	No spurs observed	No spurious signal within 30 dB of carrier	15	VCXO 1, coherent (Goldstone first acq) mode
1	HP	MGA	1	ON	0	4	No spurs observed	No spurious signal within 30 dB of carrier	16	VCXO 1, coherent mode
1	HP	MGA	2	OFF	0	4	−155 dBm	−155.0 ± 1 dBm	35	Threshold value is average of 3 measurements
1	HP	MGA	2	ON	0	4	−155 dBm	−155.0 ± 1 dBm	43	
2	HP	LGA	2	OFF	0	4	−154 dBm	−155.0 ± 1 dBm	38	
1	HP	MGA	1	OFF	0	4	1.95 deg rms	5.7 deg rms	40	U/L level −100 dBm
1	HP	MGA	2	OFF	0	4	1.74 deg rms	5.7 deg rms	9	U/L level −100 dBm
1	HP	MGA	2	OFF	0	4	1.77 deg rms	2.86 deg rms	25	U/L level −100 dBm
1	HP	MGA	2	OFF	0	4	14.80 deg rms	22.9 deg rms		U/L level −144 dBm
2	HP	LGA	2	OFF	0	4	1.73 deg rms	2.86 deg rms	20	U/L level −100 dBm
2	HP	LGA	2	OFF	0	4	16.00 deg rms	22.9 deg rms		U/L level −144 dBm

Test date (1974)	Test title	Test No.	Deep Space Network										
			BLK III RCV	BLK III EXC	PRA RNG	CMD	Uplink doppler, Hz/s	Uplink offset, kHz	CMA SUBC offset	SDA SUBC offset	CAR SUP	Bit rate	EXC
10/25	Downlink threshold	V. 1	1	1	OFF	OFF	NA	NA	NA	NA	III	128	1
		V. 3	1	1	OFF	OFF	NA	NA	NA	NA	III	128	2
		V. 5	1	1	OFF	OFF	NA	NA	NA	NA	HI	128	1
			1	1	OFF	OFF	NA	NA	NA	NA	HI	128	1
		V. 6	1	1	ON	OFF	NA	NA	NA	NA	HI	128	1
			1	1	ON	OFF	NA	NA	NA	NA	HI	128	1
10/26	Spacecraft ranging delay	VI. 2	1	1	ON	OFF	NA	NA	NA	NA	HI	128	1
		VI. 4	1	1	ON	OFF	NA	NA	NA	NA	HI	128	1
		VI. 9	1	1	ON	OFF	NA	NA	NA	NA	HI	128	1
		VI. 10	1	'	ON	OFF	NA	NA	NA	NA	HI	128	1
10/26	Ranging system acquisition time	VII. 1	1	1	ON	OFF	NA	NA	NA	NA	HI	128	1
		VII. 2	1	1	ON	OFF	NA	NA	NA	NA	HI	128	1
10/26	Bit error rate	VIII. 1	1	1	OFF	OFF	NA	NA	NA	NA	LO	8 (UNC)	1
		VIII. 2	1	1	OFF	OFF	NA	NA	NA	NA	LO	32 (UNC)	1
10/28	Telemetry erasure rate	IX. 1	1	1	OFF	ON	NA	NA	NA	NA	HI	128	1
10/27		IX. 2	1	1	ON	ON	NA	NA	NA	NA	HI	512	1
		IX. 3	1	1	OFF	ON	NA	NA	NA	NA	HI	1024	1

Table 1 (contd)

Spacecraft							Test data		Test Time, min	Test comments
RCV	PWR	ANT	TWT	RNG	S/C DM	S/C FM	Performance	Criteria		
1	HP	MGA	1	OFF	0	4	−158.8 dBm	−159.5 ± 3 dBm	21	Noncoherent mode
1	HP	MGA	2	OFF	0	4	−158.7 dBm	−159.5 ± 3 dBm	20	Noncoherent mode
2	HP	LGA	1	OFF	0	4	−158.3 dBm	−159.5 ± 3 dBm	19	Coherent mode; U/L level −100 dBm
2	HP	LGA	1	OFF	0	4	−158.7 dBm	−159.5 ± 3 dBm	18	Coherent mode; U/L level −144 dBm
1	HP	MGA	1	ON	0	4	−159.0 dBm	−159.5 ± 3 dBm	20	Coherent mode; U/L level −100 dBm
1	HP	MGA	1	ON	0	4	−159.0 dBm	−159.5 ± 3 dBm	22	Coherent mode; U/L level −100 dBm
1	HP	HGA	1	ON	0	4	S/C delay: 1364 ns		15	−100 dBm U/L
1	HP	MGA	1	ON	0	4	S/C delay: 13.70 ns	No requirement	15	−100 dBm D/L
1	MP	MGA	2	ON	0	4	S/C delay: 1384 ns	RNG stability: ±500 ns	22	"Phase reversal" vs prototype spacecraft
1	MP	MGA	2	ON	0	4	S/C delay: 1369 ns		15	VI 2, 4, 10 discrete VI 9 continuous
1	HP	MGA	1	ON	0	4	22 min 40 s	<45 min	25	Continuous spectrum
1	HP	MGA	1	ON	0	4	1 min 18 s	<2 min	10	Discrete spectrum U/L level −134.5 dBm D/L level −135.0 dBm
1	HP	MGA	1	OFF	0	4	0 errors in 10^4 bits	10^{-4}	210	U/L −148.1 dBm D/L −135 dBm
1	HP	MGA	1	OFF	0	4	0.09×10^4	10^{-4}		Uncoded mode
1	HP	MGA	2	OFF	0	4	D/L threshold −147.5 D/L level −128.3	10^{-3}	230	D/L levels providing 10^{-3} erasure rate were below link criteria
1	HP	MGA	2	ON	0	4	D/L threshold −141.0 U/L level −137.9	10^{-3}	200	Test to estimate telemetry performance by distribution of computations/frame
1	HP	HGA	2	OFF	0	4	D/L threshold −138.4	10^{-3}	60	

Test date (1974)	Test title	Test No.	Deep Space Network								CAR SUP	Bit rate	EXC
			BLK III RCV	BLK III EXC	PRA RNG	CMD	Uplink doppler, Hz/s	Uplink offset, kHz	CMA SUBC offset	SDA SUBC offset			
10/26	Subcarrier frequency and phase jitter	X. 1	1	1	OFF	OFF	NA	NA	NA	NA	HI	128	1
		X. 2	1	1	OFF	OFF	NA	NA	NA	NA	HI	128	2
		X. 3	1	1	OFF	OFF	NA	NA	NA	NA	HI	128	2
10/26	Spacecraft command performance	XI. 1	1	1	OFF	ON	NA	NA	NA	NA	HI	128	1
		XI. 2	1	1	ON	ON	NA	NA	NA	NA	HI	512	1
10/27		XI. 3	1	1	OFF	ON	NA	NA	NA	NA	HI	1024	1

NOTE: See Table 3 for definition of terms used.

Table 1 (contd)

| Spacecraft | | | | | | | Test data | | Test Time, min | Test comments |
RCV	PWR	ANT	TWT	RNG	S/C DM	S/C FM	Performance	Criteria		
NA	LP	LGA	NA	OFF	0	4	0.835 deg rms 32,768 Hz	1.15 deg rms 32,768 Hz	25	S/C DHE OSC No. 1 Chain 1
NA	LP	LGA	NA	OFF	0	4	0.84 deg rms 32,768 Hz	1.15 deg rms 32,768 Hz	24	S/C DHE OSC No. 1 Chain 2
NA	LP	LGA	NA	OFF	0	4	0.86 deg rms 32,768 Hz	1.15 deg rms 32,768 Hz	25	S/C DHE OSC No. 2 Chain 2
1	HP	MGA	2	OFF	0	4	54 commands accepted and processed	All commands accepted by spacecraft	20	VCXO 1, coherent, command S/C @ 512 Hz
1		MGA		ON	0	4	54 commands accepted and processed	All commands accepted by spacecraft	14	U/L @ −142.1 dBm (2.9 dB above command threshold)
2	HP	HGA	2	OFF	0	4	23 commands accepted and processed	All commands (continuous) accepted and processed	14	VCXO 2, coherent, command S/C @ 448 Hz U/L @ −138.1 dBm (5.9 dB above command threshold)

Test date (1974)	Test title	Test No.	Deep Space Network									
			BLK III RCV	BLK III EXC	PRA RNG	CMD	Uplink doppler, Hz/s	Uplink offset, kHz	CMA SUBC offset	SDA SUBC offset	CAR SUP	Bit rate
11/26	Spacecraft maximum sweep and acquisition rate	I.1	−106 dBm 23.412423	−108.5 dBm 22.038540	OFF	OFF	500	−30 to +32.5	NA	NA	HI	2048
			−106 dBm 23.412423	−108.5 dBm 22.038540	OFF	OFF	500	+30 to −32.9	NA	NA	HI	2048
11/26	Uplink threshold	III. 1	−110 dBm 23.412423	22.038540	OFF	OFF	NA	NA	NA	NA	HI	128
		III. 3	−113 dBm 23.412481	22.038594	OFF	OFF	NA	NA	NA	NA	HI	128
11/26	Downlink threshold	V. 1	23.412401	−110 dBm 22.038520	OFF	OFF	NA	NA	NA	NA	HI	128
11/26	Ranging system acquisition time	VII.1	−112 dBm 23.412401	−112 dBm with mod 22.038520	ON	OFF	NA	NA	NA	NA	HI	128
11/27	Telemetry performance	IX. 1	−112 dBm 23.412401	−109 dBm 22.038520	OFF	ON	NA	NA	NA	NA	HI	128
		IX. 3	−116 dBm 23.412483	−107 dBm 22.038595	OFF	ON	NA	NA	NA	NA	HI	1024
11/27	Spacecraft command performance	XI. 1	−117 dBm 23.412423	−113.5 dBm 22.038540	ON	ON	NA	NA	NA	NA	HI	128
		XI. 3	−116 dBm 23.412482	−108 dBm 22.038494	ON	ON	NA	NA	NA	NA	HI	1024

NOTE: 1. Block III receiver 1, exciter 1 used for all tests.
2. See Table 3 for definition of terms used.

Table 2. DSN/Helios F-1 spacecraft telecommunications test summary

Spacecraft								Test data		Test time, min	Test comments
EXC	RCV	PWR	ANT	TWT	RNG	S/C DM	S/C FM	Performance	Criteria		
1	1 & 2	HP	LGA	2	OFF	0	4	Acquired and tracked	Acquire at best lock; track to +32.5 kHz	71	2115.699 kHz best lock frequency S/C receiver 1
1	1 & 2	HP	LGA	2	OFF	0	4	Acquired and tracked	Acquire at best lock; track to −32.5 kHz		
1	1	HP	LGA	2	OFF	0	4	−158.8 dBm	To be measured	40	Average of 3 runs; link variance 1.5 dB p-p
1	2	HP	LGA	2	OFF	0	4	−159.0 dBm	To be measured	34	Average of 3 runs; link variance 1.5 dB p-p
1	1	HP	LGA	1	OFF	0	4	−158.3 dBm	−139.0 ± 2 dBm	24	Average of 3 runs; link variance 1.5 dB p-p
1	1	HP	LGA	1	ON	0	4	1-min acquisition 98738 RU	TBD	23	15 components discrete; 1 min integration time
1	1	HP	LGA	2	OFF	0	4	Decommutated data satisfactory	30 min of decommutated data	83	Link variance 3 dB p-p
1	2	HP	LGA	2	OFF	0	4	Decommutated data satisfactory when TCD in lock	30 min of decommutated data	74	Link variance 15 dB p-p; TCD out of lock periodically
1	1	HP	LGA	2	OFF	0	4	All good commands (114 commands)	All commands successfully received by spacecraft	46	Discrete ranging on commands 501-506
1	2	HP	LGA	2	OFF	0	4	All good commands (118 commands)	All commands successfully received by spacecraft	39	Discrete ranging on commands 501-502

Table 3. Definitions for Tables 1 and 2

ANT	Spacecraft antenna
Bit rate	Clock frequency of the telemetry bit information
BLK III exciter	The standard DSN S-band exciter equipment
BLK III receiver	The standard DSN S-band receiving equipment
CAR SUP	Downlink carrier suppression due to telemetry modulation
CMA SUBC offset	Command modulation assembly subcarrier frequency offset relative to nominal
CMD	Telemetry and command data handling command modulation
EXC	Spacecraft S-band exciter equipment
HGA	High-gain antenna
LGA	Low-gain antenna
MGA	Medium-gain antenna
PRA RNG	Planetary ranging assembly modulation
PWR	Spacecraft transmitter power mode
RCV	Spacecraft S-band receiving equipment
RNG	Spacecraft ranging channel
S/C DHE	Spacecraft data handling equipment
S/C DM	Spacecraft data mode
S/C FM	Spacecraft data format
SDA SUBC offset	Subcarrier demodulator assembly subcarrier frequency offset relative to nominal
TWT	Traveling wave tube amplifier
UNC	Uncoded
Uplink doppler	Ramp rate of the uplink carrier frequency
Uplink offset	Uplink carrier frequency offset relative to the spacecraft recei/er rest frequency

A Demonstration of Radio Interferometric Surveying Using DSS 14 and the Project ARIES Transportable Antenna*

K. M. Ong, P. F. MacDoran, J. B. Thomas, H. F. Fliegel, L. J. Skjerve, and D. J. Spitzmesser
Tracking and Orbit Determination Section

P. D. Batelaan
Communications Elements Research Section

S. R. Paine
DSN Engineering Section

M. G. Newsted
Trend Western Corporation

A precision geodetic measurement system (ARIES for Astronomical Radio Interferometric Earth Surveying) based on the technique of very long baseline interferometry has been designed and implemented through the refurbishment of a 9-m transportable antenna, together with the 64-m Goldstone antenna (DSS 14) of the Deep Space Network. A series of experiments designed to demonstrate the inherent accuracy of the transportable interferometer concept was performed on a 307-m baseline during the period from December 1973 to June 1974. This short baseline was chosen in order to obtain a comparison with a conventional survey with few-centimeter accuracy and to minimize interferometry errors due to transmission media effects, source locations, and Earth orientation parameters. These interferometry measurements, representing approximately 28 hours of data, were in excellent agreement with the survey baseline in all dimensions within the formal uncertainty of 3 cm. The ARIES transportable antenna has now entered its next phase of demonstrations over a 180-km baseline (Goldstone to JPL) and has initiated a tectonic motion monitoring program within the southwestern United States.

I. Introduction

In recent years, the technique of independent-station radio interferometry (commonly called "very long baseline interferometry" or VLBI) has been continuously developed and to some degree successfully applied to the problem of accurately determining baseline vectors between fixed reference points on Earth relative to an "inertial" coordinate system defined by the virtually time-invariant directions of extragalactic radio sources. Astronomers and geophysicists alike have been enthusiastic about the use of this new technique as an accurate geodynamic/geodetic measurement tool.

Since other interferometry baseline measurements (e.g., Refs. 1–4) have been summarized elsewhere (e.g., Ref. 5), they will not be discussed in detail here. All of those previous VLBI experiments utilized non-portable antennas that, unfortunately, lack the mobility that would be required in an extensive geodetic monitoring program. For example, a program to thoroughly monitor global plate tectonics or even a regional strain field, such as in the seismically active Southern California region, would require accurate geodetic measurements of many reference baselines. Furthermore, in a test of the recently advanced dilatancy/diffusion model for earthquakes (Refs. 6–8), it would be especially important to be able to make frequent measurements in three dimensions in areas that are suspected of dilatant behavior. Since it is not economically feasible to build a large network of fixed interferometer antennas all over the world to monitor such complex crustal motions, the question arises whether accurate interferometric surveying is possible with a system in which one element, or perhaps both elements, of the interferometer are transportable, as described in Ref. 9.

In pursuit of this question, a preliminary signal-to-noise analysis at the Jet Propulsion Laboratory (JPL) indicated that, with existing low-noise receivers, an antenna with a diameter of approximately 10-m could be used in conjunction with the Goldstone Mars Deep Space Station (DSS 14) 64-m antenna, provided that the incoming radio signals were recorded with a relatively wide bandwidth (greater than ~2 MHz). Fortunately, a wide-band recording system with a 2-MHz bandwidth already existed at the time in the form of the Mark II Very Long Baseline (VLB) System of the National Radio Astronomy Observatory (NRAO) (Ref. 10). Consequently, under Project ARIES (for *Astronomical Radio Interferometric Earth Surveying*), a surplus U.S. Army 9-m transportable satellite communications station was obtained and modified at JPL for the specific purpose of demonstrating independent-station interferometry with a portable antenna. The transportable antenna, which will be referred to as the ARIES station, was made ready for its first interferometry experiments in the fall of 1973.

Before the technique of independent-station interferometry, including portable-antenna interferometry, can gain acceptance as a valuable geodetic/geodynamic measurement tool, a series of demonstration experiments are first required to establish its reliability and accuracy at the centimeter level. Among the many possible demonstrations, a short baseline experiment is one of the most effective for several reasons, as summarized by Thomas et al. (Ref. 5). Briefly, short baseline interferometry experiments can lead to accurate three-dimensional, Earth-fixed baseline measurements that expose and therefore effectively test many potential interferometer problems. More importantly, a geometrically complete, centimeter-level accuracy demonstration is possible for a short baseline since conventional survey techniques can measure short baselines in three-dimensions with accuracies at the centimeter level.

In addition to demonstrating portable station interferometry, the present experiments were motivated by the difficulties encountered in comparing survey and interferometry baselines at the 10- to 20-cm level during the analysis of the 16-km Goldstone experiments (Ref. 5). The accuracy of that comparison was significantly degraded by survey uncertainties due to geoid variations and possible interferometer instrumental effects. Since an independent accuracy check was desired, an even shorter baseline demonstration was conducted in which geoidal uncertainties were less significant. Thus, the ARIES antenna was placed approximately 307 meters away from the 64-m antenna for these portable antenna demonstrations. (See photograph, Fig. 1. The apparent relative size of the antennas is inaccurate due to the difference in their distances from the camera. The true sizes of the antennas may be visualized by noting that the subreflector of the Mars antenna is approximately the same diameter as the ARIES antenna.)

In summary, the purpose of this series of ARIES 307-m baseline experiments was to demonstrate the following capabilities of independent-station radio interferometric surveying:

(1) Attainment of few-centimeter *formal uncertainties* in three dimensions.

(2) Demonstration of few-centimeter *accuracy* in three dimensions by comparing with a conventional survey.

(3) Accurate measurement of small known changes in the baseline vector.

II. Instrumentation

Even though the basic concepts behind radio interferometry are ostensibly simple, the details involved in instrumentation, data reduction, and analysis are quite involved. Since many of these aspects of interferometry have been amply described elsewhere (e.g., Refs. 5 and 11–17), attention will be focused primarily on the features that are specific to the present transportable system.

The present system employs the Goldstone 64-m Mars antenna with an operational system noise temperature of 20–50 K and an efficiency of approximately 0.55, in conjunction with the transportable 9-m ARIES antenna with a system noise temperature of approximately 200 K and efficiency of 0.50. The system noise at ARIES was added almost entirely at the first stage of amplification, while for the Mars antenna, it was a sum of instrumental noise, background radio-frequency noise, and source noise. The group delay variation effect experienced at the Mars station in previous measurements (Ref. 5) has been overcome for the present experiments by the use of a superconducting magnetic shield surrounding the traveling-wave maser amplifier.

As illustrated in Fig. 2, a fixed and transportable antenna pair simultaneously receive random radio signals emitted by a compact extragalactic radio source. Because of a difference in the raypaths from the extragalactic radio source to each station, reception of the signals will be delayed at one antenna relative to the other. This "geometric delay," τ_g, and its time derivative (proportional to the so-called "fringe frequency," ν_f) are the primary observables of an interferometer. Both quantities are sensitive functions of the baseline vector between the two antennas. Therefore, by observing many different radio sources widely spread over the sky, one can obtain an accurate three-dimensional determination of the baseline vector by means of a simultaneous least-squares fit to the ensemble of measured delay and fringe frequency values. In the present experiments, the delay measurements are the main observables.

There is, at each station, a very stable frequency reference that is used to derive the local oscillator signals for the radio receivers and to drive the station clock. At the ARIES station, a Hewlett-Packard rubidium (HP5065A) oscillator served as the frequency reference for the local oscillator and the timing signals; at the Mars station, a JPL hydrogen maser was used. The radio receiver output is digitally sampled and time-tagged according to the clock signals. This stream of time-tagged digital data is then input to a magnetic tape recorder at each station. In the present implementation, the NRAO Mark II 4-Mbit/s recording system (Ref. 10) is used.

In order to determine the time delay observable with high precision, the extragalactic radio signals are recorded in two separate frequency channels and the so-called "bandwidth synthesis" technique (Refs. 13 and 18) is employed. In the present ARIES system, the signals were received at two 2-MHz frequency bands centered at 2311 and 2271 MHz, and recorded on alternate seconds at a 4-Mbit/s rate using Mark II terminals at each site. A block diagram of the system configuration is shown in Fig. 3. The delay values produced by this system possessed uncertainties due to system noise that ranged between 0.05 and 0.5 ns for correlated flux strengths between 2 and 20 Jy. (1 Jy $\equiv$ 1 Jansky $\equiv$ 1 flux unit $= 1 \times 10^{-26}$ watts/ m²/Hz.) The techniques of extracting the time delay and fringe frequency observables will be discussed next.

III. Data Reduction Technique

In these ARIES experiments, about a dozen compact radio sources were observed simultaneously at the two antennas in 20–30 separate scans of approximately 10-minute duration over a total time span of 6–10 hours. After each experiment, the 5-cm-wide video tapes on which the data were recorded at each station were brought together for digital cross correlation using the Mark II Processor Playback System at NRAO, Charlottesville, Virginia (Ref. 10). The resulting post-correlation computer tapes, which contain the highly compressed data usually referred to as "stopped fringes," were then taken back to JPL for further reduction and analysis with an IBM 370 computer at the California Institute of Technology. The data reduction software for fringe processing, which was designed and developed at JPL for the IBM 370, extracts the phase as a function of time (phase tracking), refines the phase model used for "stopping the fringes" in the Mark II Processor, and obtains the delay (by two-channel bandwidth synthesis) for each radio source observed. The delay model, phase model, phase tracking, bandwidth synthesis techniques, and radio source locations used for these experiments are essentially the same as those employed for the 16-km Goldstone experiments detailed in Refs. 5 and 13, and will not be described here.

Each measured delay value can be modeled as a sum of a geometric delay, instrumental delays, and any differential delays due to the transmission media. For the present system, the instrumental delay terms can, in the ideal case, be collectively modeled as a constant offset ("clock offset") and a linear drift ("clock rate difference"), but must

sometimes be given a more complicated form to account for oscillator instabilities. As mentioned earlier, for a baseline that is only 307 meters in length, the transmission media delays should be nearly equal along the two raypaths so that they virtually cancel out in the measured delay. Furthermore, relative to other delay uncertainties, the geometric delay for this baseline is insensitive to source location and Earth orientation errors at the arc second level. Since the relevant source locations and Earth orientation parameters have been independently measured at the 0.03–1.0 arc second level, they are more than adequate for the present experiments.

Based on the above model, the delay values collected on a given day can be simultaneously fit by means of a weighted least-squares procedure (Ref. 5) in which the three baseline components and two instrumental parameters (in the ideal case) are "solve-for" parameters. Quoted ("formal") errors in these solve-for quantities are estimated by means of a covariance analysis based on post-fit residuals.

IV. Conventional Survey of the 307-m Baseline

Over a 7-month period the ARIES transportable station occupied two different positions separated by about 0.5 m, approximately 307-m east-southeast of the Mars station. The site occupied before January 16, 1974 is called Site A, and the other is called Site B. The baseline vector between the two antennas is most conveniently defined to be the vector extending from the intersection of the azimuth and elevation axes of one antenna to the corresponding point on the other antenna. This vector has been measured by means of local surveys in terms of geodetic coordinates and then transformed to the Conventional International Origin (CIO) frame. (In the CIO frame, the z-axis points toward the 1903.0 mean pole, the x-axis toward the Greenwich meridian, while the y-axis completes a right-handed coordinate frame.) The conventional surveys were performed with respect to a first-order control point (MARS △) established by the U. S. Coast and Geodetic Survey (now the National Geodetic Survey) in 1966. An additional control point (ARIES △) was placed near the ARIES antenna. The baseline vector between antennas was then obtained by combining three separate conventional surveys: Teledyne, Inc. for MARS △ to MARS antenna in 1966; M&Q Pacific for MARS △ to ARIES △ in 1974; and JPL for ARIES △ to ARIES antenna in 1974. The resulting survey baseline coordinates, which have been transformed to the CIO frame, are presented in Table 1 along with their estimated errors (1 σ).

V. Interferometry Results and Comparison With Survey

During the period from December 1973 to June 1974, four successful interferometry experiments between the ARIES transportable antenna and the 64-m Mars station were conducted. The first of these experiments (on December 22, 1973) was performed with the ARIES antenna at its Site A position, whereas the Site B position was occupied for all subsequent experiments. For each experiment, an attempt was made to fit the measured delay values with the "ideal" five-parameter model discussed above. However, because of oscillator instabilities in these experiments, it was found that either 6 or 7 parameters were necessary in order to obtain good fits to the measured delay values. In the December 22, 1973, April 24, 1974, and June 18, 1974 experiments, the rubidium oscillator apparently underwent an abrupt frequency shift in the midst of the observations so that independent parameters for both the offset and the clock-rate (giving a 7-parameter fit) were required on either side of the discontinuity. On the other hand, in the June 5, 1974 experiment, which contained approximately 10 hours of data, the oscillators behaved well enough so that all 29 delay measurements could be fit by 6 parameters (the 5 "ideal" parameters plus a frequency rate parameter). Delay residuals for this last experiment are given in Fig. 4. For each experiment, an analysis of post-fit residuals revealed the presence of unmodeled noise in addition to known system noise. Therefore, an extra noise term, estimated on the basis of the χ^2-analysis, was included in the final least-squares solution for the baseline and instrumental parameters (Ref. 5). The source of this extra-noise term was possibly the unmodeled short-term ($\approx$1 hour) instability of the rubidium oscillator. A summary of each experiment, including root-mean-square delay residuals and the unmodeled noise level for each experiment, is given in Table 2. The resultant baseline vectors are given in Table 3, where a weighted average of all Site B solutions is also included.

Table 4 compares the displacement vector (Site B–Site A) as derived from the combined interferometry data with the one derived from survey. It is seen that the two methods are in good agreement within the data noise level of 8 cm. (The relatively large data noise is due mainly to the 7-cm uncertainty in the Site A interferometry solution.)

A summary of the interferometry results and a comparison with the survey is given in graphical form in Fig. 5. Note that the December 1973 experiment, which was performed with the ARIES antenna at Site A, has

been adjusted to the Site B position by use of the accurately determined survey displacement vector. The bracketed values represent the weighted averages of the last three Site B measurements.

One important feature of these particular interferometry results is that in some cases the error in the Y-component of the baseline vector is larger than the other components, both in terms of its formal error estimate and in terms of the agreement with the survey. This Y-component weakness was caused by an inadequate geometric distribution of source directions, due either to poor observing strategy or to the loss of scheduled observations. It should be possible to design future measurements so that this weakness is eliminated.

VI. Conclusions

These measurements completed the first phase of a series of Project ARIES experiments designed to demonstrate the suitability of a transportable, independent-station radio interferometric system for accurate geodetic measurements. In this first phase, a 307-m baseline near the 64-m Mars station at Goldstone has been surveyed both conventionally and interferometrically. Results of these experiments show that the transportable interferometer possesses an inherent accuracy of a few centimeters in three dimensions for short baselines, and is a potentially powerful geodetic measurement tool. Specifically, the following capabilities of the present transportable radio interferometer have been demonstrated for a 307-m baseline:

(1) With approximately 28 hours of observations, a formal uncertainty (precision) of 3 cm in each component of the baseline can be achieved.

(2) Comparison of the interferometer baseline with conventional survey indicates that the 3-cm precision can be regarded as the *accuracy* of the system.

(3) The interferometer has successfully detected a small intentional change in baseline with approximately 8-cm accuracy. This relatively large uncertainty was due mainly to the single six-hour measurement of the Site A position.

In addition, these ARIES experiments have isolated and demonstrated at the few-centimeter level the following performance of the instrumental and analytic subsystems on the 307-m baseline:

(1) The achievement of an adequate signal-to-noise ratio for delay measurements using the 9-m/64-m interferometer system with a 4-Mbit/s record rate.

(2) The experimental evaluation of oscillator instability in terms of bandwidth synthesis and baseline vector solutions. In this regard, we have found that the rubidium frequency standard is marginally adequate.

(3) The successful integration of the NRAO 2-MHz-bandwidth Mark II digital recorder and cross-correlation system.

(4) The adequacy of the group delay stability of the interferometer instrumentation.

(5) The adequacy of the two-channel bandwidth synthesis subsystem.

(6) The development and validation of post-correlation software for delay observable generation and multiparameter estimation of the baseline and instrumental parameters.

VII. Outlook

Project ARIES has now entered its second phase of demonstration experiments. The transportable antenna is currently deployed at JPL and will occupy several sites throughout the seismically complex region of Southern California in the near future. The baselines to be surveyed in this second phase will range from 100 to 300 km in length. These baselines are particularly important since some geophysicists now believe that the crustal uplifting due to rock dilatancy, which is possibly premonitory to earthquakes, can be observed in the regions spanning a few hundred kilometers (Refs. 7 and 8). With these longer baselines, however, new challenges for Project ARIES must be met in order to achieve a system accuracy of 1–3 cm. First, the troposphere, ionosphere, and space plasma will introduce appreciable uncertainties in the time delay, since raypath dissimilarities will be greater for widely spaced antennas. Calibration of these differential propagation media delays will require special-purpose instrumentation such as the water vapor microwave radiometer (for calibrating the "wet" troposphere) and dual-frequency reception (for calibrating charged-particle effects). For these longer baselines, radio source locations and Earth orientation parameters must be calibrated or modeled at the 0.03 arc second level. Such calibration should be obtainable from independently conducted interferometry experiments on *intercontinental* baselines. With these anticipated improvements, the ARIES interferometer should be capable of three-dimensional measurements of baselines spanning hundreds of kilometers with an accuracy of a few centimeters.

Acknowledgments

References

1. Cohen, M. H., "Accurate Positions for Radio Sources," *Astrophys. Lett.*, Vol. 12, p. 81, 1972.

2. Hinteregger, H. F., et al., "Precision Geodesy via Radio Interferometry," *Science*, Vol. 178, p. 396, 1972.

3. Ryle, M., and Elsmore, B., "Astrometry with the 5-km Radio Telescope," *Mon. Not. Roy. Astron. Soc.*, Vol. 164, p. 223, 1973.

4. Shapiro, I. I., et al., "Transcontinental Baselines and the Rotation of the Earth Measured by Radio Interferometry," *Science*, Vol. 186, p. 920, 1974.

5. Thomas, J. B., et al., "A Demonstration of an Independent-Station Radio Interferometry System with 4-cm Precision on a 16-km Baseline," submitted to *J. Geophys. Res.*, 1974.

6. Nur, A., "Dilatancy, Pore Fluids, and Premonitory Variations of t_s/t_p Travel Times," *Bull. Seism. Soc. Am.*, Vol. 62, p. 1217, 1972.

7. Whitcomb, J. H., Garmany, J. D., and Anderson, D. L., "Earthquake Prediction: Variations of Seismic Velocities Before the San Fernando Earthquake," *Science*, Vol. 180, p. 632, 1973.

8. Anderson, D. L., and Whitcomb, J. H., "Time Dependent Seismology," *J. Geophys. Res.* (in press).

9. Shapiro, I. I., and Knight, C. A., "Geophysical Applications of Long Baseline Radio Interferometry," in *Earthquake Displacement Fields and the Rotation of the Earth*, pp. 284–301, edited by L. Mansinha, D. E. Smylie, and A. E. Beck, Springer-Verlag, New York, 1970.

10. Clark, B. G., "The NRAO Tape Recorder Interferometer System," *Proc. IEEE*, Vol. 61, p. 1242, 1973.

11. Counselman, C. C., III, "Very-Long-Baseline Interferometry Techniques Applied to Problems of Geodesy, Geophysics, Planetary Science, Astronomy, and General Relativity," *Proc. IEEE*, Vol. 61, p. 1225, 1973.

12. Cohen, M. H., "Introduction to Very-Long-Baseline Interferometry," *Proc. IEEE*, Vol. 61, p. 1192, 1973.

13. Thomas, J. B., "An Analysis of Long Baseline Radio Interferometry, Part III," in *The Deep Space Network Progress Report*, Technical Report 32-1526, Vol. XVI, pp. 47–64, Jet Propulsion Laboratory, Pasadena, Calif., Aug. 15, 1973.

14. Moran, J. M., "Very Long Baseline Interferometric Observations and Data Reduction," Harvard College Observatory and Smithsonian Astrophysical Observatory preprint, 1974; to be published in *Methods of Experimental Physics*, Vol. XII, edited by N. Carleton, Academic Press, New York.

15. MacDoran, P. F., "Radio Interferometry for Study of the Earthquake Mechanism," *Proceedings of the Conference on Tectonic Problems of the San Andreas Fault System, Stanford Univ. Publ. Geol. Sci.*, edited by R. L. Kovach and A. Nur, Vol. 13, p. 104, 1973.

16. MacDoran, P. F., "Radio Interferometry for International Study of the Earthquake Mechanism," *Acta Astron.*, Vol. 1, p. 1427, 1974.

17. Whitney, A. R., Ph.D. Thesis, Massachusetts Institute of Technology, 1974.

18. Rogers, A. E. E., "Very Long Baseline Interferometry with Large Effective Bandwidth for Phase Delay Measurements," *Radio Sci.*, Vol. 5, p. 1239, 1970.

Table 1. Conventional survey baseline vector between the ARIES antenna (Site A and Site B) and the Mars antenna (ARIES minus Mars) in the CIO frame

Baseline component	Site A, m	Site B, m
X	221.89 ± 0.02	221.73 ± 0.02
Y	-172.11 ± 0.03	-172.47 ± 0.03
Z	-123.26 ± 0.02	-123.51 ± 0.02
Total length l	306.68 ± 0.02	306.87 ± 0.02

Table 2. Summary of interferometry experiments

Experiment date	Site	Total duration of experiment,[a] h	Number of observations[b]	Number of sources observed	Number of fit parameters	RMS fit delay residual, ns	Unmodeled delay noise, ns
12/22/73	A	6.0	17	9	7	0.31	0.25
4/23/74	B	7.0	20	14	7	0.24	0.15
6/5/74	B	9.7	29	11	6	0.20	0.13
6/18/74	B	5.8	19	12	7	0.35	0.18

[a]Including antenna move times.

[b]Each observation approximately 10 minutes.

Table 3. Interferometry results for the ARIES 307-m baseline experiments

Experiment date	Site	X, m	Y, m	Z, m	l, m
12/22/74	A	$221.79 \pm .07$	$-172.14 \pm .07$	$-123.33 \pm .07$	$306.64 \pm .07$
4/23/74	B	$221.70 \pm .04$	$-172.39 \pm .07$	$-123.57 \pm .06$	$306.82 \pm .07$
6/5/74	B	$221.72 \pm .04$	$-172.53 \pm .04$	$-123.52 \pm .04$	$306.90 \pm .04$
6/18/74	B	$221.72 \pm .06$	$-172.66 \pm .10$	$-123.57 \pm .08$	$306.99 \pm .10$
Weighted average	B	$221.71 \pm .03$	$-172.51 \pm .03$	$-123.54 \pm .03$	$306.90 \pm .03$

Table 4. Comparison of the interferometry displacement vector between Sites A and B (B − A) with the survey value

Type data	ΔX, cm	ΔY, cm	ΔZ, cm	Δl, cm
Interferometery	-8 ± 8	-37 ± 8	-21 ± 8	26 ± 8
Survey[a]	-16 ± 1	-36 ± 1	-25 ± 1	19 ± 1
Interferometer −	8 ± 8	-1 ± 8	4 ± 8	7 ± 8

[a]The survey displacement vector is a special local measurement on a very short (~0.5 m) distance and thus possesses a smaller formal uncertainty ($\lesssim$1 cm) than the values quoted in Table 1.
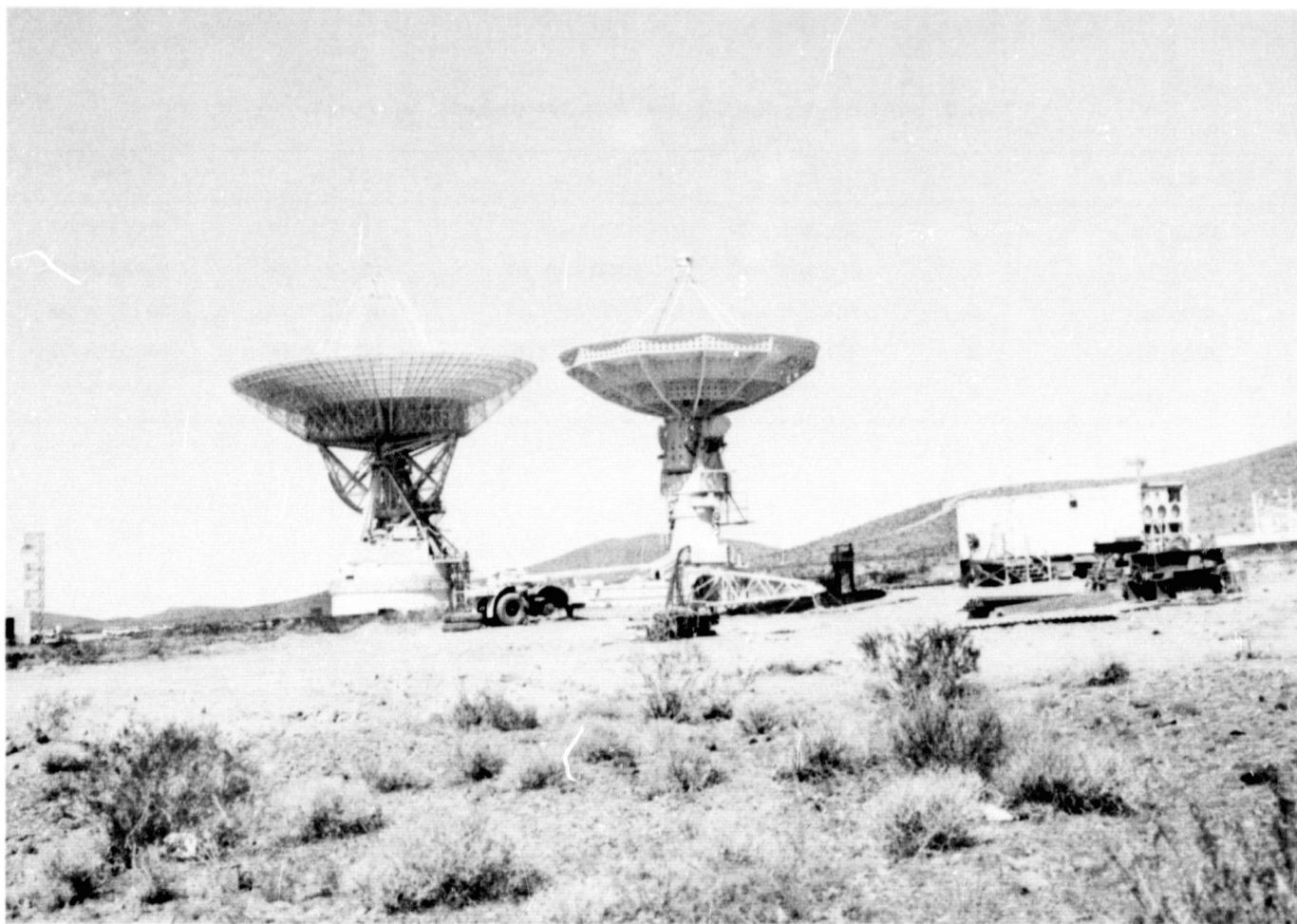
Fig. 1. The 307-m baseline between the 64-m Mars antenna (left) and the 9-m ARIES antenna (center); ARIES electronics and control trailer on right

ORIGINAL PAGE IS OF POOR QUALITY

DIFFERENCE IN
TIME OF ARRIVAL
$$\tau_g \approx \frac{\vec{B} \cdot \hat{s}}{C}$$

EXTRAGALACTIC
RANDOM RADIO
SIGNALS

$\hat{s}$

FIXED
ANTENNA

TRANSPORTABLE
ANTENNA

BASELINE
VECTOR $\vec{B}$

MAGNETIC TAPE

CALIBRATIONS

BASELINE
VECTOR

SIMULTANEOUS
MULTI-PARAMETER
SOLUTION
(GEN PURPOSE-
COMPUTER)

DELAY,
DELAY
RATE
OBSERV-
ABLES

PHASE
TRACKING
BANDWIDTH
SYNTHESIS
(GEN PURPOSE
COMPUTER)

STOPPED
FRINGES

CROSS CORRELATION
SIGNAL DETECTION
(MINI-COMPUTER)

Fig. 2. Schematic diagram of the Project ARIES transportable antenna interferometer system

Fig. 3. Block diagram of ARIES radio system configuration
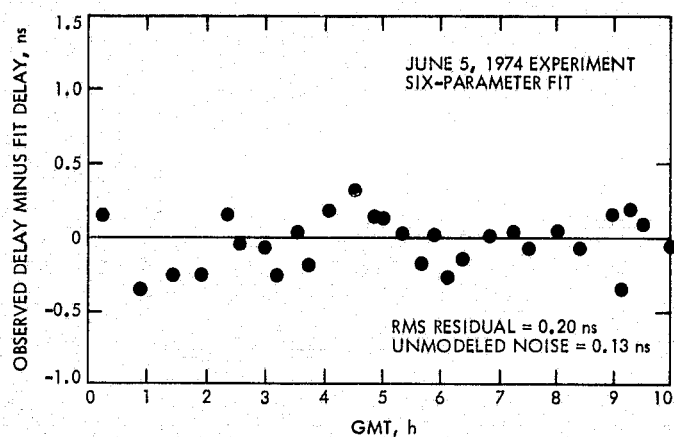
Fig. 4. Delay residuals for the ARIES experiment on June 5, 1974
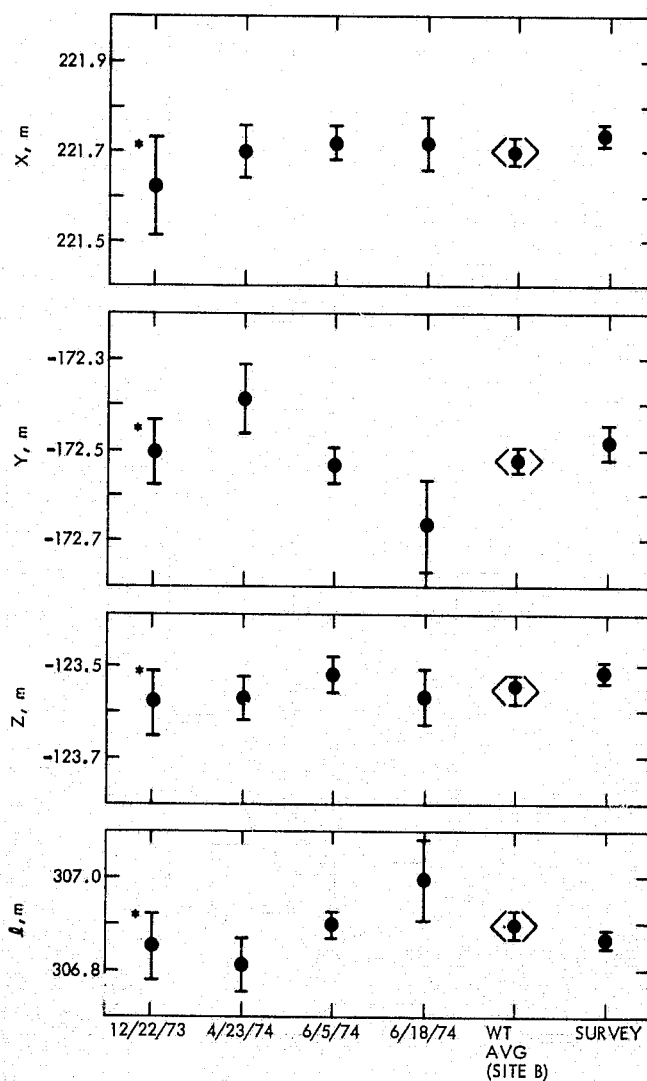
*DEC '73 ARIES POSITION (SITE A) ADJUSTED
TO POST–FEB '74 POSITION (SITE B) BY
$\Delta X = -16$ cm, $\Delta Y = -36$ cm, $\Delta Z = -25$ cm, $\Delta \ell = 19$ cm

Fig. 5. ARIES 307-m baseline vector measurement: comparison
of interferometer with survey

System Performance of the Dual-Channel Mu-II Sequential Ranging

W. L. Martin
Communications Systems Research Section

This article discusses the purposes and performance of the Dual-Channel Mu-II Sequential Ranging equipment in both the laboratory and field. Measurements were made to quantify the degradation introduced by the exciter, receiver, Ranging Subsystem, and spacecraft transponder. Additionally, both long- and short-term group delay stability is discussed. Finally, experimental data obtained during the Mariner Venus/Mercury 1973 mission are presented to show the utility of the machine.

I. Introduction

The Dual-Channel Sequential Ranging System (Fig. 1) was designed to support the Mariner Venus/Mercury 1973 (MVM'73) radio science experiments. Experimental objectives included a study of the interplanetary plasma and an investigation of the solar corona.

A radio signal is delayed as it passes through a plasma field. Magnitude of this delay is dependent upon both the field's density and the frequency of the radio wave. Theoretically the differential delay resulting from two radio signals of different frequency passing through a common plasma field is proportional to the ratio of those frequencies squared. Thus, if the frequencies are known, measurement of the differential delay allows the unique solution of field density.

MVM'73 was the first space mission to fly a two-frequency (S- and X-band) ranging transponder. It provided a premier opportunity to measure the total columnar electron density as well as the plasma dynamics. Past missions have been restricted to the latter since they carried a single-frequency (S-band) transponder. While the plasma dynamics are scientifically interesting, the inability to determine total columnar electron density represented a potential source of error preventing the full realization of other experimental objectives.

For example, both the Mariner 1969 and 1971 missions included a relativity experiment wherein the objective was to differentiate between Einstein's theory of general relativity and a modification of that theory proposed by Brans–Dicke.

The experiment consisted of measuring the range over a protracted period in order to establish the spacecraft's orbit with a high degree of confidence. These range measurements continued as the spacecraft passed behind the Sun and the Sun–Earth–probe angle became small, on the order of 1 degree. As the signal's ray path approached the Sun, the intense gravitational field resulted in a warping of the time-space field such as to make the apparent distance appear greater than that predicted by the spacecraft's orbit. This difference is due to the relativistic delay and is the subject of the theories promulgated by Einstein and Brans–Dicke.

Since only 7% separates the delays predicted by the two theories, a high degree of precision is required to differentiate between them. Unfortunately, plasma from the solar corona also introduces a delay in the received signal. While its magnitude is only a small fraction of the relativistic delay, the two are indistinguishable, and the size of the coronal delay is sufficiently large so it cannot be ignored. Thus, models have been formulated which attempt to quantify the coronal delay as a function of Sun–Earth–probe angle. The problem is that these are necessarily steady-state representations which approximate the average expected delay.

On the other hand, the solar corona is actually a highly dynamic body wherein day-to-day variations can reach a substantial fraction of the total coronal delay. Therefore, the modeling technique contains an intrinsic error limiting the accuracy of delay determination and hence the relativity experiment. Clearly, what is needed is an actual, daily, measurement, not only to test the corona model, but also for the correction of range data around superior conjunction. The dual-channel, S–X, ranging equipment provides this capability for the first time. But faith in the measurements made by this device must necessarily depend upon a trust in the ranging machine itself. Therefore, the remainder of this article is devoted to presenting and interpreting test data collected over a period of months with the Dual-Channel Sequential Ranging System.

II. Code Correlation Characteristics

To isolate the components introducing errors, correlation measurements were made in the Telemetry Development Laboratory (TDL) using a variety of system configurations including:

(1) The ranging equipment alone.

(2) The ranging equipment connected to a wide-band 10-MHz modulator.

(3) The ranging equipment connected to a Block III Receiver/Exciter Subsystem using a wide-band zero-delay device.

(4) The ranging equipment connected to a Block III Receiver/Exciter Subsystem using an MVM'73 prototype transponder.

Figure 2 pictorially summarizes the four test configurations. Correlation curves are generated by connecting the equipment in one of the four modes. After acquiring the range in a normal manner, the local reference (receiver) coder is shifted by its smallest increment (7.5 or 15 nanoseconds depending upon the reference frequency), and a new phase measurement is made. This process of shift and measure is continued through one complete code cycle. Both the 0- and 90-degree accumulators are integrated over the period of each phase measurement, and this number, representing the degree of correlation, is recorded at the conclusion of the measurement.

When plotted, the two channels represent the familiar code correlation curves (see Fig. 3). Of course, Fig. 3 represents a theoretical, and hence idealized, correlation function. In actuality, bandpass limitations and non-uniform phase shifts between the fundamental code frequency and its harmonics cause a distortion of the correlation relationship. These nonlinearities can result from imperfections in the ranging equipment itself, or from code waveform distortion occurring within the associated Deep Space Station (DSS) Receiver/Exciter Subsystem or within the spacecraft's transponder. Thus, the purpose of these tests was to investigate the contribution of each aforenamed subsystem to total system error. During the first test, the Ranging Subsystem's transmitter code output was connected, through an attenuator, to its receiver 1 input. Because of the automatic gain control (AGC) amplifier's wide-band characteristics, the range code is passed directly through to the analog-to-digital converter and thence to the correlator. To foreclose a significant droop in the range code due to the amplifier's low-frequency cutoff, a 2-MHz code was selected for this test.

Under normal operating conditions the equipment receives a 10-MHz carrier, phase modulated with the ranging code. Where as here the code is present without the 10 MHz, correlation against a model containing a 10-MHz reference will result in the integral of samples over the interval being zero. Thus, the internal reference must be disabled. Fortuitously, this can easily be accomplished via the 10-MHz disable switch conveniently located on the machine's front panel.

Figure 4 summarizes the results of the "base band" test. Since a 2-MHz code, rather than the usual 500-kHz code, was used for this test, only 32 steps were required to shift its phase through one complete cycle. This resulted in a rather large spacing between points, as will be observed in the quadrature channel where the individual steps are plotted, and accounts for the roughness of the solid curve.

Note that the spacing of the peak points is different from all others. This is due to the local (receiver) code never being perfectly in phase with the transmitter code because the 15-nanosecond shift available with a 66-MHz reference is too coarse. Thus, the correlator output at this point is less than it would have been had the 2 codes been in phase. This causes an apparent distortion in the correlation curve which is not actually present in the machine and is one of the reasons why a 132-MHz reference was selected in preference to the 44-MHz alternative available from the Block IV exciter. In the presence of noise this apparent quantization does not reduce the accuracy of the range measurement.

The intrinsic accuracy of the machine is determined by the linearity of the correlation curve, for it is this relationship between reference and quadrature channels that translates into a phase measurement. Linearity in turn is affected by, among other things, code waveform both within and without the machine. It is useless to generate a perfect transmitter code and an ideal modulator, exciter, and spacecraft transponder if the local code used for correlation purposes is defective, for the result is but the product of the two waveforms and the poorer will prevail. Thus, when one asks a 1-nanosecond accuracy in range, he is requiring a phase measurement to be better than 0.05%, placing stringent requirements on code waveforms.

As discussed earlier, precision and stability were primary objectives. They were achieved by providing wide bandwidths and careful control over all code waveforms. High-speed logic was used to ensure that transition times were short and symmetry was good.

Comparing the phase calculated using the measured correlation curve (Fig. 4) with that obtained with a perfect square wave (and hence an ideal correlation function), yields the error curve of Fig. 5. Note the peaks occurring at $\pi/2$ intervals due to the distortion in the correlation function at its maximum and minimum values. As discussed supra, this distortion is a product of the quantization and delay experienced in this particular test and would be expected to disappear under normal operating conditions. Thus, the slight difference in amplitude of the error function due to slightly greater

distortion in the reference channel would also probably disappear.

The important information presented by Fig. 5 can be summarized as follows: First, the error function is substantially periodic at $\pi/2$ intervals. Second, the error at the actual tracking point ($\pi/4 + n\pi/2$) is virtually nonexistent. Third, the average value over 2π is approximately zero, showing the machine contains no biases. Fourth, the maximum error experienced was on the order of 2 nanoseconds and this was probably due to quantization.

In order to ascertain the degradation in performance resulting from the interconnection with other equipment, similar tests were run using a more normal operating mode. Figure 6 shows the test results using the 10-MHz wide-band modulator (see Fig. 2). This is similar to the previous test in that only the ranging equipment is under test; however, now the input is receiving a 10-MHz phase-modulated carrier as it does when connected with a DSS receiver. Additionally, the typical 500-kHz range code is employed rather than the 2-MHz code.

Observe the high degree of linearity in the sides of the correlation function. The slight rounding at the peaks is due to bandpass restrictions in the modulator; however, this distortion is small compared with that which appears using other configurations.

The error function, Fig. 7, is plotted for one-half of the period (0 to π). Its maximum amplitude is approximately the same as that measured during the baseband test and occurs at the peaks of the correlation function. At other locations the error is substantially zero. Figure 7 also includes an apparent negative bias that results from the method by which code phase is established. In fact, it is part of the system delay that has not been removed and therefore should be ignored.

Continuing with the system tests, Fig. 8 is a plot of the correlation function when the system is connected to a standard DSS Block III Receiver/Exciter Subsystem through a zero-delay device (refer to configuration diagram Fig. 2). A zero-delay device comprises a wide-band crystal mixer which converts a part of the transmitted energy to the receive frequency and is so named because its through-put time is exceedingly small.

Careful inspection of Fig. 8 reveals some nonlinearity in the correlation function. This is likely due to a non-uniform shift in the phase of the higher-order range code harmonics with respect to the fundamental frequency. Note, also, the somewhat greater rounding at the peaks of

the correlation curves. This is consistent with the non-uniform phase-shift theory in that the rounding is indicative of poor high-frequency response in the system. As the response begins to roll off, it becomes uneven with the result that the phase-frequency characteristic is nonlinear. This in turn results in a disproportionate phase shift in the high-order harmonics and the nonlinear correlation curve.

The effect is clearly evident in the error curve of Fig. 9. Here the amplitude has increased from approximately 2 nanoseconds to more than 7 nanoseconds. Note, also, that the area under the error function is substantially greater than that indicated in Figs. 5 and 7. This results not only from the increased amplitude, but, also, from an increase in the error value at all code phases. The latter results from the nonlinearity in correlation function caused by non-uniform harmonic phase shift.

The final system test results appear in Fig. 10. For this measurement a Block III exciter was connected to a Block III receiver via the MVM'73 prototype transponder (see Fig. 2). This, then, represents a hardware complement similar to that which would be found in the field during an actual mission track. The tests were run at relatively strong ranging signal levels in order to properly identify the system's characteristics. However, the total uplink power was kept at −120 dBm in order to ensure a noise-limited condition at the spacecraft transponder's limiter and, hence, linear performance (i.e., no material reconstruction of the range code).

Here the degradation is readily apparent by comparing Fig. 10 with any of the preceding correlation curves. Not only has the linearity suffered badly, but, also, the peak-rounding is so great that the curve is becoming nonlinear at the equal power points for the reference and quadrature channels. Moreover, careful inspection reveals that this rounding is asymmetrical with respect to the true peak. Again, this follows from the restricted bandwidth; however, in this case the spacecraft is the limiting element.

The degradation is clearly evident in the error function (Fig. 11). Amplitude is some 8 times greater than that measured in the baseband test. Moreover, the magnitude remains fairly high for all code phases, indicating substantial high-order harmonic phase shift. Further indication of this shift appears from the asymmetrical character of the error curve, that is, the sharp increase followed by the relatively slow decline. The message here is that the correlation function is not symmetrical with respect to its peak, with the result that the optimal

tracking point has been shifted from the normal, $\pi/4$, point.

Examination of Fig. 10 reveals that the once triangular correlation curve now approximates a sine wave. Some possibilities for improvement in system performance suggest themselves. It is obvious from the foregoing discussion that the greatest degradation occurs in the transponder. This means that the transponder's characteristics of bandwidth and harmonic phase shift are the dominant factors in shaping the correlation curve and, hence, the overall system performance. From here it follows that small variations in ground equipment bandwidth will not affect system delay since the transponder's relatively narrow bandwidth will have removed most code harmonics. Thus, the spacecraft's characteristics dominate, and, if a method could be found to quantify the distortion introduced by the transponder, the overall ranging accuracy could be improved.

One method is to measure the correlation characteristics of each transponder as was done here with the MVM radio (Fig. 10). These measurements can be incorporated as corrections to the linear phase estimator algorithm employed in the ranging system. Using this technique the ranging equipment could be exactly matched to each spacecraft.

A second alternative is to filter the higher-order harmonics between the DSS receiver and the ranging equipment. In this case the phase shift introduced in the harmonics by the transponder is unimportant since only the fundamental remains after the filtering. Preliminary tests show that, when used in conjunction with an arc tangent phase estimator algorithm, the filtering method reduces errors to about the level of the ranging equipment alone.

Both alternatives are under active investigation. Unless dramatic improvements in transponder design are forthcoming, one of them will probably be necessary to meet the accuracy requirements of future missions.

III. System Stability

Another aspect of accuracy is stability. By this is meant the system's ability to produce the same result over a period of time where conditions remain relatively unchanged. Stability can be further subdivided into short-term and long-term components.

Short-term stability may be defined as the capacity to remain invariant over periods from 8 to 12 hours, such as

would be experienced during a single pass. This character-istic is important because the equipment is only calibrated prior to, and occasionally after, each track. Changes occurring during the pass are indistinguishable from the parameter being measured, either range, or the change in range due to particle dynamics (DRVID). These variations impose an upper bound on the system's accuracy and every effort should be made to minimize them.

Long-term stability refers to the system's ability to produce consistent results over a period of months. This is, of course, inexorably related to short-term stability in many respects, for most of the factors influencing one will also affect the other. Frequently, a situation will arise which forecloses a ranging calibration either prior to or following a pass. The reasons can vary from overcommit-ment of station tracking time to equipment malfunctions that require repair during the normal calibration periods. In a situation such as this, it is desirable to use the calibration of the previous day or, perhaps, of the previous week if tracks are infrequent. This is only possible if the delay will not have changed during the period and therefore long-term stability becomes very important.

As noted in an earlier section, considerable care was taken to ensure high stability in the Ranging Subsystem. To evaluate the success of this effort, the range code was connected, via the wide-band 10-MHz modulator, to the ranging unit's input (see Fig. 2). This utilized the minimum amount of external equipment necessary to make a meaningful stability measurement.

A normal range acquisition was made and the machine was allowed to continually remeasure the range at 10-minute intervals for more than 16 hours. The results are plotted in Fig. 12. During the entire period the peak-to-peak variation was less than 60 picoseconds (60×10^{-12} seconds). Moreover, the average variation during the same period was on the order of 30 picoseconds. This corresponds to a change in one-way range of less than 1/4 inch (approximately 5 millimeters) over the 17-hour period!

While the relative contributions of the modulator and Ranging Subsystem are inseparable, the size of the change probably makes further consideration of this matter unnecessary. Unless one is willing to postulate larger drifts in opposite directions for each piece of equipment, which almost perfectly compensate one another, and which situation is highly unlikely, then the only conclusion left is that neither equipment changes significantly.

Long-term stability of the *entire ground system* was evaluated by plotting ranging calibration data obtained at DSS 14 over a period of several months. The particular configuration consisted of the Ranging Subsystem herein described, a standard Block III exciter and the new Block IV receiver. The zero-delay device at DSS 14 had been improved so as to eliminate the air path and therefore a problem with RF reflections which had been found near the face of the dish.

The calibrations, made at S-band, are plotted in Fig. 13 for a period from February through the middle of June 1974. Because of different path lengths, only data obtained with the 100-kW transmitter were plotted.

Note the remarkable consistency throughout the entire period. The average delay was found to be 3.470 microseconds and the standard deviation was less than 4 nanoseconds (approximately 1/2 meter in one-way range). One can discern evidence of cyclic behavior whose period is approximately 25 days. After the system had stabilized following day 70, the day-to-day variation is extremely small compared with the cyclic characteristic. Some effort should be expended to identify the source of this change, whereafter the total variation (peak-to-peak) could probably be reduced to less than 5 nanoseconds. If this were done, daily calibration may be found unnecessary.

As a further check on long-term stability, differential group delay was plotted for a somewhat longer period using both the 100- and 20-kW transmitters. The results appear in Fig. 14. Here the data can be separated into three distinct groups. During the early part of the year, just prior to Mercury encounter, there was considerable activity at DSS 14 in readying the new Block IV receiver for the critical period. The effect of this activity is evident as an increased instability in differential delay prior to day 70.

On or about day 75, cables traversing the elevation bearing were replaced, resulting in a substantial change in differential delay. Thereafter, the day-to-day variation became smaller and the cyclic behavior more evident. From day 80 through day 135 the average delay diminished by only 1 nanosecond, although the periodic signature resulted in a standard deviation of about 4.5 nanoseconds.

The station was inactivated for a period of time following day 135. During this period certain unidentified changes took place, causing the differential delay to decrease by 6.7 nanoseconds. This reconfiguration also appears to have had a stabilizing effect in that the average

delay remained unchanged during the following 1-1/2 months. Moreover, the cyclic variation appears to be increased in frequency and reduced in amplitude. Thus, careful scrutiny of the alterations made during this period may provide a clue as to its cause.

The conclusion reached from this compendium of information is that the entire ground system exhibits fairly stable behavior over substantial periods of time, particularly if left undisturbed. Further work should be undertaken to identify the source of the cyclic behavior.

IV. Experimental Results

In the final analysis, the test of any system is in the utility of information which it produces. As noted in the introduction to this section, one limitation on the accuracy of relativity experiments has been the absence of a dynamic corona model. Obviously, the best model is obtained from actual measurements made through the time near superior conjunction.

The two-frequency capability of this system provided a unique opportunity to measure not only the dynamics but also absolute coronal delay. The effect of the solar corona upon group delay will be found in Fig. 15 and is presented through the courtesy of T. Howard of Stanford University, team leader of Mariner 10 Radio Science Experiments.

No attempt will be made to interpret these data, which are far beyond the purpose or scope of this presentation. Suffice it to say that the graph amply demonstrates the system's ability to resolve not only the magnitude of delay but, also, its day-to-day variation. Theoretical computations have confirmed the correctness of the data contained in the figure.

One final measurement deserves mention. On day 171, approximately 2 weeks after superior conjunction, the ranging equipment was configured to provide rapid, multiple acquisitions. Only three range code components were employed, which were sufficient to resolve the differential delay resulting from the solar corona. Some 25 points were obtained over a 4-hour period, approximately one point every 10 minutes. The purpose here was to demonstrate the machine's ability to resolve high-frequency fluctuations in coronal density, which caused changes in differential group delay. The data are plotted in Fig. 16.

The predicted signal level available on day 171 was such that the expected variation in delay due to noise was small compared with the changes actually observed. Again, interpretation of these data is not within the purpose of this work, and the data are included simply to show the capabilities of the equipment.

V. Conclusions

All this leaves a question as to what can and should be done to improve the entire system's accuracy. The foregoing evidence suggests several conclusions.

First, the ranging equipment, standing by itself, appears quite adequate. The tests have shown that improvements in this subsystem would not materially affect the overall system performance.

Second, accuracy and stability with the Block III Receiver/Exciter Subsystem are fairly good. While bandwidth limitations are clearly present and some nonlinearity exists due to non-uniform harmonic phase shift, these distortions do not appear to have a substantial effect on stability. Work should be undertaken to eliminate the non-uniform phase shifts that probably occur within the exciter. Because it was unavailable for many of these tests, no conclusions are reached with respect to performance with the Block IV equipment.

Third, the dominant source of error is within the spacecraft's transponder. From this it follows that the maximum yield in terms of performance improvement for manpower invested would be obtained by concentrating on this unit.

If one accepts these conclusions as true, then the only reasonable course is in terms of spacecraft transponder development. To attempt alternate "fixes" with respect to the ground equipment is to treat symptoms and not causes, and it will prove both expensive and relatively unproductive in the long term. The underlying problem is one of bandwidth. It is too narrow. A limited bandwidth may have had merit in the days of the 26-m (85-ft) antennas, 10-kilowatt ground transmitters, and pseudonoise ranging systems. Today there are 64-m (210-ft) antennas, 100-kilowatt transmitters, and sequential ranging equipment, and the relevant considerations have changed accordingly. Now the question is no longer whether we can measure range at all, but, rather, how accurately can we measure it. Whereas a 20-meter accuracy was sufficient but a few years ago, now uncertainties greater than 5 meters can invalidate whole experiments. Tomorrow the requirements will press to a few centimeters.

Viewed from this perspective the answer seems clear: widen the bandwidth. Increasing the present 1.5-MHz

transponder bandwidth to 12 MHz would result in less than a 10-dB loss in signal-to-noise ratio. To produce the same uncertainty in phase, the already short integration time would have to be increased by a factor of 8, provided that the code frequency remained constant. However, if channel bandwidth limitations imposed by the Federal Communications Commission permitted, the code frequency could, and should, be increased. Remembering the equation for phase uncertainty (Ref. 1)

$$\sigma = 2T[N_0/(2st)]^{1/2}$$

where T is the code bit period.

It is obvious that increasing the code frequency to 2 MHz will result in the same phase noise without changing integration time! But, the higher code frequency will have resulted in improved accuracy for the reason that time, and hence range, has been quantized into smaller units. Thus, the answer is not one of patching an existing and outmoded system, but rather in re-evaluation and change of that system in light of today's experimental requirements.

Acknowledgments

Reference

1. Goldstein, R. M., "Ranging With Sequential Components," in *The Deep Space Network*, Space Programs Summary 37-52, Vol. II, pp. 46–49, Jet Propulsion Laboratory, Pasadena, Calif., July 31, 1968.
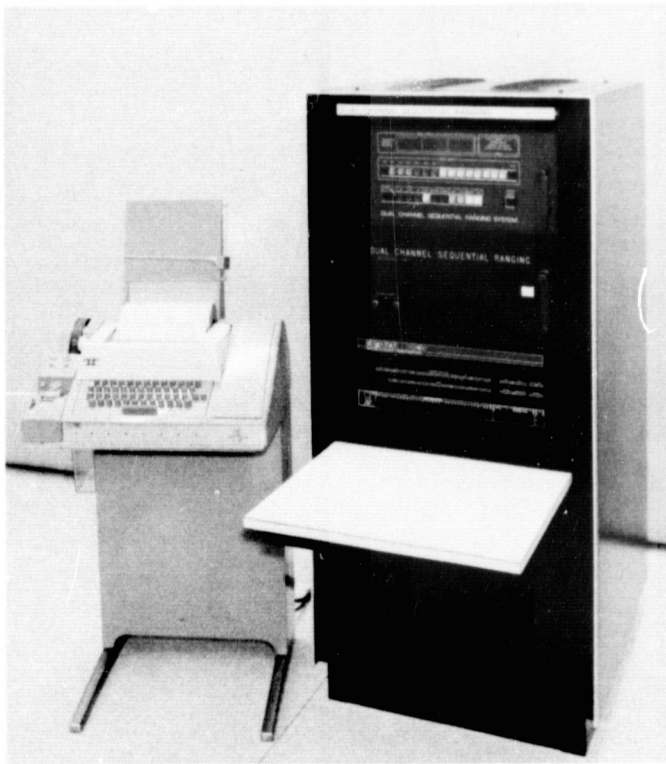
Fig. 1. Dual-Channel Sequential Ranging System
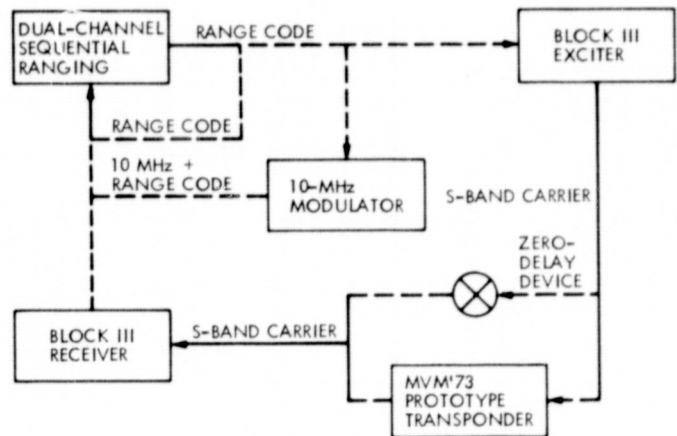
Fig. 2. Ranging test configuration
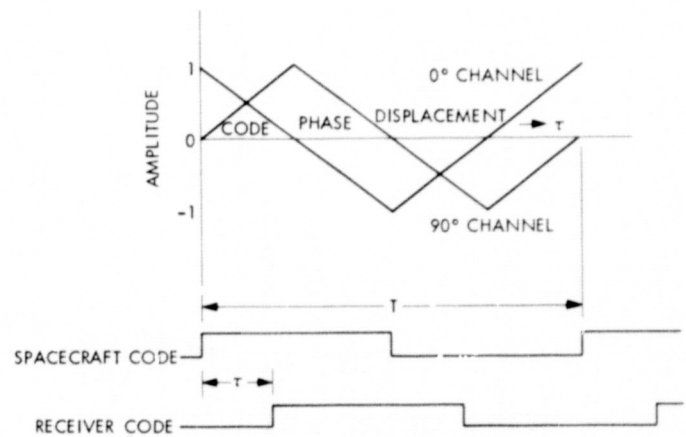
Fig. 3. Theoretical code correlation characteristics
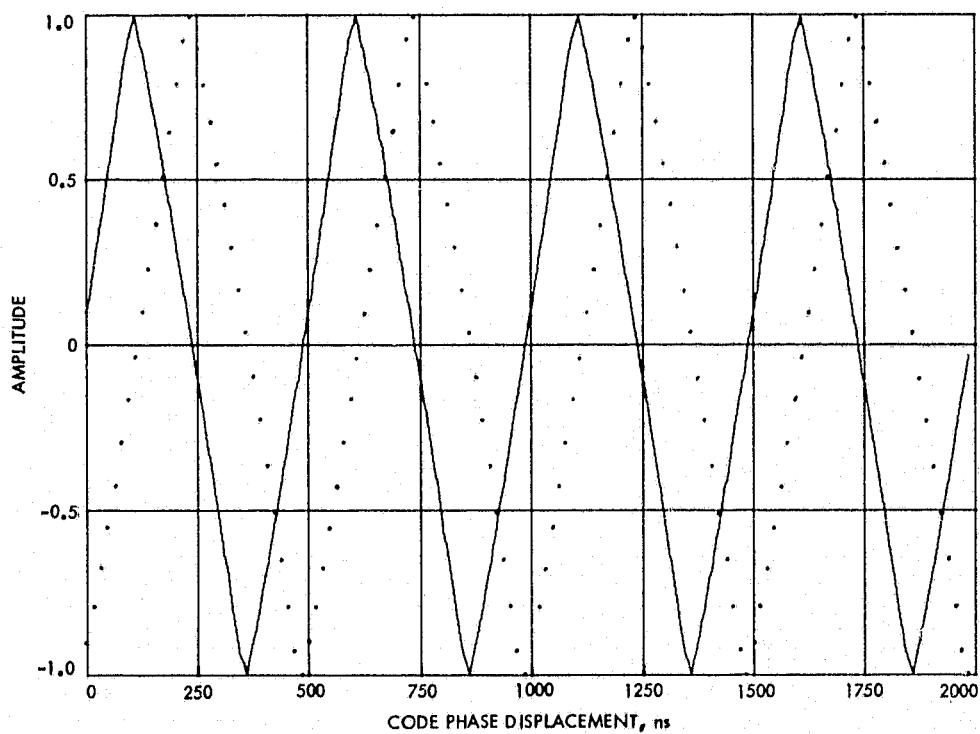
Fig. 4. 2-MHz code correlation characteristics
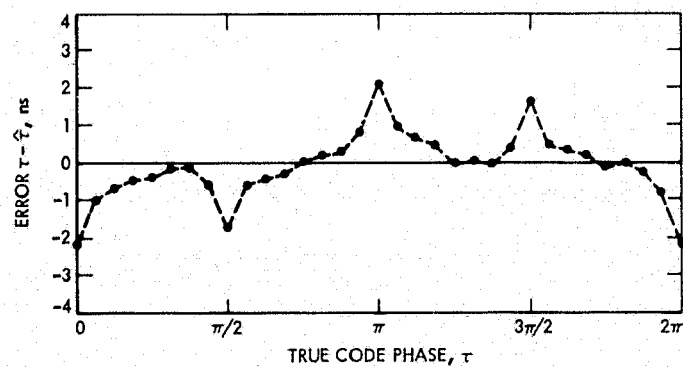
Fig. 5. Error in tau estimate for 2-MHz code baseband test
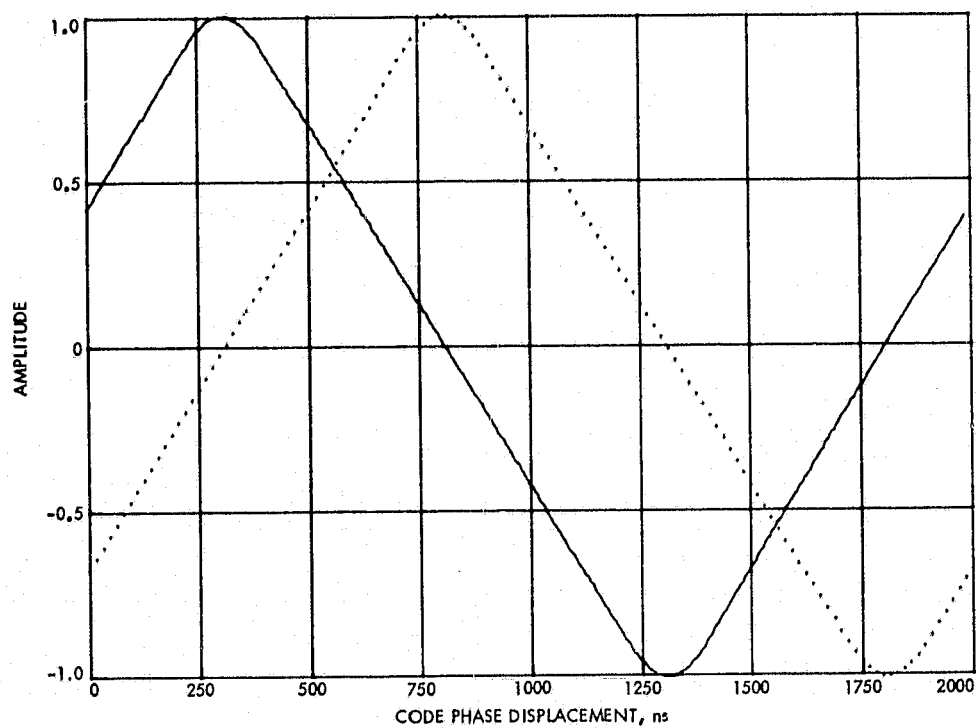
Fig. 6. 500-kHz code correlation characteristics using wide-band modulator
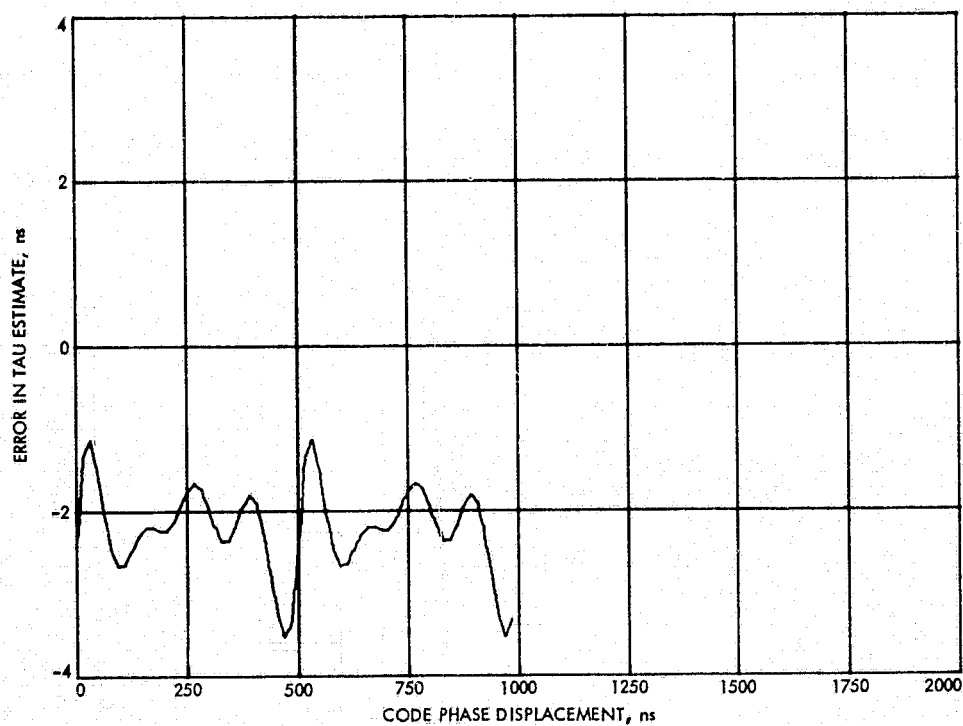
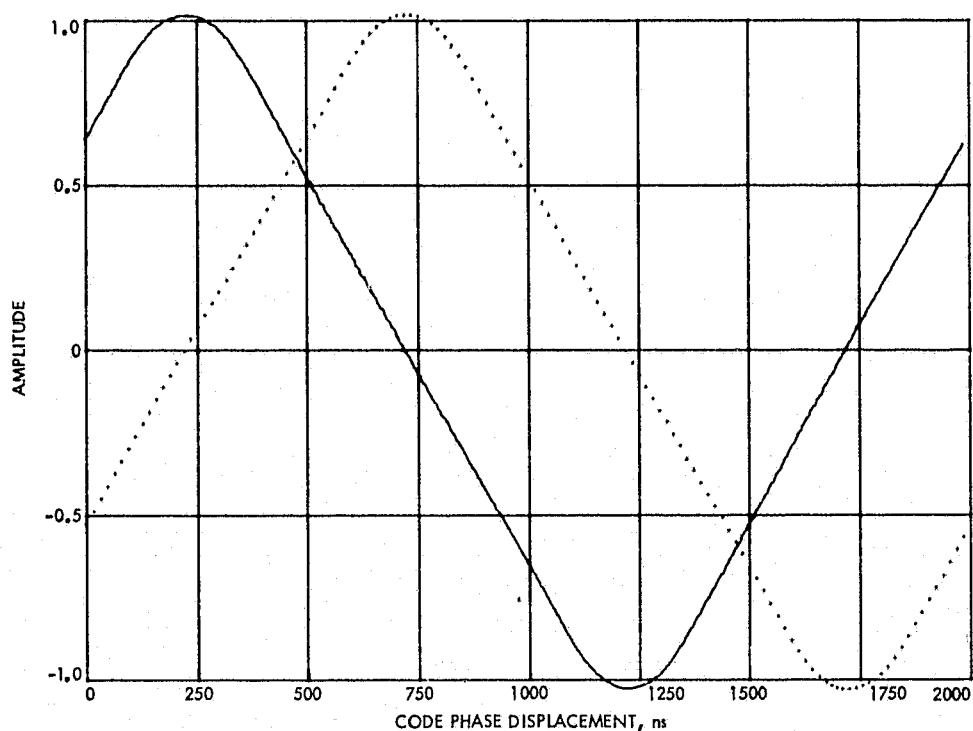Fig. 7. Error in tau estimate, 500-kHz code using wide-band modulator

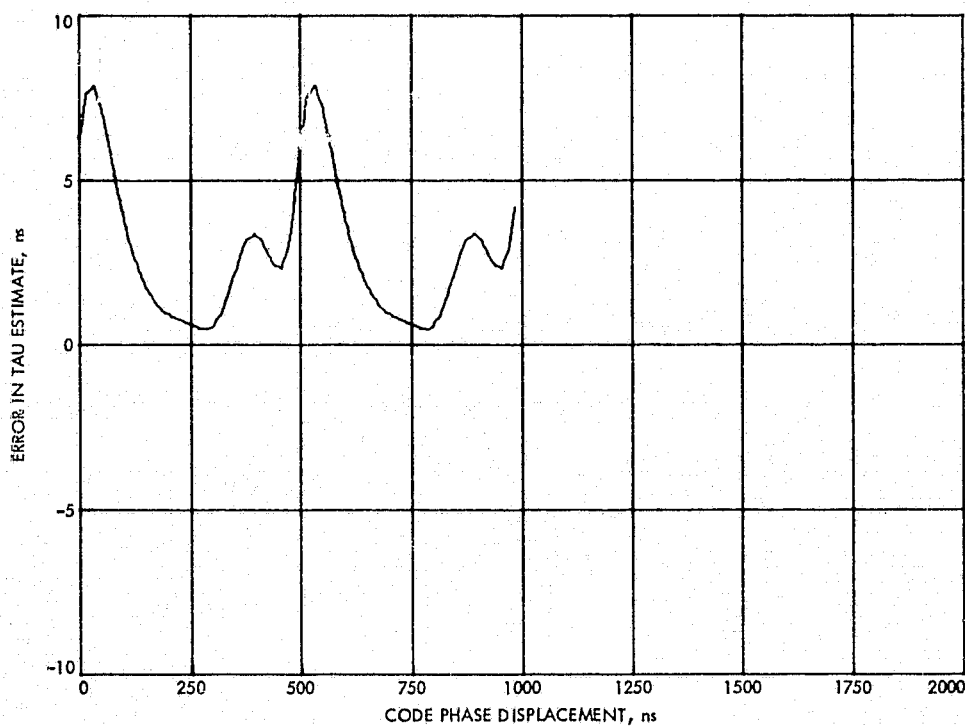Fig. 8. 500-kHz code correlation characteristics using Block III
receiver—exciter/zero-delay configuration

Fig. 9. Error in tau estimate with 500-kHz code using Block III
receiver—exciter/zero-delay configuration
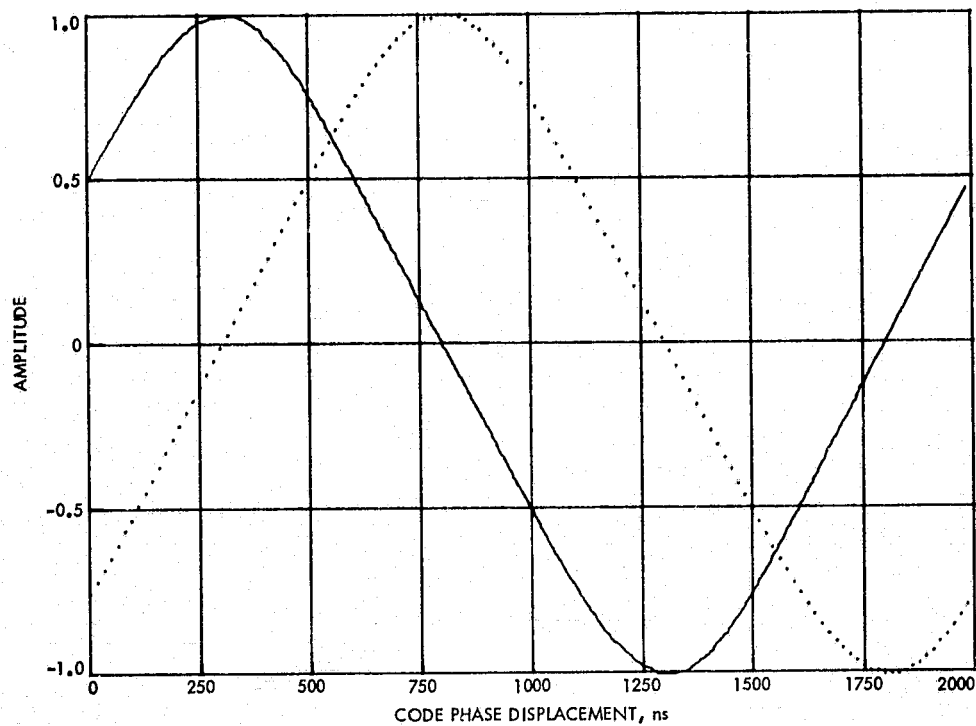
Fig. 10. 500-kHz code correlation characteristics using Block III
receiver–exciter/MVM transponder configuration
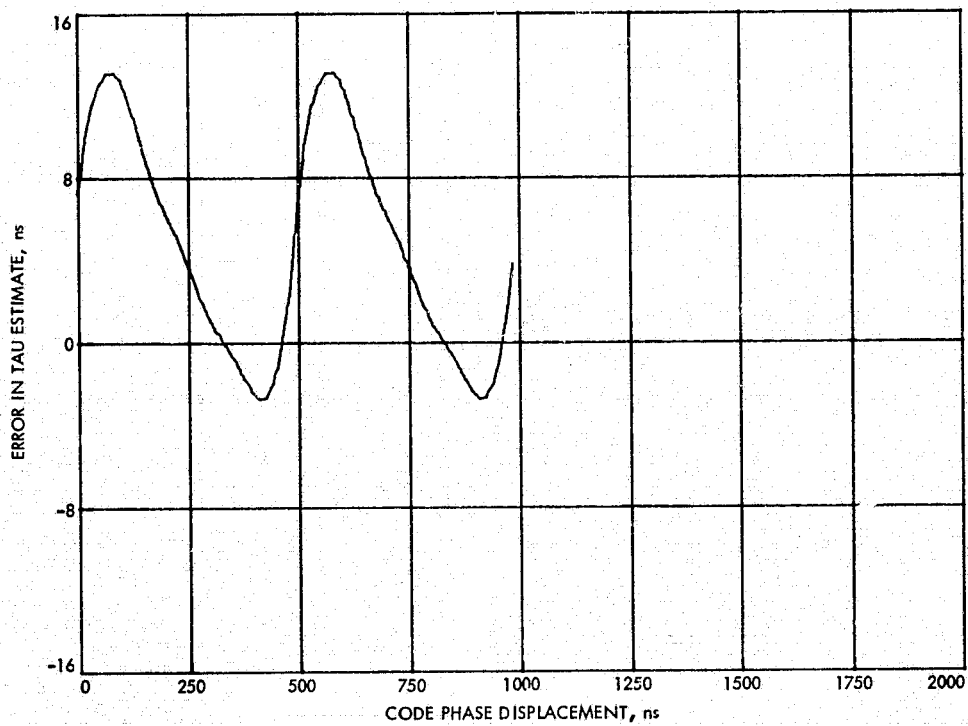
Fig. 11. Error in tau estimate with 500-kHz code using Block III
receiver–exciter/MVM transponder configuration
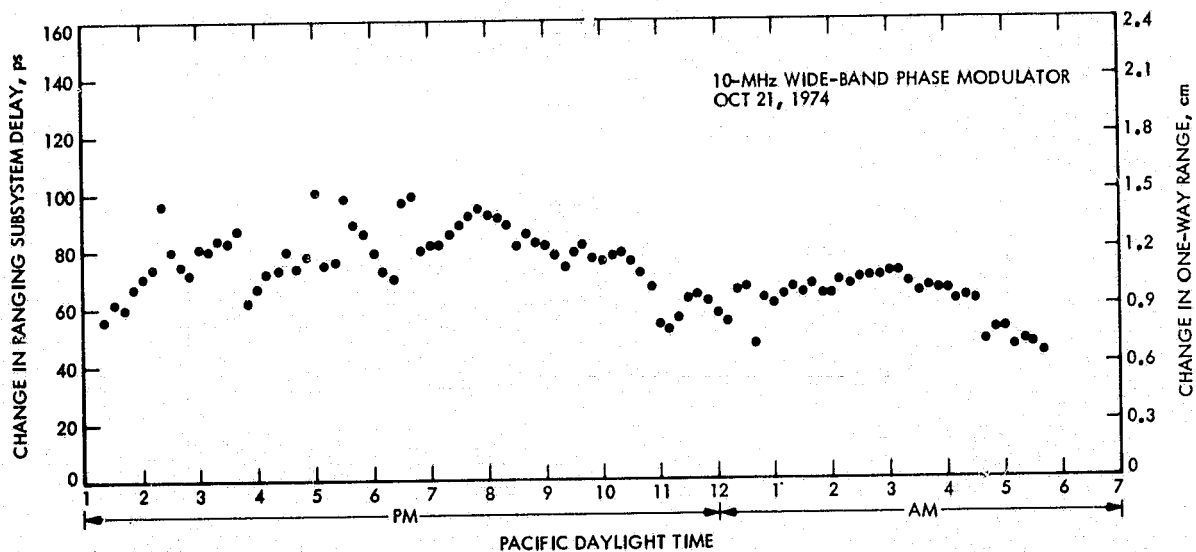
Fig. 12. Results of Ranging Subsystem stability test
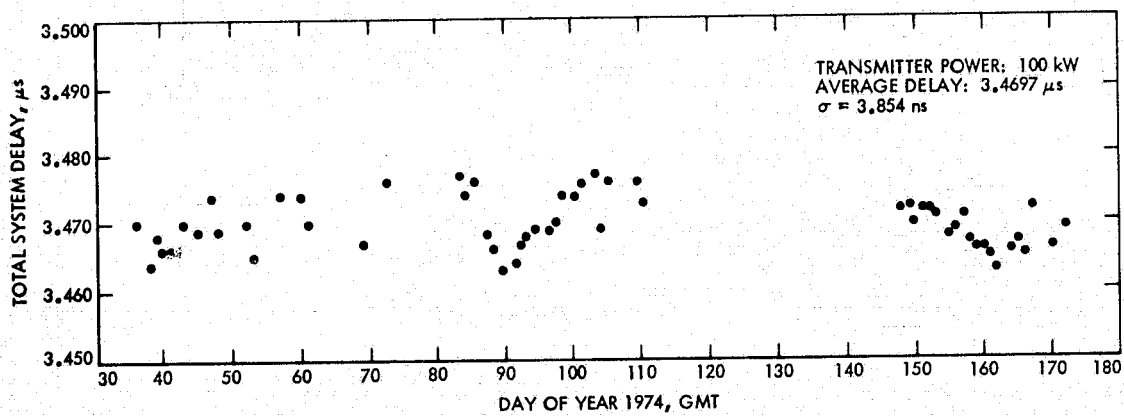
Fig. 13. Mu-II S-band ranging zero-delay calibrations at DSS 14 using Block IV receiver and Block III exciter
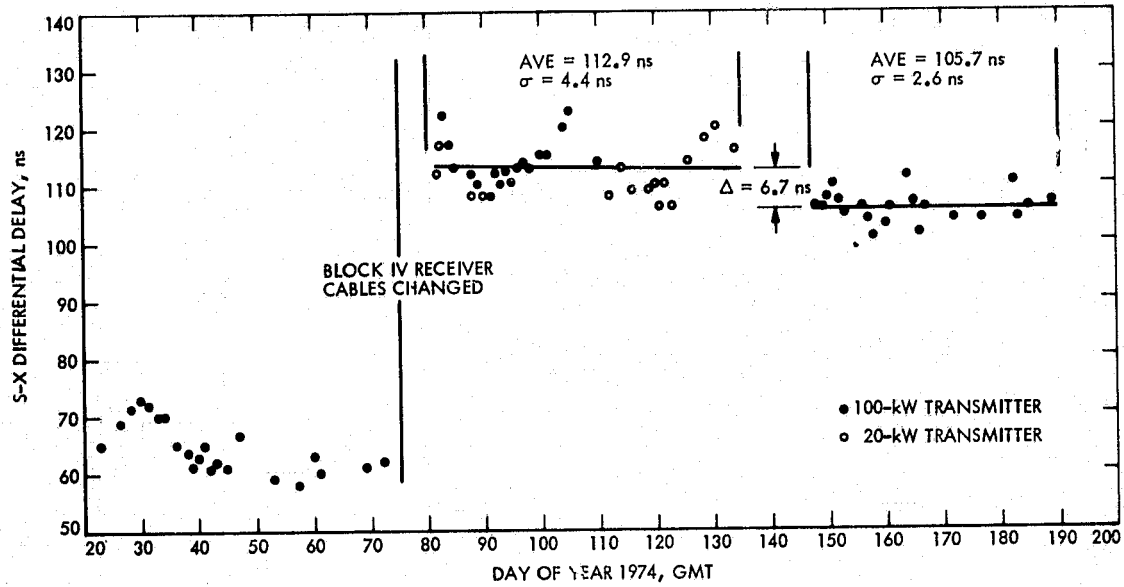
Fig. 14. S—X differential zero-delay calibrations at DSS 14 using Block IV receiver and Block III exciter
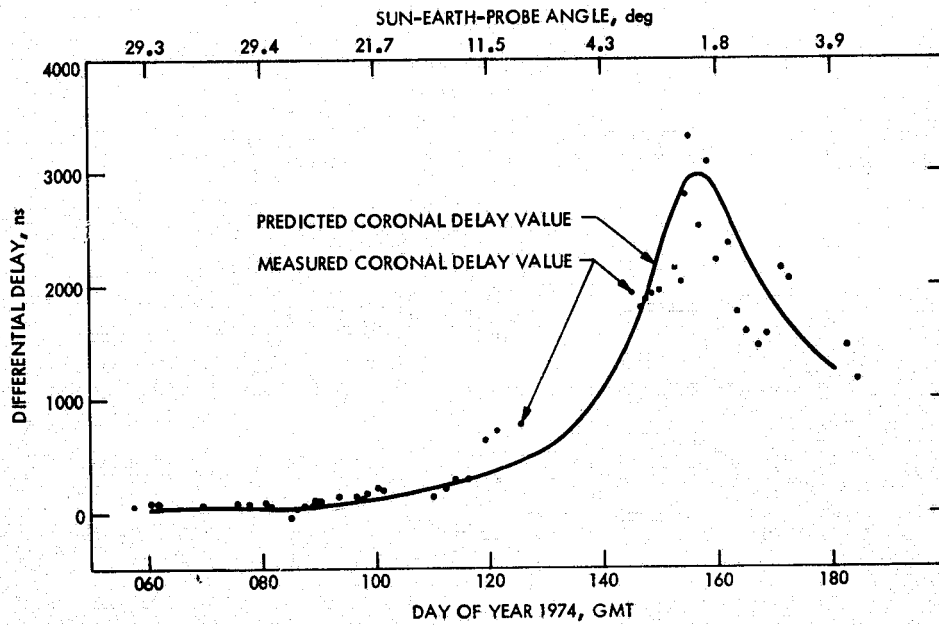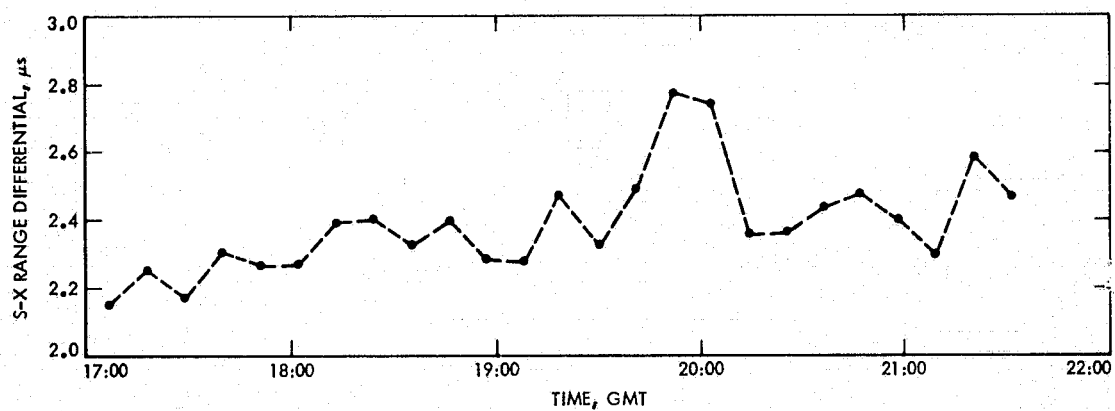

Fig. 15. Mariner 10 S—X differential range at DSS 14

Fig. 16. Coronal dynamics measured by differential range on day 171, 1974

A Fabrication Method for 64-m Antenna Radial Bearing Wear Strip Segments

H. D. McGinness and H. P. Phillips
DSN Engineering Section

R. E. Renner
Fabrication Shops Section

In the construction of the 64-m antennas for the DSN the fabrication of the radial bearing wear strips has been a difficult problem, and one that was not solved satisfactorily during the initial construction. A test project carried out in the JPL machine shop has shown the feasibility of a direct machining process, using a tracer or tape controlled planer. This process can be used for the manufacture of replacement wear strips for those presently installed on the antenna, and can be used with higher hardness steels giving an improved wear life of these components.

I. Introduction

On the DSN 64-m antennas, fabrication of the radial bearing runner wear strip segments to the desired flatness tolerance has been very difficult and not completely successful. The wear strips are hardened steel plates 2.86 m (112.5 in.) long formed to an arc 36 deg long on a 4.57-m (15-ft) radius. The manufacturing process that has been used consists of grinding the wear strips flat and then cold-forming them to the desired radius. The cold-forming process has caused a transverse warpage which prevents proper seating of the wear strip on the runner, and requires machining of the outer surface of the wear strip at final assembly. This paper describes a project carried on in the JPL machine shop to test a method of machining

these segments to the desired arc on a planer, holding the desired flatness, and without resorting to the use of a very large boring mill. The fabrication technique is applicable to replacement parts or new construction.

II. Fabrication Problem

The 64-m antenna radial bearings are made up of three 2-wheel trucks running against the 10 hardened wear strip segments on the face of the 9.14-m (30-ft) diameter runner. The original wear strips were made of T1 steel with a hardness of approximately 24 Rockwell C and a yield strength of 6.9×10^8 N/m² (100,000 psi). The manufacturing process used consisted of grinding the plates in the flat to a thickness tolerance of ±0.05 mm

(0.002 in.) to assure that the machined concentricity of the runner would be maintained in the hardened wear strip face and that there would be a minimum ~ across adjacent segment ends. The segments were then cold-formed to the desired radius (the outside radius of the runner) and attached to the runner with counterbored cap screws. It was found that the cold-forming produced an anticlastic distortion of the wear strips in the form of an outward curvature that prevented proper seating of the wear strips on the runner (Fig. 1). The resulting gaps were filled with shim material to distribute the wheel loads from the wear strip into the runner, and the outer surfaces were machined on a very large boring mill to assure a flat outer surface. The shimming process is not satisfactory because it leaves hard spots that cause high local contact stresses on the wheel and the wear strip, which will lead to premature failure of these components.

III. Test Program

The objective of the test was to determine if the wear strip segments could be machined in the final arc form on a planer, using a tracer attachment, and maintaining the desired thickness tolerance. The test was made using heat-treated 4130 steel rather than T1 because the higher hardness obtainable would be needed in the future construction of larger antennas of similar configuration. The fabrication process used was as follows:

A plate of annealed 4130 steel (oversized to allow for finish machining) was rolled to the approximate curve and then heat-treated to 32–38 Rockwell C. The curved plate edge was machined and then placed on a planer table, edge lengthwise, using angle plates for support, and standard hold-down bolts for clamping (Fig. 2).

A full length template was computer programmed and machined on a numerical control mill to an accuracy of ± 0.05 mm (0.002 in.).

A hydraulic tracer attachment was set up on the planer, and a special outrigger unit was fabricated to follow the contour, thus positioning a tool to machine the test bearing plate to the required contour on the planer.

The planer action was chosen so that the tool marks would be in alignment with the antenna guide rollers, and would not set up a Brinell action that a milling slab cutter might do. The outer surface was machined in two halves. This was required because the hydraulic tracer attachment used could not move the tool away from the work fast enough on the return stroke to clear the convex side of the wear strip. Upon machining the inside surface, the tool swept the entire length, since the return stroke was across the concave side of the wear strip and there was no clearance problem.

The tool geometry was ground to a compromise between the "mean" allowable positive rake and the allowable negative rake.

The feed rate was 3.4 mm/s (80 in./min) controlled primarily by the reaction time of the tracer cylinder.

The problems encountered in the prototype test were primarily in the outrigger attachment, which chattered badly if actuated too rapidly, and in the hydraulic tracer unit, which was too slow to maintain the normally required feed rate.

The inspection technique used was twofold. First, while the part was being machined, the thickness was checked to determine if the two sides were parallel and/or how much out of parallel. The test final piece was 0.38 mm (0.015 in.) out of parallel. It is felt that a numerically controlled (NC) machine, cutting full length instead of two halves as the test was run, would easily hold 0.127 to 0.25 mm (0.005 to 0.010 in.) parallel.

Second, the part was then released, and placed in a free state with an indicator taking the place of the tool bit. The part was moved through its longitudinal cycle to determine how closely it matched the template contour. The test piece checked to within 0.508 mm (0.20 in.) of the template. An NC machine, cutting full length, should be within 0.254 mm (0.010 in.).

IV. Summary of Test Results

The results of this test are summarized as follows:

(1) The longitudinal planer method appears to be desirable to keep the tool marks running in the direction of the mating bearing rollers.

(2) A more desirable machine would be an actual "hydraulic tracer planer," which would be used in place of the attachment, or, better still, a numerically controlled planer. The latter would be the more desirable as all of the machine functions could be programmed beforehand, thus allowing higher speed.

(3) A final thickness variation of 0.127 mm (0.005 in.) can be expected. This would cause an undesirable step across the adjoining segments and would require hand work in the final assembly.

(4) It appears that the process of forming the plate cold, heat treating it, and then machining it on an appropriately equipped planer is a practical way of achieving the desired final dimensional accuracy. Some hand working of the steps across adjacent segments may be required at final assembly, but the end product will be much more satisfactory than achieved so far. The proposed method should also be competitive with the previous method on a cost basis, and can be used for replacement parts as well as for new construction.
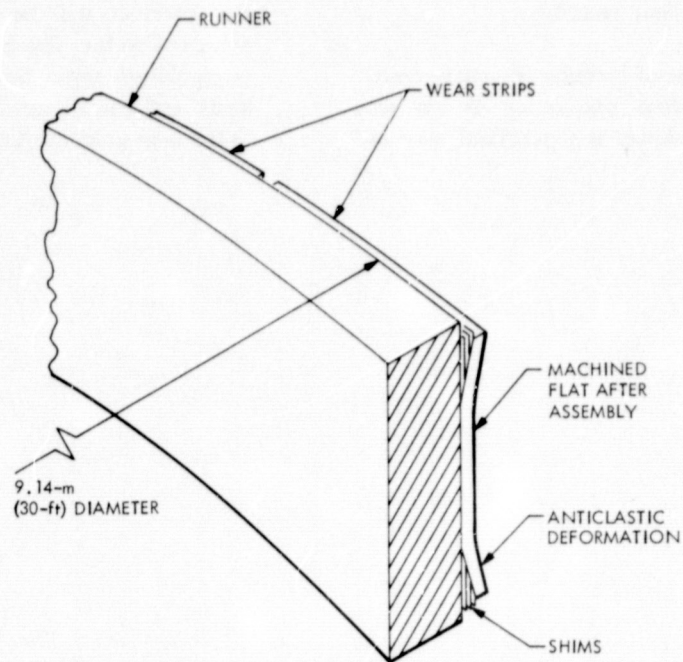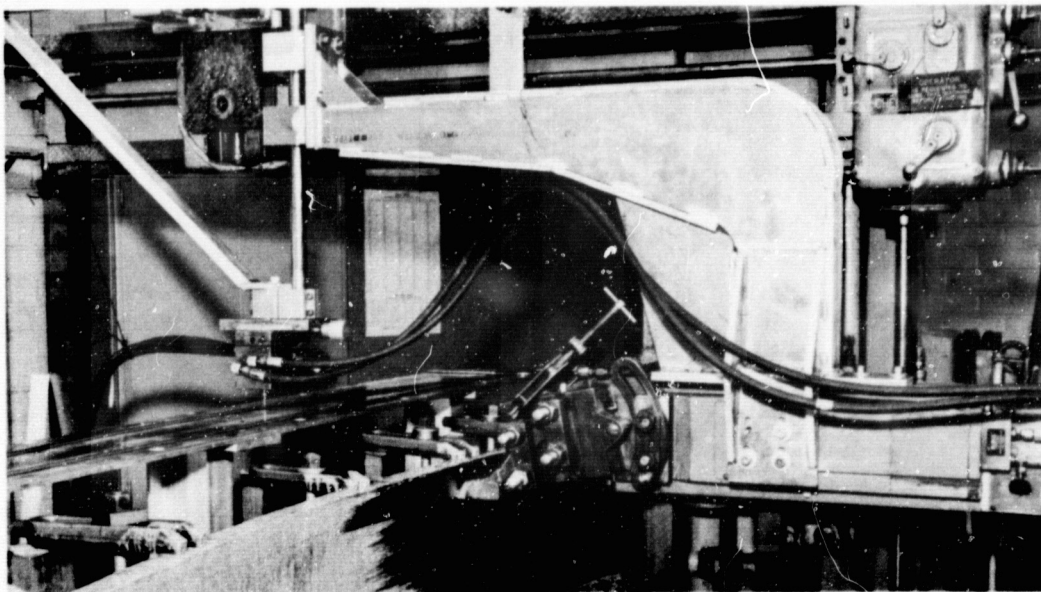
Fig. 1. Runner and wear strip details

Fig. 2. Planer tracer control setup

Operating Noise Temperature Calibrations of the S-Band Systems at DSS 14 for Calendar Year 1974

M. S. Reid and D. W. Veelik
Communications Elements Research Section

A previous article summarized the system operating noise temperatures of the receiving systems at DSS 14 for the calendar year 1973. This article reports recent precision system temperature measurements on the S-band receiving systems at DSS 14 and presents a summary for the calendar year 1974.

A previous article (Ref. 1) summarized the system operating noise temperatures of the receiving systems at DSS 14 for the calendar year 1973. This article reports recent precision system temperature measurements on the S-band receiving systems at DSS 14 and presents a summary for the calendar year 1974.

The S-band megawatt transmit (SMT) cone was in operation on the 64-m antenna at DSS 14 throughout 1974. Figure 1 shows a summary of the data for the whole year. System operating noise temperature in kelvins is plotted against time in day number and date. The configuration for the upper data set is the SMT cone, with the maser in the Module 3 area, operating in the diplexed mode. The low-noise receive-only path, operating with the maser in the SMT cone, is shown in the lower data set. All measurements were made at 2295 MHz with the antenna at zenith. Measurements made in clear weather are plotted as solid circles, and measurements made in

overcast weather or rain are plotted as open circles. There are 402 data points in the upper set excluding the unclear weather data. The average of these 402 clear weather measurements is 22.8 K and the standard deviation is 0.55 K. There are 60 clear weather measurements of the SMT cone low-noise path. The average of these data is 13.2 K and the standard deviation is 0.45 K. Most of the measurements, but not all, were made with the reflex feed system retracted. No distinction has been made in Fig. 1 between dichroic feed extended and retracted because the dichroic feed system does not degrade the SMT cone performance at high elevation angles (above 30 deg) (Ref. 1). The SMT cone was removed from the antenna on January 27, 1975.

Figure 2 is a plot of the system operating noise temperature of the polarization diversity S-band (PDS) and the S-band polarization diversity (SPD) cones. On September 28/29, 1974, the PDS cone was replaced by

the SPD cone, which is the standard DSN S-band cone at all three 64-m antenna stations. This change is shown in Fig. 2. In this figure also, measurements made in overcast or rain conditions have been clearly separated and excluded from the averages. All measurements were made at 2295 MHz with the antenna at zenith.

The noise temperature of the diplexed PDS cone shows a significant improvement in the second half of the year, and the PDS low-noise path shows an even greater improvement. Several changes were made in the PDS system, which could account for these lower noise temperatures in the latter part of the year. A bad rotary joint was replaced, and this improved both the low-noise path and the diplexed-noise temperatures. Furthermore, during September the PDS cone underwent a major configuration change. The following equipment was removed from the cone: two rotary joints, a quarter-wave plate, the cosine taper, orthomode transducer, an H-plane bend, the waveguide band-reject filter, a waveguide switch, and associated waveguide runs. A crossguide coupler was removed and replaced with a loop coupler, which reduced the waveguide path by approximately 13 cm. These changes were reflected by a marked improve-

ment in operating noise temperature as shown in the figure. Additional changes in the PDS cone prior to the Mariner 10 Mercury II encounter were the removal of the diplexer and the transmit filter. Insufficient measurements were recorded during these changes to yield a good average.

Two sets of SPD cone data are included in Fig. 2. The lower set shows the SPD cone diplexed measurements. The average of these 131 data points is 21.2 K and the standard deviation is 0.68 K. Measurements made with the SPD cone, diplexed, and the maser in the Module 3 area, are shown in the upper set. The average of these 22 measurements is 25.3 K and the standard deviation is 1.1 K.

All measurements in this report (most of which were made by station personnel at DSS 14) were made with the Y-factor technique of switching between an ambient termination and the horn. Most of the data points are based on a single Y-factor measurement, and the remainder were made with a precision technique of multiple Y-factors which has been discussed elsewhere (Refs. 2, 3, and 4). Table 1 is a summary of the averages of all the measurements.

References

1. Reid, M. S., and Gardner, R. A., "System Noise Temperature Calibrations of the Research and Development Systems at DSS 14," in *The Deep Space Network Progress Report*, Technical Report 32-1526, Vol. XIX, pp. 100–104, Jet Propulsion Laboratory, Pasadena, Calif., Feb. 15, 1974.

2. Stelzried, C. T., "Operating Noise-Temperature Calibrations of Low-Noise Receiving Systems," *Microwave J.*, Vol. 14, No. 6, p. 41, June 1971.

3. Stelzried, C. T., and Reid, M. S., "Error Analysis of CW Signal Power Calibration With Thermal Noise Standards," in *Supporting Research and Advanced Development*, Space Programs Summary 37-38, Vol. IV, pp. 189–191, Jet Propulsion Laboratory, Pasadena, Calif., Apr. 30, 1966.

4. Reid, M. S., and Stelzried, C. T., "Improved RF Calibration Techniques: System Operating Noise Temperature Calibrations of the JPL Research Cones," in *The Deep Space Network*, Space Programs Summary 37-62, Vol. II, pp. 86–87, Jet Propulsion Laboratory, Pasadena, Calif., Mar. 31, 1970.

Table 1. System operating noise temperature and other data for the SMT, SPD, and PDS cones for calendar year 1974

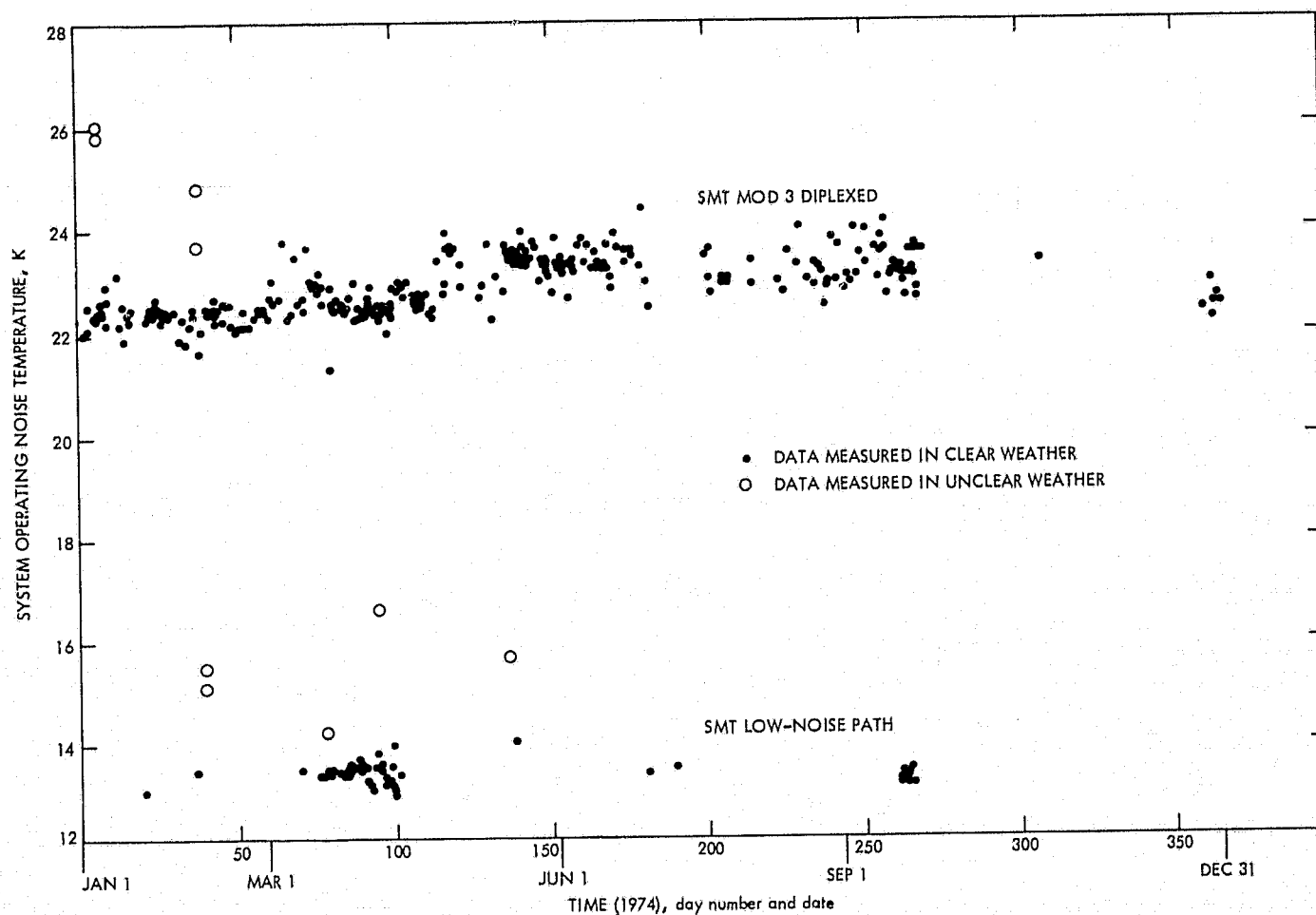| Cone and maser	System operating noise temperature			Maser gain, dB	Follow-up noise temperature, K	Number of measurements	Nominal maser noise temperature, K
	Average, K	Standard deviation	Number of measurements				
SMT cone MOD 3 maser Diplexed	22.8	0.55	402	45.0	0.19	6	
SMT cone SMT maser Low-noise path	13.2	0.45	60	48.6	0.09	6	2.1
SPD cone SPD maser Diplexed	21.2	0.68	131				
SPD cone MOD 3 maser Diplexed	25.3	1.07	22				
PDS cone PDS maser Diplexed Before mod.	24.1	0.79	52				
PDS cone PDS maser Diplexed After Mod.	22.2	1.1	4				
PDS cone PDS maser Low-noise path Before mod.	20.4	0.56	18				4.3
PDS cone PDS maser Stripped cone	14.6	1.1	2				

Fig. 1. System operating noise temperature of the SMT cone as a function of time for calendar year 1974
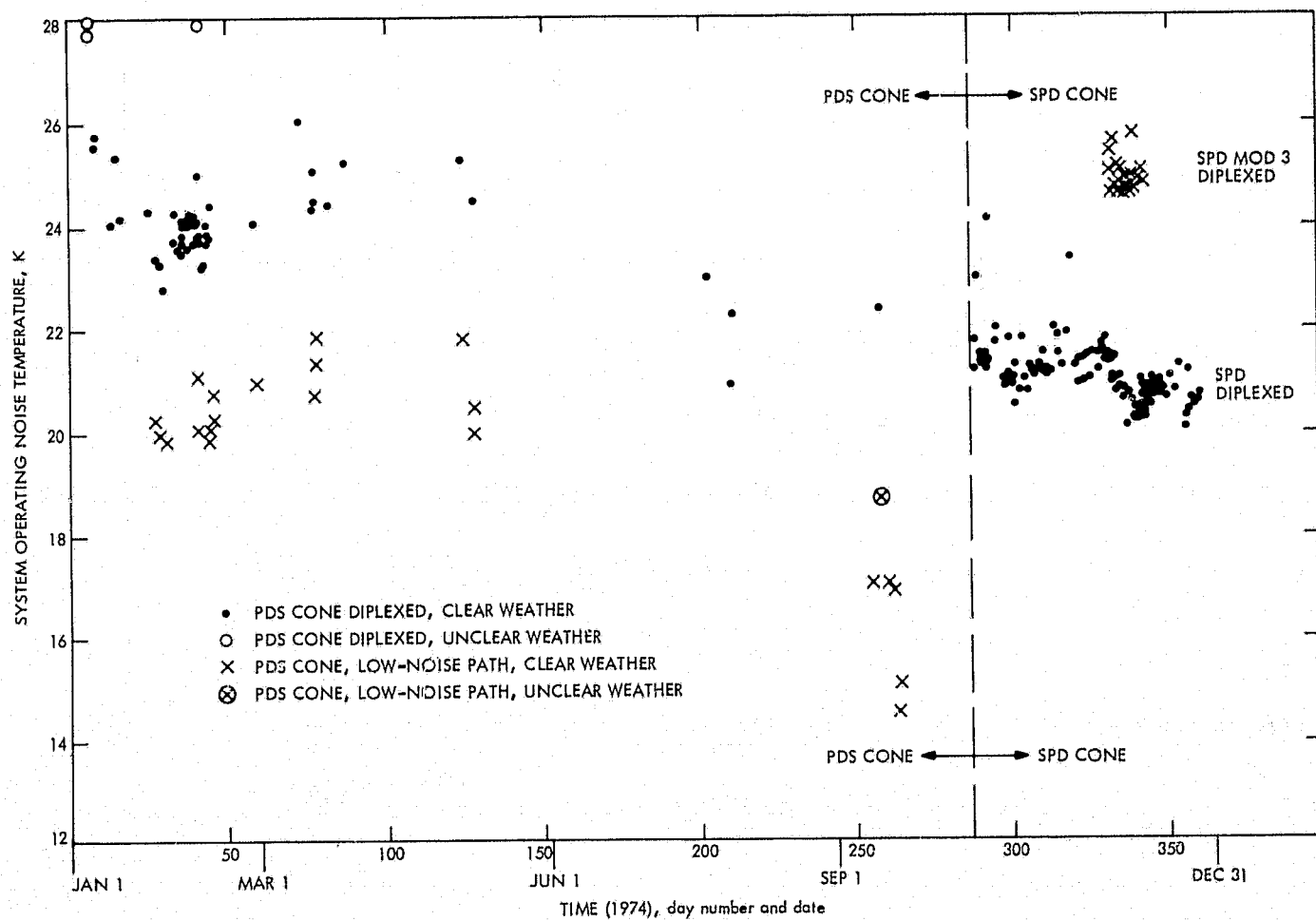
Fig. 2. System operating noise temperature of the PDS and SPD cones as a function of time for calendar year 1974

High-Viscosity Oil Filtration for Hydrostatic Bearings

H. D. McGinness and H. P. Phillips
DSN Engineering Section

In the operation of hydrostatic bearings, such as are used on the azimuth axis of the Deep Space Network 64-m antennas, the use of high-viscosity fluids offers advantages in operation clearances and in power consumption. One problem in using high-viscosity oils is that of appropriate filter selection. A test program was undertaken to determine the characteristics of commercially available filter elements used with high viscosity fluids. The test data forms the basis for selecting filter elements for use with fluids in the range of 2500 Saybolt second viscosity.

I. Introduction

In the operation of large hydrostatic bearings, such as are used to support the azimuth motion of the DSN 64-m antennas, the use of higher viscosity fluids provides a choice of higher film height between moving parts, lower power consumption by the high-pressure pumps, or a combination of these. However, the application of these fluids presents problems of filtration because of the high viscosities.

Typical filter elements for use with hydraulic oils are rated for fluids with viscosities in the range of 0.006 to 0.300 N-s/m² (30 Ssu to 1500 Ssu). For higher viscosities there is a tendency to extrapolate these ratings—a questionable practice when the viscosities to be used may range from 0.480 to 0.840 N-s/m² (2400 Ssu to 4200 Ssu). In order to develop a basis for the application of conventional filtering elements to these high-viscosity fluids,

Fram Corporation, under contract to JPL, conducted a series of tests on flows, pressure drops, and effects of water entrainment on several types of filtering elements using a high-viscosity oil of a type applicable to hydrostatic bearings.

II. Effect of Viscosity on Hydrostatic Bearing Operational Parameters

A hydrostatic bearing consists of a recessed pad and a runner (Fig. 1). High-pressure oil is forced through the pad recess to escape as a thin film between the runner and the pad. The pressure in the recess is directly related to the load applied on the pad. In operation the pad will lift, increasing the film height, until the pressure required to force the fluid out through the film is in equilibrium with the pressure due to the load.

The bearing film height, h, is determined from laminar flow consideration to be

$$h = K_1 \left[\frac{Q \cdot \mu}{W} \right]^{1/3} \qquad (1)$$

The pumping power, H, required to force the oil through the bearings is given by

$$H = K_2 \left[\frac{W^2 \cdot h^3}{\mu} \right] \qquad (2)$$

Where K_1 and K_2 are constants related to the size and configuration of the pads and recesses, Q is the oil flow, W the applied load on the pad, and μ the absolute viscosity, all in compatible terms.

From these it can be seen that for a fixed fluid flow and bearing load the film height for a particular bearing configuration varies as the third root of μ, the fluid viscosity.

Similarly, if the film height is maintained constant, the pumping power will vary inversely with the oil viscosity.

III. Test Program

The tests were conducted using Exxon EP5 lubricating oil, having a viscosity of 0.820 N-s/m² (4107 Ssu) at 29°C (85°F). The temperature-viscosity relationship of this oil is shown in Fig. 2. The test set up is shown in Fig. 3.

The series of tests listed in Table 1 was conducted to establish the flow versus pressure drop relationship of various filters.

The data recorded for Tests 1, 3, 4, 7, and 8 were the flow rates at temperatures of 29, 32, 35, and 38°C (85, 90, 95, and 100°F), with differential pressures of 1.38 × 10⁻⁴, 2.07 × 10⁻⁴, and 3.45 × 10⁻⁴ N/m² differential (2, 3, and 5 psi).

The data recorded for Test No. 9 were the flow rate at temperatures of 29, 32, 35, and 38°C (85, 90, 95, and 100°F) with differential pressures of 0.69 × 10⁻⁴, 1.38 × 10⁴, 2.07 × 10⁻⁴ N/m² (1, 2, and 3 psi).

The data recorded for Tests 2, 4, and 6 are flow rates at 29°C (85°F), with differential pressure at 2.07 × 10⁻⁴ N/m² (3 psi), 32°C (90°F) at 2.07 × 10⁻⁴ N/m (3 psi), 35°C (95°F) at 2.07 × 10⁻⁴, N/m² (3 psi), 38°C (100°F) at 2.07 N/m² (3 psi), and 29°C (85°F) at 1.38 × 10⁻⁴, 2.07 × 10⁻⁴, and 3.45 × 10⁻⁴ N/m² (2, 3, and 5 psi).

The flow rate for Tests 1 through 9 was accomplished by volumetric measurement of flow through the filter return line. The temperature was maintained using the ASTM 51F thermometer as the control.

The volumetric samples (3000 to 4000 ml) required to establish the flow rate through the filters were taken only when the temperature was within 0.06°C (0.1°F) of the required temperature and was stable. A minimum of four volumetric samples were taken over a minimum of one hour at each temperature-differential pressure setting 29°C (85°F) at 1.38 × 10⁻⁴ N/m² (2 psid), 29°C (85°F) at 2.07 × 10⁻⁴ N/m² (3 psid).

To determine the effects of water on the filter elements, the elements used for Tests 2, 4, and 6 were submerged in water for a minimum of twelve hours before testing was accomplished. Test results are summarized in Table 2.

Test No. 11 was viscosity versus temperature on Exxon Spartan EP5 Lube Oil. The results of this test are shown on Fig. 2.

IV. Conclusion

Commercial filters are satisfactory for filtering oil in the viscosity range of 2400 to 4200 Ssu. The test results provides satisfactory basis for selecting filter elements for such applications.

Table 1. Flow versus pressure drop tests

Test No.	Fram filter element	Type of test
1	C-744-15-0	Flow versus differential pressure
2	C-744-15-0	Flow versus differential pressure using a water-wetted element
3	C-709	Flow versus differential pressure
4	C-709	Flow versus differential pressure using a water-wetted element
5	C-788-40HTO	Flow versus differential pressure
6	C-788-40HTO	Flow versus differential pressure using a water-wetted element
7	C-703-10	Flow versus differential pressure
8	C-703-25	Flow versus differential pressure
9	C-703-40	Flow versus differential pressure
10	None	Viscosity versus temperature for Exxon EP5 Lubricating oil

Table 2. Test results

Temperature, °C	ΔP, N/m² × 10⁴ (psi)	Test 1 C-744-15-0 15 μm paper	Test 2 C-744-15-0 15 μm paper (Water wet)	Test 3 C-709 25 μm paper	Test 4 C-709 25 μm paper (Water wet)	Test 5 C-788-40HTO 40 μm paper	Test 6 C-788-40HTO 40 μm paper (Water wet)	Test 7 C-703-10 10 μm screen	Test 8 C-703-25 25 μm screen	Test 9 C-703-40 40 μm screen
					Flow, m³/sec × 10⁴ (gal/min)					
29	0.69 (1)		0.757 (1.20)							3.89 (6.16)
	1.38 (2)	0.82 (1.30)	1.29 (2.05) 1.17 (1.85)	1.77 (2.81)	1.53 (2.43)	1.68 (2.66)	1.67 (2.64)	0.59 (0.94)	1.74 (2.77)	8.74 (13.86)
	2.07 (3)	1.17 (1.85)	1.94 (3.07)	2.50 (3.96)	2.93 (4.65) 2.21 (3.50)	2.51 (3.99)	2.64 (4.18) 2.52 (3.99)	0.95 (1.50)	2.50 (3.96)	12.49 (19.8
	3.45 (5)	1.94 (3.08)		3.90 (6.18)	3.53 (5.59)	4.20 (6.65)	4.20 (6.65)	1.75 (2.77)	4.37 (6.93)	
32	0.69 (1)									5.80 (9.2)
	1.38 (2)	1.07 (1.69)		1.97 (3.13)		2.20 (3.49)		0.65 (1.03)	2.08 (3.30)	9.37 (14.85)
	2.07 (3)	1.49 (2.33)	1.46 (2.31)	2.88 (4.57)	3.12 (4.95)	2.93 (4.65)	3.20 (5.08)	0.97 (1.54)	3.12 (4.95)	17.49 (27.72)
	3.45 (5)	2.34 (3.71)		4.68 (7.42)		4.72 (7.49)		1.87 (2.97)	5.00 (7.92)	
35	0.69 (1)									6.24 (9.9)
	1.38 (2)	1.18 (1.87)		2.50 (3.96)		2.51 (3.99)		0.83 (1.32)	2.34 (3.71)	12.49 (19.8)
	2.07 (3)	1.77 (2.81)	1.75 (2.77)	3.54 (5.61)	3.53 (5.59)	3.53 (5.59)	3.92 (6.21)	1.29 (2.05)	3.50 (5.54)	18.74 (29.7)
	3.45 (5)	3.03 (4.80)		5.35 (8.48)		5.87 (9.31)		2.19 (3.47)	6.25 (9.90)	
38	0.69 (1)									7.00 (11.1)
	1.38 (2)	1.59 (2.52)		2.88 (4.57)		3.32 (5.26)		0.95 (1.50)	2.91 (4.62)	18.74 (29.7)
	2.07 (3)	2.24 (3.55)	2.19 (3.47)	4.11 (6.51)	4.20 (6.65)	4.72 (7.49)	4.47 (7.09)	1.53 (2.42)	4.69 (7.43)	Over 19 (30)
	3.45 (5)	3.58 (5.67)		6.50 (10.30)		7.05 (11.17)		2.50 (3.96)	7.50 (11.88)	

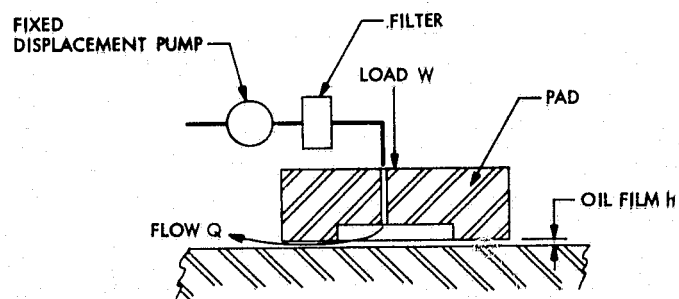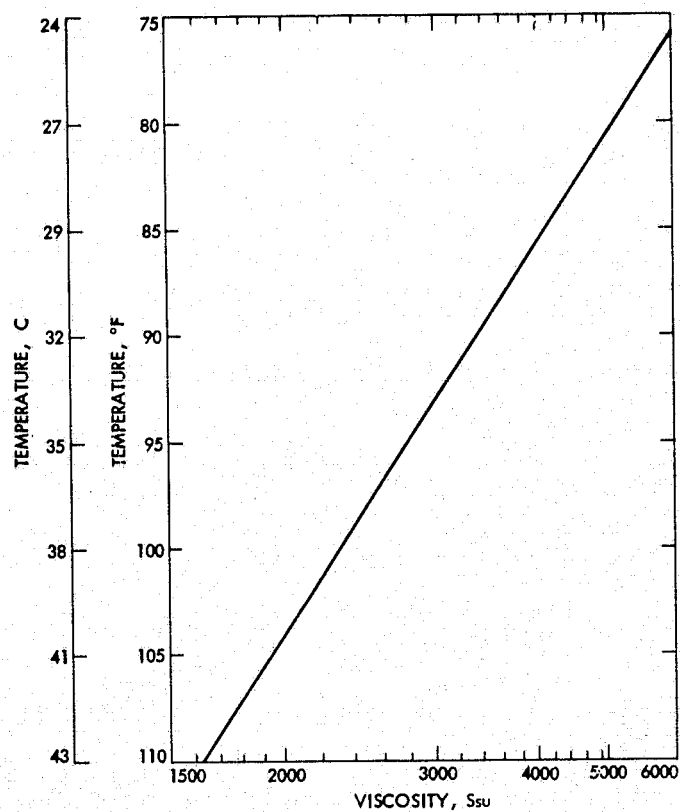Two entries under Tests 2, 4, and 6 indicate different tests.

Fig. 1. Typical hydrostatic bearing

VISCOSITY, Ssu

TEMPERATURE, °C (°F)	DYNAMIC VISCOSITY, m^2/s	Ssu
25.6 (78)	0.001206	6000
29.4 (85)	0.00888	4107
32.2 (90)	0.00703	3255
34.9 (94.9)	0.00603	2793
37.2 (99)	0.00522	2400
43.3 (110)	0.00357	1600

Fig. 2. Viscosity versus temperature, Exxon E.P.5 lubricating oil

Fig. 3. Flow schematic of oil test facility

Long Frame Sync Words for Binary PSK Telemetry

B. K. Levitt
Communications Systems Research Section

Sequences of length 16 to 63, which possess correlation properties suited to frame sync applications for binary phase-shift-keyed (PSK) telemetry, have been found. From a storage viewpoint, these sequences all have the advantage of being generated by a 5- or 6-bit linear feedback shift register.

Consider the problem of determining a suitable frame sync word for a digital communication link employing binary phase-shift-keyed (PSK) modulation. For uncoded data received over the additive white Gaussian noise channel, the optimum procedure for locating the received sync words is based on a bit correlation rule (Ref. 1). In the block-coded case, the optimum sync word search requires a word correlation rule (Ref. 2); however, practical considerations often dictate the use of the suboptimal bit correlation approach.

For example, if format constraints require that the sync word not contain an integral number of block code words, the bit correlation scheme is much less complex than the optimum frame sync rule (Ref. 2, p. 1130). In the case of convolutionally coded telemetry as well, the suboptimal bit correlation sync word search is desirable from a complexity viewpoint.

Suppose the sync word is a K-bit binary sequence of ± 1's, $s = (s_0, s_1, \cdots, s_{K-1})$, with the nonperiodic (Ref. 3, p. 195) autocorrelation function

$$C_\ell = \sum_{i=0}^{K-1-\ell} s_i s_{i+\ell}; \qquad 0 \le \ell \le K \qquad (1)$$

In a binary PSK modulation system, because the derived carrier reference in the receiver has an inherent 180 deg phase ambiguity, the detected data stream will be inverted with probability $\frac{1}{2}$ (e.g., Ref. 4). Consequently, when a bit correlation sync rule is used, the probability of false synchronization is minimized by selecting a sync word s for which $|C_\ell|$ is minimized over the range $1 \le \ell \le K - 1$. That is, ideally the autocorrelation function of s should have the property

$$|C_\ell| \le 1; \qquad 1 \le \ell \le K - 1. \qquad (2)$$

Sequences satisfying this constraint are called Barker codes (Ref. 5); they are optimum sync words for the channels of interest. Unfortunately, no binary sequences of length greater than 13 satisfy the Barker restriction of Eq. (2) (e.g., Ref. 6).

Generally, if sync words s with suitable autocorrelation functions are considered, frame sync performance improves exponentially with increasing length K. For $K > 13$, the Barker constraint must be relaxed somewhat, although it is still desirable that $|C_\ell|$ be near zero for $\ell \neq 0$. To this end, Neuman and Hofman (Ref. 7) have argued that the following criterion can be used to select good frame sync words for arbitrary lengths K. They define a "minimum distance"

$$D_{\min} \equiv \min\{D_\ell : 1 \leq \ell \leq K - 1\}, \qquad (3)$$

where the parameter

$$D_\ell \equiv K - \sqrt{\ell} - |C_\ell|. \qquad (4)$$

Note that

$$D_{\min} \leq D_{K-1} = K - 1 - \sqrt{K-1}. \qquad (5)$$

A good K-bit sync word s for the channels of interest is one for which $D_{\min}$ is near the upper bound of Eq. (5). Using computer search techniques, Neuman and Hofman found sequences which maximized $D_{\min}$ over *all* binary K-tuples, for the range $7 \leq K \leq 24$. Massey has demonstrated by simulation that these Neuman-Hofman sequences compare favorably with Barker codes for frame sync applications when $K \leq 13$ (Ref. 1, Tables 1 and 2).

For longer lengths K, the Neuman-Hofman search procedure for a good K-bit sync word involves a prohibitively large number of candidates: even though complimentary and reversed sequences yield identical $D_{\min}$'s, 2^{K-2} binary K-tuples must still be compared. In order to keep the computer search time for longer sync words within practical limits, only a small subset of all possible sequences can be examined; hopefully, the size of this subset should grow linearly, rather than exponentially, with K.

For a given large value of K, it is proposed that the sync word search be confined to the subset of binary K-tuples which are prefixes of pseudo-noise sequences (maximum-length linear recurring sequences; e.g., Ref. 8, p. 75) of length $2^L - 1$, where L satisfies the inequality

$$2^{L-1} < K + 1 \leq 2^L. \qquad (6)$$

Pseudo-noise (PN) sequences have periodic (Ref. 3, p. 195) autocorrelation functions of the form

$$C_\ell = \sum_{i=0}^{K-1} s_i s_{i+\ell} = \begin{cases} K & ; \quad \ell = 0 \\ -1 & ; \quad 1 \leq \ell \leq K - 1. \end{cases} \qquad (7)$$

Where the subscript $i + \ell$ is modulo 2. Of course, for frame sync applications, it is the *non-periodic* autocorrelation C_ℓ that is of interest. Nonetheless, PN sequences are sufficiently pseudo-random that the subset defined above contains some excellent sync words, as shown below. Furthermore, a PN sequence of length $2^L - 1$ can be generated by an L-stage linear feedback shift register, which is advantageous from a storage viewpoint.

To demonstrate the merit of the shortened sync word search procedure described above, it was used to find good sync words of lengths 16 to 63. For a given K in the range $16 \leq K \leq 31$, $D_{\min}$ was maximized over all possible K-bit prefixes of 31-bit PN sequences ($L = 5$ according to Eq. (6)). Neglecting reversed PN sequences, there were only 3 distinct 5-stage linear feedback shift register configurations to consider (Ref. 9, Appendix C): these are completely described by the linear recursion formulas in Table 1A. Each configuration generates any of 31 different PN sequences (which are cyclic permutations of one another), depending upon which 5-bit initializing sequence $s' = (s_0, s_1, s_2, s_3, s_4)$ is used (excluding the all-1 sequence). Thus, for each K in the stated range, 93 candidate sync words were compared. The best sync words found are listed in Table 2: for a given length K, the sync word s consists of the *first* K bits generated by the indicated shift register configuration, initialized by the designated sequence s'.

Similarly, for $32 \leq K \leq 63$, $D_{\min}$ was maximized over K-bit prefixes of 63-bit PN sequences. Here, there were 3 distinct 6-stage linear feedback shift register arrangements of interest (Ref. 9, Appendix C), described by the recursion formulas of Table 1B. So 189 possible sync words were compared for each K in this range, and the best are listed in Table 2. Also, out of curiosity, the K-bit prefixes of these 63-bit PN sequences were tested with respect to $D_{\min}$ as possible sync words for $16 \leq K \leq 31$. As indicated in Table 2, for 4 values of K in this range, a sync word derived from a 63-bit PN sequence has a larger $D_{\min}$ than the best 31-bit derivative. In fact, for $K = 17$ the sync word derived from a 63-bit PN sequence has a $D_{\min}$ which equals the upper bound of Eq. (5).

To demonstrate how close the $D_{\min}$'s of the sync words in Table 2 approach the upper bound of Eq. (5), they are plotted in Fig. 1.

References

1. Massey, J. L., "Optimum frame synchronization," *IEEE Trans. Commun.*, Vol. COM-20, pp. 115–119, April 1972.

2. Levitt, B. K., "Optimum frame synchronization for biorthogonally coded data," *IEEE Trans. Commun.*, Vol. COM-22, pp. 1130–1133, August 1974.

3. Turyn, R., "Sequences with small correlation," in *Error Correcting Codes*, H. B. Mann, Ed., New York: John Wiley & Sons, Inc., 1968, pp. 195–228.

4. Stiffler, J. J., *Theory of Synchronous Communications*, Prentice-Hall, Inc., Englewood Cliffs, N.J., 1971.

5. Barker, R. H., "Group synchronization of binary digital systems," in *Communication Theory*, pp. 273–287. W. Jackson, Ed. Butterworth, London, England, 1953.

6. Turyn, R., "On Barker codes of even length," *Proc. IEEE*, September 1963.

7. Neuman, F., and Hofman, L., "New pulse sequences with desirable correlation properties," in *Proceedings of the National Telemetry Conference*, pp. 272–282, Washington, D.C., April 1971.

8. Golomb, S. W., *Shift Register Sequences*. Holden-Day, Inc., San Francisco, Calif., 1967.

9. Peterson, W. W., *Error-Correcting Codes*. MIT Press, Cambridge, Mass., 1961.

Table 1. Linear recursion formulas for generating 31-bit PN sequences from 5-stage linear feedback shift registers (the s_i's are ± 1)

Configuration	Formula
5A	$s_i = s_{i-3} \cdot s_{i-5}$
5B	$s_i = s_{i-1} \cdot s_{i-2} \cdot s_{i-3} \cdot s_{i-5}$
5C	$s_i = s_{i-1} \cdot s_{i-3} \cdot s_{i-4} \cdot s_{i-5}$

Table 2. Recursion formulas for generating 63-bit PN sequences from 6-stage shift registers

Configuration	Formula
6A	$s_i = s_{i-5} \cdot s_{i-6}$
6B	$s_i = s_{i-1} \cdot s_{i-4} \cdot s_{i-5} \cdot s_{i-6}$
6C	$s_i = s_{i-1} \cdot s_{i-3} \cdot s_{i-4} \cdot s_{i-6}$

Table 3. Listing of best K-bit frame sync words derived from 31- and 63-bit PN sequences.

K	Upper bound on D_{min} $K-1 - \sqrt{K-1}$	D_{min}	$\|C_\ell\|_{max}$ $(1 \le \ell \le K-1)$	Configuration	Initializing sequence, s'
16	11.13	10.26	3	5A	1,−1,−1,−1,1
16	11.13	10.26	3	5B	−1,−1,1,1,−1
17	12.00	10.84	4	5A	1,−1,−1,−1,1
17	12.00	12.00	4	6B	1,1,−1,−1,−1,−1
18	12.88	11.55	4	5A	1,1,−1,1,1
18	12.88	11.55	4	5C	1,−1,1,1,1
18	12.88	12.00	4	6B	1,1,1,−1,−1,−1
19	13.76	12.88	4	5C	1,−1,1,1,1
20	14.64	13.68	3	5C	1,−1,1,1,1
21	15.53	14.59	5	5B	−1,−1,−1,−1,−1
21	15.53	14.64	4	6B	1,−1,−1,−1,−1,−1
22	16.42	15.53	4	5B	−1,−1,−1,−1,−1
23	17.31	16.00	4	5B	−1,−1,1,1,−1
24	18.20	16.64	5	5A	−1,1,1,−1,−1
24	18.20	16.64	5	5C	−1,−1,1,1,1
25	19.10	17.76	5	5A	1,−1,1,1,1
26	20.00	18.76	5	5C	−1,−1,1,1,1
26	20.00	18.88	5	6A	1,−1,−1,−1,−1,−1
27	20.90	19.55	5	5A	1,1,−1,−1,−1
28	21.80	20.20	5	5B	−1,1,−1,−1,−1
29	22.71	21.53	5	5A	1,−1,−1,−1,−1
30	23.61	22.26	4	5E	1,−1,1,−1,−1
31	24.52	23.31	4	5C	1,1,1,−1,−1
32	25.43	22.90	6	6B	−1,1,−1,−1,1,−1
33	26.34	23.80	5	6A	1,−1,−1,1,1,−1
34	27.26	24.88	6	6C	−1,1,1,1,−1,1
35	28.17	25.80	5	6A	−1,1,−1,−1,1,1
36	29.08	26.90	4	6A	−1,−1,1,−1,−1,1
37	30.00	27.43	7	6A	1,−1,1,1,−1,1
37	30.00	27.43	7	6B	1,1,−1,−1,1,1
38	30.92	28.42	5	6A	−1,1,1,1,−1,−1
39	31.84	29.13	7	6A	−1,1,−1,−1,−1,1
40	32.76	30.34	6	6C	−1,−1,−1,1,1,1
41	33.68	30.90	7	6A	−1,1,−1,−1,−1,1
41	33.68	30.90	7	6C	−1,1,1,1,1,−1
42	34.60	31.80	8	6C	−1,1,1,1,1,−1
43	35.52	32.64	7	6A	1,1,1,−1,−1,1
44	36.44	33.80	7	6C	1,1,1,−1,1,1
45	37.37	34.34	8	6C	1,−1,−1,1,−1,1
46	38.29	35.17	8	6C	1,−1,1,−1,−1,1
47	39.22	36.00	7	6C	−1,−1,−1,1,−1,1
48	40.14	36.92	7	6B	1,−1,1,1,1,−1
49	41.07	38.00	7	6C	1,1,−1,1,1,−1
50	42.00	38.90	7	6A	−1,1,−1,1,−1,−1
51	42.93	40.00	7	6C	1,1,1,1,−1,1
52	43.86	40.92	7	6A	1,−1,1,1,1,1
53	44.79	41.68	8	6C	−1,1,−1,−1,1,1

Table 3 (contd)

K	Upper bound on D_{min} $\frac{}{K-1 - \sqrt{K-1}}$	D_{min}	$\|C_\ell\|_{max}$ $(1 \leq \ell \leq K-1)$	Configuration	Initializing sequence, s'
54	45.72	42.92	7	6C	$-1,1,-1,1,-1,1$
55	46.65	43.76	7	6C	$1,-1,1,1,1,1$
56	47.58	44.76	6	6A	$1,1,1,1,-1,1$
57	48.52	45.61	6	6C	$-1,-1,1,-1,-1,-1$
58	49.45	46.00	7	6C	$1,1,1,1,-1,-1$
59	50.38	47.22	7	6A	$-1,-1,1,1,-1,-1,-1$
60	51.32	48.00	8	6C	$1,1,1,-1,-1,1,1$
61	52.25	49.43	6	6A	$1,1,1,1,-1,1$
62	53.19	50.34	6	6B	$-1,1,1,1,-1,-1$
63	54.13	51.52	6	6B	$1,-1,1,1,-1,1$
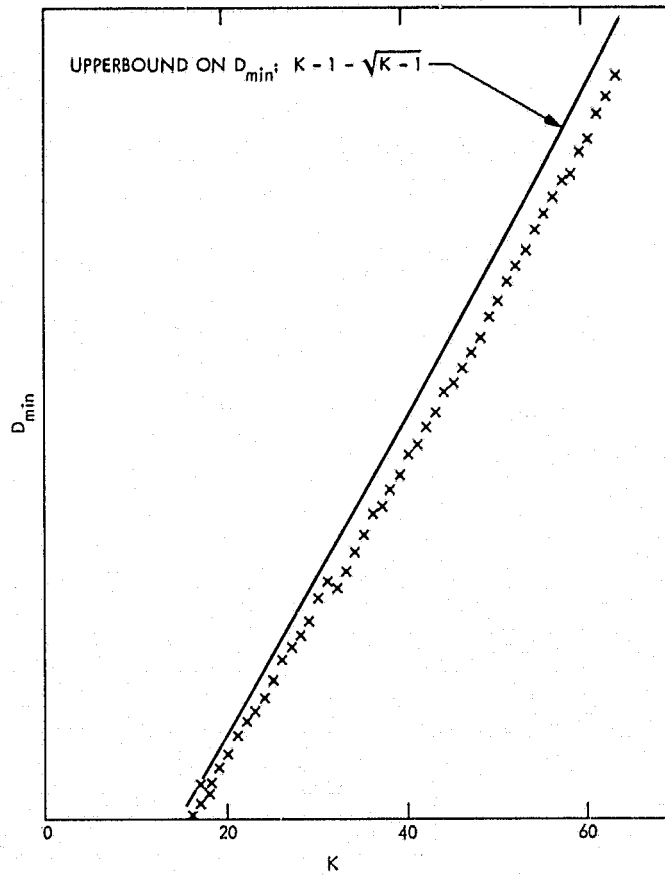
Fig. 1. Measure of correlation properties of K-bit sync words in
Table 3 using Neuman-Hofman distance parameter D_{min}

A Multiple-Rate Digital Command Detection System With Range Cleanup Capability

J. R. Lesh
Communications Systems Research Section

A multiple-rate command transmission and detection scheme that utilizes a composite signal as a subcarrier is described. The composite subcarrier is constructed in such a way that it can be used for ranging. Furthermore, the ranging and command signals can be processed in a near-optimal fashion with the same detector system. The performance of the detector system is analyzed and found to be consistent with realistic mission requirements.

I. Introduction

Most space vehicles employ phase-locked receivers that track the unmodulated (or residual) uplink carrier signal. As a result, all information transmitted to the spacecraft must be such that, when modulated onto the carrier signal, the information contained in the modulation sidebands falls outside the receiver tracking loop bandwidth. Because of this, information signals containing a large amount of low-frequency energy (such as command signals) must first be modulated onto an intermediate carrier (or subcarrier) before finally being modulated onto the carrier.

The introduction of the subcarrier, however, is not a "cure-all," since in order to coherently demodulate the information signal one must now coherently track the subcarrier in addition to the carrier and data. The standard approach to all of the above is to provide independent tracking loops to "track out" all of the information contained in each of the carriers. It seems ironic that after going through all this trouble to eliminate the information contained in these carriers many spacecraft systems employ a second channel (subcarrier), the phase of which is used to gather range information.

In this article a command detector system is described that uses a composite signal as a subcarrier. This composite subcarrier is designed in such a way that it can also convey range information. As a result it is possible to perform essentially optimum detection of the command and ranging signals with the same detector. A preliminary analysis indicates that the performance of the detection system is adequate for most spacecraft missions.

Before discussing the system let us consider a few constraints within which the system must operate. First, we will make the command bit rate coherently related to the subcarrier rate. The reason for this is ease of generation of command signals on the ground as well as the reference signals in the spacecraft. Actually, we will consider only systems wherein the subcarrier and bit rates are related by a power of 2, although this constraint is not absolutely necessary. Second, we will consider systems having multiple command rate capabilities with the proviso that the lowest symbol rate is one symbol per second and that a particular symbol rate will be used only if the symbol energy-to-noise density ratio at that symbol rate exceeds 10 dB ($P_e \leq 10^{-5}$). Finally, we will allow the received signal at the spacecraft to undergo a doppler frequency shift. However, we will restrict the doppler magnitude (fractional shift δ in Hz/Hz) to less than 10^{-6}. Although many spacecraft missions actually experience absolute doppler shifts in excess of this amount the majority of this shift is predicted and compensated for at the ground transmitter. Thus, a bound of 10^{-6} appears to be reasonable for the doppler that the spacecraft actually experiences.

II. System Description

The system described here is motivated by the range cleanup loop discussed by Hurd (Ref. 1). This cleanup loop is actually a generalization of a phase-locked loop wherein the loop voltage-controlled oscillator (VCO) is replaced by a VCO/function generator combination. The function generator provides a synchronous version of a square wave signal modulated by the particular range code component that is being received. In addition the function generator also provides a second signal consisting of the same square wave signal modulated by the next lower range code component.

Also provided with the clean-up loop are two correlators. One of these correlates the received signal with the same composite function generator signal which is being used in the loop to derive the loop error signal. As long as this correlator output is sufficiently high we know that we are tracking with the proper range code reference. The second correlator compares the received signal with the other function generator (next range code) signal. If this correlator output becomes sufficiently high we know that the received signal has undergone a change in the range code component. Detection of this change causes the function generator to shift references enabling the loop to track the new composite signal. Likewise, the correlation detector references are changed so that they are looking for the present composite signal as well as the next lower composite signal.

If one thinks about the operation of the cleanup loop for a moment, it soon becomes apparent that the loop is no more than a phase-locked loop with a detector for sensing when the loop is in lock. Consequently, one would think that by adding an in phase data integrator leg (which already exists in the lock detector circuitry) and a mechanism whereby the effect of data modulation could be removed from the error channel, the cleanup loop could be converted to a subcarrier demodulator and bit (symbol) detector where the subcarrier is actually the composite range signal. A mechanism whereby this can be accomplished is shown in Fig. 1.

Before describing the operation of the system let us consider the structure of the composite signal we will use as a subcarrier. The subcarrier signal consists of a square wave of frequency f_{sc} phase modulated by one of its own subharmonics. For example if f_{sc} denotes a square wave of frequency f_{sc} then the ith possible composite subcarrier (also denoted c_i, the ith ranging code) is represented by

$$c_i = \overline{f_{sc}} \oplus \overline{\frac{f_{sc}}{2^i}}$$

where $\oplus$ indicates modulo 2 addition if the square wave levels are $\{0,1\}$ or multiplication if the levels are $\{+1,-1\}$. In order to use these signals as subcarriers the code components must be used sequentially. For example, we initially send component c_1. After a sufficient period of time we send c_2, and so on. (Note that c_1 is a square wave signal of frequency $f_{sc}/2$.)

With the aid of the flow chart of Fig. 2 we can now explain the operation of the demodulator/detector. Initially all the switches in Fig. 1 are in the acquisition (ACQ) position and the function generator is outputting components c_1 and c_2. As long as no signal is received by the demodulator, neither the c_1 nor the c_2 correlators in the lock detector will accumulate to sufficiently high value. As soon as component c_1 is received at the demodulator the signal (which is filtered and sampled at the Nyquist rate) is applied to the transition sample selector of the phase-locked (cleanup) loop. The tracking loop consists of an all-digital second-order phase-locked loop such as the one discussed by Holmes and Tegnelia (Ref. 2) with the VCO replaced by a cleanup loop function generator. A more detailed discussion of how the loop operates is given in Ref. 2.

After a sufficient length of time the tracking loop will lock on to the received component c_1, and the c_i correlator in the lock detector will detect its presence. The system will continue in this mode indefinitely unless either the signal is lost or the c_2 correlator detects the presence of c_2. If c_2 is detected the function generator changes the signals c_1 and c_2 to c_2 and c_3 respectively and the system will continue indefinitely in this state until signal is lost or c_3 is detected, etc. Note that by supplying the signal labeled by c_i to the spacecraft transmitter the "cleaned up" range signal can be transmitted back to the ground.

Let us now associate with each ranging component c_i a particular command symbol rate. In particular let the symbol rate correspond to the frequency of the signal which when modulated onto f_{sc} produces the composite subcarrier. In other words when component c_i is sent, the corresponding symbol rate will be $f_{sc}/2^i$ symbols per second. Furthermore, since the symbol and subcarrier timing was specified as synchronous we see that detection of c_i corresponds to detection of the rate associated with c_i as well as the sequential determination of symbol timing at that rate. (Sequential symbol timing is determined by examining the sign of the c_{i+1} correlator at the time c_{i+1} is detected. This is the same process whereby range ambiguity is removed in the sequential ranging system.)

Recall that the switches in Fig. 1 were all set to the ACQ position. This is to allow efficient detection of the sequence of code components. However, once we reach the date rate at which we desire to send commands we must change all the switches to the DEMOD position. Since code components c_i and c_j, $i \neq j$ over an appropriate integration time are orthogonal, a convenient way to notify the detector that c_i corresponds to the desired command symbol rate is to follow the unmodulated transmission of $\overline{c_i}$ by a transmission of c_i (complement). Thus, the c_i correlator would serve not only as a c_i signal presence indicator but also as an end of acquisition detector. Once the end of acquisition sequence is detected, and the switches placed in the DEMOD position, the system is ready to demodulate and detect command data as well as track the c_i range code component. Note also that this demodulator does not have the characteristic phase ambiguity problem that most suppressed carrier tracking loops have, since we can define the transmission of $\overline{c_i}$ as actually the transmission of c_i with an all zeros command modulation signal.

Once the device is in the DEMOD mode the command symbol stream is integrated (accumulated) over the ap-

propriate symbol time T_s and the symbol detected. The symbol sign is then applied to the lock detector to remove the effects of data modulation on the lock detector accumulators. Likewise, the symbol sign is injected into the loop to remove data modulation on the loop error signal. Finally, we note that a signal from the lock detector representing the c_i correlator most significant bit (MSB) is applied to the loop after the second loop accumulator. This signal normally is not needed by the loop. However, during the time that $\overline{c_i}$ is being received to indicate the end of the acquisition sequence, the loop error signal will be complemented and hence cause the tracking loop to correct in the wrong direction. Note also that the c_i correlator will produce a highly negative rather than a positive correlation during this time. Consequently if the total accumulation time of the two loop accumulators matches the accumulation time of the lock detector, the loop error signal can be inverted so that the loop retains lock.

III. System Design

The parameters associated with the demodulator/detector are as follows (Ref. 2):

$\Delta_2 =$ integral control phase bump size

$\Delta_1 =$ proportional control phase bump size

$n = \Delta_1/\Delta_2$

$f_{sc} =$ subcarrier (basic) frequency

$T_{sc} = \dfrac{1}{f_{sc}}$

$T_s =$ symbol time

$L =$ phase bump exponent (i.e., $\Delta_2 = 2^{-L}$)

$K =$ subcarrier frequency exponent (i.e., $f_{sc} = 2^K$)

$M =$ number of subcarrier cycles per phase bump

$W =$ bandwidth (one sided) of the pre-sampling filter $= \dfrac{8}{T_{sc}}$

$\alpha = \dfrac{1}{16} =$ portion of each subcarrier cycle used for linear signal transition (Ref. 2)

$m =$ number of actual signal transitions occurring in M subcarrier cycles $\approx 2M$

$A =$ received signal amplitude (outside the linear transition region)

$N_0 =$ one-sided noise spectral density

C-2

Using these definitions we can specify the system constraints as

$$T_s \geq 1 \text{ second} \tag{1}$$

$$\frac{A^2 T_s}{N_0} \geq 10 \tag{2}$$

$$\delta \leq 10^{-6} \tag{3}$$

We also impose the additional constraints that

$$r \geq 2 \tag{4}$$

$$\sigma_L < 0.1 \text{ (radians)} \tag{5}$$

$$\frac{M T_{sc}}{\tau_2} \leq \frac{1}{3} \tag{6}$$

where r is the loop damping parameter, σ_L is the rms loop phase error and τ_2 is the loop secondary time constant. The constraint given by Eq. (6) is necessary to ensure that the loop will be stable in light of the fact that the loop accumulator produces a transport delay in the loop transfer function (Ref. 3, pp. 19–20). Using Eq. (6) and the fact that

$$\tau_2 = M T_{sc} \frac{\Delta_1}{\Delta_2} \tag{7}$$

results in the requirement

$$n \geq 3 \tag{8}$$

We will choose $n = 4$ for ease of implementation (although it may be necessary to increase n to 6 in order to retain stability at strong signal levels).

It was also shown in Ref. 2 that

$$\sigma_L^2 = \frac{\pi^3 N_0}{256 \, n M T_{sc} A^2} + \frac{\pi^{5/2} n \sqrt{N_0}}{2^L \sqrt{M T_{sc} A^2}} \tag{9}$$

and

$$r = \frac{16 \, n^2 \sqrt{2 M T_{sc} A^2}}{2^L \sqrt{N_0}} \tag{10}$$

Now, if the constraints Eqs. (4) and (5) are to be satisfied then we must require that

$$\xi \geq \max\left[\frac{1}{2} \log_2\left(\frac{25\pi^3}{64n}\right), \quad L + \log_2\left(\frac{\sqrt{\pi}}{8n^2\sqrt{2}}\right) \right] \tag{11}$$

and

$$L \geq \log_2\left[\frac{25\pi^{5/2} n \, 2^\xi}{\left(2^{2\xi} - \frac{25\pi^3}{64n}\right)} \right] \tag{12}$$

be simultaneously satisfied where

$$\xi = \frac{1}{2} \log_2\left(\frac{M T_{sc} A^2}{N_0}\right) \tag{13}$$

The equality portions of Eqs. (11) and (12) are shown in Fig. 3 for $n = 4$. Also shown in Fig. 3 is the line $L = 8$, which is the minimum value of L necessary to keep the phase bump quantizing error variance within reason. This results in an acceptable solution region as shown by the shaded region of Fig. 3.

It remains to determine the values of M and T_{sc}. Note that thus far all of the performance parameters depend on the product $M T_{sc}$. The two can be separated, however, by selecting M such that the variance of the phase error buildup due to doppler is less than 0.01 $(\text{rad})^2$. Toward this end we have from Ref. 2:

$$\phi_d \triangleq 2\pi M \delta \leq \frac{2\sqrt{3}}{10} \tag{14}$$

from which we get

$$M \leq 5.45 \times 10^4 \tag{15}$$

For implementation reasons we would like M to be a power of 2. Thus, we consider candidate solutions of the form $M = 2^i$, $i = 1, 2, \cdots, 15$. Noting that large M corresponds to high subcarrier frequencies (which is desirable for ranging applications) we conservatively choose $M = 2^{14}$. Then, from Fig. 3, Eq. (13), and the design point condition

$$\frac{A^2 T_{s_{max}}}{N_0} = \frac{A^2}{N_0} = 10 \tag{16}$$

we find that $T_{sc_{min}} = 2^{-14}$. The significant loop design parameters then become

$$M = 2^{14}, \qquad T_{sc} = 2^{-14}$$
$$L = 8, \qquad\qquad n = 4 \tag{17}$$

from which all of the other parameters can be calculated.

Having chosen the loop parameters we now turn to the lock detector accumulators. Recall that Eq. (17) is suffi-

cient to guarantee a symbol error probability of 10^{-5} whenever antipodal signals of mean value $\pm A$ are received and integrated for $T_{s_{max}} = 1$ sec. However, the lock detectors must distinguish between signals having mean values of $-A$, 0, $+A$ where the zero mean value results from correlating with one of the orthogonal signals. This means that the lock detectors are working at a 6 dB disadvantage relative to the symbol detector. If we desire the same error statistic (i.e., 10^{-5}) for miss and false alarm probabilities then we can simply increase the lock detector accumulation times by a factor of 4. This means that *a priori* (i.e., before symbol rate is known) we must accumulate over 4 seconds in the lock detectors. However, once the actual rate has been determined the lock detector accumulation times can be reduced to $4\,T_s$ seconds.

Recall that in the last section we stated that the lock detector most significant bit signal could be used to correct the direction of the loop phase error when c_K was being received *if* the accumulation times of the loop accumulators and the lock detector matched. However, we have just required that the lock detector accumulate over four loop accumulation times. This presents no problem if we split the in-phase lock detector accumulator into two sections such that the first section accumulation time matches that of the loop. Figure 4 is a revised block diagram showing how this can be accomplished. (Note: the notation Σ/X means that the input is accumulated until the accumulation time, or the accumulation index equals X.)

IV. Loop Performance

From the equations of Ref. 2 one can easily find that the design point values for the present design are

$$w_L = 0.44\,\text{Hz}$$
$$r = 2.52 \tag{18}$$
$$\sigma_L = 5.67\,\text{deg}$$

These expressions are computed based on a linearized model of the loop phase detector. It turns out that the loop detector actually operates in a region where the linear theory does not apply. In order to improve our performance estimates we will use equivalent linearization about the particular average phase detector operating point. Toward this end let

$$A_{eq}(\phi) = \frac{\partial}{\partial \phi}\{E[\hat{\phi}|\phi]\} \tag{19}$$

be the equivalent phase gain when the loop phase error is ϕ. Since the loop is operating at a high loop signal-to-noise ratio (SNR) we can model the loop phase error as a gaussian process with mean zero and variance σ_L^2. In this case we can average Eq. (19) over this distribution to get

$$\overline{A_{eq}} = \frac{\sqrt{\frac{2\rho}{\pi}}}{\pi\alpha}\left(\frac{1}{1 + \frac{\rho\,\sigma_L^2}{\pi^2\alpha^2}}\right)^{1/2} \tag{20}$$

where

$$\rho = \frac{mA^2}{N_0 W} \tag{21}$$

is the sample SNR. By using Eq. (20) in place of A_{eq} of Ref. 2 one obtains results that include the effects of limiter suppression. Note, however, that these equations require a recursive procedure for evaluation. Figures 5, 6 and 7 illustrate the behavior of r, w_L and σ_L as ρ varies. Note that the design point value of ρ is 4 dB. Also shown for comparison in Figs. 5 through 7 are the corresponding results using the linear theory.

It should be noted that the sequential acquisition procedure described earlier requires that the tracking loop be free of cycle slipping. Thus, we would like the mean time to slip $T(2\pi)$ to be extremely large. Viterbi (Ref. 4) has shown that at high values of loop SNR ρ_L, the mean time to slip, is well approximated by

$$T(2\pi) \approx \frac{\pi}{2w_L}e^{2\rho_L}. \tag{22}$$

Since $\rho_L \approx 1/\sigma_L^2 \approx 100$ and $w_L \approx 1.0$ we see that cycle slipping while tracking a signal component is indeed an extremely rare event. Consequently, we can assume that cycle slipping can occur only during the time required to detect a code component change, since during this time the loop is operating with the wrong phase reference signal. Hurd (Ref. 5) has shown that if a second-order loop experiences a loss of signal at time $t = 0$ the phase error variance $\sigma_L^2(t')$ at time $t = t'$ is given by

$$\frac{\sigma_L^2(t')}{\sigma_L^2(0)} = 1 + \frac{4r^2}{r^2 + 1}w_L t' + \frac{4(2r^2 + 1)r^2}{(r^2 + 1)^3}(w_L t')^2$$
$$+ \frac{16r^4}{3(r^2 + 1)^4}(w_L t')^3 \tag{23}$$

Using the design point values for the loop parameters and the lock detector time of 4 seconds for t' yields

$$\sigma_L^2(4 \text{ seconds}) = 0.141 \text{ rad}^2 \qquad (24)$$

Finally, the application of Eq. (22) results in a mean time to slip when experiencing a code change of 4.52×10^6 seconds.

V. Lock Detector Performance

Recall that our model for the filtered subcarrier signal has a linear region of length $T_{sc}/16$ surrounding each subcarrier transition and that the received signal is sampled at $16 f_{sc}$. Now, if the phase error is small then out of any 16 consecutive samples we will have seven with mean value $+A$, seven with mean value $-A$ and two samples which are zero mean. (This is strictly true when the square wave is unmodulated and is a pessimistic approximation whenever modulation is present.) If each sample is hard limited to ± 1 and multiplied by the in-phase correlator reference signal the mean value of the sampled input to the accumulator will be

$$\mu_s = \frac{7}{8} \text{erf}\left(\sqrt{\frac{R_s}{2^{K+4}}} \right) \qquad (25)$$

where R_s is the symbol energy to noise ratio and 2^K represents the number of subcarrier cycles per symbol time T_s. Note also that the variance of the sampled values is $1 - \mu_s^2 \approx 1$. The accumulator sums these samples for 4 seconds, accumulating a total of 2^{20} samples, and compares the summation against a threshold value of T. If Σ represents the value of the accumulation then the probability that the in-phase signal will not be detected, given that it is being received, is given by

$$P_m \triangleq \Pr\left\{ \sum < T \left| \begin{array}{c} \text{signal} \\ \text{present} \end{array} \right\} = \frac{1}{2} \text{erfc}\left[\frac{(7)2^{17}\text{erf}\sqrt{\dfrac{R_s}{2^{K+4}}} - T}{2^{10}\sqrt{2}} \right]$$

$$(26)$$

Likewise, the probability that the in-phase signal will be detected, given that it is not being received, is

$$P_f = \Pr\left\{ \sum \geq T \left| \begin{array}{c} \text{signal} \\ \text{absent} \end{array} \right\} = \frac{1}{2} \text{erfc}\left(\frac{T}{2^{10}\sqrt{2}} \right)$$

$$(27)$$

Figure 8 illustrates the behavior of the false alarm and miss probabilities as the threshold varies. It should be

noted that the probability of a miss is more critical in a sequential system, since the probability of not acquiring is the probability of the union of the miss events whereas the probability of false acquisition is the product of the constituent false alarm probabilities. Therefore, the threshold should be chosen in such a way as to favor the miss probability at the expense of the false alarm probability. We shall assume that $T = 2500$ is chosen which implies that $P_m \approx 10^{-6}$ and $P_f \approx 10^{-2}$ at the design point. Note that these are the component probabilities, not the overall system probabilities, which are discussed later.

A. Acquisition Sequence

We note first that the first signal component c_1 must be sent for a sufficiently long time for the tracking loop to acquire the signal. Based on the experimental evidence of Ref. 2 we see that after receiving the signal for a period of time equal to 60 loop update times (60 seconds in our case) the loop will have acquired with a probability of $1 - 10^{-5}$. Now, note that the time of arrival of the change from code c_i to c_{i+1} does not necessarily coincide with the start of one of the lock detector accumulator cycles. Thus, in general the code change will occur within an accumulator window making the detection of c_{i+1} at the end of this window very unreliable. Therefore, it is necessary that when a code change occurs the new code must be transmitted for a minimum of two lock accumulator intervals (8 seconds in our case). Actually, it may be necessary to transmit each new component for three lock detector intervals so that the loop phase error can stabilize during the third interval. We will, however, assume for now that two intervals are sufficient.

Since each of the codes must be transmitted in sequence, we have that the minimum acquisition time for the demodulator/detector when operating at a symbol rate such that

$$T_s = 2^K T_{sc} \qquad (28)$$

is

$$T_{ACQ_{\min}}(K) = 8K + 60 \text{ seconds} \qquad (29)$$

At the lowest symbol rate this corresponds to a minimum acquisition time of 172 seconds.

B. Acquisition Statistics

The two acquisition statistics of interest are the probability of not acquiring, given that the preamble was transmitted, and the probability of falsely acquiring, given

that the preamble was not sent. If we define A_K as the event that the transmission of c_K was missed (not detected) then the probability $P_{NA}(K)$ of not acquiring at the rate for which $T_s = 2^K T_{sc}$ is upper bounded by

$$P_{NA}(K) \leq \sum_{k=1}^{K} \Pr\{A_k\} + \Pr\{A_{\bar{K}}\} \qquad (30)$$

where $\Pr\{A_{\bar{K}}\}$ is the probability of missing when $\bar{c}_K$ is transmitted. Recalling that $\Pr\{A_1\} = 10^{-5}$, $\Pr\{A_j\} = 10^{-6}$ for $j \neq 1$, and $P_{NA}(K) \leq P_{NA}(14)$ yields

$$P_{NA}(K) \leq 10^{-5} + 1.4 \times 10^{-5} = 2.4 \times 10^{-5} \qquad (31)$$

For false acquisition at rate K we have that

$$P_{FA}(K) = \left[\prod_{k=1}^{K} (P_{f_k}) \right] P_{f_{\bar{K}}} \qquad (32)$$

where P_{f_i} is the probability of falsely detecting the presence of component c_i. If we assume that 64 symbols per second is the highest symbol rate for the unit then

$$P_{FA}(K) \leq P_{FA}(K = 8) = 10^{-18} \qquad (33)$$

It appears that these statistics are compatible with most mission design values.

VI. Conclusions

Described herein is a method for transmitting command information on a subcarrier signal which can also be used for ranging. Next, a detector system was described that was capable of detecting the command modulation without destroying the range information. The detector was then analyzed and found to have false acquisition and failure to acquire probabilities which are compatible with realistic mission requirements. However, seldom does one obtain something in one area without giving up something in another, and this is no exception. In order to use the system described herein one must be willing to accept the increased acquisition time associated with sequential detection. The minimum acquisition time appears to be approximately twice that achievable in more conventional systems. Methods whereby the acquisition time can be reduced as well as experimental verification of these preliminary findings will be subjects of a future article.

References

1. Hurd, W. J., "Digital Clean-Up Loop Transponder for Sequential Ranging System," in *Supporting Research and Advanced Development*, Space Programs Summary 37-66, Vol. III, pp. 18–27, Jet Propulsion Laboratory, Pasadena, Calif., Dec. 31, 1970.

2. Holmes, J. K., and Tegnelia, C. R., "A Second Order All Digital Phase Locked Loop," *IEEE Trans on Commun.*, Vol. COM-22, No. 1, January 1974, pp. 62–68.

3. Simon, M. K., and Springett, J. C., *The Theory, Design, and Operation of the Suppressed Carrier Data Aided Tracking Receiver*, Technical Report 32-1583, Jet Propulsion Laboratory, Pasadena, Calif., June 15, 1973.

4. Viterbi, A. J., *Principles of Coherent Communication*, McGraw-Hill, New York, 1966.

5. Hurd, W. J., "Performance of a Phase Locked Loop During Loss of Signal," in *Supporting Research and Advanced Development*, Space Programs Summary 37-66, Vol. III, pp. 28–32, Jet Propulsion Laboratory, Pasadena, Calif., Dec. 31, 1970.
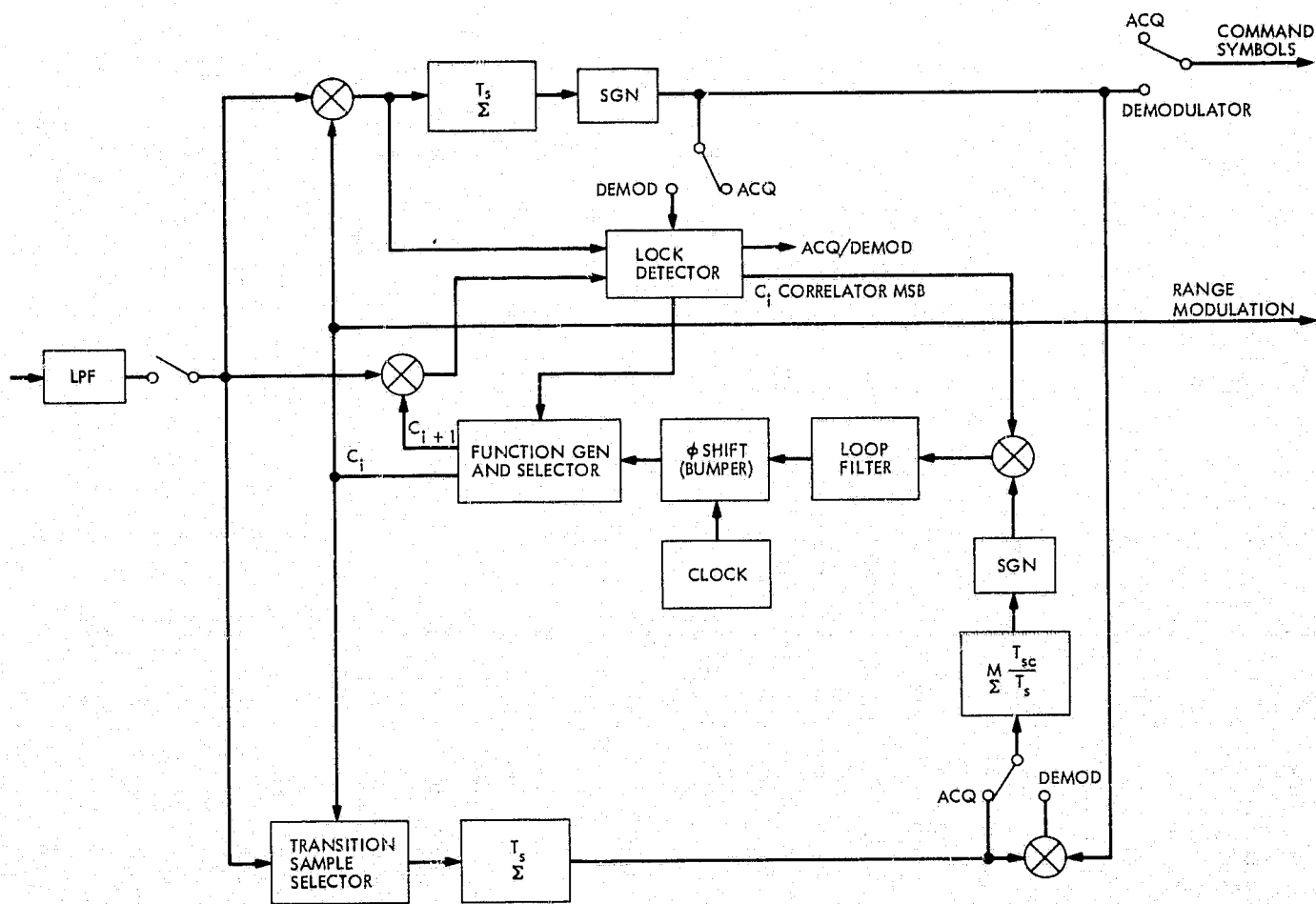
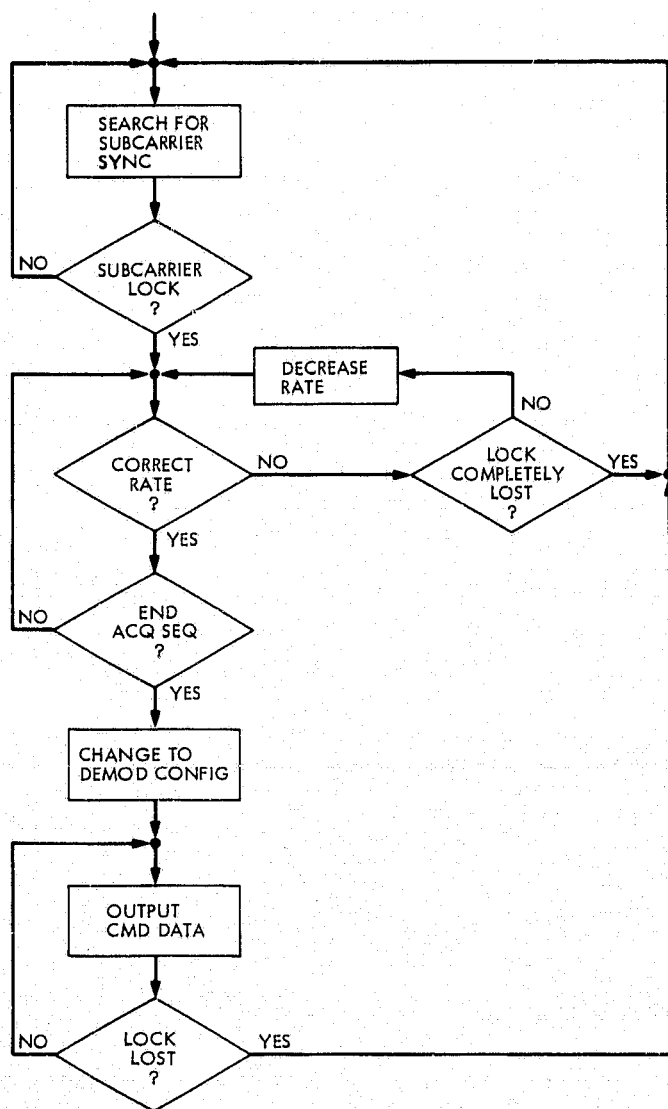Fig. 1. Block diagram of demodulator/detector system

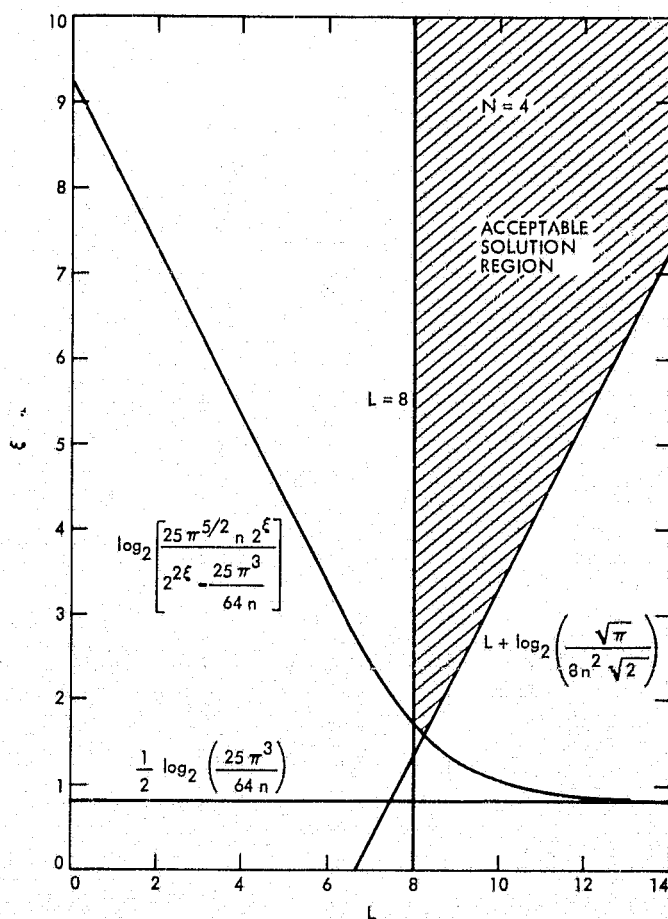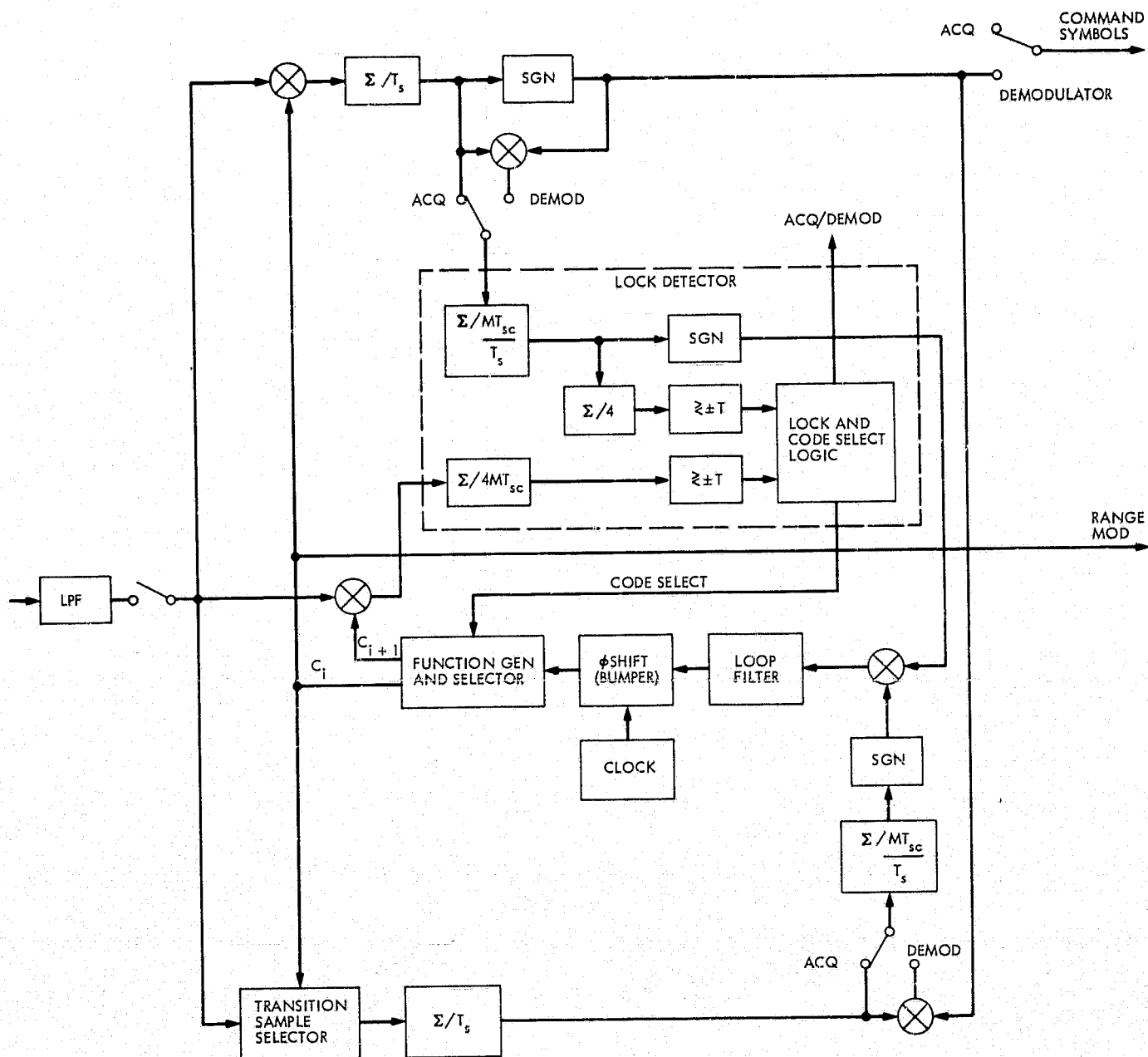Fig. 2. Flow chart of demodulator/detector operation

Fig. 3. Parametric representation of ξ and L

$$\log_2\left[\frac{25\,\pi^{5/2}\,n\,2^{\xi}}{2^{2\xi}-\frac{25\,\pi^3}{64\,n}}\right]$$

$$L + \log_2\left(\frac{\sqrt{\pi}}{8\,n^2\,\sqrt{2}}\right)$$

$$\frac{1}{2}\,\log_2\left(\frac{25\,\pi^3}{64\,n}\right)$$

Fig. 4. Revised block diagram of demodulator/detector
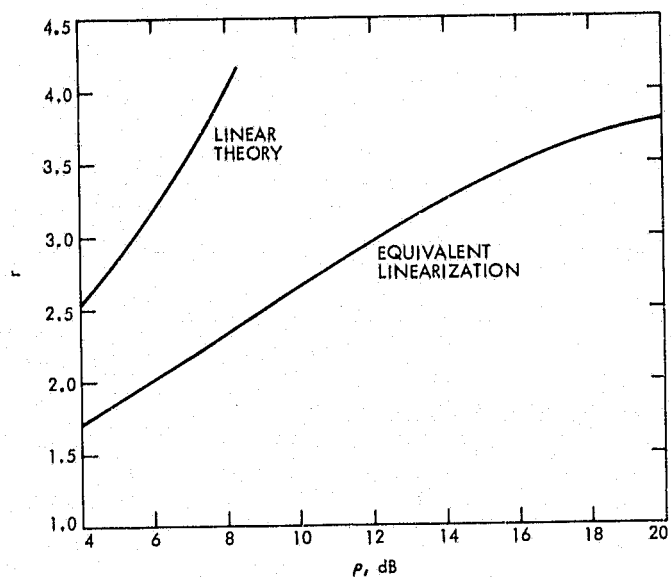
Fig. 5. Variation of damping parameter r with sample SNR
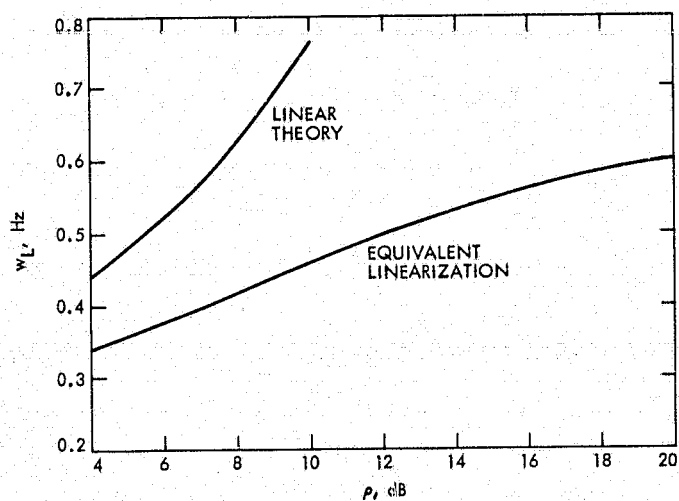
Fig. 6. Variation of loop bandwidth with sample SNR
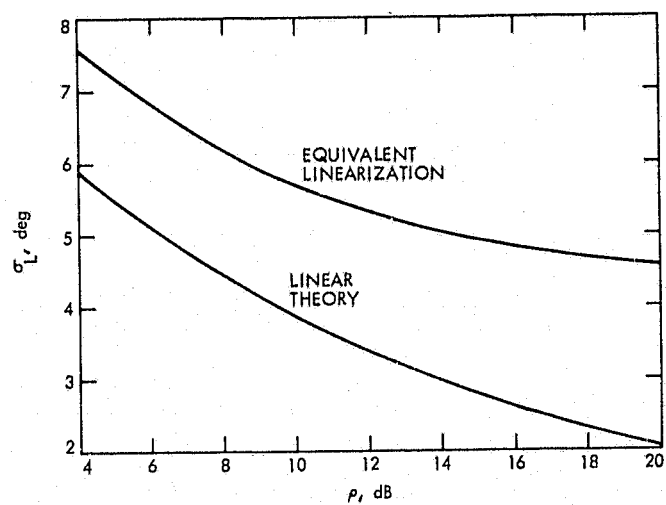
Fig. 7. Variation of rms loop phase error with sample SNR
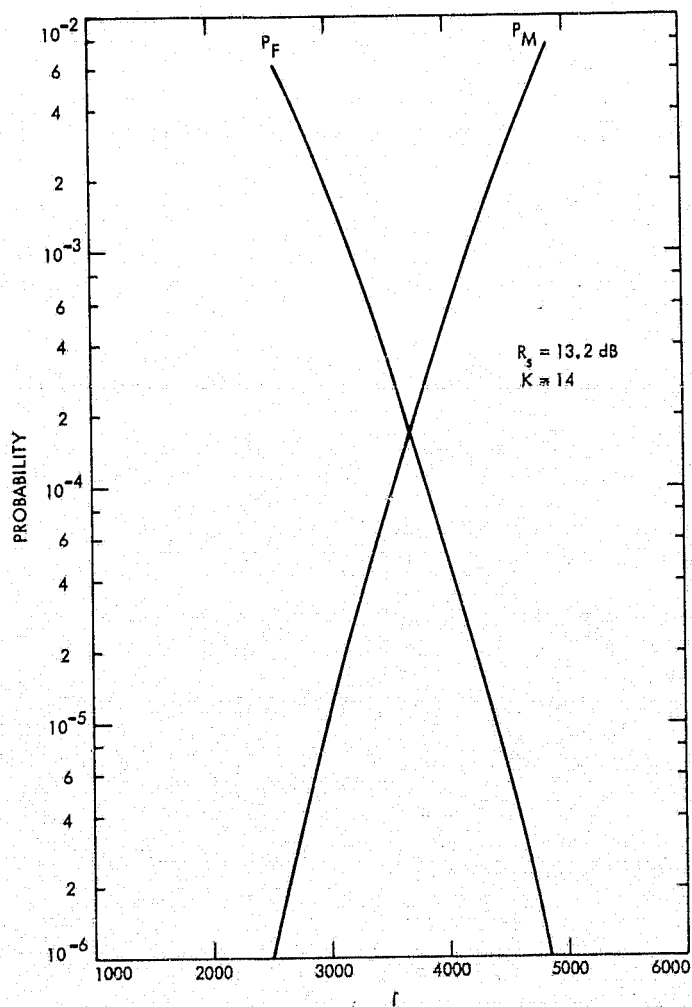
Fig. 8. Comparison of false alarm and miss probabilities vs threshold

Analysis of the Signal Combiner for Multiple Antenna Arraying

R. A. Winkelstein
Communications Systems Research Section

The signal-to-noise ratio of video data received from the second Mariner 73-Mercury encounter was improved by arraying two available 26-m antennas with the 64-m antenna normally used for reception. Specially designed digital equipment was used to combine the signals received by the three antennas. Analysis of this equipment shows that the received signals which arrived with relative time differences up to 50 μs were correctly aligned by the combining equipment to an accuracy within 50 ns. Observed error rates during the encounter track verified the system improvement to within 0.1 dB of the predicted 0.8 dB value.

I. Introduction

On September 21, 1974, the two 26-m antennas at DSSs 12 and 13 were arrayed with the 64-m antenna at DSS 14 to enhance the received video data from the second Mariner 73 Mercury encounter. The signals received at each of the three antennas were first translated to baseband frequency by coherent mixing with the carrier frequency. Then the baseband signals from the two smaller antennas were sent to DSS 14 over the microwave link. The baseband signal received at the DSS 14 antenna was given a fixed delay by sending it over a round-trip route on the microwave link. After arrival over the microwave link at DSS 14, the three baseband signals were fed to specially designed digital equipment whose function was to align the signals time-wise to each other

and combine them for further processing by the DSS 14 receiver.

A description of the signal combining equipment has been given by H. Wilck (Ref. 1). This report describes the analysis techniques used to design the combining equipment and to predict its performance during the Sept. 21 encounter.

II. Signal Combination

Table 1 lists the relevant signal parameters predicted for the encounter on September 21. These parameters provided the main design criteria for the combining equipment and were within the measurement tolerances

of the actual values. Requirements on the signal combining equipment were twofold. First, the three baseband signals had to be automatically and continuously aligned timewise so that the data components of the signals would add coherently when the signals were summed. Secondly, the signals had to be summed using optimal summing ratios to provide the maximum possible signal-to-noise ratio in the combined output signal.

A block diagram of the signal combiner is shown in Fig. 1. The three baseband signals first pass through variable attenuators which are adjusted to provide equal readings on the power meters. The signals from DSSs 12 and 13 are then filtered to prevent aliasing by analog-to-digital conversion equipment in the phase tracking channels. These phase tracking channels align the signals to match the signal from DSS 14, which is used as the reference. The three signals are then summed to provide the optimum signal-to-noise ratio at the output of the summing amplifier. A filter in front of the power meter monitoring the signal from DSS 14 is used to provide an equal noise bandwidth for comparison to the other two power meter readings.

The baseband signals may be considered to consist of a signal power, S_i, plus a noise power, N_i, $i = 1,2,3$, where the value of i corresponds to each of the three antennas. Therefore, the signal-to-noise ratio of the baseband signal from the ith antenna is

$$SNR_i = \frac{S_i}{N_i} \qquad (1)$$

Assuming that the noises in the three baseband signals are uncorrelated to each other so that noise power adds linearly as contrasted to the fact that signal data voltages add linearly, the signal-to-noise ratio, SNR_s, at the output of the summing amplifier is

$$SNR_s = \frac{(\sqrt{S_1} + \alpha_2\sqrt{S_2} + \alpha_3\sqrt{S_3})^2}{N_1 + \alpha_2^2 N_2 + \alpha_3^2 N_3} \qquad (2)$$

where α_i is a voltage attenuator ratio at the ith input to the summing amplifier, α_1 is set to unity. Eq. (2) is maximized when

$$\alpha_2 = \frac{N_1\sqrt{S_2}}{N_2\sqrt{S_1}}, \qquad \alpha_3 = \frac{N_1\sqrt{S_3}}{N_3\sqrt{S_1}} \qquad (3)$$

Under these conditions, Eq. (2) becomes

$$SNR_s = SNR_1 + SNR_2 + SNR_3 = SNR_1 \cdot A_r \qquad (4)$$

where

$$A_r = 1 + \frac{SNR_2}{SNR_1} + \frac{SNR_3}{SNR_1} \qquad (5)$$

The ratio of SNRs in Eq. (5) are equal to the ratio of R's in Table 1, from which

$$\frac{SNR_2}{SNR_1} = \frac{SNR_3}{SNR_1} = -10\,\text{dB} = 0.1 \qquad (6)$$

Eq. (5) therefore becomes

$$A_r = 1.2 = 0.8\,\text{dB} \qquad (7)$$

Thus, adding the received signals from the two smaller antennas to the signal received by the larger antenna provides an improved signal-to-noise ratio of 0.8 dB compared to the use of the larger antenna alone.

To determine the sensitivity of A_r in Eq. (5) to non-optimum values of α_i, Eq. (3) is modified to

$$\alpha_2 = \theta_2 \frac{N_1\sqrt{S_2}}{N_2\sqrt{S_1}}, \qquad \alpha_3 = \theta_3 \frac{N_1\sqrt{S_3}}{N_3\sqrt{S_1}} \qquad (8)$$

where α_2 and α_3 vary from optimum as θ_2 and θ_3 vary from unity. Eq. (4) then becomes

$$SNR_s = SNR_1 \cdot B_r \qquad (9)$$

where

$$B_r = \frac{\left(1 + \theta_2 \dfrac{SNR_2}{SNR_1} + \theta_3 \dfrac{SNR_3}{SNR_1}\right)^2}{1 + \theta_2^2 \dfrac{SNR_2}{SNR_1} + \theta_3^2 \dfrac{SNR_3}{SNR_1}} \qquad (10)$$

The loss in improvement due to nonoptimum α_i is the ratio of B_r to A_r and is plotted in dB in Fig. 2 for variations in θ, and hence in α, up to $\pm 30\%$. From Fig. 2, it is seen that the loss is less than 0.07 dB when α_2 and α_1 are within 30% of optimum.

The actual values of α_2 and α_3 indicated in Fig. 1 may be determined by noting that the power inputs, P_i, to the summing amplifier are

$$P_i = S_i + N_i \qquad (11)$$

From Table 1

$$R_i = \frac{S_i T_B}{N_{oi}} \qquad (12)$$

where T_B is the data bit time, the reciprocal of the data rate, and N_{oi} is the one-sided noise spectral density for the ith input to the summing amplifier. Moreover,

$$N_i = N_{oi}B \qquad (13)$$

where B is the low-pass filter one-sided noise bandwidth. For a 1-MHz resistance-capacitance (RC) low-pass filter, B is 1.57 MHz. Using Eqs. (11), (12), and (13), Eq. (3) becomes

$$\alpha_2 = \sqrt{\frac{P_1 R_2 (R_2 + T_B B)}{P_2 R_1 (R_1 + T_B B)}}, \qquad \alpha_3 = \sqrt{\frac{P_1 R_3 (R_3 + T_B B)}{P_3 R_1 (R_1 + T_B B)}}$$

$$(14)$$

For equal powers, Eq. (14) gives α_2 and α_3 equal to 0.3.

III. Phase Tracking Channel

The heart of the signal combiner is the phase tracking channel. Its function is to provide a continuously variable amount of time delay in order to match the signal at the summing amplifier to the reference baseband signal from DSS 14. This variable delay compensates for the change in signal arrival time at the different antennas as the Earth rotates during the mission viewing period. The time delay variations listed in Table 1 include the fixed microwave link delay time from the 26-m antennas to DSS 14, because the signal combining equipment is located at DSS 14. Since the phase tracking channel can provide only positive time delays, the baseband signal is given a fixed delay of 110 μs by sending it through the microwave link on a round-trip route.

A block diagram of phase tracking channel A is shown in Fig. 3. Equipment shown for channel A below the broken line in Fig. 3 is duplicated for channel B. The baseband signal from DSS 13 is converted to digital form by an 8-bit analog-to-digital (A/D) converter sampled at approximately a 2.5-MHz rate. These digital values are placed in a first-in first-out (FIFO) memory system which provides the proper amount of time delay. The digital values are read out of the FIFO at a fixed 2.5-MHz rate, reconverted to analog form by an 8-bit digital-to-analog (D/A) converter, and then added to the other baseband signals in the summing amplifier.

Sign bits from the FIFO output are compared to sign bits of the DSS 14 baseband signal obtained from a 1-bit A-D converter. This comparison is carried out and aver-

aged by the quadrature correlator for periods of one second. At the end of each second, the quadrature correlator develops a digital number directly proportional to the phase timing error between the two signals. This digital number or count is scaled by a digital attenuator and converted to an analog control voltage by the 16-bit (D/A) converter. The scaling factor of the digital attenuator is preset by a manual front panel control for an optimum tradeoff between the loop transient and noise responses.

The control voltage out of the 16-bit D/A converter is used to control the search oscillator of a frequency synthesizer. This causes a slight change, Δf, in the 2.5-MHz synthesizer output frequency used to strobe the FIFO input. As a result, the FIFO system delay is changed in the direction to force the error count out of the quadrature correlator to zero. At this time, the two signals are in phase, and the output count developed by the in-phase correlator is at a maximum. The in-phase correlator count is displayed on the front panel and is used to aid the initial loop acquisition and to indicate correct system operation.

Analysis of the phase tracking channel control loop may be carried out by aid of the Laplace block diagram of Fig. 4. Here the input to the loop is taken to be the time offset between the channel input baseband signal and the DSS 14 baseband reference signal. The output is the loop error signal and is equivalent to the timing error between the two baseband signals as seen by the summing amplifier. A key requirement of the loop analysis is to determine the limits of the various components of this output error.

A. Control Loop Description

1. FIFO memory system. The FIFO memory system consists principally of the FIFO memory and the fill counter as is shown in Fig. 5. The memory can hold up to 512 8-bit words which are input to the memory using the input strobe, and output from the memory using the output strobe. These strobes are independent of each other and are generated asynchronously. However, as the name "first-in first-out" suggests, the sequence of words out from the memory is the same as the sequence of words into the memory.

The resident time of a particular 8-bit word in memory is the delay time, and is proportional to the number of words in the memory as indicated by the fill counter. If the input strobe is slightly higher in frequency than the

output strobe, the memory will gradually fill until the FIFO FULL signal becomes true. Conversely, if the input strobe is slightly lower in frequency than the output strobe, the memory will gradually empty until the FIFO EMPTY signal becomes true. The fill counter obtains the count number by counting the difference between the input strobes and output strobes. This count number is also displayed on the front panel to aid in acquisition and to indicate correct equipment operation by comparison to precalculated values. The reset signal sets both the memory and counter to zero when the system is reset or initially started.

In terms of the Laplace block diagram (Fig. 4) the FIFO memory system produces an output time difference between the two baseband signals as a function of the input frequency Δf indicated in Fig. 3. The FIFO memory operation is similar to that of an integrator in that the rate of change of time delay is proportional to Δf. Accordingly, the Laplace transfer function of the system is given as G_f/s, where s is the Laplace complex frequency and G_f is the system gain constant. At a 2.5-MHz strobe rate, each word in memory represents a 0.4 μs time delay. Thus G_f is 0.4 μs/Hz/s.

2. *In-phase correlator.* Although the in-phase correlator is not part of the phase tracking control loop, its description is prerequisite to a description of the quadrature correlator. The correlation of two signals is simply the average of their product. When the signals to be correlated are represented by only their respective sign bits, as is done in the phase tracking control loop, then this product is most easily generated by an exclusive-or circuit, as is shown in Fig. 6. V_1 and V_2 are the baseband signal voltages. The exclusive-or circuit activates a counter which is incremented when V_1 and V_2 are the same and decremented when V_1 and V_2 are different.

At the end of each second, the accumulated count in the in-phase correlator is stored in a front panel display for operational verification. The counter is then reset to zero in preparation for the next second's count. Since the signals are input at the digitized rate of 2.5 MHz, the count for noise-free in-phase signals can reach a maximum of 2.5 million. Thus 7 binary coded decimal (BCD) digits are required in the counter.

Normalized plots of the output count as a function of the delay, τ, of V_2 with respect to V_1 are shown in Fig. 7. Normalization of these plots, known as correlation curves,

assigns a value of unity as the maximum count generated. Fig. 7(a) is the correlation curve of signals which contain only the square wave subcarrier frequency. τ_1 is the quarter period of the subcarrier frequency. From Table 1, τ_1 is found to be 1.41 μs. $C_1(\tau)$ and $C_2(\tau)$ are equations of the indicated portions of the correlation curve.

Fig. 7(b) is the correlation curve of signals containing no subcarrier frequency, but rather only random data known as pseudo-noise (PN) data. τ_2 is the data period, which from Table 1 is found to be 8.5 μs. The correlation curve of actual signals containing both subcarrier frequency and PN data is shown in Fig. 7(c). This curve is the product of the curves in Figs. 7(a) and 7(b). The bracketed expression in Fig. 7(c) indicates the correlation of the time function signals V_1 and V_2.

3. *Quadrature correlator.* The quadrature correlator, similar to the in-phase correlator, each second produces a count which is a function of the relative signal delay. To be useful as a control element in a tracking loop, the quadrature correlator should produce a count of zero when the input signals are exactly aligned. When the signals are not aligned, the count should be proportional to the time difference, τ. Such a correlation curve is obtained by advancing and delaying the correlation curve of Fig. 7(c) by an amount γ as shown respectively in Figs. 7(d) and 7(e). The desired correlation curve is half the difference of the curves in Figs. 7(d) and 7(e) as shown in Fig. 7(f). The equation of the control portion of the curve in Fig. 7(f) is obtained in a step by step manner from the previous curves of Fig. 7 and is found to be

$$C_7(\tau) = -\left(\frac{1}{\tau_1} + \frac{1}{\tau_2} - \frac{2\gamma}{\tau_1\tau_2}\right)\tau \qquad (15)$$

Fig. 8 shows the quadrature correlator which provides the correlation curve of Fig. 7(f). The delay γ is obtained from the four-bit shift registers. Since the shift registers are clocked at the data rate of 2.5 MHz, each bit provides a delay of 0.4 μs. Therefore γ is 1.6 μs and $C_7(\tau)$ is found to be $-0.56\ \tau$.

The quadrature correlator count represents an integral of the input signal phase difference averaged over a time period of one second. After each second, the quadrature correlator count register is reset to zero as is the in-phase correlator counter. Hence the operation of the quadrature correlator is equivalent to that of an integrate-and-dump circuit with gain constant G_c shown in Fig. 4. G_c, the

product of the magnitude of the slope of Eq. (15) and the normalization factor K, is

$$G_c = 0.56\, K \text{ counts}/\mu s/s \qquad (16)$$

where K, the normalization constant for the curves in Fig. 7, is the counts per second displayed by the in-phase correlator when the signals are aligned.

It may be noted that G_c of Eq. (16) is somewhat dependent on the type of data being transmitted. Thus Eq. (16) is strictly true only for PN data. For the extreme case of all zeros data or all ones data, G_c becomes $0.71\, K$. At the opposite extreme of alternating ones and zeros data, G_c is found to be $0.41\, K$. Therefore the G_c of Eq. (16) is within 27% of any data type actually transmitted.

The Laplace block of an integrate-and-dump circuit, shown as the quadrature correlator in Fig. 4, is derived in the appendix.

4. Quadrature correlator noise. Since the inputs to the quadrature correlator each contain a sizable noise component before sampling, it is to be expected that the count developed by the quadrature correlator has a statistical variance or noise component associated with it. This is the noise input to the loop at the output of the correlator shown in Fig. 4. For proper operation of the quadrature correlator within the control loop, this noise must be small with respect to the K in Eq. (16).

K is estimated from the Table 1 data by reference to the probability density curves of Fig. 9. These curves of the baseband signal distribution before sampling are assumed to be Gaussian with means E_i corresponding to the square root of S_i in Eq. (1). Since 2.5 million samples are taken each second, K may be considered to be

$$K = 2.5 \cdot 10^6 \langle X_1 \rangle \qquad (17)$$

where $\langle X_1 \rangle$ denotes the statistical mean of X_1, an input random variable to the in-phase correlator counter. In terms of the probability that V_1 is equal to V_2, $P(V_1 = V_2)$

$$X_1 = \begin{array}{l} 1 \text{ with } P(V_1 = V_2) \\ -1 \text{ with } P(V_1 \neq V_2) \end{array} \qquad (18)$$

Therefore

$$\langle X_1 \rangle = P(V_1 = V_2) - P(V_1 \neq V_2)$$
$$= 2P(V_1 = V_2) - 1 \qquad (19)$$

But

$$P(V_1 = V_2) = P(V'_1 > 0)\, P(V'_2 > 0)$$
$$+ P(V'_1 < 0)\, P(V'_2 < 0)$$
$$= P(V'_1 > 0)\, P(V'_2 > 0)$$
$$+ [1 - P(V'_1 > 0)][1 - P(V'_2 > 0)] \qquad (20)$$

where V'_1 and V'_2 are the baseband signals before sampling. The probability that V'_1 is greater than zero is found by integrating the probability density curve for V'_1 from zero to infinity. In terms of the error function, erf

$$P(V'_i > 0) = \frac{1}{2} + \frac{1}{2}\text{erf}\left(\frac{E_i}{\sqrt{2}\,\sigma_i}\right) \qquad (21)$$

where σ_i is the root mean square of the corresponding noise power N_i of Eq. (1) and the error function is defined as

$$\text{erf}(x) = \frac{2}{\sqrt{\pi}} \int_0^x e^{-t^2}\, dt \qquad (22)$$

Using the notations of Eqs. (12) and (13)

$$R_i = \frac{E_i^2 T_B}{N_{oi}}, \qquad \sigma_i^2 = N_i = N_{oi} B \qquad (23)$$

Using Eq. (23), Eq. (21) becomes

$$P(V'_i > 0) = \frac{1}{2} + \frac{1}{2}\text{erf}\left(\sqrt{\frac{R_i}{2T_B B}}\right) \qquad (24)$$

Using Eqs. (20) and (24), Eq. (19) becomes

$$\langle X_1 \rangle = \text{erf}\left(\sqrt{\frac{R_1}{2T_B B}}\right)\text{erf}\left(\sqrt{\frac{R_2}{2T_B B}}\right) \qquad (25)$$

which is evaluated using the values in Eq. (14) and tables of the error function (Ref. 2). From Eqs. (17) and (25), K is found to be approximately 53,000 counts.

The quadrature correlator noise N_y has variance σ_y^2 given by

$$\sigma_y^2 = 2.5 \cdot 10^6 \langle X_2^2 \rangle \qquad (26)$$

where X_2 is the random variable into the quadrature correlator counter. Assuming input signals which contain only noise and no data or subcarrier frequency

$$X_2 = \begin{cases} 1 \text{ with probability of } 1/4 \\ -1 \text{ with probability of } 1/4 \\ 0 \text{ with probability of } 1/2 \end{cases} \quad (27)$$

Squaring Eq. (27) gives

$$X_2^2 = \begin{cases} 1 \text{ with probability of } 1/4 \\ 1 \text{ with probability of } 1/4 \\ 0 \text{ with probability of } 1/2 \end{cases} \quad (28)$$

and the mean of X_2^2 is

$$\langle X_2^2 \rangle = 1/2 \quad (29)$$

From Eqs. (26) and (29), the standard deviation, σ_y, of the quadrature correlator noise, N_y, is found to be

$$\sigma_y = 1118 \text{ counts} \quad (30)$$

The ratio of σ_y to K is less than 3% which is highly satisfactory for tracking loop operation.

5. Digital attenuator. The digital attenuator is a left-shift shift register whose number of left shifts is controlled by a front panel thumbwheel switch setting. Each left shift provides a gain attenuation of one half. The circuitry is arranged with respect to the D-A converter of Fig. 4 so that the digital attenuator gain, G_a, is

$$G_a = 2^{R-10} \quad (31)$$

where R is the thumbwheel switch reading, settable from 0 to 15.

6. Digital-to-analog converter. The 16 bit D/A converter may be represented by the well-known zero-order hold circuit described in sampled-data control system texts (Ref. 3). Accordingly, its transfer function, H_d, is

$$H_d = G_d \frac{Z-1}{Zs} \quad (32)$$

where G_d is a gain constant, s is the Laplace complex frequency, Z is e^{sT}, and T is the sampling period which in this system is one second. Since an input of $\pm 2^{15}$ counts produces an output of ± 10 volts, G_d is

$$G_d = \frac{10}{2^{15}} \frac{\text{volts}}{\text{count}} \quad (33)$$

7. Synthesizer. The frequency synthesizer provides a coherent stable waveform whose frequency is set by front panel switch settings, which in this system is 2.5 MHz. Also contained within the synthesizer is a voltage controlled oscillator called a search oscillator whose output frequency may be algebraically added to the front panel dialed frequency. A ± 10-v control voltage range produces a $\pm \Delta f_s$ search oscillator frequency range where Δf_s may be adjusted in decade steps. Thus the gain of the synthesizer, G_s, is

$$G_s = \frac{\Delta f_s}{10} \frac{\text{Hz}}{\text{volt}} \quad (34)$$

In the present system, Δf_s was set to 10 Hz.

B. Control Loop Analysis

To assure effective phase tracking control loop operation and to determine the limits of phase timing error, the control loop was analyzed for the following:

(1) Loop stability using the root locus method.

(2) Output phase error caused by the input signal characteristics.

(3) Loop jitter caused by the quadrature correlator noise.

(4) Output phase error caused by the search oscillator DC offset.

1. Root locus analysis. Feedback control loop stability is readily found from a root locus analysis which plots in the complex plain the roots of the denominator of the closed-loop transfer function, G_{cl}, as a function of an open-loop gain constant G. In the phase tracking control loop

$$G = G_f G_c G_a G_d G_s T^2 \quad (35)$$

$$G_{cl} = \frac{1}{1 + G_{ol}} \quad (36)$$

where G_{ol} is the open-loop transfer function. From Fig. 4, the open-loop transfer function is found to be

$$G_{ol} = \frac{G}{T^2} \frac{1}{s} \frac{(Z-1)^2}{Z^2} \quad (37)$$

When analyzing systems containing both continuous and sampled-data components, it is customary to convert the entire system into a sampled-data equivalent system. This is accomplished by taking the Z-transform (Ref. 3)

of all relevant equations. Thus the Z-transform of Eq. (37) is

$$G_{ol} = \frac{G(Z+1)}{2Z(Z-1)} \tag{38}$$

and Eq. (36) becomes

$$G_{cl} = \frac{Z(Z-1)}{Z^2 - \left(1 - \frac{G}{2}\right)Z + \frac{G}{2}} \tag{39}$$

The root locus plot is shown in Fig. 10. Since the plot is symmetric about the real axis, only the top half is shown. In the Z plain of sampled-data system analysis, gains which move the poles outside the unit circle cause unstable loop operation. From Fig. 10, it is seen that stable loop operation is obtained for any gain less than 2.0.

In actual operation during the Mariner-Mercury encounter, K's of 100,000 counts were observed. Δf_s was set to 10 Hz as previously stated, and R was set to 4. This provided a loop gain of 0.11.

2. Input analysis. The input analysis determines the steady-state loop error resulting from various types of input functions. From Eq. (38) and Fig. 10, it is seen that a single open-loop pole exists at the value of Z equal to one. Sampled-data control system theory indicates that this condition ensures zero steady-state error for a step input. However, a finite steady-state loop error does exist for an input ramp function. This is of concern since the last entry in Table 1 shows that such a ramp is expected.

To find the steady-state loop error resulting from an input ramp function, reference is made to the input analysis block diagram of Fig. 11, which is a rearrangement of Fig. 4. $R(s)$ is the input time offset Laplace function, and $E(s)$ is the time error output Laplace function. Intermediate Laplace functions within the loop are denoted by X and Y. An asterisk after a Laplace function is used to denote the equivalent sampled-data or Z-transformed function of the indicated Laplace function.

From Fig. 11, the loop equations are

$$E(s) = R(s) - Y^* \frac{1}{s^2} \tag{40}$$

$$X = \frac{G}{T^2} \frac{R(s)}{s} - Y^* \frac{G}{T^2} \frac{1}{s^3} \tag{41}$$

$$Y^* = X^* \frac{(Z-1)^2}{Z^2} \tag{42}$$

Taking the Z-transform of Eqs. (40) and (41) results in

$$E^* = R^* - Y^* \frac{TZ}{(Z-1)^2} \tag{43}$$

$$X^* = \frac{G}{T^2} \left(\frac{R(s)}{s}\right)^* - Y^* \frac{G}{2} \frac{Z(Z+1)}{(Z-1)^3} \tag{44}$$

Solving for E^* from Eqs. (42), (43), and (44) gives

$$E^* = R^* - \frac{\frac{G}{TZ}\left(\frac{R(s)}{s}\right)^*}{1 + \frac{G}{2}\frac{Z+1}{Z(Z-1)}} \tag{45}$$

The steady-state output loop error, E_{ss}, is found by using the final value theorem for sampled-data systems.

$$E_{ss} = \lim_{Z \to 1} ((Z-1)E^*) \tag{46}$$

$R(s)$ for a ramp input is

$$R(s) = \frac{R_a}{s^2} \tag{47}$$

where R_a is the ramp rate constant. The Z-transforms for $R(s)$ and $R(s)/s$ become

$$R^* = \frac{R_a TZ}{(Z-1)^2} \tag{48}$$

$$\left(\frac{R(s)}{s}\right)^* = \frac{R_a T^2 Z(Z+1)}{2(Z-1)^3} \tag{49}$$

From Eqs. (45), (46), (48), and (49)

$$E_{ss} = \frac{R_a T}{G} \tag{50}$$

Using R_a from Table 1, T equal to 1 s, and G equal to 0.11 gives

$$E_{ss} = 25\,\text{ns} \tag{51}$$

3. Noise analysis. The diagram of Fig. 4 may be rearranged to form the Laplace diagram for noise analysis shown in Fig. 12. N_y^* is the quadrature correlator noise, and $J(s)$ is the Laplace function of the time error jitter

signal out of the loop. Since N and J are random processes, it is desired to find the root mean square or standard deviation of J, σ_J. Assuming a flat constant power spectral density for N_y^*, sampled-data noise theory gives

$$\frac{\sigma_J^2}{\sigma_y^2} = \frac{1}{\pi} \int_0^\pi |H_J(Z)|^2 \, d\theta, \qquad Z = e^{i\theta} \qquad (52)$$

where σ_y is obtained from Eq. (30), $H_J(Z)$ is the transfer function of Fig. 12, and i is the square root of minus one. The equations for Fig. 12 are found similarly as was done for Fig. 11, and $H_J(Z)$ is found to be

$$H_J(Z) = \frac{J^*}{N_y^*} = \frac{\dfrac{G_1 T}{Z-1}}{1 + \dfrac{G}{2}\dfrac{Z+1}{Z(Z-1)}} \qquad (53)$$

where G_1 from Fig. 12 is $G/G_c T^2$. Using Eqs. (16), (52), and (53)

$$\sigma_J = \frac{\sigma_y}{0.56\,K} \sqrt{\frac{G}{2}\frac{1+\dfrac{G}{2}}{1-\dfrac{G}{2}}} \qquad (54)$$

For σ_y equal to 1118 counts, K equal to 100,000 counts, and G equal to 0.11

$$\sigma_J = 5\,\text{ns} \qquad (55)$$

Eq. (54) shows that the loop jitter becomes infinite when G is made equal to 2. This agrees with the determination from the root locus analysis of loop instability at values of G greater than 2.

4. Search oscillator dc offset analysis. The phase tracking loop operates with the search oscillator frequency at zero when the loop is locked to a constant time offset input. If the transfer characteristic of the search oscillator is such that zero frequency out occurs for an input voltage of E_o volts rather than the desired value of zero volts, then the loop at locked conditions will act to generate a search oscillator control voltage of E_o volts. This E_o, called the search oscillator DC offset voltage, represents a finite loop error since zero error would result in a zero quadrature correlator count and a subsequent zero voltage out of the D/A converter.

To minimize this search oscillator DC offset error, careful adjustment of the search oscillator trimming components was made. In addition, a precision adjustable DC compensating circuit was incorporated into the equipment in order to null E_o. Requirements for this nulling were determined from the DC offset analysis Laplace diagram of Fig. 13.

In Fig. 13, a third rearrangement of Fig. 4, $D(s)$ is the Laplace function of the search oscillator DC offset voltage.

$$D(s) = \frac{E_n}{s} \qquad (56)$$

$L(s)$ is the Laplace function of the loop error due to the search oscillator DC offset voltage. Using analysis techniques similar to the input analysis of Fig. 11, L^* is found to be

$$L^* = \frac{G_s\, G_f\, E_o\, T}{Z-1} \frac{1}{Z-1+\dfrac{G}{2}\dfrac{Z+1}{Z}} \qquad (57)$$

From the final value theorem of Eq. (46), the steady-state output error, L_{ss}, is

$$L_{ss} = \frac{G_s\, G_f\, E_o\, T}{G} \qquad (58)$$

Using the value of 4 mV for E_o, and the remaining constants as previously indicated, L_{ss} is found to be

$$L_{ss} = 15\,\text{ns} \qquad (59)$$

Thus to constrain the loop error due to the search oscillator DC offset to be within 15 ns, the DC offset must be nulled to within 4 mV. Pre- and post-calibration procedures for the encounter mission indicated that this nulling accuracy was indeed accomplished. The sum of the three sources of loop output error described by Eqs. (51), (55), and (59) is equal to 45 ns.

Table 2 lists the signal combiner constants described in the above analysis.

IV. Operational Verification

The actual improvement in signal-to-noise ratio realized by the combining equipment can be estimated from a plot of bit error rate of the processed data over the encounter track period. This plot is shown in Fig. 14. The gradual increase of bit error rate at the beginning and end of the track is due to the lower antenna elevations and hence higher noise inputs at those times.

Toward the end of the track during the time indicated in Fig. 14, the combining equipment was switched out, and only the signal from DSS 14 was processed. During this time, the bit error rate increased from 0.037 to 0.052. This is equivalent to a loss of 0.7 dB in signal-to-noise ratio. Thus the actual improvement due to antenna arraying was within 0.1 dB of the calculated prediction.

V. Conclusion

Analysis of the equipment used to combine the baseband signals from three antennas during the Mariner-Mercury encounter on Sept. 21, 1974 shows that signals arriving at the antennas with a time disparity of over 50 μs were aligned in time to an accuracy better than 50 ns. Moreover, the signals were combined in such a manner as to increase the signal-to-noise ratio of the signal at one antenna by the sum of the signal-to-noise ratios of the signals at the other two antennas. Also shown is that satisfactory equipment operation is relatively insensitive to the key equipment parameters of signal mixing ratios and tracking loop gain.

A plot of the bit error rate during the encounter track shows that the actual combiner improvement in signal-to-noise ratio was 0.7 dB, a value within 0.1 dB of predicted theoretical maximum.

References

1. Wilck, H., "A Signal Combiner for Antenna Arraying," in *The Deep Space Network Progress Report 42-25*, pp. 111–117, Jet Propulsion Laboratory, Pasadena, California, February 15, 1975.

2. Abramowitz, M., and Stegun, A., *Handbook of Mathematical Functions*, National Bureau of Standards Applied Mathematics Series 55, U.S. Government Printing Office, Washington, D.C., June 1964.

3. Kuo, B. C., *Analysis and Synthesis of Sampled-Data Control Systems*, Prentice-Hall, Inc., Englewood Cliffs, N.J., 1963.

Table 1. Design parameters

Symbol	Description	Value
R_1	ST_B/N_0 at DSS 14	1.6 dB
R_2	ST_B/N_0 at DSS 13	-8.4 dB
R_3	ST_B/N_0 at DSS 12	-8.4 dB
	Subcarrier frequency	177.1 kHz
$1/T_B$	Data rate	117.6 kbits/s
	DSS 13 to DSS 14 time delay	28–92 μs
	DSS 12 to DSS 14 time delay	13–67 μs
	DSS 14 microwave round trip delay	110 μs
R_a	Maximum rate of change in time delay of the signals from DSS 12 and 13 with respect to the signal from DSS 14.	10 μs/h

Table 2. Signal combiner constants

Symbol	Description	Value
A_r	Maximum predicted signal-to-noise ratio improvement using arraying	0.8 dB
a_1, a_2	Summing amplifier constants for the baseband signals from DSS 13 and DSS 12	0.3
B	Low-pass filter noise bandwidth	1.57 MHz
G_f	FIFO gain constant	0.4 μs/Hz/s
G_c	Quadrature correlator gain constant	0.56 K counts/μs/s
K	Observed in-phase correlator count	100,000 counts
σ_y	RMS quadrature correlator noise	1118 counts
G_a	Digital attenuator gain constant	2^{R-10}
R	Digital attenuator thumbwheel switch setting	4
G_d	16 bit D/A gain constant	$10/2^{15}$ V/count
G_s	Synthesizer gain constant	$\Delta f_s/10$ Hz/V
Δf_s	Search oscillator decade setting	10 Hz
T	Control loop sampled-data period	1 s
G	Open-loop gain constant	0.11
E_{ss}	Loop output error due to ramp input	25 ns
σ_J	RMS loop jitter	5 ns
E_o	Search oscillator DC offset after nulling	4 mV
L_{ss}	Loop output error due to E_o	15 ns
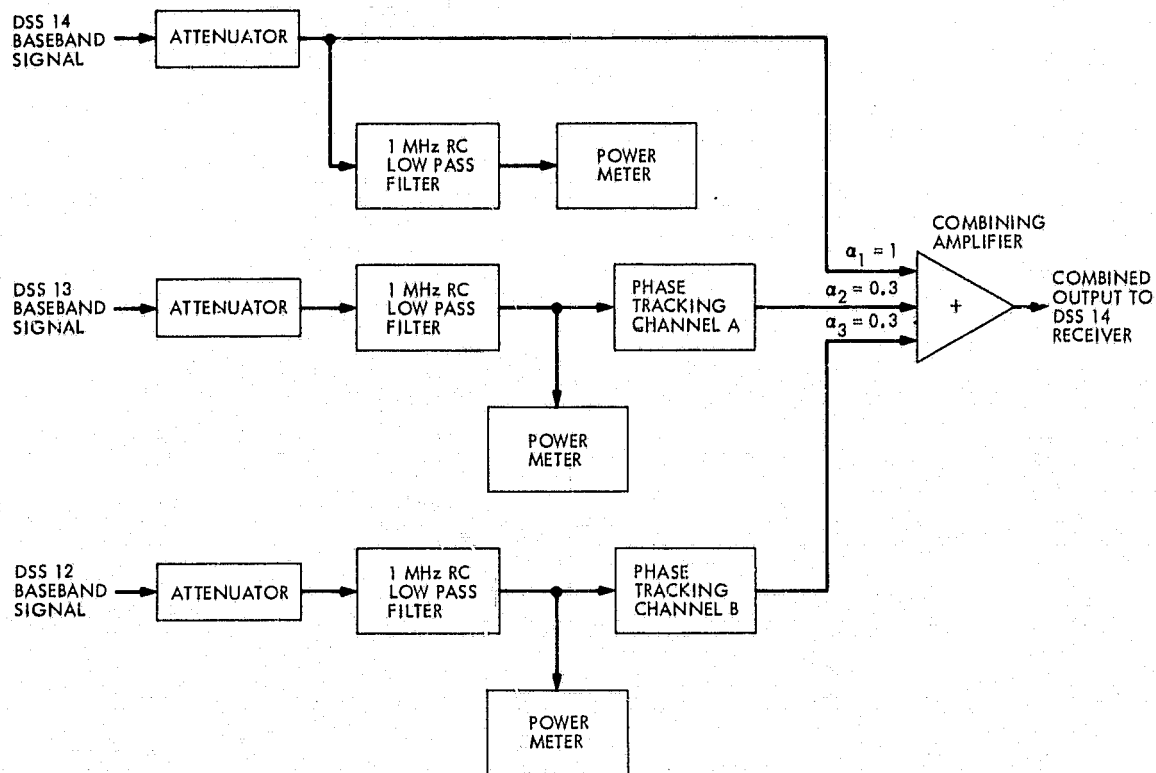
Fig. 1. Signal combiner block diagram
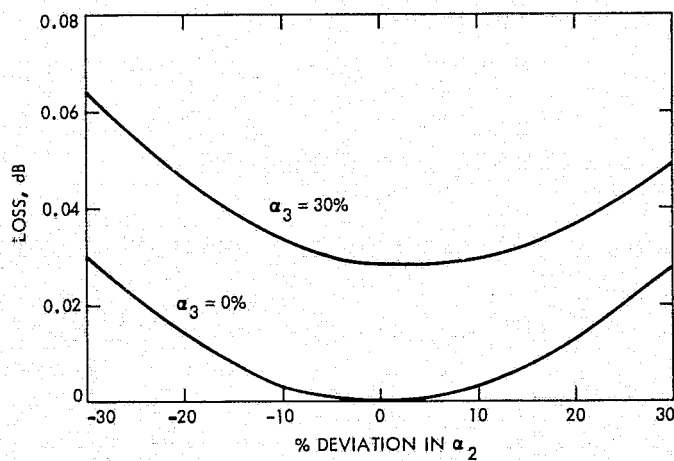
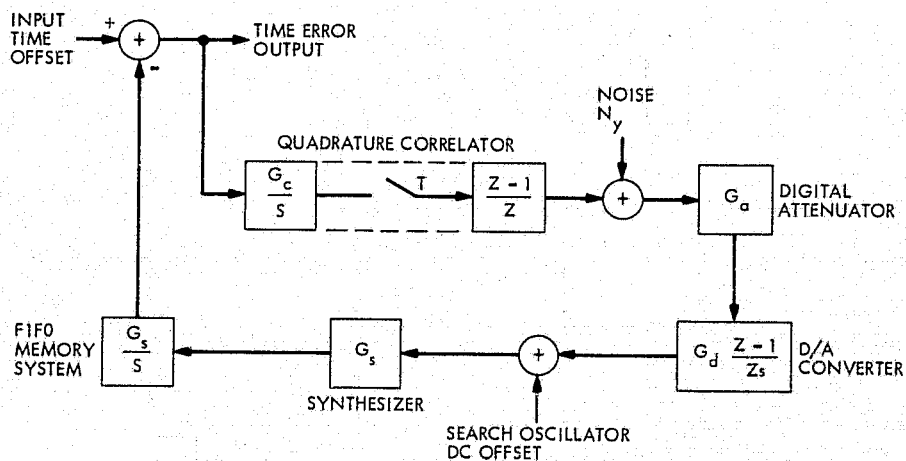Fig. 2. dB loss for nonoptimum α
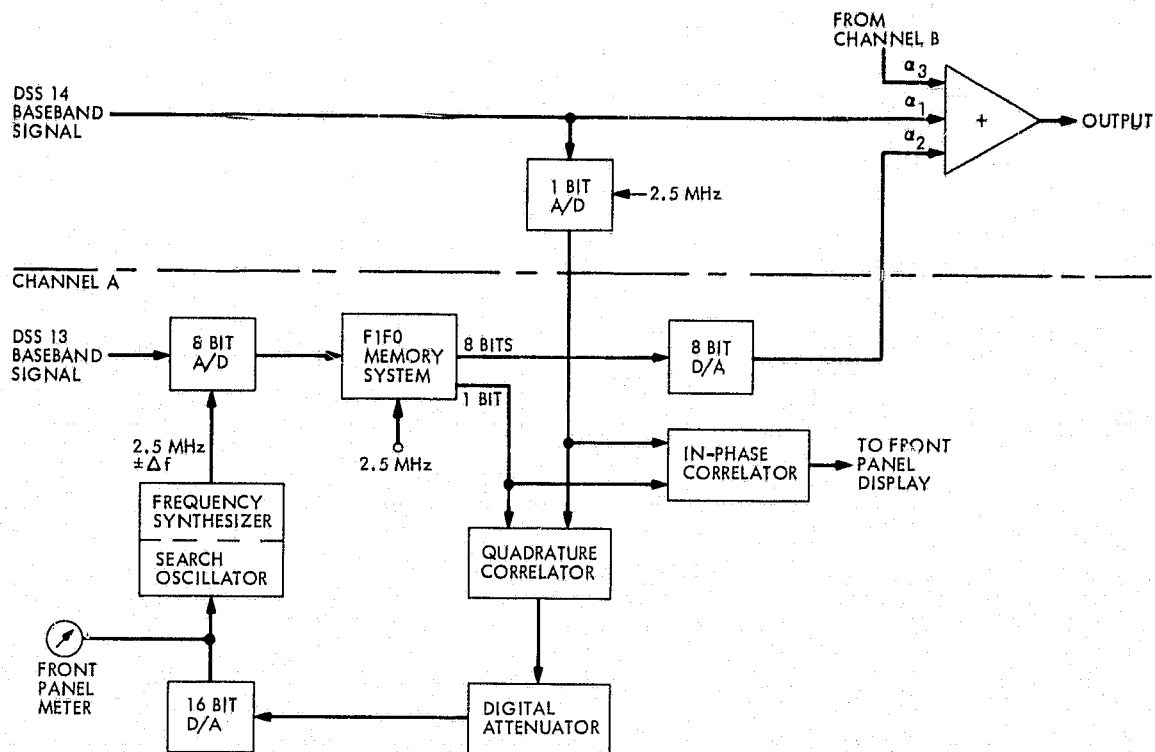
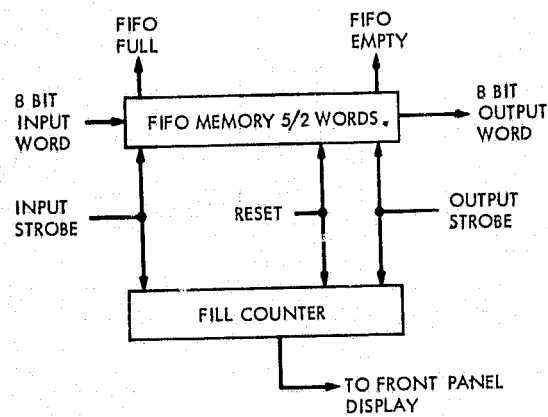Fig. 3. Phase tracking channel

Fig. 4. Laplace block diagram
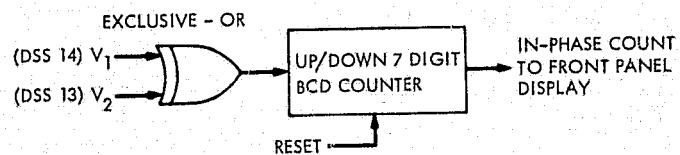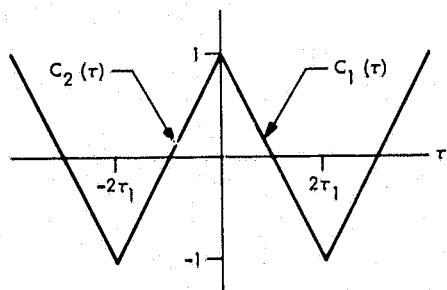
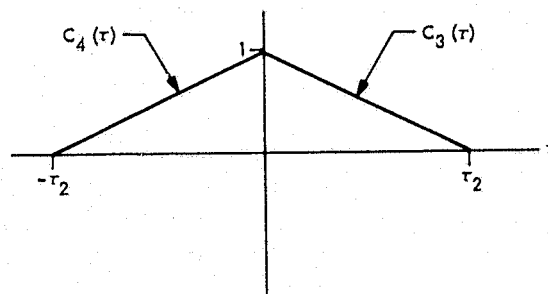**Fig. 5. First-in first-out memory system**

Fig. 6. In-phase correlator

(a) SUBCARRIER ONLY

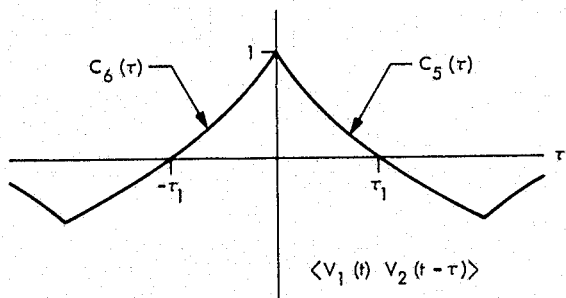$C_1(\tau) = 1 - \dfrac{1}{\tau_1}\tau$

$C_2(\tau) = 1 + \dfrac{1}{\tau_1}\tau$

(b) PN DATA ONLY

$C_3(\tau) = 1 - \dfrac{1}{\tau_2}\tau$
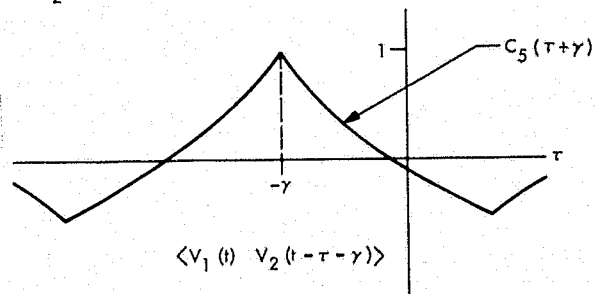
$C_4(\tau) = 1 + \dfrac{1}{\tau_2}\tau$

(c) SUBCARRIER WITH PN DATA

$\langle V_1(t)\, V_2(t-\tau)\rangle$

$C_5(\tau) = C_1(\tau)\, C_3(\tau) = 1 - \left(\dfrac{1}{\tau_1} + \dfrac{1}{\tau_2}\right)\tau + \dfrac{1}{\tau_1\,\tau_2}\,\tau^2$
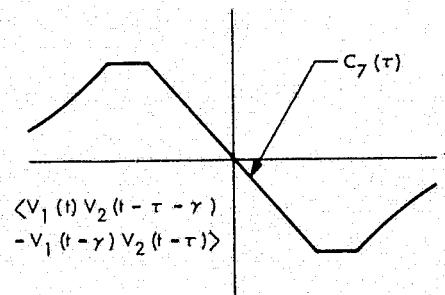
$C_6(\tau) = C_2(\tau)\, C_3(\tau) = 1 + \left(\dfrac{1}{\tau_1} + \dfrac{1}{\tau_2}\right)\tau + \dfrac{1}{\tau_1\,\tau_2}\,\tau^2$

(d) V_2 DELAYED

$\langle V_1(t)\, V_2(t-\tau-\gamma)\rangle$

$C_5(\tau+\gamma) = 1 - \left(\dfrac{1}{\tau_1} + \dfrac{1}{\tau_2}\right)\gamma + \dfrac{\gamma^2}{\tau_1\,\tau_2} - \left(\dfrac{1}{\tau_1} + \dfrac{1}{\tau_2} - \dfrac{2\gamma}{\tau_1\,\tau_2}\right)\tau + \dfrac{\tau^2}{\tau_1\,\tau_2}$

(e) V_1 DELAYED

$\langle V_1(t-\gamma)\, V_2(t-\tau)\rangle$
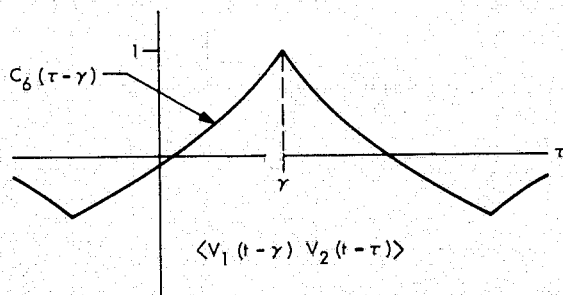
$C_6(\tau-\gamma) = 1 - \left(\dfrac{1}{\tau_1} + \dfrac{1}{\tau_2}\right)\gamma + \dfrac{\gamma^2}{\tau_1\,\tau_2} + \left(\dfrac{1}{\tau_1} + \dfrac{1}{\tau_2} - \dfrac{2\gamma}{\tau_1\,\tau_2}\right)\tau + \dfrac{\tau^2}{\tau_1\,\tau_2}$

(f) QUADRATURE CORRELATOR CURVE

$\langle V_1(t)\, V_2(t-\tau-\gamma) - V_1(t-\gamma)\, V_2(t-\tau)\rangle$

$C_7(\tau) = \dfrac{1}{2}\left(C_5(\tau+\gamma) - C_6(\tau-\gamma)\right) = -\left(\dfrac{1}{\tau_1} + \dfrac{1}{\tau_2} - \dfrac{2\gamma}{\tau_1\,\tau_2}\right)\tau$

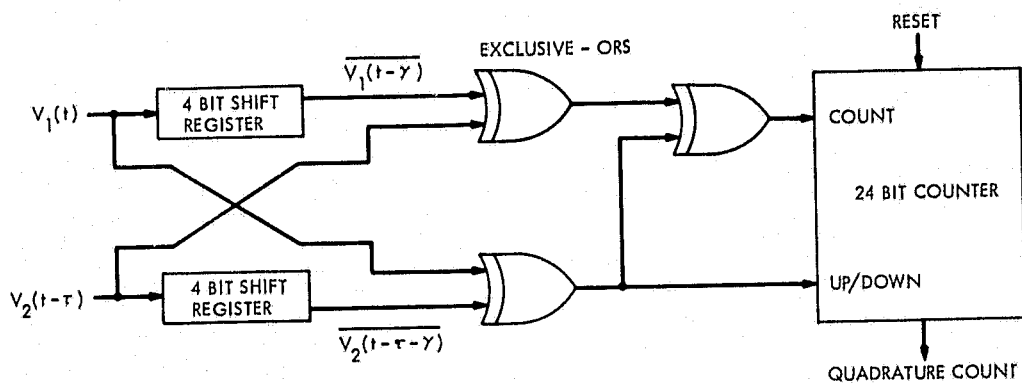**Fig. 7. Correlation curves**
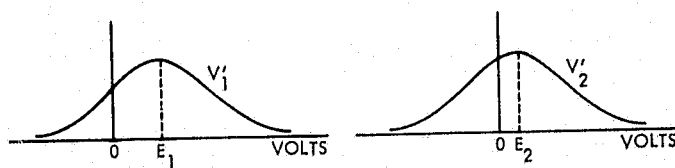
Fig. 8. Quadrature correlator
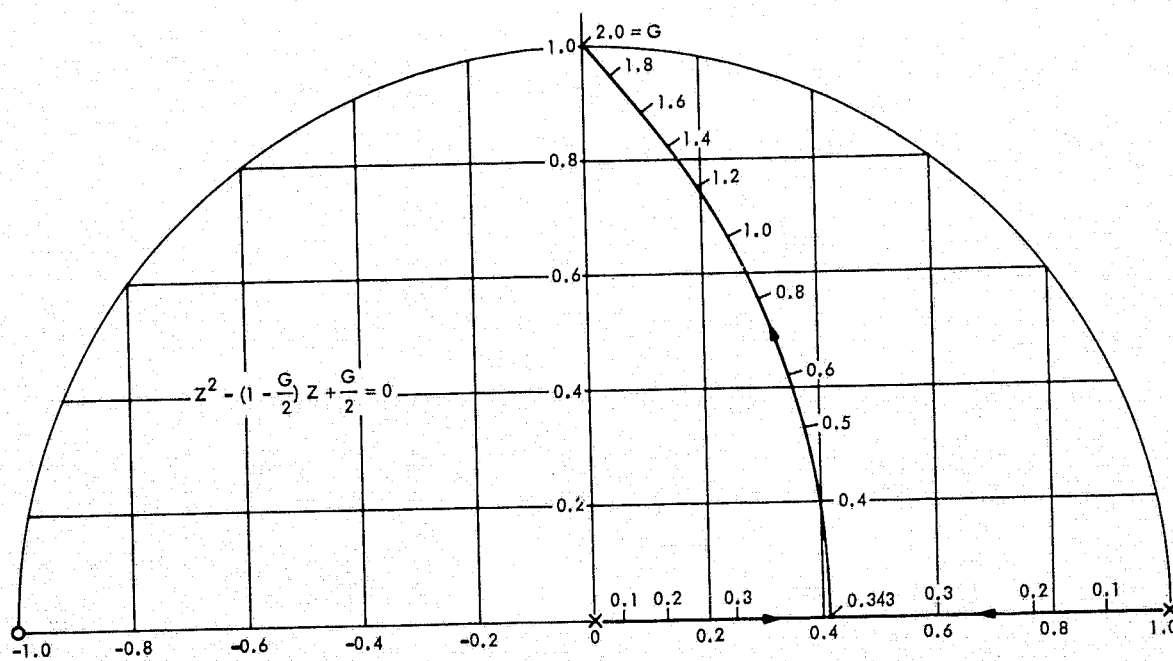

Fig. 9. Probability density curves

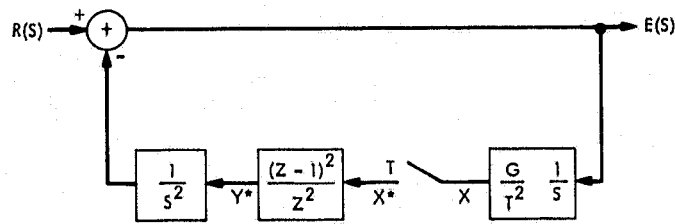**Fig. 10. Phase tracking loop root locus**

Fig. 11. Input analysis Laplace diagram
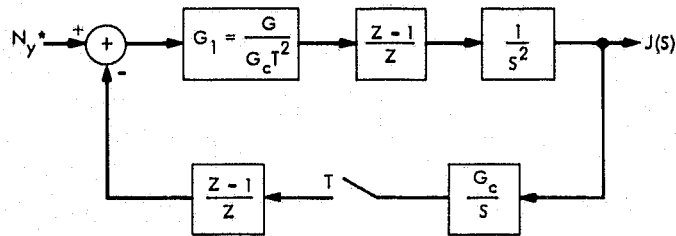

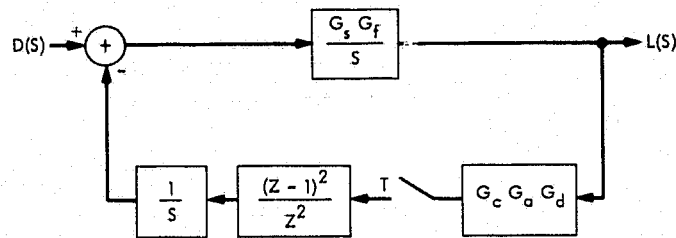Fig. 12. Noise analysis Laplace diagram

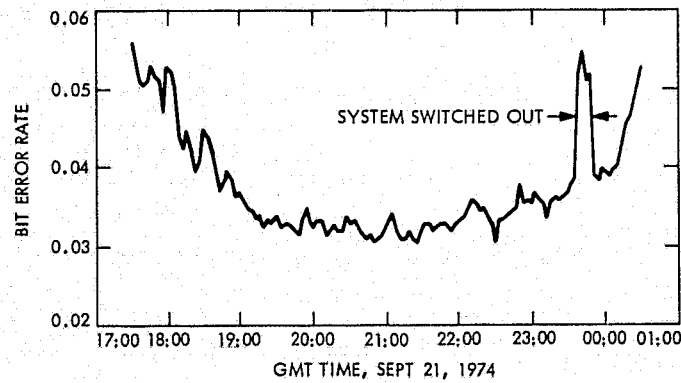Fig. 13. DC offset analysis Laplace diagram

Fig. 14. Bit error rate during encounter

Appendix

Derivation of Integrate-and-Dump Sampled Data Function

A conceptual circuit for the integrate-and-dump function is shown in Fig. A-1. $R(s)$, the Laplace function of the continuous input, is fed to an integrator of gain G. Periodically, at intervals of T seconds, an impulse function is fed to the integrator. This impulse function, properly scaled by the attenuator, sets the integrator output, $C(s)$, exactly to zero. A small amount of pure delay approaching zero in the limit, is required to decouple the zeroing of the output and the formation of the impulse function.

Equations for the loop variables are

$$C(s) = G\frac{R(s)}{s} - X^* \frac{G}{s} \qquad \text{(A-1)}$$

$$X(s) = \frac{1}{G} C(s) e^{-\delta sT}, \qquad \delta \to 0 \qquad \text{(A-2)}$$

Since $X(s)$ contains a pure delay term, its Z-transform is

$$X^* = \frac{1}{G} C(Z,m)_{m=1-\delta}, \qquad \delta \to 0 \qquad \text{(A-3)}$$

where $C(Z,m)$ is the modified Z-transform of $C(s)$. Taking the modified Z-transform of Eq. (A-1) and allowing δ to approach zero as a limit gives

$$C(Z,m)_{\substack{m=1-\delta \\ \delta \to 0}} = G\left(\frac{R(s)}{s}\right)^* - X^* \frac{G}{Z-1} \qquad \text{(A-4)}$$

From Eqs. (A-3) and (A-4), X^* is found to be

$$X^* = \frac{Z-1}{Z}\left(\frac{R(s)}{s}\right)^* \qquad \text{(A-5)}$$

and Eq. (A-1) becomes

$$C(s) = G\frac{R(s)}{s} - \frac{G}{s}\frac{Z-1}{Z}\left(\frac{R(s)}{s}\right)^* \qquad \text{(A-6)}$$

$C(s)$ is sampled at the instant before the impulse function sets it to zero. Thus the Z-transform of $C(s)$ is

$$C^* = C(Z,m)_{m=1} = G\frac{Z-1}{Z}\left(\frac{R(s)}{s}\right)^* \qquad \text{(A-7)}$$

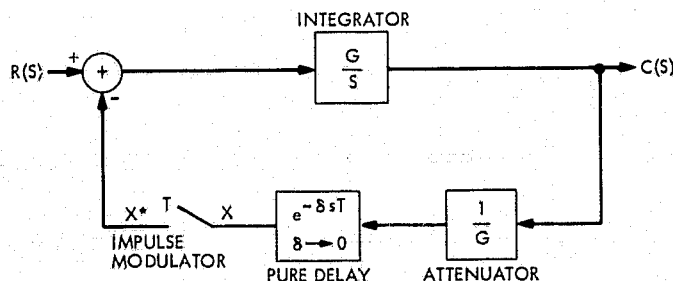A block diagram representing Eq. (A-7) is used for the quadrature correlator in Fig. 4.

Fig. A-1. Integrate-and-dump Laplace diagram

DSN Research and Technology Support

E. B. Jackson

R. F. Systems Development Section

The activities of the Development Support Group in operating and maintaining the Venus Deep Space Station (DSS 13) and the Microwave Test Facility are discussed and summarized and progress noted during the period December 16, 1974 through February 15, 1975. Major activities include preparation for a planned "automated station" demonstration and hardware/ software testing therefor, observations of rotation constancy of various pulsars, continued collection of Faraday rotation data with which to effect correction of spacecraft data for Earth's ionosphere effects, solar energy instrumentation data collection activities, 400-kW X-band radar, Block IV receiver/exciter testing at DSS 14, and testing for electromagnetic compatibility with the proposed Goldstone surveillance radar. Extensive DSN 100-kW klystron testing, routine clock synchronization transmissions, and radio science support activities are also reported.

During the two-month period ending February 15, 1975, the Development Support Group, in operating the Venus Deep Space Station (DSS 13) and the Microwave Test Facility (MTF), made progress on various programs as discussed below. To meet budgetary limitations, the contractor staffing of the Development Support Group was reduced from 16 to 10 and the operating hours of the Venus Station from 80 to 40 hours per week, both actions effective on February 3, 1975.

I. In Support of Section 331

A. Station Automation

In support of the station automation program (RTOP 68—Station Monitoring and Control Technology), which will demonstrate an automated station by performing a pulsar track under complete, remote, computer control at DSS 13, we provided 62-3/4 hours of testing. The software for on-site operation is essentially complete, and the

intercommunications among the computers is complete and functioning. Pulsar observations, complete with data collection, are being done under control of the master computer (the SDS-930 at the Venus Station) during these tests.

B. Pulsar Observations

In support of Pulsar Rotation Constancy (OSS-188-41-52-09), we provided 64-1/2 hours of pulsar observations, during which the pulsars tabulated in Table 1 were observed, and precise pulse-to-pulse timing, pulse shape, and pulse power content were measured. These observations, which use the 26-m antenna and SDS-930 computer for data collection, were made at 2388 MHz, using left-circular polarization (LCP).

II. In Support of Section 333

A. Faraday Rotation Data Collection

Observing Applications Technology Satellite Number 1 (ATS-1) at 137.25 MHz, two complete receiving systems record the angle the received electric field vector makes with the horizon. The data are recorded onto an analog chart recorder, a digital printer, and punched paper tape for later computer processing at JPL. The data are mailed to JPL at the end of each day's observations, and, after processing, are used to correct observed spacecraft doppler and range data for the effects of passing through the Earth's ionosphere. These data are collected automatically 24 hours/day, 7 days/week.

B. Sky Survey/NAR Reliability Testing

Using the 26-m antenna, the station receiver, and the Noise Adding Radiometer (NAR), data are automatically collected at night and during weekend hours when the station is unmanned. The antenna is fixed in position at 180-deg azimuth, and observations are made at several fixed elevation positions. During this period, observations were made for a total of 613-1/4 hours, at elevation angles of 80.6 through 81.9 deg, at a frequency of 2295 MHz, right-circular polarization (RCP).

C. Radio Star Calibration

As part of the Antenna Gain Standardization Program, observations are made at DSS 13 to determine received flux density of a number of radio sources. These observations, at 2278.5 MHz, RCP, were made of radio sources Cygnus A, Virgo A, and 3C123, using the 26-m antenna, the station receiver, and the NAR. The NAR has control of the antenna offsets and provides a semi-automated data collection cycle, as well as recording the data.

D. Solar Energy Instrumentation

In support of RTOP 69—Tracking Station Operations Technology, the Solar Energy Instrumentation Data Acquisition System (SEIDAS), which was relocated from DSS 14 to DSS 13, has had additional sensors added. SEIDAS currently has two pyrheliometers and three pyranometers, as well as sensors which measure air temperature, dew point, pressure, and wind speed. The data are recorded onto magnetic tape for later processing by the 1108 computer at JPL.

III. In Support of Section 335

A. Microwave Power Transmission

In preparation for testing of the final array of "rectennas," additional cable pairs were extended from the collimation tower to the operations building (G-51). (These pairs formerly terminated at building G-63.) Additionally, at the collimation tower, a three-phase, 100-ampere ground fault interrupter (GFI) was installed to increase personnel protection.

In preparation for the modifications necessary to the structure of the collimation tower, several prospective contractors visited the facility. At the end of the reporting period, the contract was awarded to Plas-Tal Corporation of Sante Fe Springs, California; they visited the site to make final measurements preparatory to fabricating the necessary steel.

B. X-Band Radar

With continued maintenance and operations support from us, the X-band radar was used to successfully obtain returns from the rings around the planet Saturn, as well as the minor planet Eros, when it came close to Earth in January 1975. The ring observations were made at a power output of 150 kW per klystron (two klystrons installed), but for the Eros observations the power output was successfully raised to 200 kW per klystron.

A variable load was fabricated to test the traveling-wave tube (TWT) power supplies; one of the Logimetrics power supplies failed during test. The other Logimetrics power supply is installed and powering the Varian TWT. The helix drivers have also been installed, and the system is functioning well although some temporary equipment still remains.

C. DSS 14 Block IV Receiver/Exciter

In support of the implementation of the Block IV receiver/exciter at DSS 14 for use during the Viking mission, we aided in the installation and testing of the

receiver and exciter control panels, interface testing, and various troubleshooting. Also, using a test facility setup at DSS 13, we modified, repaired as necessary, and tested various modules for the system using newly generated test procedures with which to measure performance. Although some monitoring and other interface functions are still undergoing test, the Block IV receiver/exciter at DSS 14 is functioning well.

D. Goldstone Surveillance Radar

With the higher intensities of non-ionizing radiation now being emitted by the Goldstone antennas, a way to avoid accidental irradiation of aircraft which may fly into the dangerous part of the antenna beam is desirable. As part of the planning for the possible installation of a short-range surveillance radar, we made measurements of the possible interference between such a radar and the normal DSN operations of spacecraft reception.

Using an FPS-18 type radar as a baseline, measurements were made at DSS 14 using a simulated radar operating at 2835 MHz. Appropriate pulsed signals having a peak level of −10 dBm were coupled into the maser, and their effect upon the demodulation of telemetry was examined. With the station demodulating telemetry with a signal-to-noise ratio (SNR) of 3.6 dB, no difference in the computer's estimation of SNR could be detected between the radar on/radar off configuration. However, this telemetry test was only of short duration and a longer test at higher powers is planned. Examination of the RF performance of the receiver and monitoring system was also performed during the 10-hour test period.

E. DSN Klystron Testing (100 kW)

In support of the implementation of the 100-kW transmitters into DSS 43/63, extensive testing of the X-3060 klystrons to be employed has been conducted at DSS 13. These klystrons have been modified by Varian Associates, the manufacturer, and incorporate a new cathode design.

Although some difficulty has been experienced with klystron dimensional variations that affect both body current and installation into the socket tank, complete parameter testing and a 12-hour "stability" run at 100-kW output power have been completed on klystron serial numbers A6-17-R2, H5-30-R2, K5-24-R1, and L5-34-R1.

IV. In Support of Section 391

Differential VLBI

In support of the Differential VLBI Experiment (OTDA 310-10-60-56), DSS 13, in conjunction with DSS 63, provided 8-1/4 hours of station support. During an actual 5-1/4 hours of observation, 28 radio sources were observed with a new source being selected every 12 minutes. Observations were made at 2290 MHz, using the 26-m antenna adjusted to receive RCP. The data were recorded on a special recorder installed for this experiment.

V. In Support of Section 422

A. Clock Synchronization Transmissions

As scheduled by the DSN, transmissions were made as tabulated in Table 2 for a total duration of 12-1/2 hours. These transmissions are made at 7149.9 MHz, using the 9-m antenna equipped with a 100-kW transmitter.

B. Viking Mission Configuration Tests, DSS 14

In support of the configuration testing at DSS 14, which is necessary in preparation for the Viking missions, we have provided on-site support to assure correct operation of the Block IV receiver/exciter, or to aid in troubleshooting in the event the system does not perform as expected. Except for some monitoring difficulties, we have supported the telemetry and command configuration testing to a successful conclusion insofar as the installed equipment will allow. A total of 88 hours of support was provided to this testing effort.

VI. In Support of Section 825

Planetary Radio Astronomy

In support of the Planetary Radio Astronomy Experiment (OSS 196-41-73-01), we observe the planet Jupiter and various radio calibration sources. Received flux density, at 2295 MHz, LCP/RCP, is measured using the 26-m antenna, the station receiver, and the NAR. Observations were made as tabulated in Table 3 and are made semi-automatically with the 26-m antenna offsets under the control of the NAR.

Table 1. Pulsars observed at DSS 13 (December 16, 1974
through February 15, 1975)

0031−07	0823+26	1706−16	2021+51
0329+54	0833−45	1749−28	2045−16
0355+54	1133+16	1818−04	2111+46
0525+21	1237+25	1911−04	2218+47
0628−28	1604−00	1929+10	
0736−40	1642−03	1933+16	

Table 2. Clock synchronization transmissions (December 16,
1974 through February 15, 1975)

Station	Number of transmissions
DSS 42	3
DSS 43	3
DSS 61	3
DSS 62	1
DSS 63	2

Table 3. Radio calibration sources observed at DSS 13
(December 16, 1974 through February 15, 1975)

3C17	3C138	3C353
3C48	3C147	PKS 0237-23
3C123	3C348	1C5146

Diagnostic and Control Panel for the Coherent Reference Generator

C. F. Foster
R. F. Systems Development Section

This report describes the diagnostic and control system developed for the Coherent Reference Generator (CRG). All elements of this assembly are designed to have configuration control, failure analysis, and fault location performed either manually or by a remote computer. The mechanical control portion provides the selection of a frequency standard as well as either computer or manual mode of operation. To facilitate rapid system repair, all CRG input and output, signal levels, and power supply levels are monitored for performance within their specified limits, with the failed elements triggering the CRG alarm, and displaying the location of failure on the front panel.

I. Introduction

The Diagnostic and Control Panel for the Coherent Reference Generator (CRG) is designed in accordance with the requirements set forth in DSIF Standard Design Requirements 00001. This panel features fully automated performance monitoring, including indicators that allow the operator to determine the operational status of each module, as well as the presence of all input signal levels. Frequency standard selection is made by a single front panel switch, as is manual/computer selection, and fault indicator test. The elimination of complex displays, multiple switches, and controls assures the necessary performance requirements to minimize operator expense. To provide for future growth, this panel incorporates computer interface and control logic so that system

configuration, failure analysis, and fault location can be performed by a remote computer. The computer capability is designed such that all the necessary logic is on plug-in cards. This allows sites presently without computer control to eliminate the cost of the computer interface/control logic until such time that a computer does become available; then, to achieve full computer capability, all that will be required is to purchase the necessary cards and plug them into prewired sockets.

II. Implementation

A simplified block diagram of the Diagnostic and Control Panel (Fig. 1) shows the major logic functions. All inputs and outputs are internally monitored at the module level, and signal presence confirmation signals are

presented to the Diagnostic Panel as active transistor–transistor logic (TTL) "low" levels. All module status as well as power supply and switch conditions are fed in parallel to the CRG's good/bad alarm. If anything is out of tolerance, even if a module is not plugged in, the operator is alerted by an audio alarm and the remote computer sees a fail signal.

For description, this panel easily breaks down into two major functions: manual control and computer control. In the manual control mode, the frequency standard selection is accomplished with a mechanical fail safe switch so that if ac power is momentarily interrupted, the operator will not have to re-select the frequency standard. This switch also establishes the code for the station 1-MHz clock driver to assure that the proper secondary standard is selected in the event the primary fails. The individual module status lights shown in the lower-left corner of Fig. 2 indicate the location of a failed module using a grid system whereby each separate panel in the cabinet is numbered starting from the top as A1, A2, etc., and modules within a panel are numbered left to right as A1, A2, and A3 (i.e., the third module from the left in the sixth panel would be located by a light at position A6A3 in the front panel module grid). This method of module identification greatly reduces the cost of expansion and change, as control panel engraving will not have to be changed when modules are added. The input signal display, upper-left corner of Fig. 2, indicates if either the 1-MHz or the 5-MHz signal is not present, and if the 0.1-MHz or 10-MHz is not present. The station clock standard indicates the presence of the 1-MHz primary and secondary standards. This indicator provides a monitor on the backup frequency standard, which is automatically placed into service in event of a primary standard failure. Other front panel indicators display power supply and backup battery status. The condition of each coaxial switch in the frequency standard selector is displayed, as they are designed to be replaced by the operator in the event of failure. A test switch is designed into the front panel for the operator to check proper operation of the indicator lights. Four pushbutton switches select the

primary frequency standard, with adjacent lights verifying that the correct sequence of switch operations has taken place. A front panel switch with a mechanical lock selects either manual or computer mode of operations.

In the computer mode all front panel indicators operate. The computer interface is designed to be fully compatible with DSN Standard Interface Specification ES508534, and incorporates the hybrid handshaker circuit (Ref. 1). A single status output alerts the computer in the event of a Coherent Reference Generator failure, thus allowing the computer to perform functions other than continually monitoring all the individual modules. When the computer is alerted that there is an anomaly in the CRG, the DSN standard interface protocol is put into effect to interrogate the module status word generator, thereby locating and displaying the fault for operator action. Computer configuration control is initiated through the standard interface circuit only if the computer/manual switch is in computer mode.

The control circuit is designed using shift registers as digital filters to eliminate the possibility of noise on the interface lines from changing the frequency standard selection. The control sequence requires the computer to place the code corresponding to the frequency standard to be selected on data transfer lines (2) through (5) along with a separate control bit on data line (1) of the interface. After the handshaker has cycled through the proper protocol, an XEQ command generated by the handshaker is applied to the decoder, and the command is transferred to the frequency standard selector. The decoder has a volatile memory that is protected against power line outage by a backup battery system, thereby providing fail safe operation in both computer and manual modes.

III. Conclusion

The Diagnostic and Control Panel has been developed and fully tested in the laboratory. It has been installed and is operating at DSS 14, meeting all design goals. Present plans call for adding this capability to the remaining Coherent Reference Generators installed in the 64-m net.

Reference

1. Foster, C. F., *Complete Logical Operation and Test Procedure of Handshaker Circuit*, Spec. TP510942A, in preparation (JPL internal document).
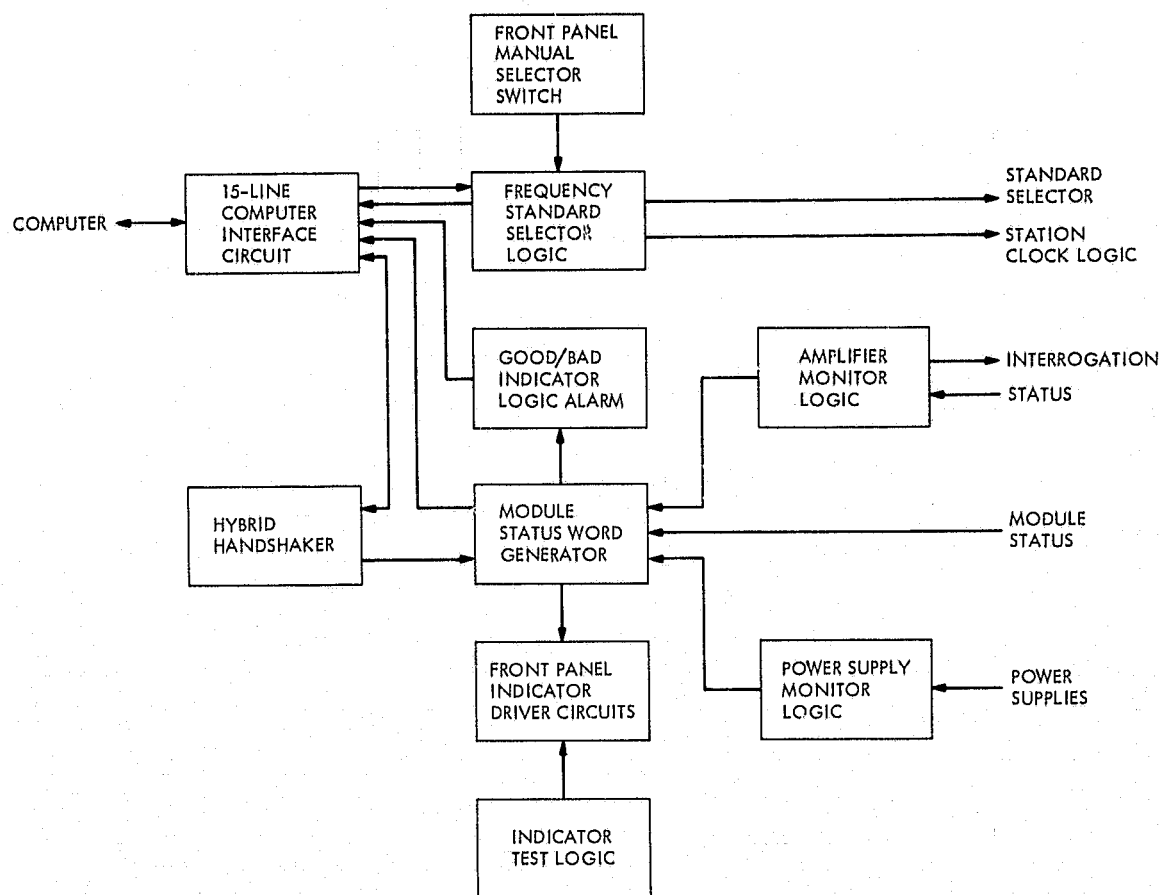
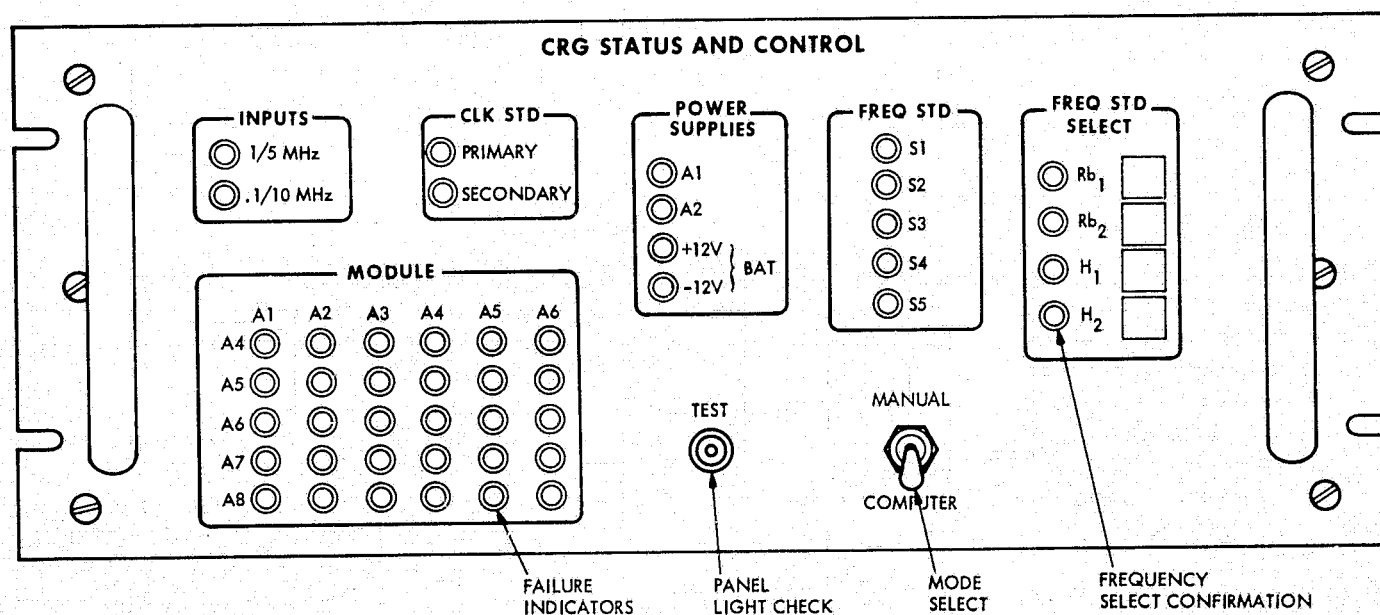Fig. 1. Diagnostic and Control Panel simplified block diagram

Fig. 2. Coherent Reference Generator Diagnostic and Control Panel

Automation of Data Gathering and Analysis
for the Fourth-Harmonic Analyzer

Y. L. Grigsby
R. F. Systems Development Section

The Fourth-Harmonic Analyzer is used to measure the magnitude of the fourth harmonic of the S-band transmitter in waveguide for any mode or combination of modes to develop operational techniques in measuring harmonics. The gathering and analyzing of data have been automated to reduce the number of man-hours needed to perform this task by hand.

I. Introduction

An analyzer called the Fourth-Harmonic Analyzer has been developed (Fig. 1) to measure the magnitude of the fourth harmonic of the S-band transmitter in waveguide for any mode or combination of modes and to develop operational techniques to establish measurement accuracy in measuring harmonics. (Refer to Ref. 1 for technical information on the analyzer.) Previously it took two people two hours to gather the data. An additional two days were needed to analyze the data. With the use of a PDP-11/20 computer along with its real-time programming and operating system, RT-11, and a general microwave digital power meter, the time required for gathering and analyzing data is drastically reduced.

II. Summary

A PDP-11/20 with RT-11 program was used to analyze data of the Fourth-Harmonic Analyzer. A program was written to (1) read the voltage standing wave ratio (VSWR) values from a file stored on Digital Equipment Corporation (DEC) tape, (2) read the power-level data typed in at the teletype (TTY), (3) save the power-level data on paper tape, (4) analyze the data, (5) compute the total power, and (6) provide the option of listing only the total power or the total power, all data, and calculated values. The preliminary results were within ±1.8 dB of the measured harmonic input. The time required to gather and analyze data was reduced from two days to three hours.

The automation of data gathering and analyzing is the first step in establishing measurement techniques and instrument precision. With automation many tests can be run to achieve maximum accuracy in a laboratory environment prior to inserting the analyzer into the high-power microwave system and making the actual power measurements. The time required for gathering and analyzing data is drastically reduced.

III. Previous Analyzing Techniques

The power level at each port was read by a power meter and recorded on a work sheet. In the laboratory only the test procedure requires placing objects, such as metal, in the waveguide to obtain various combinations of modes. The data gathering process took two people two hours. One person alone took an additional two days to analyze the information and calculate the total power. The calculation involved 960 pieces of data.

The analyzer has a total of 240 ports. The ports are divided into nine groups labeled A through I. Each group contains 30 ports with the exception that there are no ports for C16 through C30 and G16 through G30. For programming purposes the ports become a 9 × 30 matrix.

Using the measured VSWR of each port, the measured power levels were corrected for all ports. The corrected values were then summed and multiplied by the insertion loss to obtain the total power. For each port, a total of four data values were used (two given data values and two computed values), giving a grand total of 960 values.

IV. Automation Techniques

To automate the procedure of gathering and analyzing data, the following equipment was used:

(1) PDP-11/20 computer with RT-11 operating system.

(2) Teletype or cathode-ray tube (CRT) terminal.

(3) Fourth-Harmonic Analyzer.

(4) General microwave digital power meter with test probe.

Figure 2 shows how the equipment is set up.

A program was written to analyze the data and compute the total power. The program also has the option of listing only the total power or the total power, all data, and calculated values. The flowcharts (Figs. 3–8) describe in more detail how the program works. The measurements are typed in at the TTY or CRT from the recorded data. Each data value typed in is saved by the high-speed paper-tape punch. The VSWR values are stored and read from a file maintained on DECtape. This is possible because one advantage of RT-11 Basic is the ability to read and write data files while running a basic program. All measurements are analyzed in the computer and the process of analyzing data which took two days was reduced to three hours.

If a listing of the analysis (all data and calculated values) is required at a later date, the data on paper tape are fed through the high-speed paper-tape reader. A second program was written for the sole purpose of reading the data (measured power levels) off of paper tape, reading the VSWR values off of a file on DECtape, analyzing all data, and reproducing a complete listing of the analysis. The paper tape saved time because it eliminated the need of typing in the data at the TTY again.

V. PDP-11/20 and RT-11

One outstanding feature of RT-11 is its ability to link an assembly language routine with a basic program. This feature makes it possible to insert the test probe into a port of the analyzer, read the power level, and transmit the data to the assembly language routine in the computer. The basic program then calls on the assembly language routine for the data. The linkage of an assembly language routine to a basic program works on the same principle as fortran and its subroutine. This linkage will completely eliminate the need of typing in data at the TTY in the future.

VI. Future Plans

In the near future the gathering and analyzing of the data for the Fourth-Harmonic Analyzer will be fully automated. Data will no longer have to be recorded on a data sheet and typed in at the TTY. There will be a direct connection between the digital power meter and the computer. As the power levels are displayed and read by the meter, they will automatically be stored in the computer by way of the "data line" (see Fig. 2). The entire task will require only one person instead of the two people required to perform the present automation techniques.

Reference

1. Smith, R. H., "Fourth Harmonic Analyzer," in *The Deep Space Network Progress Report 42-20*, pp. 121–123, Jet Propulsion Laboratory, Pasadena, Calif., Apr. 15, 1974.
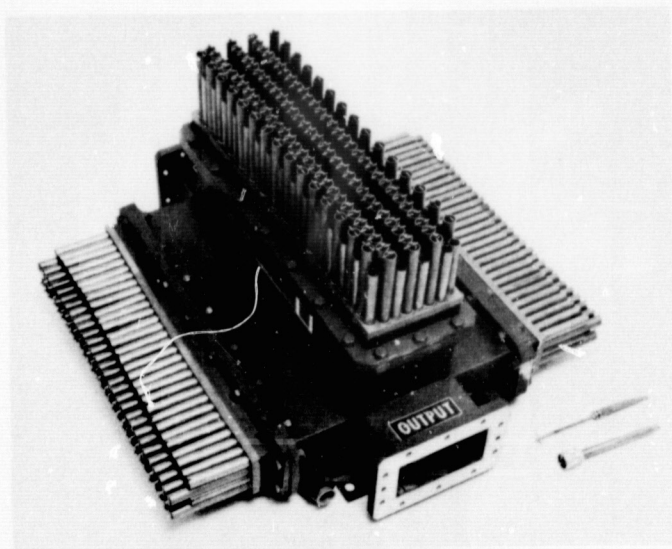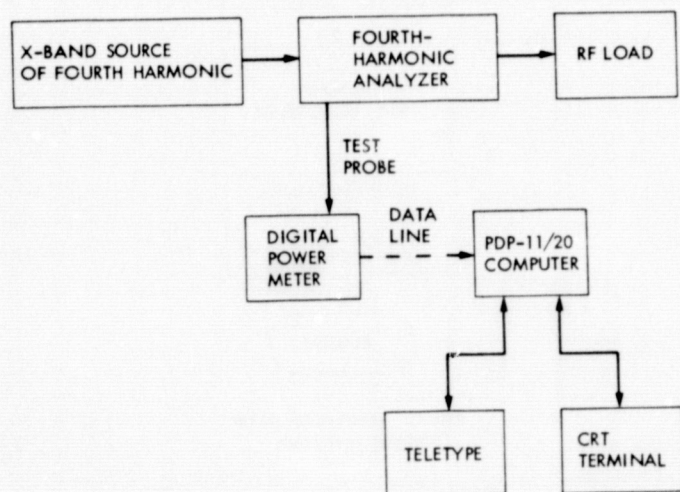
Fig. 1. Fourth-Harmonic Analyzer

Fig. 2. Laboratory equipment setup for automation of harmonic analysis
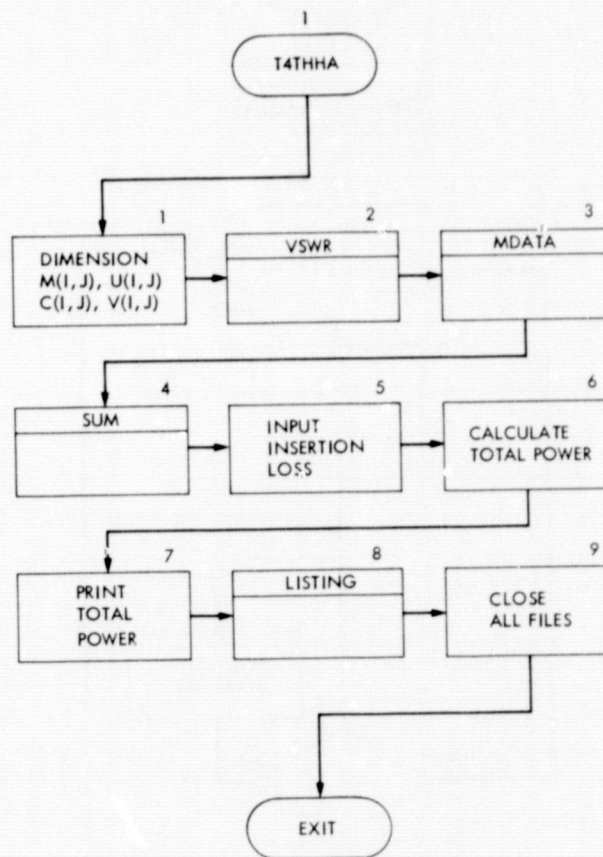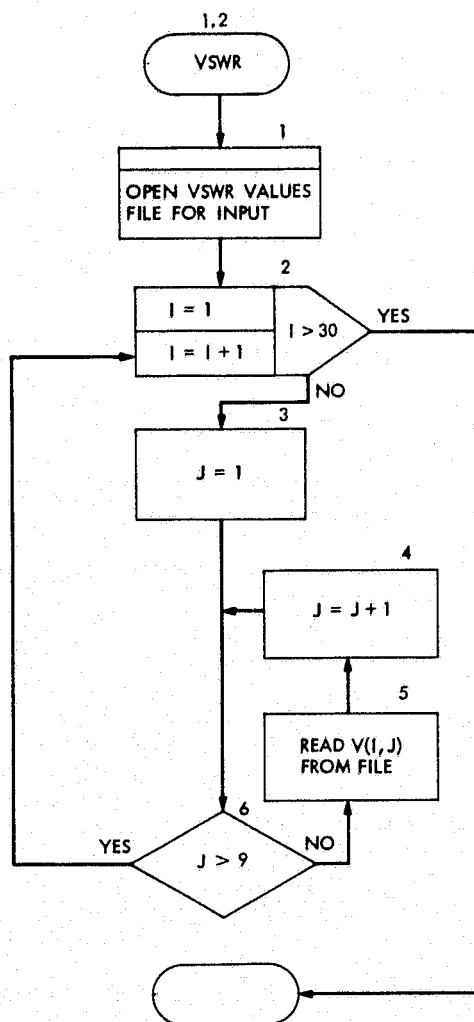

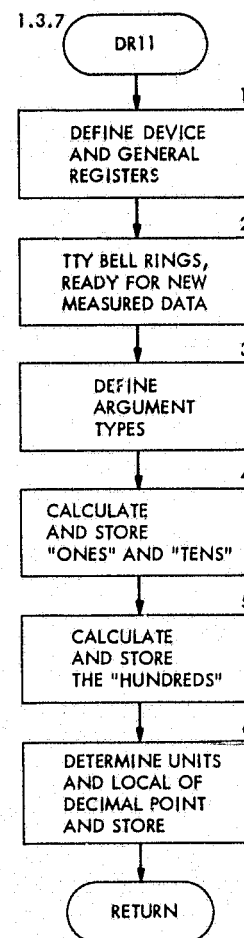Fig. 3. General flowchart data analysis

Fig. 4. Read VSWR data from DECtape

Fig. 5. Measured data
input and save
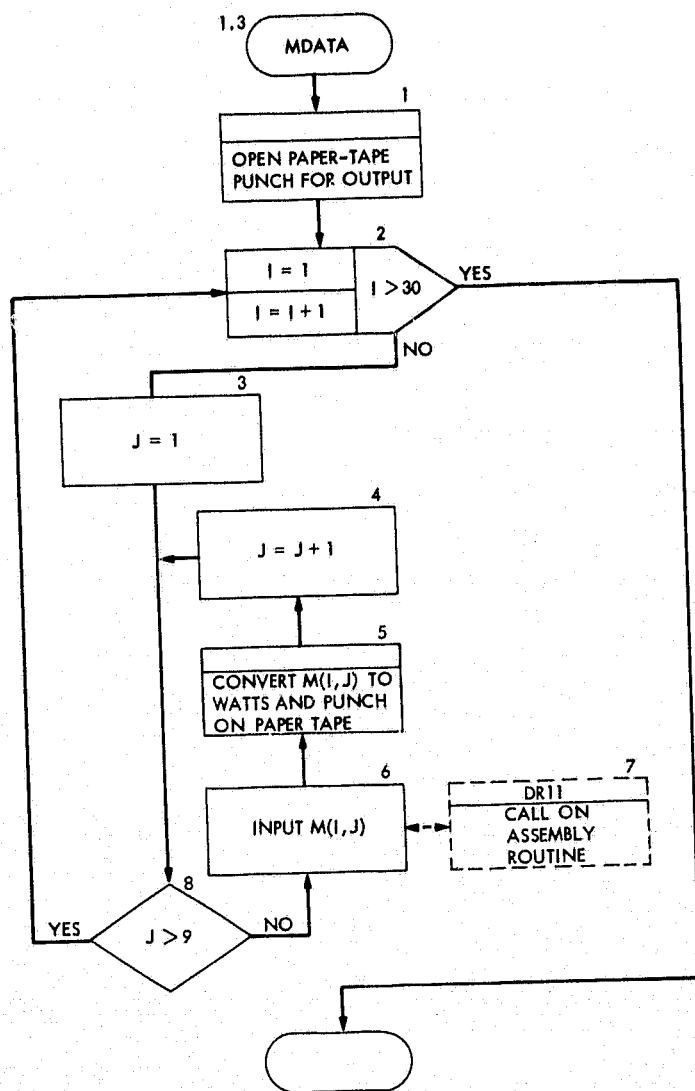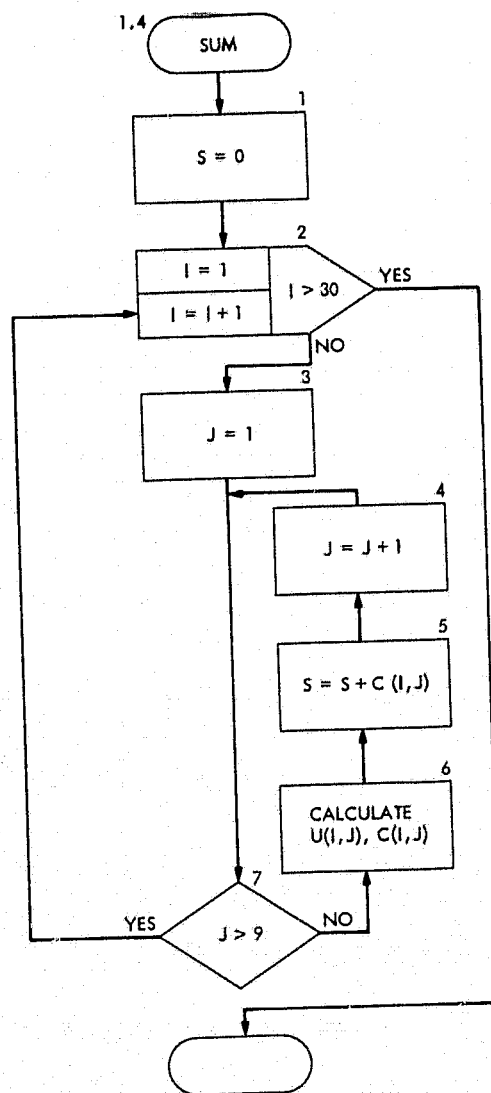
Fig. 6. Assembly language routine
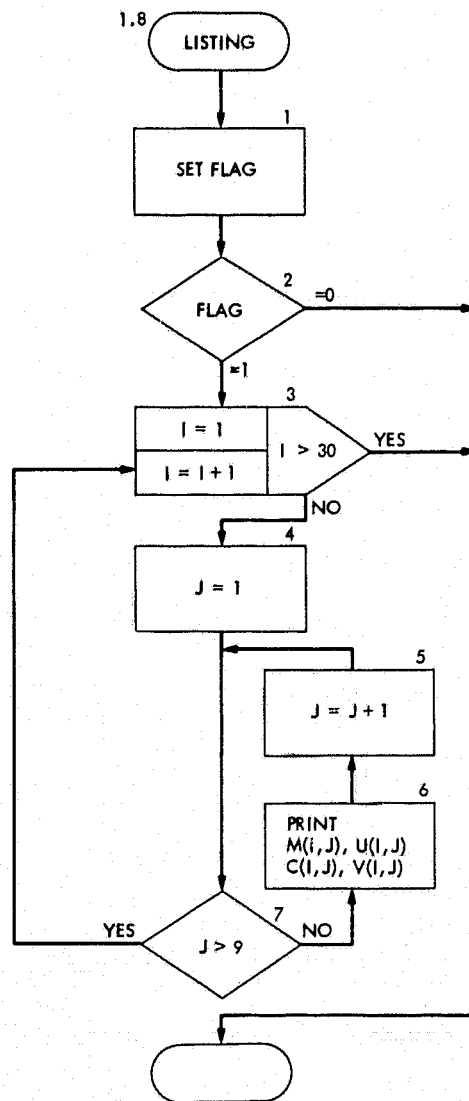

Fig. 7. Correct measured data

Fig. 8. List all data and results

Goldstone Solar Energy Instrumentation Project: Description, Instrumentation, and Preliminary Results

M. S. Reid, R. A. Gardner, and O. B. Parham
Communications Elements Research Section

A solar energy instrumentation project has been initiated at Goldstone in order to support the investigation of Goldstone as a possible site for a demonstration project by acquiring fundamental information about solar radiation characteristics at that location and by helping to build an adequate technological base for the engineering of solar-based energy systems suitable for Goldstone. The initial instrumentation and results for the first three months of operation are discussed and presented in tabular and graphical form.

I. Introduction

The Goldstone Space Communications Complex has several unique characteristics which make it appropriate for consideration as a solar energy demonstration project that could attain a high degree of energy self-sufficiency and possibly make a significant contribution to the achievement of a national goal of energy independence. This work supports the investigation of Goldstone as a possible site for a demonstration project by acquiring fundamental information about solar radiation characteristics and by helping to build an adequate technological base for the engineering of solar-based energy systems suitable for Goldstone.

The work unit is divided into two parts, which are of nearly equal importance and magnitude and have nearly concurrent schedules. Both parts require the acquisition of data over extended periods. Part A acquires solar radiation and meteorological data to improve the accuracy of probabilistic models essential to engineering design. Part B acquires performance data on measurement equipment placed at Goldstone for feedback to the technological base to improve the basic physical models used for system analysis and evaluation.

Solar collectors potentially suitable for a solar-electric-hydrogen fuel generation subsystem at Goldstone will be analyzed to determine what site-peculiar information is needed to specify, design, and evaluate them. The information falls into three classes: (1) insolation, both specular and diffuse; (2) meteorological, such as wind speed and direction, temperature, relative humidity, etc.;

and (3) environmental, such as dust and sand deposition and erosion. The information does not include characteristics that can be determined by measurement at places other than Goldstone, such as absorptivity and emissivity, or other properties of materials.

Raw data from measurements are not directly usable for the engineering of solar collectors or for the analysis of complete solar-hydrogen fuel subsystems; the probabilistic models must be fitted to the raw data. A probabilistic insolation model will be devised for the total insolation and for the specular component as a function of collector concentration, and a probabilistic meteorological model will be devised for wind speed and direction, temperature, relative humidity, etc. In all cases, the models will include probability density functions for the year and for each month. The insolation and meteorological models will be fitted to the data to improve their accuracy and to establish the degree of correlation among the random variables in the models. This correlation, however, will not be included in the early models.

As a result of examining potentially suitable solar collectors and probabilistic models, a set of measurements will be defined. Commercial instruments have been, and will continue to be, specified and procured to make as many of the measurements as possible. Where commercial instruments are not available, such as devices for measuring the specular component of insolation as a function of collector concentration, the necessary instruments will be designed and built.

Some of the measurements are already being made under other Office of Tracking and Data Acquisition (OTDA)-funded activities (Microwave Weather Project, Operational Meteorological Data System, Conscan Project). Whenever possible, common measurements will be made by instruments already incorporated into the other data-gathering equipments.

A complete program of measurements at other NASA tracking stations is not required at this time. However, an operational meteorological data system is being implemented at DSSs 14, 43, and 63, which will incorporate a single insolation instrument, a hemispherical pyranometer. The data from each of the systems will be delivered to this project for reduction and analysis. The reduced data from DSSs 43 and 63 will serve as the basis for preliminary insolation and meteorological models for those stations when needed. By correlating the data from the three stations, it will be possible to extend the Goldstone models to obtain preliminary models for the other complexes as needed. The extension technique will be useful in devising

preliminary models for other NASA tracking stations and complexes.

Part B of the project is concerned with developing the technological base needed to analyze and evaluate an entire solar-hydrogen fuel subsystem for Goldstone, including its component parts. Particular attention will be paid to identifying the key parameters that would be needed in each case to specify devices and subsystems.

When sample collectors or other components are procured from industry (not by this project) or are supplied to JPL for evaluation, instrumentation will be developed or procured to measure actual performance. The performance data will be used to compare actual versus theoretical performance, and the information will be fed back to improve the technological base.

When a complete solar-hydrogen subsystem is installed at Goldstone (there may be more than one), instrumentation for the long-term evaluation of its performance will be developed or procured, installed, and transferred to the operations organization for maintenance and operation. Data acquisition will be monitored to assure the validity of the data. The actual performance data will be compared with the theoretical performance computed using data collected at the same time by the instruments provided under Part A.

The use of actual field test data will permit the economic feasibility of proposed modifications to the solar-hydrogen subsystem to be determined. The data will also permit an assessment of the economic factors relating to the possible installation of solar-hydrogen subsystems at other NASA tracking stations or complexes. The assessment will be facilitated through the use of preliminary insolation and meteorological models developed for the Spanish and Australian tracking complexes based on data from Part A.

II. Initial Instrumentation

A pyrheliometer was installed on the roof of the main control building at DSS 14 on June 19, 1974. A pyrheliometer is a commercial instrument which measures the total incident radiation, both specular and diffuse, over a hemisphere. Its orientation is horizontal to measure the total radiation from the sky.

This instrument is an Eppley-type pyranometer, which has a radial wire-wound differential thermopile as a detector. The hot junction receivers are blackened and the cold junction receivers are whitened. When exposed to

solar radiation, the black and white surfaces develop a marked temperature difference, and the resulting voltage is proportional to the intensity of solar radiation. The instrument has a built-in temperature compensation circuit for a standard matching condition through the range −20 to +40°C. The thermopile unit is formed of 48 artificial junctions by copper-plated Constantan wire and mounted under a precision-ground optical quartz glass hemisphere. The wavelength response is maximized from 0.32 to 2.5 microns. Instrument linearity is ±1% over 0 to 2 langleys/min (0 to 1.3956 kW/m²) and the temperature dependence is ±1.5% consistency over −20 to +40°C. Response time $(1/e)$ is 3 to 4 seconds.

The clear day data from this instrument will be useful for determining or verifying a theoretical clear day insolation model for Goldstone. Data for cloudy days will be useful for determining or verifying a probabilistic model of Goldstone insolation. This report presents the data from this instrument for the period June 19 through September 30, 1974.

Other instruments that were operating at Goldstone (DSS 14) during this period were meteorological instruments. These included temperature, barometric pressure, dew point, wind speed and direction, and rainfall. The data that are presented in this report are temperature, barometric pressure, and absolute humidity in terms of grams of equivalent water per cubic meter of air.

An automatic data acquisition assembly has been procured and is presently being commissioned. It consists of a central recording station which has the capability of interfacing with up to 10 remote stations. The remote stations will interface with transducers in a given instrument, or set of associated instruments, and condition the signals for transmission to the central station. The various signals will be time-multiplexed for transmission under the control of the central station. The central station will control the multiplexing of the remote stations so that the signals from all of them are interlaced. The station will condition the signals and record them on a magnetic tape that is computer-readable. The recording will be time-tagged.

III. The Results

The pyranometer output is a voltage which is calibrated in terms of langleys per minute (kW/m²) of solar flux. The data system recorded one data point per minute. When these data are plotted on a daily basis, the result is a curve of langleys per minute (kW/m²) versus time. Figures 1 through 5 show samples of these daily graphs which cover

the range of weather conditions experienced at Goldstone since the start of this project. Figure 1 is a clear day. Figure 2 shows some noon haze in an otherwise clear day. Figure 3 is the graph of a day with clouds in the afternoon. Figure 4 shows a day with fast moving clouds, and Fig. 5 is the graph of a heavily clouded day. It must be noted that the peaks in Figs. 4 and 5 are higher than would be expected from a clear day. This is due to reflection off large white clouds not in the direct sun-line.

Computer integration of the area under these curves yields the total energy received for the day. The units are kW/m², sometimes quoted as langleys, where 1 langley = 1.1630×10^{-2} kWh/m².

Table 1 is a listing of the pyranometer data by day number and date for the period June 19 through September 30, 1974. The table lists peak energy for the day in kW/m² and total received energy for the day in kWh/m². These two columns list measured data only, and only those days have been included when data were recorded continuously throughout the sunrise-to-sunset period. The next column lists total energy for the day in kW/m² as determined by a theoretical clear day model. This model is the JPL theoretical clear day model for Goldstone based on the ASHRAE formula (Ref. 1). The next column in the table lists the dimensionless ratio of measured total daily radiation to total daily radiation by the clear day model.

One of the first objectives of this project is to determine a clear day model of solar insolation at Goldstone from which a probabilistic model of cloudy day insolation can be built. On those days with light or moderate clouds the graph of langleys per minute (kW/m²) versus time was curve-fitted to remove the effects of the clouds and thus simulate a clear day. This was possible on a number of days when the langleys per minute (kW/m²) curve could be filled in with reasonable certainty. The curve with cloud effects removed was integrated to yield a corrected clear day total energy. The last column in the table lists these data.

Figure 6 is a plot of the daily measured peak energy as a function of time for the period June 19 through September 30, 1974. Figure 7 is a plot of daily total energy together with a curve of the JPL clear day model for Goldstone. Figure 8 shows daily total energy for all clear days, both real and corrected, for the period June 19 to September 30 above. The standard deviation of these data from the clear day model is 0.316 kWh/m² or about 4%. Some data points, however, are above the model and

this is under investigation. Figure 9 is a graph of the ratio of measured data to clear day model. The data are total daily energies and the horizontal line indicates measured data equal to the clear day model.

Figures 10 through 13 show certain meteorological parameters measured at DSS 14 for the same period as the solar figures. Ambient temperature and daily maximums, minimums, and means are plotted in Figs. 10 and 11; Fig. 12 is barometric pressure. Figure 13 shows absolute humidity in terms of grams of equivalent water per cubic meter of air calculated from measured dew point and ambient temperature.

IV. Conclusion

Preliminary data have been obtained and reduced. The results demonstrate the clear requirement for more data and more consistent data acquisition. Other measuring instruments will be added when they are built or procured and more efficient data analysis techniques will be investigated and implemented.

Reference

1. *ASHRAE Handbook of Fundamentals*, American Society of Heating, Refrigerating and Air-Conditioning Engineers (ASHRAE), Inc., New York, 1972.

Table 1. Solar insolation data, specular and diffuse, for Goldstone for the period June 19 through September 30, 1974

Day number	Date	Peak, kW/m²	Measured total energy, kWh/m²	Clear day model, kWh/m²	Ratio data/model	Clear and corrected total energy, kWh/m²
171	Jun 20	0.973	8.300	9.176	0.905	8.392
172	Jun 21	1.004	8.503	9.173	0.927	8.605
173	Jun 22	1.000	8.454	9.171	0.922	8.536
174	Jun 23	0.999	8.464	9.169	0.923	8.554
175	Jun 24	0.991	8.182	9.166	0.893	8.278
176	Jun 25	0.969	8.232	9.162	0.898	8.302
177	Jun 26	1.008	8.551	9.157	0.934	8.638
178	Jun 27	1.027	8.824	9.151	0.964	8.906
179	Jun 28	1.026	8.738	9.145	0.955	8.822
180	Jun 29	0.995	8.471	9.138	0.927	8.540
181	Jun 30	0.988	8.373	9.131	0.917	8.373
196	Jul 15	1.157	6.349	8.932	0.711	
197	Jul 16	0.985	8.172	8.913	0.917	8.172
199	Jul 18	1.017	8.260	8.873	0.931	8.495
200	Jul 19	1.098	4.140	8.853	0.468	
201	Jul 20	1.060	7.669	8.831	0.868	
202	Jul 21	0.968	7.994	8.809	0.907	8.163
203	Jul 22	1.046	7.137	8.790	0.812	
204	Jul 23	1.173	6.501	8.770	0.741	
212	Aug 1	0.932	6.823	8.587	0.795	7.994
213	Aug 2	1.034	4.966	8.561	0.580	
225	Aug 13	0.991	7.895	8.197	0.963	8.013
226	Aug 14	0.972	7.861	8.162	0.963	7.929
227	Aug 15	1.007	8.140	8.127	1.002	8.181
228	Aug 16	1.018	8.200	8.091	1.013	8.262
229	Aug 17	1.020	8.183	8.055	1.016	8.219
230	Aug 18	1.069	7.848	8.018	0.979	
231	Aug 19	0.997	7.942	7.981	0.995	8.059
232	Aug 20	1.008	7.707	7.924	0.973	8.083
233	Aug 21	1.005	7.981	7.904	1.010	7.981
234	Aug 22	1.000	7.914	7.870	1.006	7.914
235	Aug 23	1.015	7.991	7.836	1.020	7.991
236	Aug 24	0.992	7.808	7.802	1.001	7.808
239	Aug 27	1.014	7.976	7.694	1.037	7.993
240	Aug 28	0.975	7.363	7.657	0.962	7.520
241	Aug 29	0.946	7.357	7.619	0.966	7.502
242	Aug 30	1.028	7.623	7.581	1.006	
247	Sept 4	0.923	6.510	7.377	0.882	
248	Sept 5	0.927	6.921	7.336	0.943	7.141
249	Sept 6	0.873	6.618	7.294	0.907	6.639
250	Sept 7	0.873	6.513	7.251	0.898	6.545
251	Sept 8	0.849	6.441	7.209	0.893	6.494
252	Sept 9	0.858	6.510	7.165	0.909	6.517
253	Sept 10	0.859	6.553	7.122	0.920	6.565
254	Sept 11	0.855	6.444	7.077	0.911	6.444
256	Sept 13	0.851	6.433	6.988	0.921	6.448
257	Sept 14	0.861	6.502	6.942	0.937	6.520
258	Sept 15	0.858	6.509	6.896	0.944	6.541
259	Sept 16	0.858	6.447	6.850	0.941	6.468

Table 1 (contd)

| Day number	Date	Peak, kW/m²	Measured total energy, kWh/m²	Clear day model, kWh/m²	Ratio data/model	Clear and corrected total energy, kWh/m²
260	Sept 17	0.855	6.421	6.803	0.944	6.436
261	Sept 18	0.853	5.752	6.756	0.851	
264	Sept 21	0.822	6.094	6.613	0.922	6.117
265	Sept 22	0.822	6.066	6.565	0.924	6.066
271	Sept 28	0.860	6.173	6.276	0.984	6.204
272	Sept 29	0.849	6.029	6.227	0.968	
273	Sept 30	0.863	5.873	6.178	0.951	6.360
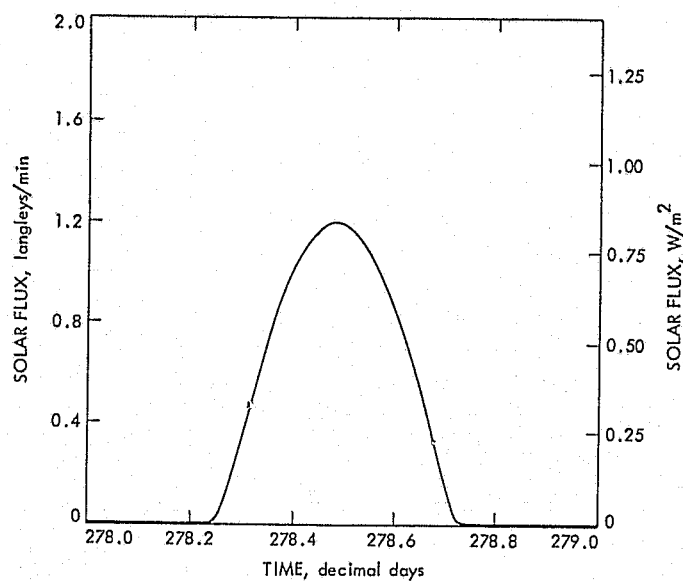
Fig. 1. Plot of pyranometer output versus time for day number 278, October 5, 1974

Fig. 2. Plot of pyranometer output versus time for day number 240, August 28, 1974
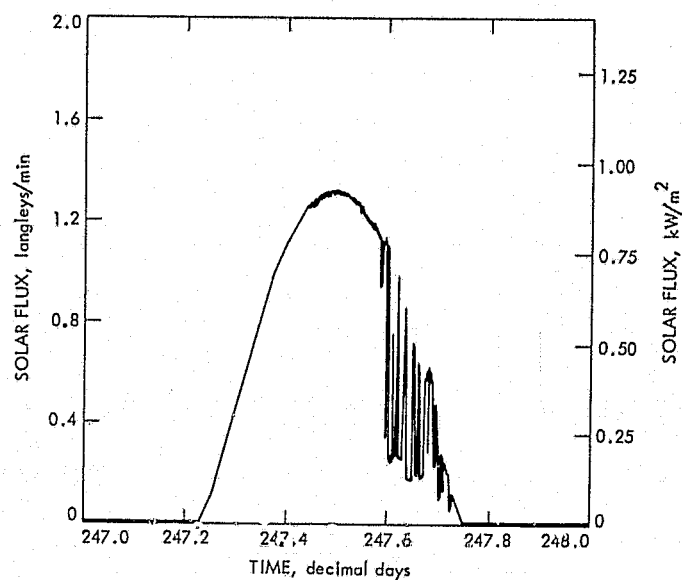

Fig. 3. Plot of pyranometer output versus time for day number 247, September 4, 1974
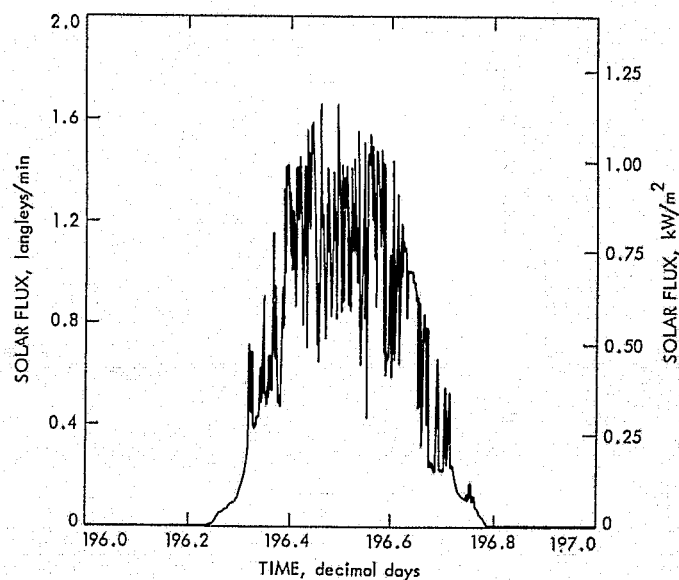
Fig. 4. Plot of pyranometer output versus time for day number 196, July 15, 1974
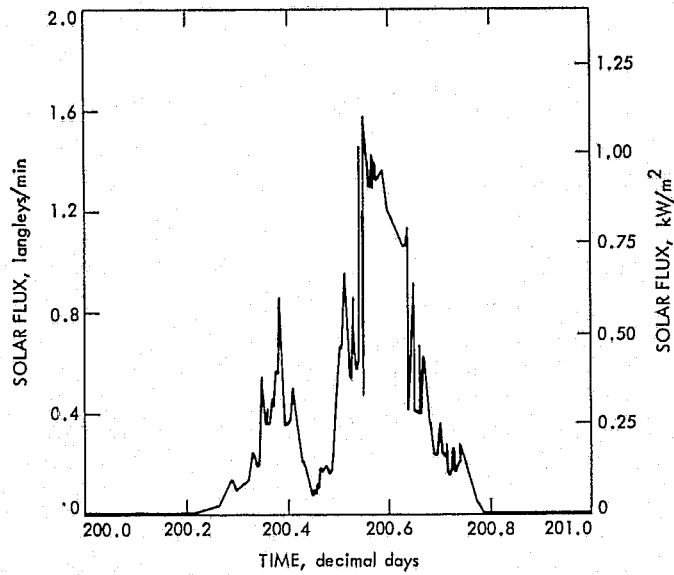
Fig. 5. Plot of pyranometer output versus time for day number 200, July 19, 1974
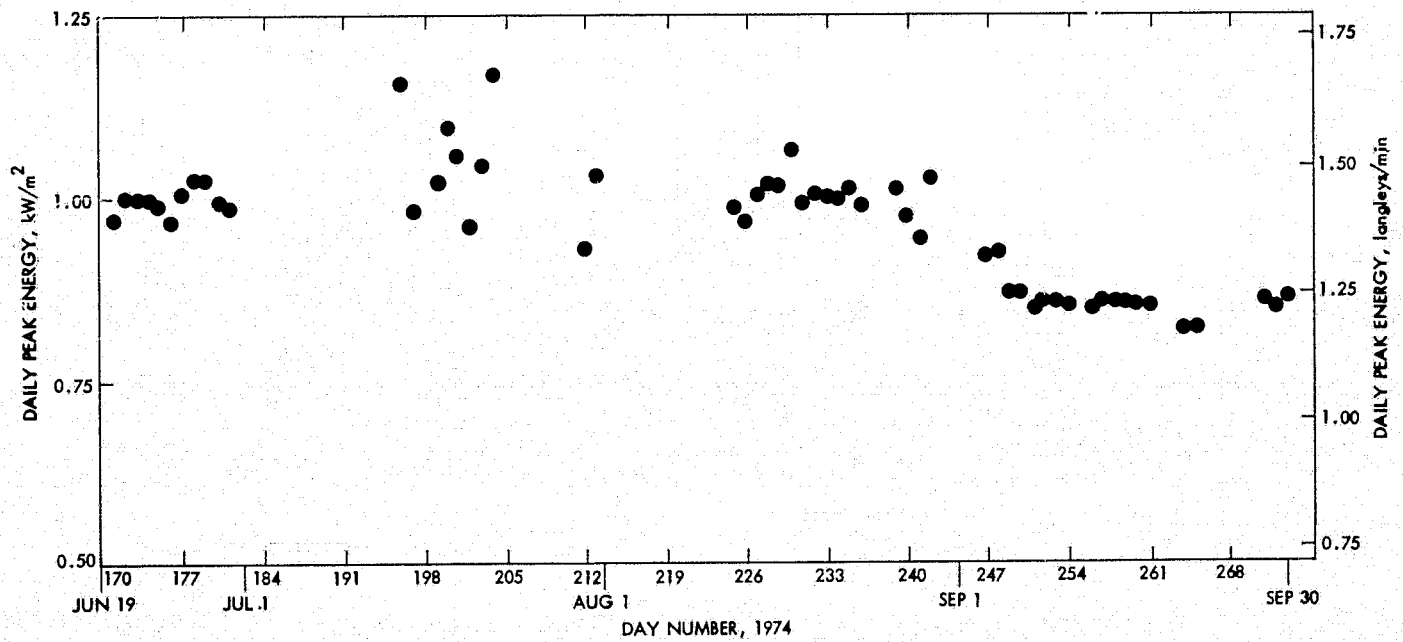
Fig. 6. Daily Peak Solar Insolation for Goldstone for the Period June 19 through September 30, 1974
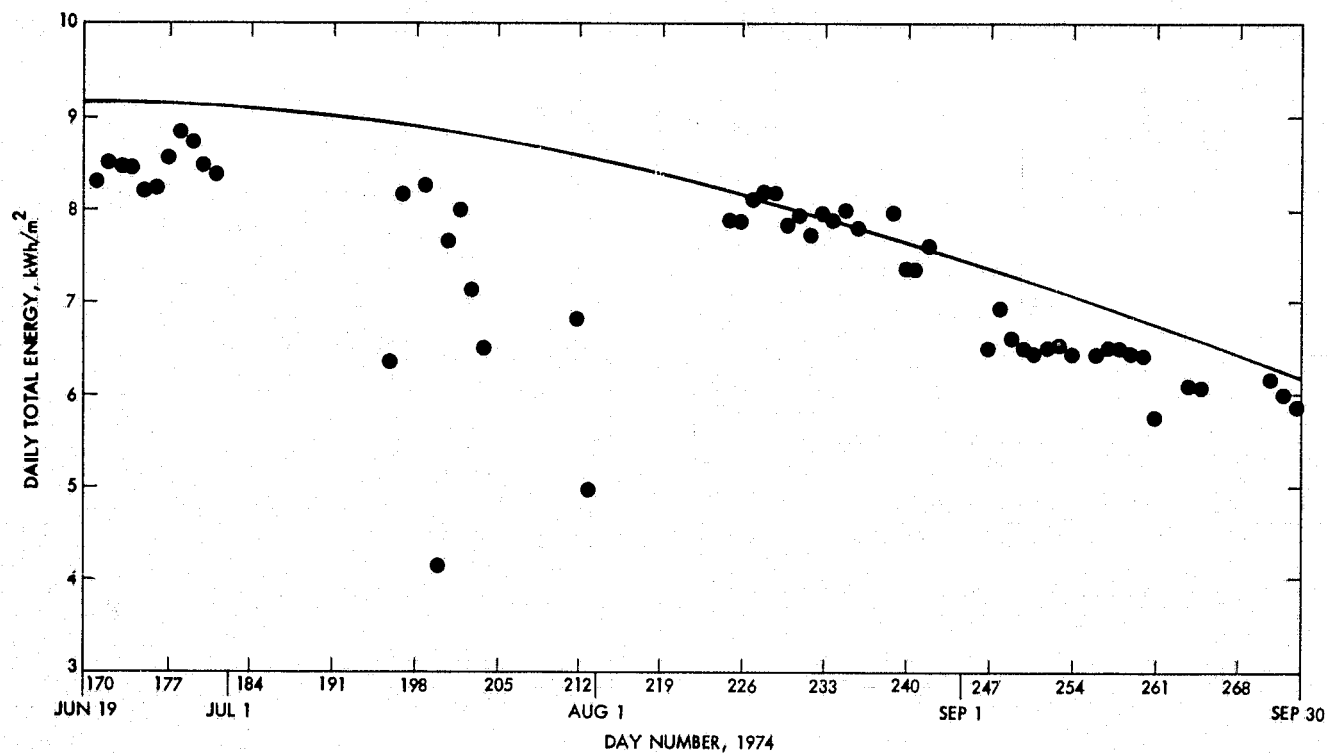
Fig. 7. Daily total energy as a function of time for the period June 19 through September 30, 1974
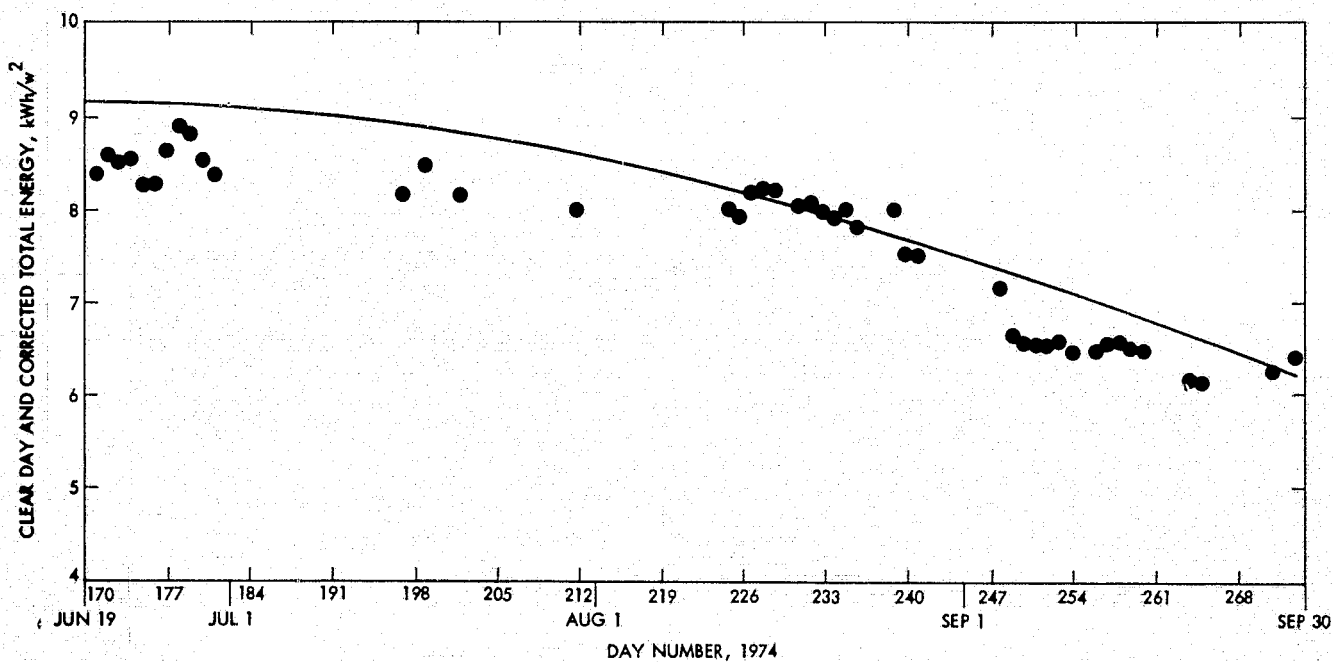
Fig. 8. Clear day total energy, actual and corrected, for the period June 19 through September 30, 1974
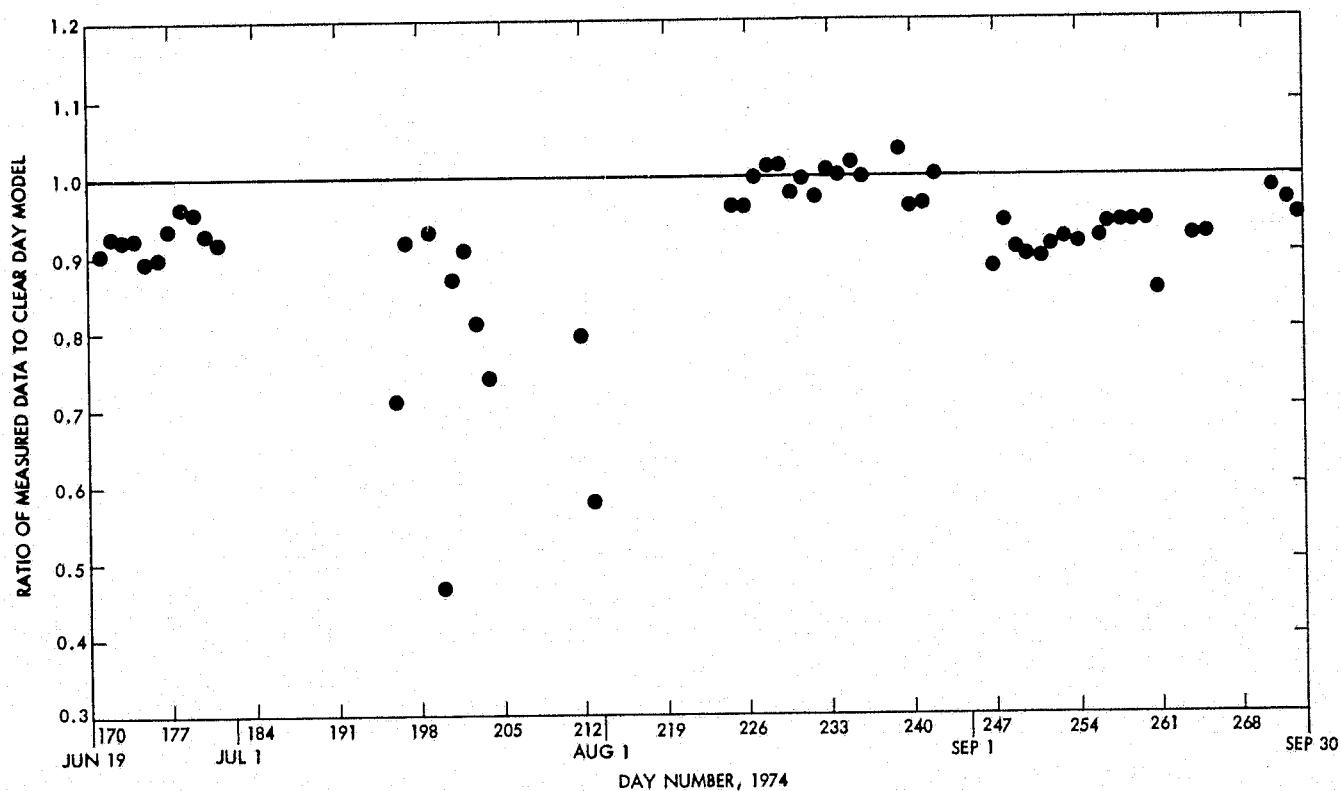
Fig. 9. Ratios of measured data to clear day model, for the period June 19 through September 30, 1974
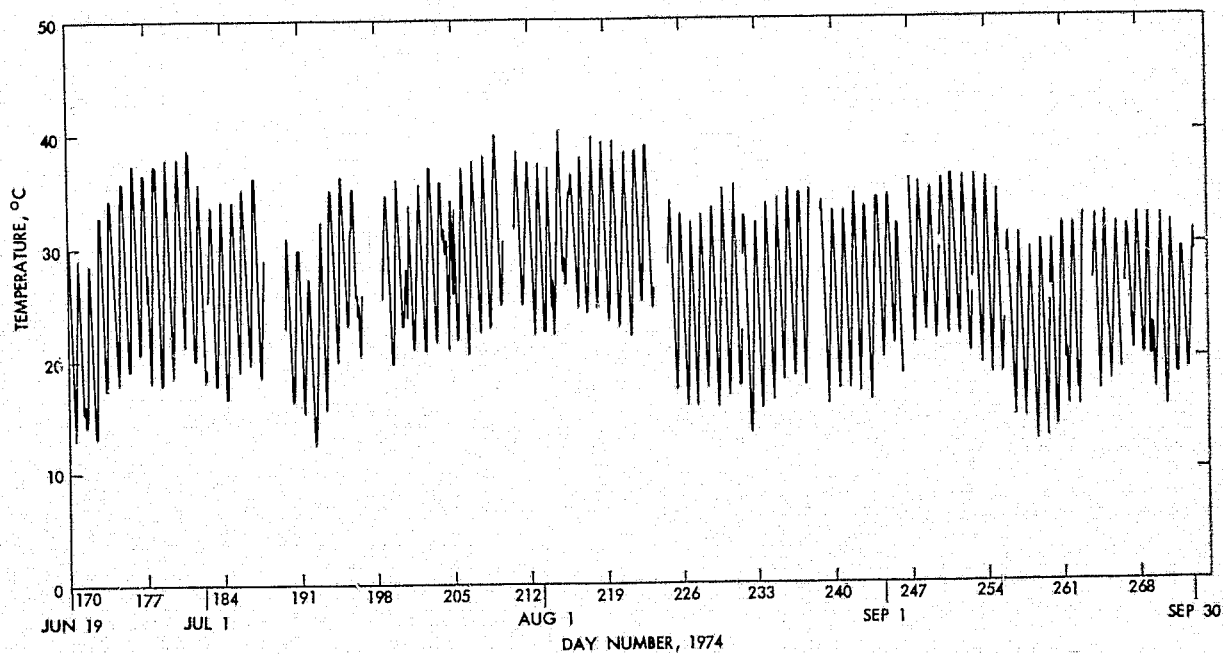
Fig. 10. Ambient temperature at Goldstone, DSS 14, for the period June 19 through September 30, 1974

Fig. 11. Daily maximum, minimum, and mean temperatures for Goldstone for the period
June 19 through September 30, 1974
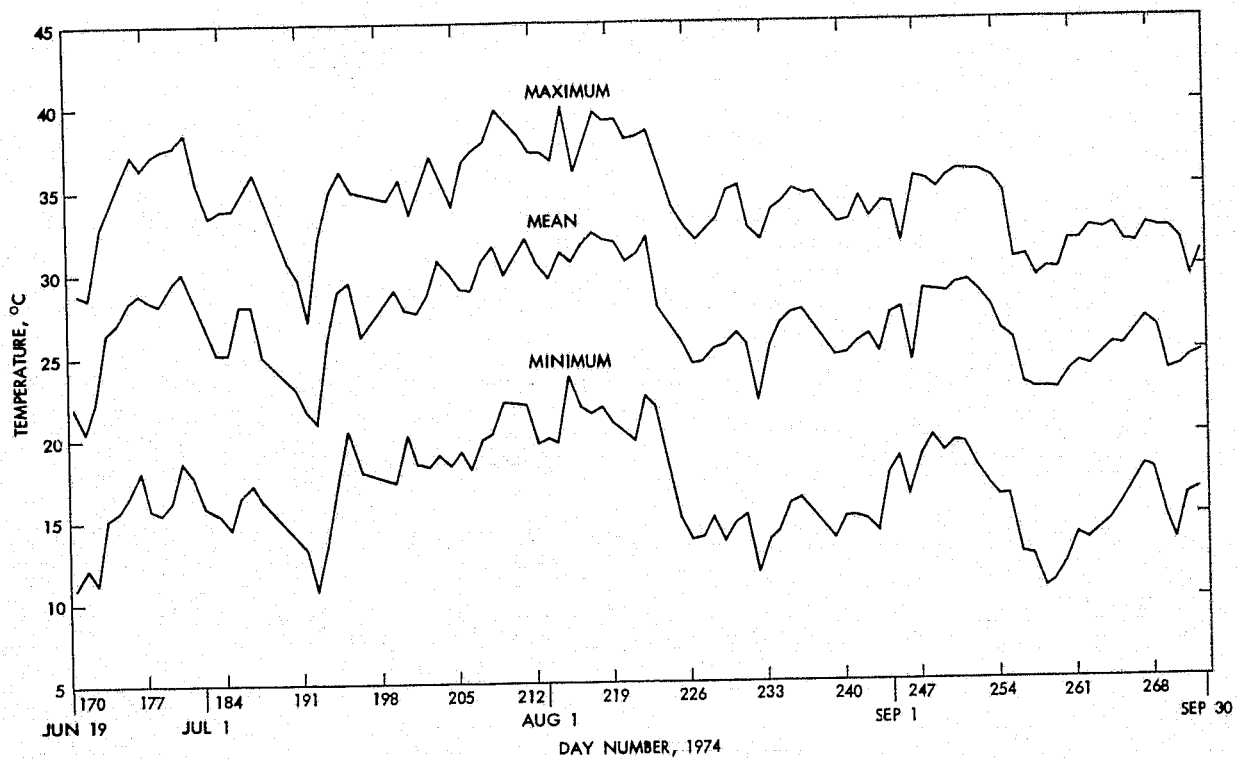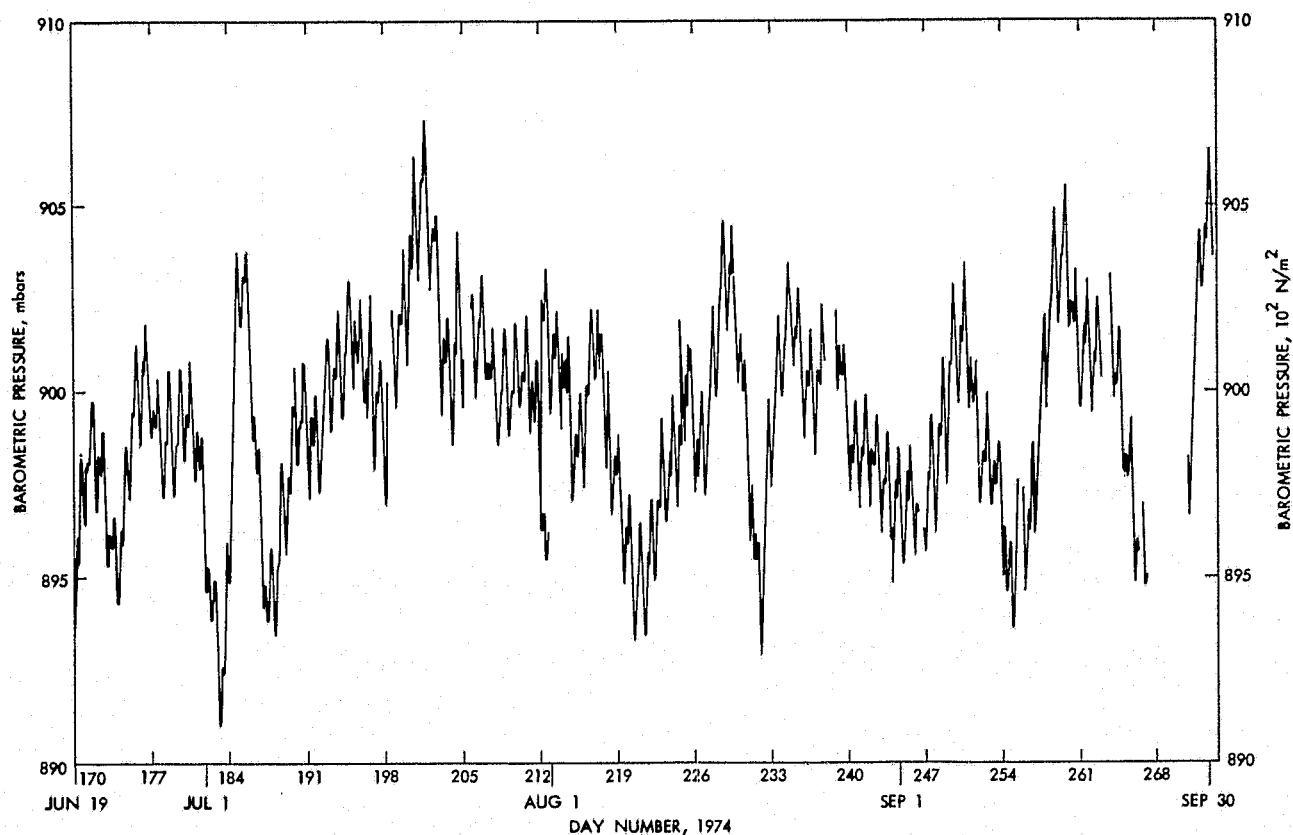
Fig. 12. Goldstone barometric pressure for the period June 19 through September 30, 1974
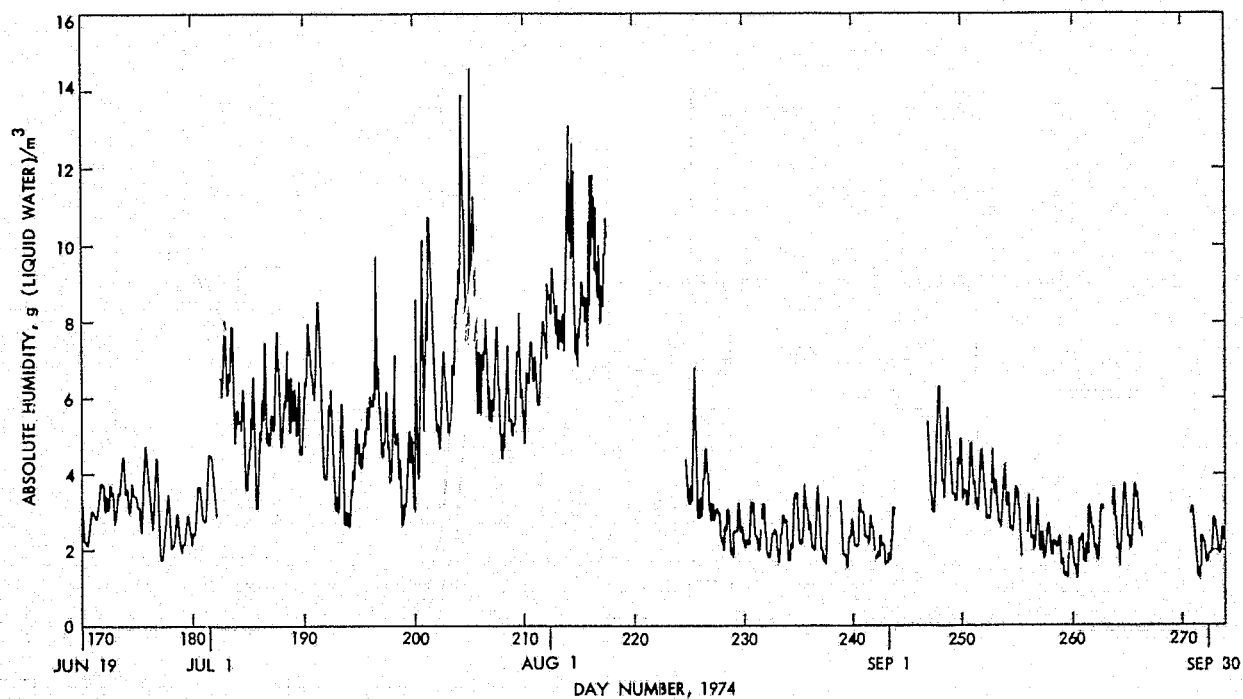
Fig. 13. Absolute humidity at Goldstone, DSS 14, for the period June 19 through September 30, 1974

Software for Multicomputer Communications

J. W. Layland
Communications Systems Research Section

This article contains a brief discussion of the alternatives which exist for software support of intercomputer communications in a multiple minicomputer network, and a detailed description of a software package which implements a relatively flexible option on the Xerox 910/920/930 and Sigma computers. The material should be applicable to the intercomputer communication needs of the tracking stations as the number of subsystem control minicomputers within these stations increases in the near future.

I. Introduction

The tracking stations of the Deep Space Network currently use a few computers for handling telemetry and command data streams, for control of the large antenna, and for monitoring various performance measures of the station. It is expected that computerized control and monitoring of station functions will greatly increase in the near future in order to generally improve maintainability, and to increase the fraction of time that the station is available for spacecraft tracking. Given current trends, this increased computerization will likely be accomplished through a number of small computers, each of which is interfaced to some specific subset of the tracking station equipment. Each of these subsystem computers would be interfaced in some fashion with the other computers in order to enhance the coordinated operation of the station, and to enable the pooling of certain resources, such as

computer unit-record peripherals. Multiple minicomputer networks have been used successfully in industry in a variety of process control and monitoring applications. A similar multiple minicomputer network is under development as the DSN Network Control System (NCS), wherein each of the minicomputers performs a dedicated monitor/control function for the network operation as a whole. In the NCS, the separation between functional entities effects a well-defined physical interface between software development teams for each of the functions. This separation has been viewed as a means to increasing software reliability and easing some of the problems inherent in developing large multi-function systems. The communication paths which exist between the minicomputers must support the interface between the various functions of the system, hence the organization of these paths, and the associated features, represents a significant item in the overall system design.

A previous article (Ref. 1) described one approach to the capabilities and features of an intercomputer communication structure usable in these applications, and a second article (Ref. 2) is a detailed description of our "twin-coax" intercomputer communications hardware and interfaces. Within this framework, a large amount of flexibility still exists for communication modes to be supported by the software, and the overall system organization. Section II of this article contains a brief discussion of the alternatives which exist in software support of intercomputer communications; succeeding sections contain a detailed description of the software which implements one of the more complex and flexible options on our Xerox 910/930 and Sigma computers.

II. Features and Capabilities

The communications paths which are established between computers in a multicomputer structure have one primary reason for their existence: to provide distributed access to resources and/or data which are maintained as a private or localized resource for reasons of economy, reliability, or policy. In a tracking station, examples of such resources could include the current-exact antenna position, the most recent estimate of the telemetry downlink signal-to-noise ratio, the floating-point arithmetic capability needed to evaluate predict polynomials, data-storage devices, and computer input/output devices. One of the more important considerations in defining capabilities is that the overall system must be robust and tolerant of both data errors in messages and failures inside any one of the subsystems. A straightforward system organization, and one which can be the most resistant to propagation of errors is a simple hierarchy: Each subsystem minicomputer "owns" a small segment of the overall system, and performs all control, monitoring, and data handling functions associated with that segment of the system. Groups of the subsystem minicomputers are in turn owned by a supervision-type minicomputer, and so on. Capabilities which are needed by a subsystem are mostly contained within the subsystem minicomputer, and those capabilities not contained are provided by a higher level of the hierarchy. Physical communication paths exist only along vertical lines of the hierarchy. The simplicity of such an organization limits the propagation of failures through the system, makes it relatively easy to intelligently allocate resources, and restricts the growth of complexity in the software developed to support the intercomputer communications paths.

This simplicity also restricts flexibility for changes and for recovery from certain types of computer failures. The greatest flexibility would be obtained by providing a universal communication bus which allowed any computer to communicate with any other computer and/or any item of system hardware. Such flexibility enables "instant" failure recovery but also enables extensive error propagation through the system. It also appears that it would be quite difficult to build. Our overall approach (Ref. 1) utilizes a functional equivalent of the universal bus between computers, but retains "ownership" of subsystem hardware by the subsystem control computer. Logical communication paths would be established on this bus for current operations, and revised as needed for mission changes. Intercomputer communications software could be organized into a simple hierarchy using this bus, or the software could be made transparent to the bus organization, retaining its flexibility and complexity for the "applications-level" software. In the software package to be described later, the logical communication paths are not "built in" the software, but are established dynamically during program execution.

During initialization and system start-up, these communication paths would carry programs and operating data bases from a pooled storage facility to each of the subsystem control computers, and, in response to a failure in any part, additional diagnostic programs could be transferred from the same facility to the one affected unit or units. Activation and deactivation of various program parts in each subsystem would also occur in response to messages transmitted on these communication paths.

During normal operation, data describing the current status of parts of the system would be transferred from the subsystems which measured or computed those data to other subsystems which need them. Assuming a hierarchically organized system, such communication would only occur along the lines of authority within the system.

During software and system development, yet a third mode of operation occurs, where a subsystem control computer has some, but not all, of the resources needed for software development. The software loaded into the subsystem computer from the central repository is in this case the assembler/compiler for that machine's language. When this program is activated, the computer communications paths provide it access to three or more distinct and independent devices which exist as peripherals to one or more of the other computers, or which are emulated through software or data storage devices on other computers. This is closely analogous to a "remote batch" operation, except that here the computing element is local to the subsystem engineer's interest, and the unit-record peripherals are remote.

An intercomputer communications driver package has been developed which appears in principle to be capable of performing in any of these operational modes. Complete error control logic is included for data errors and errors in addressing of messages. Some features are provided, such as data type identification, and multiple logical paths between any computers, for which as yet only a hypothesized need exists—in the belief that such features were easier to include in the initial package, and then remove if not needed, than they would be to add at a later date.

III. Link-Network Software Package

The communications software package consists of a collection of interrelated subroutines which provide the direct interface between a subsystem's main, or "applications-level" program, and the intercomputer communications hardware which physically connects the computers. In addition, this package provides error detection and control logic, message formatting, buffer management, and a variety of lesser services for the calling program. The computer link-network is organized conceptually as in Fig. 1, although the physical organization may differ. Each minicomputer has a unique identifying number which is used to address messages to it from any other minicomputer through the switch "X." Up to seven distinct bi-directional logical channels may exist between any pair of computers, as determined during program execution.

Table 1 lists the subroutine entry calling sequences for the two currently existing implementations of the link-network communications package. The principal entry points are those for establishing read-requests, or requests to receive data; for writing data along a path to a specified destination computer on any of the logical channels; and for checking the completion of prior requests. Entry points in the lower half of Table 1 provide for general management of the communications paths. A description of these subroutine calling sequences and their effect appears in Section V, together with a description of the tables which must appear in the calling program. The descriptions which follow in Sections IV to VI are in sufficient detail to serve as a manual for the user of the link-network package, and may be skipped by the casual reader.

IV. Message Protocol

The adopted message format is shown in Fig. 2. It is a close derivative of the formats of the IBM Multileaving protocol, with the addition of the two address bytes. The

Multileaving terminology is used to identify the other overhead bytes, where applicable.

Both address bytes are of the form[1] X'CO' + n, where n is the computer identity number, in the range from 1 to 63. They serve to uniquely identify a communication path from computer "SRC" to computer "DST." The reverse path is denoted by a reversal of the address codes, and is always activated simultaneous with the forward path. The Block Control Byte (BCB) is of the form X'CO' + m, where m is a 4-bit block sequence counter. Blocks are numbered sequentially on any SRC/DST path-pair, and are transmitted alternately in a half-duplex fashion. Along any path-pair, the lower computer identity number designates the "master," which receives only even-numbered blocks, and sends only odd-numbered blocks. An alternate BCB form of X'FO' is used to initialize the communication path, and a BCB of X'FF' is used to terminate. Either end of a path-pair may initiate communication, but both must send and receive the initialize BCB before data communication can begin.

The Record Control Byte (RCB) and Functional Control Sequence (FCS) bytes serve to divide each path-pair into seven logically independent duplex channels. The RCB also identifies the type of message block. Each bit of the FCS signifies, when set to 1, that data may be transmitted on the corresponding logical channel. It is reset to 0 when the requested data have been received, and set to 1 when data are again requested. For example, an FCS value of X'40' signifies a data request on channel 1, and an FCS of X'31' signifies data requests on channels 2, 3, and 7. The FCS value of X'80' is used in terminating. The format of the RCB is shown in Fig. 3. The least-significant three bits of the byte identify the logical channel to which this message belongs. A type code of B'10' indicates that the message block contains data, and that the String Control Byte (SCB) contains the total byte count for the block, including overhead bytes. For data blocks, $B_1 = 1$ indicates binary (non-text) mode data, $B_2 = 1$ indicates string-compressed data, and $B_3 = 1$ indicates machine-dependent data format. $B_1 = B_3 = 0$ indicates American Standard Code for Information Interchange (ASCII) text. String-compressed data are not supported by existing software, but could be implemented within user programs. A type code of B'01' or B'00' indicates that the message block is a signal or channel operation which requires user-program action. The total message package is the six overhead bytes. Bits B_1, B_2, and B_3 and the SCB specify the signal value. No specific response to the signals is

---
[1] In the following, X'yy' means hexadecimal constant yy, and B'yy' means binary constant yy.

implemented within the communications software, but conventions should be established for specific signals to implement device/file positioning operations. A feasible set appears as Table 2. A type code of B'11' indicates a null or idle message block, which may appear during initiation, termination, or to maintain synchronism when no data are available to be transmitted on channels with active requests.

Data transferred through the link are maintained error-free and in-sequence as far as possible. Any message blocks that are received in error, are truncated, are out of sequence, or have been misrouted are discarded by the receiving error control logic. Message blocks which have been transmitted in error, or for which no reply block is received within a pre-determined time period, are retransmitted.

V. User/Software Interface

This section describes the interface between a user or applications-level program for the link-network communications package, and that package. The description is based upon the 910/930 implementation of the link software. Variations in details for the Sigma 5 implementation will be described at the end of this section.

The user program contains several tables which define the structure and status of the multicomputer network. The first of these is the Link Table (LNKTAB), which is illustrated in Fig. 4. It contains one word for each computer, which is defined to the link-network package. The most significant byte of each word contains a text character, which is the software name for the associated computer. The less significant bytes contain a pointer to the Link Control Block (LCB) for the associated computer, or they may contain zero if no LCB exists. The software name characters have been assigned sequentially starting with 'A' to facilitate table operations. The current assignments appear in Fig. 4. The LNKTAB must be set up by the user programs. The user program must also provide an address word labeled "MYNAME" which contains that computer's link name in the form X'CO' + n in the second most significant byte.

The Link Control Block contains the data used by the link-network package to control the transfer of data along the associated path-pair and maintain synchronism between the attached user programs. The format of the LCB is shown in Fig. 5. The 29 words for each LCB are provided within the user program. The first word, the LCB chain word, is pointed to by the appropriate LNKTAB entry, and by the chain of the next lower LCB,

and points in turn to the next higher LCB, or contains –1. The LCB chain word is set up by the user program; the remainder of the LCB is set up by a call to IOCLEAR. All LCBs connected to LNKTAB plus lower-level routines are initialized by calling IOCLEAR with the A-register = 0. Only the specified LCB is initialized if the A-register contains a pointer word from LNKTAB when IOCLEAR is called.

The second word of the LCB defines the current state of operation along the path-pair, and will be described in some detail in Section VI. State includes the block sequence counter, read/write mode flags, initialization flags, the error-retry counter, etc. CURBLK is a pointer to the current or most recent past transmitted block, and is –1 if said block is undefined. TIMER is the clock-count cell used to recognize lost data and is negative when ticking. The fifth through ninth words contain flags which define the state of each of the seven logical channels; they are in the same format as the FCS byte of the transmitted data block. The RDFLG and HSRDFLG, in fact, contain the next FCS to be sent, and the most recent FCS received in their most significant byte. The write-stack (WRTST$) contains a queue of data blocks which have been enabled for transmission by read-requests from the incoming FCS. The channel-write-buffer pointers (CHNWB) contain addresses of the current or most recent data blocks associated with each logical channel. If transmission is not enabled (the write is blocked or is complete), the data block address will only appear in the CHNWB. The remainder of the LCB represents a shortened dummy data block which is used for initialization, termination, and idling messages on the associated path.

Data to be transmitted by the link-network package are contained in buffers with content-specifying header. Identical buffers are used to receive data. The general format of these buffers is shown in Table 3. The QCHAIN word is used to link the buffer into FIFO queues, as needed in handling. OWNER contains the software name, computer path plus channel, to which the data buffer belongs. BUFSZE is the available data space within the buffer block, in words. Oversize incoming data blocks will be truncated to this value. WCW contains the number of words from the data portion of the buffer block which should be transmitted, and is meaningful only when data in the buffer block are being prepared for transmission.

AWCW and STATW are meaningful only after data have been transferred in or out of the buffer block. AWCW contains the number of words actually transferred, and should be equal to WCW for transmission, and

less than or equal to BUFSZE for receiving. STATW contains the link hardware cumulative status at the end of I/O transfers. The remainder of the buffer block contains the data words, including overhead bytes, actually transferred on the links. A subroutine IOBUFSET is provided to carve up an arbitrarily sized storage area into preformatted buffer blocks with space for 132 data bytes. The beginning and ending addresses of the buffer storage area are specified to IOBUFSET in the A- and B-registers, respectively. Three of these buffers are immediately transferred to a low-level subroutine for incoming data. The remainder are queued in a buffer pool. Buffer blocks are placed into this pool by calls to BUFPUT, and removed from it by calls to BUFGET with the A-register containing the buffer block address. Return from BUFPUT is to the calling-address + 1. Return from BUFGET is call + 2 if successful, and call + 1 if no buffer is available. It is a user-program responsibility to avoid losing buffers and emptying the buffer pool.

Data transfer between user programs and the link-network package is handled by five subroutines, with auxiliary services handled by three others. Arguments are transferred to these subroutines in the A- and B-registers, with the A-register identifying the intended computer/channel pair by its software link name, and the B-register pointing to a buffer block, if needed. The software link names are composed of the channel number in the least-significant byte, and the text character identifying the destination computer in the next least-significant byte. Return from the subroutines is to the call-location + 2 if the requested operation is accepted, and to call + 1 if the request was invalid or rejected. With minor exception to be noted, buffer blocks are returned to the user program via pointers in the A-register. End-action for any previously completed transfers is performed on entry to these routines.

IOSTART requests the start of operation of the identified logical channel on the specified path. If it is the first channel on the specified path to be started, a path initialization is also performed. IOSTOP terminates operation on the identified logical channel. If this is the last active channel on the specified path, that path is terminated. IOSWAIT is a convenience routine which rejects all calls until the opposite end of the path-pair has been initialized.

IOGET establishes a read-request for the identified logical channel, which is subsequently communicated via the FCS to the opposite end of the path-pair. IOPUT

attaches the buffer block in the B-register to the identified logical channel and prepares to transmit the data contained in that block along the appropriate path. The identified channel is immediately set Busy. The transmission is blocked until a corresponding read-request has been received from the opposite end of the path-pair. IOSIGNL transfers the signal bytes in the B-register into an available buffer from the pool, and then proceeds similarly to IOPUT. Any transfer request on an already busy channel is rejected.

IOCHEKR is called to test the status and availability of the incoming half of the identified logical channel. A returned value of A = –8 occurs if the channel has not been started. The value A = 0 occurs if there is no completed incoming data transfer. If a data block has been received for the identified channel, it is returned via an A-register pointer. If a signal has been received, the A-register returns the identified channel's software-link name with the addition of the bit-flag X'08' in the most-significant byte. The signal value is returned in the B-register.

IOCHEKW is called to test the status and availability of the outgoing half of the identified logical channel. A returned value of A = –8 occurs if the channel is not busy, and no read-request has been received from the opposite end of the path-pair. The value A = 0 occurs if the channel is not busy, but an active read-request has been received. The value A = –1 occurs if the channel is busy and the transmission is not complete. If the channel is busy and the transmission is complete, the channel is set to not busy, and the current buffer-block pointer (or signal value) is returned in the A-register together with a completion flag of X'08' in the most-significant byte.

A summary of subroutine calls for the 910/930 appears in Table 1, together with a rudimentary description of its action. The primary reason for the unpleasant complexity which has appeared here is the need to maintain synchronism over the independent logical channels between user programs at the opposite ends of the path-pair.

The principal difference between the link-network software package described above for the 910/930 and the corresponding package for the Sigma 5 is that the latter is embedded within a semi-permanent operating system, whereas the former is a part of the transient user program. In the Sigma 5, each defined path-pair is

considered as a re-usable resource which may be transiently owned by a user program.

The link software is accessed via the system-call instructions CAL3,12 N from either a background program or a terminal-user program. The LNKTAB and the defined LCBs are a part of the resident monitor, as are a minimal set of buffer blocks through which the actual I/O is done. Data are exchanged between the monitor buffers and corresponding user-space buffers via the IO calls. Table 1 also lists the link package calls for the Sigma 5. Two new routines have been added to manage the "ownership" of the link paths, and several routines which were accessible in the 910/930 have been subverted to these routines, or to monitor initialization. ATTACH establishes ownership of a specified path, if it is not already owned by another active job, and RELEASE frees the specified path from ownership by the current job. All owned paths are released at the end of any job step. Arguments are transferred via Register 8, corresponding to the 910 A-register, and Register 9, corresponding to the 910 B-register. Requests for operation on a path which has been terminated cause the job to be aborted. All calls, arguments, and actions are basically the same as in the 910/930 version. The principal change to be noted is that Register 9 must contain a buffer-block address within the users' area when IOCHEKR is called, to provide a place for the received data to be transferred from the monitor's buffer block.

VI. Software Internal Structure

The link-network software package has been designed to provide an elastic interface between the user-level programs which communicate through it, and the time-and-event-driven realities of the physical link communication signals. Three distinct levels of operation exist within this software. Each level consists of a collection of complete non-interrupted processes. The interface between the asynchronous processes at adjacent levels is effected via a limited set of queues and flags. Each single process was implemented using a "Structured Programming" approach (Ref. 3) to increase the understandability during design, and during possible later modifications. The interface between asynchronous processes was specified using finite state machine representations for the cause and effect relationships which had to be defined (Ref. 4). Structured programming was avoided for multiple asynchronous processes because the structuring introduces more irrelevant complexity than it removes. Requests for services by a lower level are best regarded as primitive within the upper level. The actual performance of those services proceeds in parallel with operations on the upper level, and only the events of request and completion are relevant to the progress of the upper level.

A change-of-state of the bi-level interfaces actually occurs when the lower-level process has acted upon a service request from the higher level. The top-most software level was described in terms of its calling or user interface in Section V. These calls serve to transfer the care of a data buffer between the calling user process and the queues which interface to the single intermediate-level process. One such process exists for each path-pair, and its total state is contained within the Link Control Block. The format of the state word is shown in Fig. 6. The contents of this word are altered when a block has been sent or received over the path-pair. The block number contains the block-sequence number associated with the current transmit block. The LCB is in "write mode" if a block is actively being transmitted; it is in "read mode" if a block is to be transmitted to it; or it may be in "no-mode" if there is no data to send, an idle message has just been sent, and an idle message has just been received from the opposite end. The bad-block number and associated flag are used to facilitate recovery, if possible, if a totally out-of-sequence block is received. The transmission-retry counter allows seven repeated attempts to transmit over a given path before it is declared inoperative. The path may also be declared inoperative through a terminate operation, or on receipt of a terminate message. The full-initialize bit must be set before data transfer can occur, and can only be set after initialize messages have been both received and sent on the path. It is reset when the path is declared inoperative.

The intermediate-level process functions as an end-action or "CLEANUP" operation for any messages which have been transferred over the communication paths. It interacts with the user-level interface routines via the data placed in the LCB. It requests services from the next lower-level process via calls to interface subroutines L9READ and L9WRITE, and obtains completely transferred blocks from the queues by calls to L9GET. The A-register (Register 8 for Sigma 5) for these calls contains a pointer to a data buffer block of the format described in Section V. If the link hardware is not active after the buffer in the read/write calls has been properly queued, it is activated by the software. Transfer of the data is then under control of signals from the link hardware. Whenever link hardware activity terminates with completion of data transmission for a given block, the hardware is reactivated for any block then contained in the queues of the lowest-level software process. It should be noted that the hardware can override the direction of an activation kick from the software whenever the opposite end of the path is simultaneously activating.

VII. Status and Plans

The software described herein is currently operable on three computers: the Sigma 5, Xerox 910 and 930. This small network is centered by the Sigma, which has an expandable four-way multiplexer allowing it to selectively communicate with up to four other computers. Only two machines are currently defined to the Sigma operating system, and only the 910 and 930 are currently connected. The 910 computer is interfaced via the GCF TTY lines to Goldstone, and it and the Sigma will be used with the software described here to monitor and control an automated pulsar track at the Venus Tracking Station. These two computers were previously used with a simpler intercomputer communications structure in the monitoring of Spacecraft Ranging Operations with Mariner 1971 (Ref. 5).

Several additions to this link-network structure are planned for the near future. In the software area three things will be done: the designed support for ASCII as a common-denominator text-data type will be implemented within the Sigma system and made available as part of the 910/930 package. The CLEANUP process within the Sigma 5 will be integrated with the job scheduler of the Sigma operating system so that Sigma jobs can be initiated from the opposite end of the link. Store-and-Forward logic will be added to the Sigma CLEANUP process to allow communication between the other machines without requiring an active job within the Sigma. It is also expected that the link-network software package will be translated to execute on other computer types, principally the DEC PDP-11, and the MODCOMP-II. Hardware interfaces to the twin-coax intercomputer communication links and the L9READ/WRITE level of software already exists for the PDP-11 (Ref. 2). Hardware twin-coax link interfaces for the MODCOMP-II will be implemented using the JPL-DSN 14-line interface (Ref. 6).

The entire software package occupies 1300 words on the 910/930, and slightly more on the Sigma 5 because of the complexity of the monitor interface. The required tables and buffer blocks are not included in this figure. Slightly over 1000 of the instructions are associated with the link-network structure and are independent of the physical intercomputer communications hardware. The remaining instructions represent the lowest-level hardware-driven process, and as such is tied to the use of the twin-coax links. The link-network software package is unpleasantly large, much larger than expected when initially defined in function, and as a result, a desideratum under consideration is the shrinking of this software package by limiting communication to one logical channel and one computer path for some application in the 910.

References

1 Layland, J. W., and Lushbaugh, W., "A Multicomputer Communications System," in *The Deep Space Network Progress Report*, Technical Report 32-1526, Vol. XII, pp. 195–199, Jet Propulsion Laboratory, Pasadena, Calif., Dec. 15, 1972.

2. Lushbaugh, W. A., "A Driver/Receiver Unit for an Intercomputer Communications Link," in *The Deep Space Network Progress Report*, Technical Report 32-1526, Vol. XV, pp. 109–115, Jet Propulsion Laboratory, Pasadena, Calif., June 15, 1973.

3. Dijkstra, E. W., "Structured Programming," in *Software Engineering Techniques*, pp. 83–93, NATO Science Committee, 1969.

4. Holt, A. W., et al., *Data Structure Theory and Techniques*, pp. 16–62, Final Report to Rome Air Development Center, Contract AF30(602)-4211, Task 459403, Applied Data Research, Inc., Princeton, N. J., 1969.

5. Erickson, D. E., and Layland, J. W., "An Experiment in Remote Monitoring of Mu-Ranging Operation at Mariner Mars 1971 Superior Conjunction," in *The Deep Space Network Progress Report*, Technical Report 32-1526, Vol. XV, pp. 156–166 Jet Propulsion Laboratory, Pasadena, Calif., June 15, 1973.

6. *Detail Specifications for Deep Space Network Control System, Standard Interface*, JPL Specification ES508534, 1974 (JPL internal document).

Table 1. Summary of subroutine calls

Name	Sigma CAL3,12	Arguments		Skip[a] return?	Response
		A-register (R8)	B-register (R9)		
IOGET	6	PATH/CHANNEL	—	Y	Establishes read-request
IOPUT	10	PATH/CHANNEL	BUFFER POINTER	Y	Queues buffer for writing
IOSIGNL	11	PATH/CHANNEL	SIGNAL	Y	Queues signal for writing
IOCHEKR	8	PATH/CHANNEL	BUFFER POINTER[b]	Y	A = −8, not available
					A = 0, available
					A > 0, buffer complete: B = signal value
IOCHEKW	12	PATH/CHANNEL	—	Y	A = −8, not available
					A = −1, busy
					A = 0, available
					A > 0, A = buffer pointer
IOSTART	4	PATH/CHANNEL	—	Y	Open specified channel
IOSTOP	5	PATH/CHANNEL	—	Y	Close specified channel
IOBUFSET	N/A	START	END OF SPACE	N	Initialize buffer space
IOCLEAR	N/A	0	—	N	Full initialization of all LCBs and system
		LCB-POINTER		Y	Clear specified LCB
BUFGET	N/A	—	—		A = system buffer pointer
BUFPUT	N/A	BUFFER POINTER	—	N	Returns buffer to pool
ATTACH[b]	0	PATH/CHN = 1	—	—	Claims job ownership of path
RELEASE[b]	1	PATH/CHN = 1	—	—	Releases job ownership of path

[a]910/930 only.
[b]Sigma 5 only.

Table 2. Feasible signal conventions

Operation	T	B_1	B_2	B_3	Channel	SCB
OPEN	01	0	0	0	#	I.D. Byte
CLOSE°	01	0	0	1	#	0000 0001
END FILE°	01	0	0	1	#	0000 0010
REWIND°	01	0	0	1	#	0000 0100
undefined°	01	0	0	1	#	xxxx x000
POSITION	01	0	1	0	#	I.D. Byte
SKIP	01	1	F	R	#	Number
unassigned	00	X	X	X	#	Any

° Starred operations may merge
F Indicates *File* operation if 1, record if 0
R Indicates *Reverse* direction if 1, forward if 0

Table 3. Buffer block format

Label	Contents
QCHAIN	Block Chaining Link
OWNER	Channel/Path ID
BUFSZE	Size of buffer, words (44)
WCW	Number of words to send
AWCW	Number of words sent/received
STATW	Hardware status at termination
DWD1	Data
•	to
•	send/receive
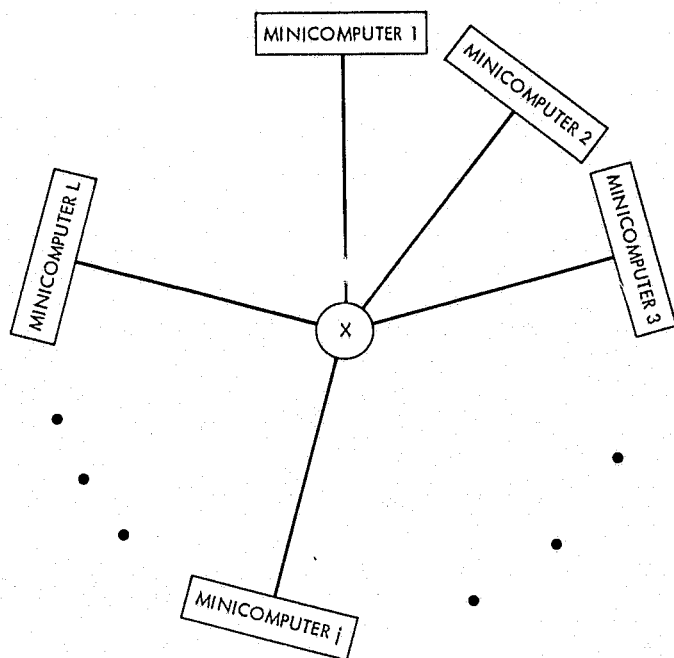
Fig. 1. Link network structure
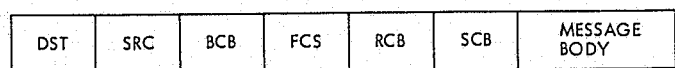
BODY MAY BE NULL

DST = DESTINATION ADDRESS
SRC = SOURCE ADDRESS
BCB = BLOCK CONTROL BYTE (BLOCK SEQUENCE NUMBER)
FCS = FUNCTION CONTROL SEQUENCE (READ FLAGS)
RCB = RECORD CONTROL BYTE (MESSAGE CONTENT IDENTIFIER)
SCB = STRING CONTROL BYTE (MESSAGE BYTE COUNT, OR "SIGNAL")
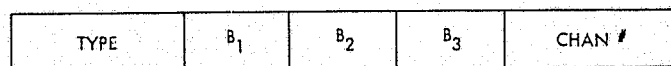
Fig. 2. Message format

Fig. 3. RCB format

Fig. 4. Link Table structure for four machines
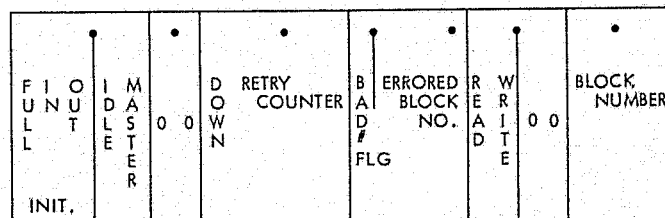

Fig. 5. LCB format

Fig. 6. LCB state word format

Confidence Bounds on Failure Probability Estimates

O. Adeyemi
Communications Systems Research Section

One common way of estimating the failure probability p of a system is to simulate the system until a fixed number, say r, failures are observed and then set $p = r/N$, where N is the number of trials required. In this paper this technique is analyzed, and, in particular, the relationship between r and the reliability of the estimator p is studied.

I. Introduction

It is often necessary to analyze the behavior of a complex system by simulation rather than by direct analysis. That is, we make a probabilistic model for the system inputs and drive the system with pseudo-random inputs generated according to the model. We then estimate various performance parameters from the result of the simulation.

Now suppose the results of the system's behavior on a particular set of inputs can be classified as either "success" or "failure." Success could be, for example, "program execution time is less than one second," "antenna converged to target in 10 seconds," or "decoder correctly recognized command," etc. In such a case we might use binomial sampling, i.e., perform a fixed number n simulations of the system, and estimate the probability p of failure by $p = k/n$, where k is the number of observed failures in n trials. But without some *a priori* knowledge of p, the number of trials n required to obtain good estimate of p will not be known. Thus a better way is to

perform trials until a desired number of failures, say r, have been observed, and then set $p = r/N$, where N is the number of trials required. It is this technique for estimating p that we shall analyze in this paper.

The sequence of successes and failures may be thought of as Bernoulli sequence in which a '0' represents a success and a '1' represents a failure. The number of successes, say X, before the r failures occur is a random variable distributed according to the negative binomial, i.e.,

$$P(X = x) = \binom{r + x - 1}{x} p^r (1 - p)^x; \qquad x = 0,1,2, \cdots \tag{1}$$

A number of methods is provided for constructing $1 - \gamma$ interval estimates for p. A *two-sided $1 - \gamma$ confidence interval* with limits p and p for p is defined as an interval (p,p) such that

$$P(p < p < p) = 1 - \gamma \tag{2}$$

The length of the interval is $L = \overline{p} - \underline{p}$. If $\underline{p} = 0$, $\overline{p}$ is called the upper $1 - \gamma$ confidence limit. The interval $(\underline{p}, \overline{p})$ is said to be the shortest $(1 - \gamma)$ interval if its length L_s is minimum among all the intervals satisfying Eq. (2). Finally a two-sided $1 - \gamma$ confidence interval $(\underline{p}, \overline{p})$ is called *symmetric* if

$$P(p < \underline{p}) = P(p > \overline{p}) = \gamma/2$$

If the number of successes before the r failures is $X = n$ and Z is the total number of trials required to obtain the r failures, then our first method gives as $1 - \gamma$ confidence limits $\underline{p}$ and $\overline{p}$ defined by

$$I_{\underline{p}}(r, n + 1) = \gamma/2$$

and $\qquad\qquad\qquad\qquad\qquad\qquad\qquad$ (3)

$$I_{\overline{p}}(r, n) = 1 - \gamma/2$$

where $I_x(A, B)$ is the Incomplete Beta Function with parameters A and B; $0 \le x \le 1$. Our computationally easier second method gives

$$\underline{p} = \frac{a}{2Z}, \quad \overline{p} = \frac{b}{2Z} \qquad\qquad (4)$$

where

$$P(\chi^2_{2r} < a) = \gamma/2 = 1 - P(\chi^2_{2r} < b),$$

χ^2_{2r} being a chi-square variate with $2r$ degrees of freedom. Limits in Eq. (4) are good for all p small enough that $-\ln(1 - p) \approx p$. In Section III we show that the shortest $1 - \gamma$ interval is $L_s = (b - a)/2Z$ where a, b are such that $h_{2r}(a) = h_{2r}(b)$, $a \ne b$, $h_{2r}(t)$ is the χ^2_{2r} density function. A table of a and b is provided for $r = 1, 2, \cdots$, 120 and $\gamma = 0.01(0.01)0.05$. This table is believed to be new.

It is important to know how good $\overline{p}$ is as an estimate of p. Suppose it is desired that $\overline{p} = r/Z$ not be more than 10% greater than p, i.e., $\overline{p} < 1.1 \times p$, where Z as in Eq. (4) is the number of trials required to obtain r failures. In Section IV it is shown in general that if $\overline{p}/p < \alpha, \alpha > 1$ is desired such that $P(p < \overline{p}) = 1 - \gamma$, then the number of failures required is bounded by

$$r \ge q \frac{\alpha^2}{(\alpha - 1)^2} \phi^2_{1-\gamma}; \quad q = 1 - p \qquad (5a)$$

where $\phi_{1-\gamma}$ is the lower $1 - \gamma$ point of the unit normal distribution. The minimum value of r that is good for all

$\overline{p}$ is thus

$$r = \frac{\alpha^2}{(\alpha - 1)^2} \phi^2_{1-\gamma} \qquad\qquad (5b)$$

The exact values of r for given α, p and γ is

$$\sum_{r}^{\lfloor \frac{r}{p\alpha} \rfloor} \binom{Z - 1}{r - 1} p^r q^{Z-r} = \gamma \qquad (6)$$

but it is not of much use because p is unknown, hence the importance of the estimate in Eq. (5b).

We shall illustrate many of our techniques with the example $p = 0.005$. This value of p is the classical maximum acceptable for the bit error probability in a deep-space television picture. For example to achieve a $\overline{p}$ which is only 10% greater than p and such that $P(p < \overline{p}) = 1 - \gamma$, $\gamma = 5\%$, by Eq. (5b) we need $r \ge 327$ whereas by Eq. (6) $r \ge 313$ would do. This shows that r estimates in Eq. (5b) are very good. For comparison a graph of r values given by Eq. (6) for $\gamma = 0.1$, $\alpha = 1.1$ (i.e., 10% error) and $0.001 \le p \le 0.05$ is plotted.

II. Methods of Construction of Confidence Limits

Method A

A usual method for constructing confidence intervals based on Eq. (1) directly is to use the maximum likelihood estimate of p, $\overline{p} = r/r + x$ (Refs. 1 and 2). If the experiment results in $X = n$ successes before r failures are obtained, then the $1 - \gamma$ symmetric confidence limits $\underline{p}$ and $\overline{p}$ for p are, respectively, the solutions to the equations

$$F_x(n, r, \overline{p}) = \sum_{x=0}^{n} \binom{r + x - 1}{x} \overline{p}^r (1 - \overline{p})^x = \gamma/2$$

and

$$\sum_{x=n}^{\infty} \binom{r + x - 1}{x} \underline{p}^r (1 - \underline{p})^x = 1 - F_x(n - 1, r, \underline{p}) = \gamma/2$$

$\qquad\qquad\qquad\qquad\qquad\qquad\qquad\qquad\qquad (7)$

It is known (see Ref. 3 for example) that the negative binomial distribution is related to the Incomplete Beta Function by

$$F_x(n, r, p) = I_p(r, n + 1); \quad 0 < r < \infty$$

where

$$I_p(m,\nu) = \frac{1}{B(m,\nu)} \int_0^p u^{m-1}(1-u)^{\nu-1}\,du$$

$$B(m,\nu) = \int_0^1 u^{m-1}(1-u)^{\nu-1}\,du \tag{8}$$

Thus p and p are such that

$$I_p(r,n+1) = \gamma/2$$

and

$$I_p(r,n) = 1 - \gamma/2 \tag{9}$$

We can read off the values p and p from the table of Incomplete Beta Functions in (Ref. 4) if r and n are fairly small, say. For larger values of r and n it is convenient to use the tables of the F-distribution and the relation

$$P(F_{v_2}^{v_1} > F_0) = I_p\left(\frac{v_2}{2}, \frac{v_1}{2}\right) \tag{10}$$

where

$$p = \frac{v_2 \cdot}{v_2 + v_1 F_0}$$

and $F_{v_2}^{v_1}$ is an F-variate with v_1, v_2 degrees of freedom. Applying Eq. (10) to Eq. (9) we see that

$$p = \frac{r}{r + (n+1)\,F_{2r}^{2(n+1)}(\gamma/2)}$$

and

$$p = \frac{F_{2n}^{2r}(\gamma/2)}{n + r\,F_{2n}^{2r}(\gamma/2)}$$

where

$$P(F_{v_2}^{v_1} > F_{v_2}^{v_1}(\gamma/2)) = \gamma/2)$$

For example, for $p = 0.005$, $r = 10$, the expected value of n is 1990. $F_{2r}^{2(n+1)}(0.025) = 2.09$, $F_{2n}^{2r}(0.025) = 1.71$ and the expected 95% symmetric confidence limits for p are

$$p = 0.0024$$

$$p = 0.0085.$$

Method B

Apart from its computational simplicity, the following construction is better suited for the range of p of interest here.

Let X_j, $j = 1, \cdots, r$ be the number of trials after the $(j-1)^{\text{st}}$ failure to the occurrence of the jth failure. Then X_j has the geometric distributions with parameter p, i.e.,

$$P(X_j \leq n_j) = 1 - (1-p)^{n_j}; \qquad n_j = 1,2,\cdots$$

The geometric distribution may be approximated by exponential distribution

$$P(X_j \leq x) = 1 - e^{-\lambda x}$$

such that $\lambda = \ln(1-p)$. With this approximation, the sequence $X_1, X_2, \cdots, X_j, \cdots, X_r$ becomes a sequence of exponentially distributed random variables with a common parameter λ. It is known that

$$Z = \sum_1^r X_j$$

is then distributed according to the Gamma distribution such that

$$W = 2\lambda Z$$

has the χ_{2r}^2 distribution with $2r$ degrees of freedom with density function given by

$$h_{2r}(x) = \frac{\lambda}{2^r \Gamma(r)} x^{r-1} e^{-x/2}; \qquad x \geq 0. \tag{11}$$

Thus a $1 - \gamma$ confidence interval for λ is given by

$$\lambda = a/2Z, \qquad \lambda = b/2Z$$

such that

$$P(a < 2\lambda Z < b) = 1 - \gamma. \tag{12}$$

a and b may be obtained from the χ_{2r}^2 table in Ref. 4. For small p we may take $p = \lambda = -\ln(1-p)$. The effect of this approximation on the confidence intervals for p is very negligible indeed.

Suppose we sample till $r = 10$ failures occur and $Z = 2000$, then we may conclude that with probability 0.95

$$p < 0.00785$$

or that with probability 0.99

$$p < 0.00939$$

Because tables of χ^2-distribution exist for high degrees of freedom this method is useful when p is small so that r is large.

By Eq. (12) it is clear that if, corresponding to a given r, it is required to have $Z_0 = X + r$ trials to achieve level $1 - \gamma$, we may stop sampling before the r failures are observed and conclude that Eq. (12) holds if the number of trials Z is already greater than Z_0.

III. Shortest Confidence Intervals

If for a fixed γ, confidence intervals of lengths L_1 and L_2 are constructed for p such that $L_1 < L_2$, we would normally prefer L_1 to L_2. In this section a method of constructing shortest confidence intervals will be given (see Ref. 5).

From Eq. (12), the length of the interval for λ is

$$L = \frac{1}{2Z}(b - a). \tag{13}$$

We want to minimize L subject to

$$\int_a^b h_{2r}(t)\, dt = 1 - \gamma \tag{14}$$

where $h_{2r}(t)$ is given by Eq. (11). Partially differentiating Eqs. (13) and (14) we have

$$\frac{\partial L}{\partial a} = \frac{1}{2Z}\left(\frac{db}{da} - 1\right)$$

and

$$h_{2r}(b)\frac{db}{da} - h_{2r}(a) = 0$$

which gives

$$\frac{\partial L}{\partial a} = \frac{1}{2Z}\left(\frac{h_{2r}(a)}{h_{2r}(b)} - 1\right)$$

$\partial L/\partial a$ is minimum when

$$h_{2r}(a) = h_{2r}(b) \tag{15}$$

That is, the a and b which gives minimum confidence length L_s are the pair satisfying Eq. (15) for $a \neq b$.

Table 1 gives the values of a and b satisfying Eq. (15) for $\gamma = 0.01(.01).05$ and $r = 1, \cdots, 120$. We think this table is new.

Let us find the *expected* length of the interval in the case $r = 10$, $p = 0.005$. In this case expected $Z = 2000$ and a, b, from the table, giving 95% confidence on p, are

$$a = 8.5841, \qquad b = 32.607393$$

Thus

$$p = a/2Z = 0.002146, \qquad p = b/2Z = 0.0081518$$

and the length $L_s = 0.0060058$.

The symmetric case given by Eq. (12) makes

$$a = 9.59083, \qquad b = 34.1696$$

from χ^2_{20} table. Thus

$$p = 0.0023977, \qquad p = 0.0085424$$

and the length $L = 0.0061447$. In this case the shortest interval results in a modest 2% gain over the symmetric 95% confidence interval.

The table we have constructed is useful not only in the case of Bernoulli parameter p but generally in constructing shortest confidence intervals for λ whenever the statistic to be employed has the χ^2_n-distribution. In all these cases the a and b giving the minimum interval and satisfying Eq. (12) can be read off from the table. When, however, the Bernoulli p is so large that $p \approx \lambda = -\ln(1 - p)$ we need to be able to get the shortest intervals directly for p. In such a case we may use the fact that by Eq. (12):

$$P(1 - e^{-a/2Z} < p < 1 - e^{-b/2Z}) = 1 - \gamma \tag{16}$$

The length of the confidence interval $L = e^{-a/2Z} - e^{-b/2Z}$ and just as in the case for λ, we want to minimize L subject to Eq. (14). It turns out that L is minimized if

$$\frac{e^{-b/2Z}}{h_{2r}(b)} = \frac{e^{-a/2Z}}{h_{2r}(a)} \tag{17}$$

If the number of trials to give r failures, Z, is large enough, which is the case either when r is larger or p is small, then Eq. (17) reduces to Eq. (15) for λ.

IV. Minimum r Required for Prescribed Estimate Accuracy

In a number of applications it is enough to show that the true value of p is almost surely less than the critical value for the system (i.e., with probability $1 - \gamma$). Since our estimate of p is based only on the value of r, the number of system failures observed and Z the number of system operations required to observe r, then it becomes important to be able to estimate the minimum number of failures that would give an estimate $p = r/z$ which is only slightly greater (5%, say) than p with very high probability. Put equivalently, the problem is to find the minimum value of r that would give an estimate p within $100\beta\%$ of p with probability $1 - \gamma$, $\beta > 0$, and small. In our terminology, this reduces to finding the least r such that

$$P\left(p\alpha > \frac{r}{Z}\right) = 1 - \gamma, \qquad \alpha = 1 + \beta \qquad (18)$$

In other words we want the probability that the true value of the parameter be less than $p\alpha^{-1}$ to be small ($= \gamma$).

Since Eq. (18) can be written as

$$P\left(Z > \frac{r}{p\alpha}\right) = 1 - \gamma$$

then, we can use the distribution of Z in Eq. (1) to calculate r for a given β and γ and each $0 < p < 1$. Thus Eq. (18) becomes

$$\sum_{r}^{\lfloor \frac{r}{p\alpha} \rfloor} \binom{Z-1}{r-1} p^r q^{z-r} = \gamma \qquad (19)$$

where $\lfloor r/p\alpha \rfloor$ is the largest integer smaller than $r/p\alpha$. We iterate the left-hand side of Eq. (19) until a value of r satisfying the equation is obtained. We note that any larger value of r would give a sum less than γ.

This method is not convenient, however. Even if the computation of r in Eq. (19) were easy, the volume of table of r values to be required to cover all p such that $0 < p < 1$, β and γ of interest, would be so large as to discourage such effort. Moreover, the value of p to use is

not known beforehand. Hence we need to have a method of evaluating r that is independent of the particular value of p. It turns out that a good bound on the minimum value of r can be obtained by considering the complementary requirement to Eq. (18) that

$$P\left(p < \frac{r}{Z}\alpha\right) = 1 - \gamma, \qquad \alpha = 1 + \beta \qquad (20)$$

That is to say that the probability that the true value of the parameter is ever greater than $p\alpha$ be very small ($= \gamma$).

We may now use the fact that the maximum likelihood estimate of p, $p = r/Z$ is, for large r, approximately normally distributed with mean p and variance

$$\sigma_p^2 = -\frac{1}{r E\left(\frac{\partial^2}{\partial p^2} \ln f(x,p)\right)} \qquad (21)$$

where

$$\begin{aligned} f(x,p) &= P(X_j = x) \\ &= p(1-p)^{x-1}; \qquad x = 1,2,3,\cdots \end{aligned}$$

X_j, $j = 1,2,\cdots$, r being the number of trials after the $(j-1)^{st}$ failure to the occurrence of the jth failure. Writing $L = \ln f(x,p)$ we have

$$E\left(\frac{\partial^2 L}{\partial p^2}\right) = -\frac{1}{p^2 q} \qquad (22)$$

and

$$\sigma_p^2 = \frac{p^2 q}{r}$$

Thus $(r/Z)\alpha$ is, for large r, approximately normally distributed with mean αp and variance $\alpha^2 p^2 q/r$ and hence

$$\left(\alpha\frac{r}{Z} - \alpha p\right)\sqrt{\frac{r}{\alpha^2 p^2 q}}$$

has the unit normal distribution.

Now Eq. (20) is equivalent to

$$P\left[p(1-\alpha)\sqrt{\frac{r}{\alpha^2 p^2 q}} < \left(\alpha\frac{r}{Z} - \alpha p\right)\sqrt{\frac{r}{\alpha^2 p^2 q}}\right] = 1 - \gamma \qquad (23)$$

Hence

$$p(1 - \alpha)\sqrt{\frac{r}{\alpha^2 p^2 q}} = -\phi_{1-\alpha} \qquad (24)$$

		r_D	r_{est}	r_{asymp}
$\gamma = 0.1$	$\beta = 0.1$	190	199	200
	$\beta = 1.05$	710	724	728
$\gamma = 0.05$	$\beta = 0.1$	313	326	327

where $\phi_{1-\alpha}$ is the lower $(1 - \alpha)$ percentile of the unit normal distribution. From Eq. (24) we see that

$$r = q \frac{\alpha^2}{(\alpha - 1)^2} \phi_{1-\alpha}^2, \qquad \alpha = 1 + \beta \qquad (25)$$

That is the value of r good for all p is

$$r = \frac{\alpha^2}{(\alpha - 1)^2} \phi_{1-\alpha} \qquad (26)$$

If we denote by r_D the r obtained by the direct method in Eq. (19) and by r_{est} (estimate) and r_{asymp} (asymptotic), respectively, those of Eqs. (25) and (26), to achieve an estimate error of less than 10% ($\beta = 0.1$) with 90% confidence ($\gamma = 0.1$) on $p = 0.005$ we need to wait for at least $r_D = 190$ successes. The corresponding $r_{est} = 199$, $r_{asymp} = 200$. Values of r for $p = 0.005$ and some values of β and γ are:

A graph of r_D for $\gamma = 0.1$, $\beta = 0.1$ and $0.001 \leq p \leq 0.05$ is plotted below.

V. Conclusion

A sequential sampling technique has been applied to the problem of estimating the failure probability of those systems whose operation history can be modeled by the Bernoulli sequence with small failure probability p. Methods of obtaining $1 - \gamma$ confidence bounds on p are presented, and several tables for constructing the limits of these bounds are indicated. The desirability of obtaining short $1 - \gamma$ confidence intervals prompts us to investigate the conditions for the shortest such intervals in this case. A new table for use in constructing these intervals for usual values of γ and a wide range of r is provided. The question of the minimum number of system failures required to achieve a prescribed accuracy of the p estimate is answered.

References

1. Hwang, D., and Buehler, R. J., "Confidence Intervals for Some Function of Several Bernoulli Parameters with Reliability Applications," *JASA*, Vol. 68, No. 341, March 1973.

2. Mood, A. M., *Introduction to the Theory of Statistics*, McGraw-Hill Book Co., New York, 1950.

3. Patil, G. P., "On the Evaluation of the Negative Binomial Distribution with Examples," *Technometrics*, Vol. 2, pp. 501–505, Nov. 1960.

4. Pearson, E. S., and Hartley, H. O., *Biometrika Tables for Statisticians*, Vol. I, Cambridge University Press, Massachusetts, 1956.

5. Guenther, W. C., "Shortest Confidence Intervals," *The American Statistician*, Vol. 23, No. 1, pp. 22–25, Feb. 1969.

Table 1. Values of *a* and *b* for the shortest confidence intervals

Table of a and b such that $h_{2r}(a) = h_{2r}(b)$ where

$$h_{2r}(x) = \frac{x^{r-1}}{2^r \Gamma(r)} e^{-x/2}, x \geq 0$$

and

$$\int_a^b h_{2r}(t)dt = 1\text{-}\gamma.$$

a is the first entry and b is the second for each γ and $n = 2r$. For example, if $\gamma = 0.05$ and $n = 2r = 20$, then

$$a = 8.5841, \qquad b = 32.607393$$

When $r = 1$, $h_2(x)$ reduces to the exponential distribution with parameter $\lambda = \frac{1}{2}$.

	γ				
$n = 2r$	0.05	0.04	0.03	0.02	0.01
4	0.0848 9.5282394	0.068 10.062034	0.0514 10.734574	0.0345 11.684643	0.0175 13.281327
6	0.607 12.802453	0.539 13.388847	0.464 14.128164	0.376 15.164491	0.264 16.900628
8	1.425 15.896601	1.3083 16.525274	1.1738 17.325344	1.01 18.436192	0.7856 20.295983
10	2.4139 18.860515	2.2528 19.531733	2.0643 20.383955	1.8296 21.565627	1.4978 23.533077
12	3.5161 21.729099	3.3147 22.439063	3.0767 23.339668	2.7771 24.583977	2.3444 26.653195
14	4.7004 24.524892	4.462 25.270476	4.178 26.216824	3.818 27.520418	3.291 29.684001
16	5.9477 27.263128	5.6743 29.04377	5.348 29.030965	4.9315 30.390159	4.316 32.641633
18	7.2452 29.954814	6.9395 30.766807	6.573 31.793831	6.103 33.20639	5.4041 35.540208
20	8.5841 32.607393	8.2477 33.449596	7.8434 34.513723	7.323 35.975951	6.5444 38.389569
22	9.9575 35.227546	9.592 36.098361	9.1515 37.198528	8.5834 38.707429	7.7289 41.196762
24	11.3613 37.81774	10.9675 38.717077	10.493 39.850243	9.8786 41.405594	8.9515 43.967203
26	12.7908 40.383458	12.3704 41.308935	11.8627 42.475229	11.204 44.074835	10.2073 46.705532
28	14.243 42.927308	13.797 43.878022	13.2574 45.076108	12.5564 46.717492	11.492 49.416424
30	15.7155 45.451379	15.2446 46.426908	14.6744 47.655306	13.9324 49.337469	12.8033 52.10051

Table 1 (contd)

$n = 2r$	γ				
	0.05	0.04	0.03	0.02	0.01
32	17.2061	16.7113	16.1115	15.3298	14.1379
	47.957866	48.957043	50.214788	51.936489	54.762048
34	18.7132	18.1951	17.5665	16.7464	15.4935
	50.448126	51.470521	52.756972	54.516847	57.403297
36	20.2352	19.6945	19.0381	18.1806	16.8685
	52.923807	53.968712	55.282712	57.079891	60.02534
38	21.7708	21.2082	20.5246	19.6308	18.261
	55.386172	56.452832	57.79397	59.627288	62.630384
40	23.3189	22.735	22.025	21.0959	19.6696
	57.836276	58.924084	60.29148	62.159881	65.219739
42	24.8786	24.2739	23.538	22.5745	21.0934
	60.274932	61.383428	62.776738	64.679327	67.793854
44	26.449	25.824	25.063	24.0657	22.5314
	62.703059	63.831749	65.250007	67.186391	70.353626
46	28.029	27.384	26.599	25.568	23.981
	65.122002	66.270743	67.712431	69.683141	72.903478
48	29.619	28.955	28.145	27.082	25.447
	67.530537	68.69785	70.165218	72.167619	75.432389
50	31.217	30.535	29.701	28.606	26.917
	69.731637	71.116189	72.607796	74.642475	77.965244
52	32.824	32.122	31.265	30.14	28.405
	72.323363	73.528802	75.043303	77.107124	80.472543
54	34.438	33.718	32.839	31.683	29.9
	74.708599	75.931784	77.467702	79.562951	82.976087
56	36.06	35.322	34.42	33.235	31.401
	77.085409	78.326562	79.885977	82.009512	85.477027
58	37.688	36.932	36.01	34.795	32.914
	79.456858	80.716237	82.294267	84.448257	87.963049
60	39.323	38.55	37.605	36.362	34.435
	81.821041	83.097149	84.699231	86.880625	90.44157
62	40.964	40.174	39.208	37.936	35.965
	84.179387	85.472433	87.095386	89.30627	92.910289
64	42.611	41.804	40.818	39.518	37.505
	86.5317	87.841859	89.484241	91.723148	95.36705
66	44.264	43.44	42.433	41.108	39.047
	88.877814	90.205233	91.868955	94.131061	97.826457
68	45.922	45.082	44.055	42.701	40.598
	91.219172	92.56239	94.245964	96.53847	100.27512
70	47.585	46.729	45.682	44.301	42.158
	93.555623	94.914796	96.618434	98.938184	102.7129
72	49.253	48.381	47.314	45.907	43.721
	95.887035	97.262298	98.986182	101.33176	105.15047
74	50.925	50.038	48.954	47.519	45.291
	98.214848	99.604764	101.34417	103.71903	107.58031

Table 1 (contd)

	γ				
$n = 2r$	0.05	0.04	0.03	0.02	0.01
76	52.602 100.53739	51.7 101.94208	50.595 103.70367	49.139 106.09652	46.871 109.99698
78	54.284 102.85459	53.366 104.27571	52.242 106.05641	50.759 108.47747	48.451 112.41801
80	55.969 105.16942	55.036 106.60554	53.894 108.40391	52.386 111.85002	50.041 114.8256
82	57.659 107.47873	56.711 108.92993	55.55 110.74766	54.017 113.21905	51.631 117.23707
84	59.352 109.78549	58.391 111.24882	57.211 113.08599	55.564 115.58116	53.231 119.6349
86	61.049 112.08811	60.072 113.56826	58.876 115.42039	57.294 117.94115	54.831 122.03622
88	62.749 114.38802	61.758 115.88202	60.546 117.74921	58.939 120.29566	56.441 124.42379
90	64.453 116.68366	53.448 118.1916	62.217 120.07862	60.589 122.64463	58.051 126.81451
92	66.161 118.975	65.142 120.49693	63.893 122.40231	62.241 124.99279	59.671 129.1914
94	67.871 121.26493	66.939 122.80096	65.573 124.72176	63.901 127.33049	61.291 131.57118
96	69.585 123.55046	68.538 125.10063	67.255 127.04	65.561 129.67038	62.911 133.95363
98	71.301 125.83446	70.241 127.39739	68.942 129.35236	67.222 132.01074	64.541 136.3221
100	73.021 128.11398	71.948 129.68971	70.632 131.66186	68.892 134.33895	66.171 138.69305
102	74.743 130.39189	73.658 131.97902	72.326 133.96693	70.562 136.66907	67.811 141.05
104	76.468 132.66669	75.369 134.26824	74.022 136.27055	72.237 138.99323	69.451 143.40928
106	78.196 134.93835	77.084 136.5529	75.721 138.57116	73.915 141.3145	71.091 145.77072
108	79.926 137.20827	78.801 138.8359	77.421 140.87169	75.595 143.63436	~ 72.74 148.11972
110	81.659 139.475	80.521 141.11573	79.125 143.16762	77.275 145.95581	74.389 150.47074
112	83.395 141.7385	82.244 143.39237	80.832 145.46042	78.964 148.26503	76.039 152.82208
114	85.132 144.00159	83.969 145.66725	82.542 147.75005	80.653 150.57575	77.698 155.16094
116	86.872 146.26141	85.697 147.93888	84.254 150.03796	82.343 152.88638	79.357 157.5106
118	88.615 148.51792	87.427 150.20867	85.968 152.3241	84.039 155.18931	81.017 159.8424

Table 1 (contd)

$n = 2r$	γ				
	0.05	0.04	0.03	0.02	0.01
120	90.359 150.77393	89.159 152.47661	87.688 154.60261	85.736 157.49208	82.677 162.18483
122	92.107 153.0252	90.895 154.7398	89.408 156.88222	87.436 159.79162	84.347 164.51316
124	93.856 155.2759	92.632 157.00251	91.128 159.16289	89.136 162.09239	86.017 166.84305
126	95.606 157.52606	94.371 159.26329	92.854 161.43588	90.842 164.3854	87.687 169.17441
128	97.359 159.77281	96.111 161.52353	94.58 163.70986	92.549 166.67809	89.367 171.49172
130	99.114 162.01754	97.855 163.77895	96.308 165.98191	94.258 168.96893	91.047 173.81046
132	100.87 164.26162	99.6 166.03379	98.038 168.252	95.968 171.25937	92.727 176.13056
134	102.629 166.50226	101.347 168.28661	99.772 170.51726	97.683 173.54349	94.407 178.45194
136	104.398 168.74223	103.096 170.5374	101.506 172.78339	99.399 175.82717	96.096 180.76083
138	108.151 170.98011	104.846 172.78754	103.243 175.04608	101.116 178.11035	97.776 183.08464
140	107.915 173.21589	106.599 175.0342	104.982 177.30674	102.836 180.39011	99.466 185.3944
142	109.681 175.44957	108.353 177.28018	106.722 179.56678	104.556 182.67077	101.166 187.6902
144	111.448 177.6825	110.109 179.52406	108.462 181.82757	106.282 184.94363	102.856 190.00224
146	113.216 179.91465	111.867 181.76583	110.208 184.08063	108.008 187.21736	104.556 192.30029
148	114.986 182.14466	113.626 184.00686	111.954 186.33443	109.735 189.49048	106.256 194.59942
150	116.759 184.37116	115.386 186.24713	113.702 188.58612	111.465 191.76011	107.956 196.89957
152	118.532 186.59821	117.15 188.4825	115.451 190.83709	113.195 194.03052	109.656 199.2007
154	120.307 188.82308	118.914 190.71846	117.201 193.08733	114.925 196.3017	111.356 201.50277
156	122.082 191.04847	120.679 192.95363	118.952 195.3368	116.66 198.56646	113.066 203.79091
158	123.861 193.26896	122.447 195.18524	120.707 197.58134	118.4 200.82484	114.776 206.07999
160	125.641 195.48861	124.216 197.41604	122.462 199.82648	120.135 203.09105	116.486 208.36997
162	127.421 197.70874	125.986 199.64601	124.222 202.0653	121.875 205.3584	118.201 210.65344

Table 1 (contd)

$n = 2r$	0.05	0.04	0.03	0.02	0.01
			γ		
164	129.203 199.92665	127.756 201.87648	125.977 204.31161	123.615 207.6113	119.911 212.94511
166	130.987 202.14234	129.531 204.10068	127.738 206.5502	125.36 209.86536	121.626 215.23025
168	132.771 204.35847	131.305 206.32672	129.499 208.78933	127.105 212.12006	123.346 217.50888
170	134.556 206.5737	133.08 208.55188	133.264 211.02351	128.85 214.37539	125.066 219.7883
172	136.345 208.78402	134.858 210.77346	133.029 213.25822	130.6 216.6243	126.786 222.06848
174	138.133 210.99609	136.637 212.99416	134.794 215.49343	132.35 218.87382	128.506 224.34939
176	139.923 213.2059	138.416 215.21529	136.56 217.72777	134.1 221.12393	130.231 226.62378
178	141.713 215.41611	140.196 217.43551	138.33 219.95715	135.85 223.37459	131.956 228.89887
180	143.506 217.62273	141.979 219.65214	140.1 222.187	137.605 225.61883	133.681 231.17464
182	145.299 219.82972	143.762 221.86918	141.87 224.41731	139.358 227.8664	135.411 233.44388
184	147.092 222.03708	145.545 224.08661	143.643 226.644	141.114 230.11032	137.141 235.71376
186	148.888 224.24084	147.331 226.30044	145.416 228.87113	142.874 232.34923	138.871 237.98432
188	150.684 226.44495	149.12 228.51067	147.192 231.09464	144.63 234.59417	140.601 240.25547
190	152.483 228.64547	150.906 230.72525	148.968 233.31858	146.39 236.83407	142.341 242.51295
192	154.282 230.84633	152.695 232.93622	150.744 235.54293	148.15 239.07445	144.071 244.7853
194	156.081 233.04751	154.487 235.14358	152.524 237.7623	149.913 241.7623	145.811 247.04399
196	157.883 235.24508	156.276 237.35526	154.304 239.98206	151.676 243.54935	147.551 249.30326
198	159.685 237.44298	158.069 239.562	156.084 242.20222	153.442 245.78187	149.291 251.5631
200	161.487 239.64118	159.862 241.76907	157.864 244.42275	155.208 248.01584	151.031 253.82349
202	163.29 241.83837	161.659 243.97121	159.648 246.6383	156.978 250.24477	152.771 256.08441
204	165.094 244.03455	163.452 246.17893	161.432 248.85421	158.744 252.47959	154.511 258.34584
206	166.901 246.22713	165.249 248.38172	163.219 251.06649	160.514 254.70936	156.261 260.5937

Table 1 (contd)

	γ				
$n = 2r$	0.05	0.04	0.03	0.02	0.01
208	168.708 248.42	167.049 250.58088	165.003 253.28311	162.284 256.93955	158.011 262.84209
210	170.515 250.61313	168.846 252.78428	166.79 255.49607	164.054 259.17012	159.751 265.10501
212	172.325 252.80266	170.646 254.98405	168.58 257.70539	165.831 261.39159	161.501 267.35438
214	174.132 254.99633	172.446 257.18411	170.367 259.91902	167.601 263.62293	163.251 269.60423
216	175.945 257.18252	174.246 259.38446	172.157 262.12899	169.381 265.84112	165.001 271.85454
218	177.755 259.37283	176.049 261.58117	173.947 264.33928	171.155 268.06778	166.751 274.10531
220	179.568 261.55953	177.852 263.77817	175.741 266.54459	172.932 270.29076	168.511 276.3426
222	181.381 263.74648	179.655 265.97543	177.535 268.75021	174.712 272.51005	170.261 278.59426
224	183.194 265.93367	181.462 268.16776	179.329 270.95613	176.492 274.72969	172.021 280.83245
226	185.008 268.11981	183.269 270.36036	181.123 273.16234	178.272 276.94968	173.771 283.08493
228	186.825 270.30234	185.073 272.55711	182.92 275.3649	180.052 279.17000	175.531 285.32397
230	188.642 272.4851	186.883 274.74633	184.717 277.56774	181.832 281.39064	177.291 287.56343
232	190.459 274.66809	188.69 276.93968	186.514 279.77086	183.612 283.61159	179.051 289.8033
234	192.276 276.85129	190.5 279.1294	888.311 281.97425	185.402 285.8195	180.811 292.04355
236	194.093 279.0347	192.31 281.31936	190.111 284.17398	187.182 288.04107	182.571 294.28419
238	195.912 281.21451	194.12 283.50956	191.911 286.37397	188.972 290.24962	184.341 296.51147
240	197.733 283.39452	195.933 285.69612	193.711 288.57422	190.759 292.46246	186.101 298.75286
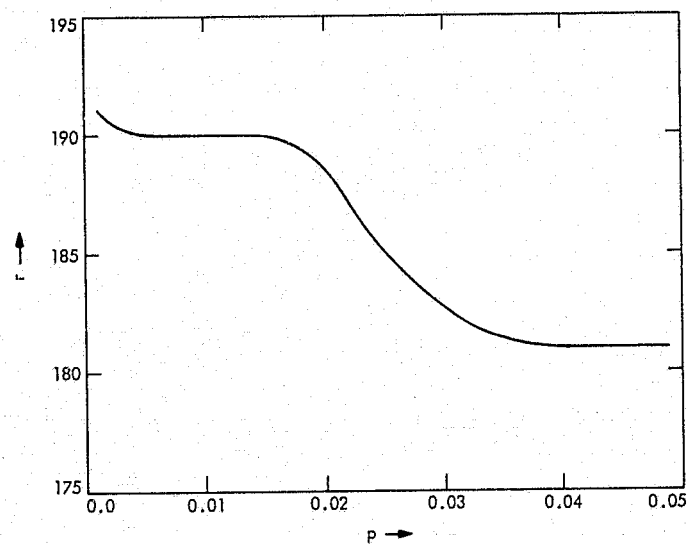
Fig. 1. Minimum number of system failures r giving 90% (i.e., $\gamma = 0.1$) confidence that estimate error is within 10% ($\beta = 0.1$), $r_{asymp} = 200$

An NCS Standard Interface for the
XDS 900 Series Computers

W. Lushbaugh
Communications Systems Research Section

The Network Control System standard interface has been adopted as a standard computer interface for all future minicomputer-based subsystem development for the Deep Space Network. This article describes a standard interface adapter for existing XDS 900 series computers that will enable the design of equipment compatible with the presently available machines and easily transferable to new minicomputers as they become available.

I. Introduction

The Network Control System (NCS) standard interface has been adopted as a standard computer-interface for all future minicomputer-based subsystem development for the DSN. In order to design and test equipment for currently existing 900-series machines and be able to transfer that equipment conveniently to new minicomputers as they become available, a standard interface adapter (SIA) is needed which can be attached to the 900 series machines. The following article provides a design overview of such an SIA.

II. Review of 900 Series I/O Structure

The 900 series XDS computers are 24-bit machines with input/output (I/O) performed in the register mode, i.e., transfers to and from an external piece of equipment are on a 24-bit basis. An energize output machine (EOM) instruction and parallel input (PIN) and parallel output (POT) instructions perform I/O on a word-by-word central processing unit (CPU) controlled basis. Executing an EOM-POT (or PIN) sequence delivers (or receives) data from the device addressed by the EOM. An EOM-POT (or PIN) sequence cannot be interrupted by an external interrupt.

Two interrupts are typically used in an I/O sequence. One is a data interrupt to signify that the input/output buffer is full/empty, while the other interrupt is used to signal special conditions such as end of message or errors.

Reference 1 gives a detailed description of the XDS 900-series computer interfacing for those who find the above description too brief.

III. Review of the Standard Interface Format

The NCS standard interface output consists of fourteen signals and a power sense line. The fourteen signals consist of eight data signals, two function code signals and four control or handshaking signals. Three of the four combinations of function codes are available for tagging data transmission while the fourth, the 1-1 condition, is reserved for commands out of the computer or status in from the device connected to that computer. Two of the control signals are used as stimulus signals; one from computer (STC) and one from the device (STD). Both of these signals are unidirectional and go true for the complete duration of a message. The remaining two signals are bidirectional control signals called response (RSP) and ready (RDY), which control the handshaking of data across the interface. Response and ready each make one complete cycle (false to true to false) for each byte transferred across the interface.

IV. Programming Characteristics of the Interface

To the programmer, the standard interface appears to be a device, with two associated EOMs. One EOM is used to channel the input or output of the data to the interface while the other is used to communicate status information to and from the program.

A typical data-out sequence is as follows. A status EOM-POT sequence is executed by the program to alert the interface that the data output mode is starting. The hardware will generate a data interrupt at this point to notify the software that the output buffer is empty. The software responds to this interrupt by executing an EOM(DATA)-POT sequence which fills the output buffer and clears the interrupt. This sequence of data interrupts and data POTs will be continued until the desired number of words has been transferred from the computer. There will be one last data interrupt telling the program that the buffer is empty, at which time a status EOM-POT sequence is executed, which terminates the data output mode and automatically clears the data interrupt. This normal data-out mode only uses one of the two interrupts, i.e., the data interrupt. If at any time during this mode, the device connected to the other end of the SIA interrupts the data out mode by either a status insert or by turning the data transmission around by initiating the data input mode, the program would be notified by a service interrupt.

The data-in mode is started by the device. The hardware in the SIA holds the data-in buffer ready when not in use so that three bytes will be transferred to the computer before the first data interrupt occurs. This data interrupt is the same physical interrupt as used in the data out mode, but no confusion can result if the interface is programmed properly. For example, the status of the device can be read at any time to clarify which type of data interrupt is occurring.

V. Status Register

The status register is the means by which software and hardware communicate. The software delivers commands to the SIA via the output status register and reads back various status information from the input status register. Despite this split input/output function, the status register is a single 24-bit register.

A list of input and output bit assignments is given in Table 1. Following is a detailed description of each signal.

C_{23}-C_{16} Command Byte/Status Byte. These 8 bits are used to communicate to the device connected to the SIA. When a command is to be sent from the computer to the device (see bit 15) the contents of these 8-bit locations are stored in the SIA and transmitted to the device at the proper time in the handshaking sequence.

When the device delivers an 8-bit status byte to the computer, these 8 bits are stored in the SIA and delivered to the computer following an EOM (STATUS)-PIN sequence. These bits are only changed when a new status byte is delivered and so are meaningless unless C_7 is set (see C_7).

C_{15} Command Flip Flop. Setting this bit via an EOM POT STATUS sequence, causes the hardware to interrupt (at the proper time) whatever I/O process is happening and send a command to the device. If this bit is not set, the contents of C_{23} through C_{16} do not get copied into the SIA.

C_{14}-C_{13}. These two bits are the two function codes to be used in the data output mode or the received function codes in the data input mode. These two bits must be set to the desired value at the beginning of each data transmission AND MUST NOT BE CHANGED until the next message.

When the hardware in the SIA detects the data input mode, it switches these two inputs from the output function code flip-flops to the input function code flip-flops, so that these two bits have different meanings depending upon what the hardware is doing.

C_{12} **Data Request.** Setting this bit causes the hardware to attempt the data output mode to the device. This request will be honored as long as the device does not override it. Resetting this flip-flop terminates the data output mode.

C_{11}, C_{10} — B_1, B_0. B_1, B_0 are interpreted in the hardware as a binary number (B_0 = LSB) giving the number of bytes per word to be transferred in the data output mode, or the number of bytes received before a data interrupt is generated, in the data input mode. It is possible to change these bits during a message, but this should only be done during a data interrupt.

C_9 **Reset SIA.** Setting a 1 in this position triggers a 100-ns pulse that resets the SIA.

C_8 **Reset Device.** Setting a 1 in this position sets a flip-flop which sends a RESET COMMAND to the DEVICE. To release the device reset, a zero must be set in this position.

C_7 **Status Byte Here.** A one read in at this position means that a status byte was received from this device. This bit causes a status interrupt and may be reset by putting a one in this position or by RESET. When this bit is set, data output mode is temporarily cut off.

C_6 **ΔSTD.** This bit is set to 1 when STD (stimulus from the device) makes a 1 to 0 transition. This bit causes a status interrupt and can be reset by putting a 1 in this position or by RESET.

C_5 **STD.** This is a raw copy of the signal stimulus from device (STD).

C_4 **Device Power.** This bit = 1 when device power is off. This will cause a status interrupt to be generated as long as this signal is set, but this can be masked out of the interrupt by a 1 in this position. Setting a 1 in this position does not affect the value read in during a status PIN.

C_3 **Device Override.** This bit is set to 1, causing a status interrupt when a data byte is received while the data request (see C_{12}) is set.

C_2-C_1, R_1-R_{11}, **Respectively.** These two bits give the number of received bytes in UNARY. Both are reset to "0" on an EOM-PIN of data (or start or reset). A data interrupt is developed when $R_1 = R_{11} = 1$ and a third byte has arrived.

C_0 **Data Interrupt.** This bit is a copy of the data interrupt.

VI. Design Philosophy

Since it was felt that most noise pulses encountered in practice are high-energy short-duration voltage spikes, and furthermore that most system noise is synchronous with a system clock, it was decided to investigate the possibility of building an asynchronous (clockless) SIA. There was a further line of thought leading to this investigation, i.e., that there is no inherent demand at either end of the interface to have a clock. Certainly the 900-series computer end of the link could use computer timing signals where necessary and the interface would supply other necessary timing signals, e.g., data here, data taken, etc. There also is no need to supply a clock at the device end, for if the device does have a clock, it will not necessarily be the 5-MHz reference required in the DSN specification.

VII. Design Results

The design objectives were completely met in that, a completely clockless interface was built and demonstrated. The heart of the system is the low-pass filtered line receiver shown in Fig. 1. The line receiver is National Semiconductor's DM8820A, a dual line receiver in a 14-pin package. Figure 1 shows one of the control signals terminated in the standard 220/330 Ω terminator and feeding an RC network consisting of the 1 kΩ resistor and the 220 pF capacitor. This RC network forms part of the low-pass filter, as the device itself with the feedback as shown also has an inherent filtering capability of about 10 MHz. The 4.3 kΩ resistor to ground from pin 3 of the DM8820A causes the device to compare the signal on pin 1 to approximately 1.7 V when the output is high, while the 1 kΩ and the diode to the output drops the comparison voltage to about 1.1 V when the output is low. The combined effects of these external components is to add hysteresis, and increase the noise rejection to greater than half the voltage swing in both the high and low signal states.

Laboratory tests of the combined filter and line receiver gave the following results: (a) A square wave input varying between 0.3 and 3.0 V of 3 MHz or higher did not get through the line receiver; (b) A single positive-going pulse of less than 200 ns never got through the line receiver, and some circuits rejected pulses as wide as 250 ns; (c) A single negative going pulse (i.e., signal normally 3 V pulsing to 0.3 V) of less than 200 ns would never trigger the output of the line receiver, and some circuits rejected pulses of 250 ns. The variation in pulse widths rejected can be attributed to variations in external components as well as variations in the line receivers themselves.

Figure 2 shows RSP (on the upper trace) and RDY (on the lower trace) of an actual handshaking sequence between the SIA for a 900-series computer as it was connected to an external test box which had the full complement of handshaking logic. The signals are as they appear inside of a short (negligible delay) cable. The horizontal calibration is 500 ns/cm, while the vertical scale is 1 V/cm, with ground at the bottom reticle and center reticle for the lower and upper traces, respectively. The upper trace showing RSP from the test box (a device), starts the sequence asserted, as the SIA on the 910 computer does not have any data ready. When the 24 bits of data are loaded into the SIA, RDY is asserted by the SIA, as seen on the lower trace of Fig. 2. Approximately 300 ns later, the device recognizes the assertion of RDY and generates a 100-ns data strobe pulse (not shown) after which RSP goes high. Approximately 250 ns later the SIA recognizes the raising of RSP, and it completes the cycle by raising RDY. A new cycle is then initiated by the device about 350 ns later, when it observes the raising of

RDY when it again lowers RSP. The total length of the handshaking sequence is about 1.3 μs. Three handshaking cycles are shown in Fig. 2, the sequence ending there, since the buffer in the SIA is now empty. All three pulses on both traces appear synchronously in Fig. 2, since the relative timing of each is derived from fixed delays rather than a system clock. This synchronous feature considerably aided in the speedy debugging of the initial design and will certainly be helpful in repairing a malfunctioning SIA or device in the future.

VIII. Conclusions

An SIA for XDS 900-series computers has been built without using a system clock. Rather than validating the signal by interrogating it with two clock pulses, the signal is assumed valid only when it is present long enough (200 to 250 ns) to pass through a low-pass filter. The resulting SIA has a peak data transmission rate of approximately 770 kilobytes/s (minus software I/O time). The unit has been successfully tested using a completely functional clockless test unit. The unit has also been successfully tested over 100 m (300 ft) of cable and connected to the precision signal power measurement unit (PSPM). The PSPM is a device with an SIA adaptor, developed by the Digital Projects Group, which uses the double clocking method of filtering the received signals.

A device is now under development which will convert the twin-coax intercomputer communications link (Ref. 2) to a device with an SIA adaptor. This will enable any computer with an SIA adaptor to communicate via coaxial cable to another computer up to 600 m away.

References

1. Martin, W. L., "Digital Communication Tracking: Interfacing with SDS 900 Series Computers," in *The Deep Space Network, Space Programs Summary* No. 37-39, Vol. III, pp. 52–65. Jet Propulsion Laboratory, Pasadena, Calif., May 31, 1966.

2. Lushbaugh, W. A., "A Driver/Receiver Unit for an Intercomputer Communications Link," in *The Deep Space Network Progress Report*, Technical Report 32-1526, Vol. XV, pp. 109–113, Jet Propulsion Laboratory, Pasadena, Calif., June 15, 1973.

Table 1. XDS 900-Series 14 line interface status register

900-Series Bit Number				
23	Least sig. bit		D1	
22			D2	
21			D3	
20		Command byte on pot	D4	Line of 14 line
19		Status byte on pin	D5	interface
18			D6	
17			D7	
16	Most sig.bit		D8	
15	CMD F.F. Set one EDM Pot status. Reset by start and when CMD sent			
14	F_0) Function codes to be used in data out mode, or			
13	F_1 } Received function codes			
12	DAT RQST. Indicates data output mode (not needed for CMD out)			
11	B_0) B_1, B_0 are interpreted in the hardware as a binary number (B_0 = LSB) giving the number of bytes per word to			
10	B_1 } be transferred in output mode, or the number of bytes received before a data interrupt is generated, in input mode			
9	Reset. Setting a one in this position triggers a one-shot pulse to reset the 900 series end of the comm. link			
8	Reset device. Setting a 1 in this position sets a flip-flop which sends a reset CMD to the device. To release the reset a 0 has to be plotted in this position			
7*	Status byte here. Cuts off data out transfer until cleared			
6*	ΔSTD. Set to 1 when STD makes a 1 to 0 transition			
5	STD. Raw copy of STD line			
4*	Device power = 1 when device power is off, masked out of status interrupt by entering a 1 in this position			
3*	Device override. Set to one when a data byte is received when the hardware is in data out mode			
2	R_1) Number of data bytes received in unary. Both are reset to 0 on EOM-PIN data or start. A data in interrupt is			
1	R_{11} } developed when $R_1 = R_{11} = 1$ and a third byte has arrived			
0	Data interrupt			

*Status bits 3, 4, 6, and 7 are either masked or reset by potting a 1 in the corresponding position of the status register. Any one of these bits set generates a status interrupt.
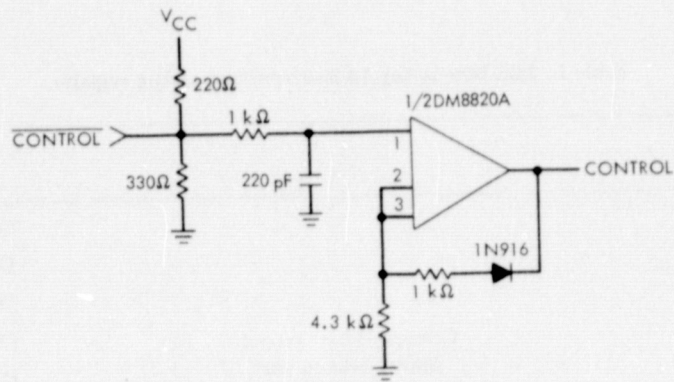
Fig. 1. Filtered line receiver with hysteresis
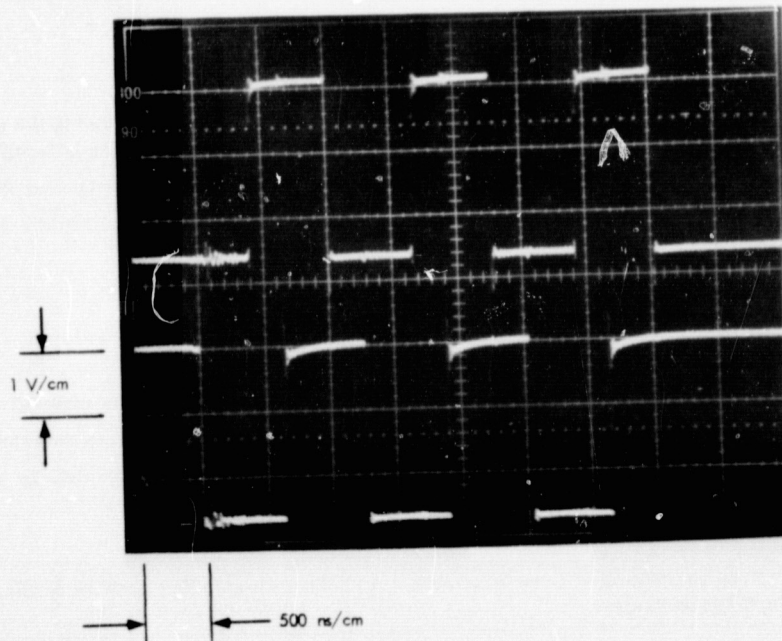
Fig. 2. RSP (TOP) RDY (BOT)

Operational X-Band Maser System

H. R. Buchanan, R. W. Hartop, J. G. Leflang, J. R.
Loreman, and D. L. Trowbridge
R. F. Systems Development Section

Laboratory tests on the first operational X-band maser system for Viking have been completed in the laboratory. Over 50-MHz bandwidth has been achieved with 45-dB gain and a noise temperature of 8 kelvins. Implementation at the 64-meter stations is scheduled for the first half of calendar year 1975.

I. Introduction

The ground support requirements for the Viking project include low noise reception in the 8400- to 8435-MHz frequency band. The design parameters of the traveling-wave maser amplifier structure were discussed in detail and preliminary test maser results were presented in an earlier report (Ref. 1). The design of the overall maser system has now been completed. The fabrication and test phase is nearing completion with implementation at the 64-meter stations scheduled during the first half of calendar year 1975. This report describes the hardware and test results.

II. Design Considerations

At the outset of the operational X-band maser program, the desired amplifier performance was established:

(a) Frequency range: 8400 to 8435 MHz

(b) Instantaneous 1-dB bandwidth: 35 MHz minimum

(c) Gain: 45 dB

(d) Noise temperature: 8 kelvins

Other decisions made in the early phase of the program were to use a superconducting magnet for improved gain and phase stability and to base the operational design of the traveling-wave maser structure and the magnets on R&D developments reported earlier (Refs. 2 and 3). The same closed-cycle cryogenic system as that used with the operational Block III S-band maser system was selected. In planning the design philosophy of the instrumentation, it was decided to utilize Block IV receiver modules in the maser monitor equipment wherever practical. This eased the design requirements, simplified station spares and maintenance, and resulted in fabrication economy. The X-band maser instrumentation was planned to be integrated with the Block III S-band maser equipment so as to utilize existing calibration equipment where feasible.

The use of existing packaging designs was stressed to minimize design and documentation costs. Provisions were made for the future addition of a second X-band maser where this could be done without adding significant cost.

III. X-Band Maser System Equipment

A block diagram of the X-band maser equipment is shown in Figs. 1 and 2. Figure 1 details the portion of the equipment installed within the X-Band Receive Only (XRO) feed cone assembly. Figure 2 details the equipment mounted in module 3 of the tricone, in the alidade compressor room, and in the station control room.

The major units housed in the XRO cone assembly are the Traveling-Wave Maser/Closed-Cycle Refrigerator (TWM/CCR) assembly and the X-band monitor receiver. The TWM/CCR assembly shown in Fig. 3 includes the helium refrigerator, which houses the traveling-wave maser structure with its field spreading coils and the superconducting magnet. The input and output waveguides with cooled low-pass filters for preventing pump leakage are also housed in the refrigerator along with the magnet charging heater and a Mistor[1] bridge circuit for measuring the magnetic field. The interior of the refrigerator is shown in Fig. 4. The TWM/CCR assembly also includes the maser calibration and pump boxes. The maser calibration box permits test signals to be routed into either the maser input or the maser output. The pump box includes two klystrons which are simultaneously combined and injected into the traveling-wave maser structure. The pump box also includes a modulator (Ref. 1) which frequency modulates the two klystrons at a 100-kHz rate.

The X-band monitor receiver elements are shown in Fig. 1. All of the elements shown are identical to Block IV receiver components. A sample of the maser output is coupled into an X-band mixer with the local oscillator (LO) signal supplied through a times 17 frequency multiplier. The intermediate frequency (IF) output is 325 MHz.

As indicated in Fig. 2, the maser output signal is transmitted to the receiver select assembly in module 3 of

---

[1] Mistor is a trade mark name for a solid-state, thin-film magnetic flux-sensitive resistor.

the tricone where the signal is distributed into four available output channels for the Block IV receiver.

The output of the X-band monitor receiver is transmitted to the IF selector box. Provisions are also made in this box to receive 325-MHz signals from the Block IV receiver. The operator selects one of these signals, which is then transmitted to the 325-MHz IF amplifier and mixer assembly, where it is mixed with a crystal-controlled 270-MHz local oscillator. A dual output is generated: one output at 325 MHz and one at 50 MHz. The 325-MHz output is transmitted to the control cabinet and into a commercial spectrum analyzer on which the passband of the maser is displayed. The 50-MHz signal is routed into S-band control cabinet No. 2, in which it can be selected for the existing Y-factor equipment for calibration purposes. The monitor receiver cabinet in the tricone also includes a times 10 frequency multiplier fed by a 47.6-MHz crystal-controlled oscillator mounted in the control room in the X-band maser control cabinet (cabinet 3). The times 10 frequency multiplier, the 325-MHz IF amplifier and mixer, and the times 6 frequency multiplier are all standard Block IV receiver modules. In addition, cabinet 3 houses the various power supplies, controls, and quartz thermometer readout for operation of the X-band maser. Figure 5 shows the equipment mounted in cabinet 3.

The compressor for operating the helium refrigerator of the X-band maser is housed in the alidade compressor room.

IV. Results

The first X-band maser system has now been assembled and has been tested in the laboratory. A typical response curve of the maser is shown in Fig. 6. It is noted that a 45-dB gain is achieved with an instantaneous bandwidth of more than 50 MHz. The noise temperature of the maser has been measured at 8 kelvins. A detailed report on the traveling-wave maser structure development is planned in the near future. The laboratory tests of the first operational system indicate that the design goals have been met with some margin to spare. It is anticipated that all three systems will be completed and installed in the 64-meter stations during the first half of calendar year 1975.

References

1. Trowbridge, D. L., "X-Band Traveling Wave Maser Amplifier," in *The Deep Space Network Progress Report*, Technical Report 32-1526, Vol. XVII, pp. 123–130, Jet Propulsion Laboratory, Pasadena, Calif., Oct. 15, 1973.

2. Clauss, R., Wiebe, E., and Quinn, R., "Low Noise Receivers: Microwave Maser Development," in *The Deep Space Network Progress Report*, Technical Report 32-1526, Vol. XI, pp. 71–80, Jet Propulsion Laboratory, Pasadena, Calif., Oct. 15, 1972.

3. Berwin, R., Wiebe, E., and Dachel, P., "Superconducting Magnet for a Ku-Band Maser," in *The Deep Space Network Progress Report*, Technical Report 32-1526, Vol. V, pp. 109–114, Jet Propulsion Laboratory, Pasadena, Calif., Oct. 15, 1971.
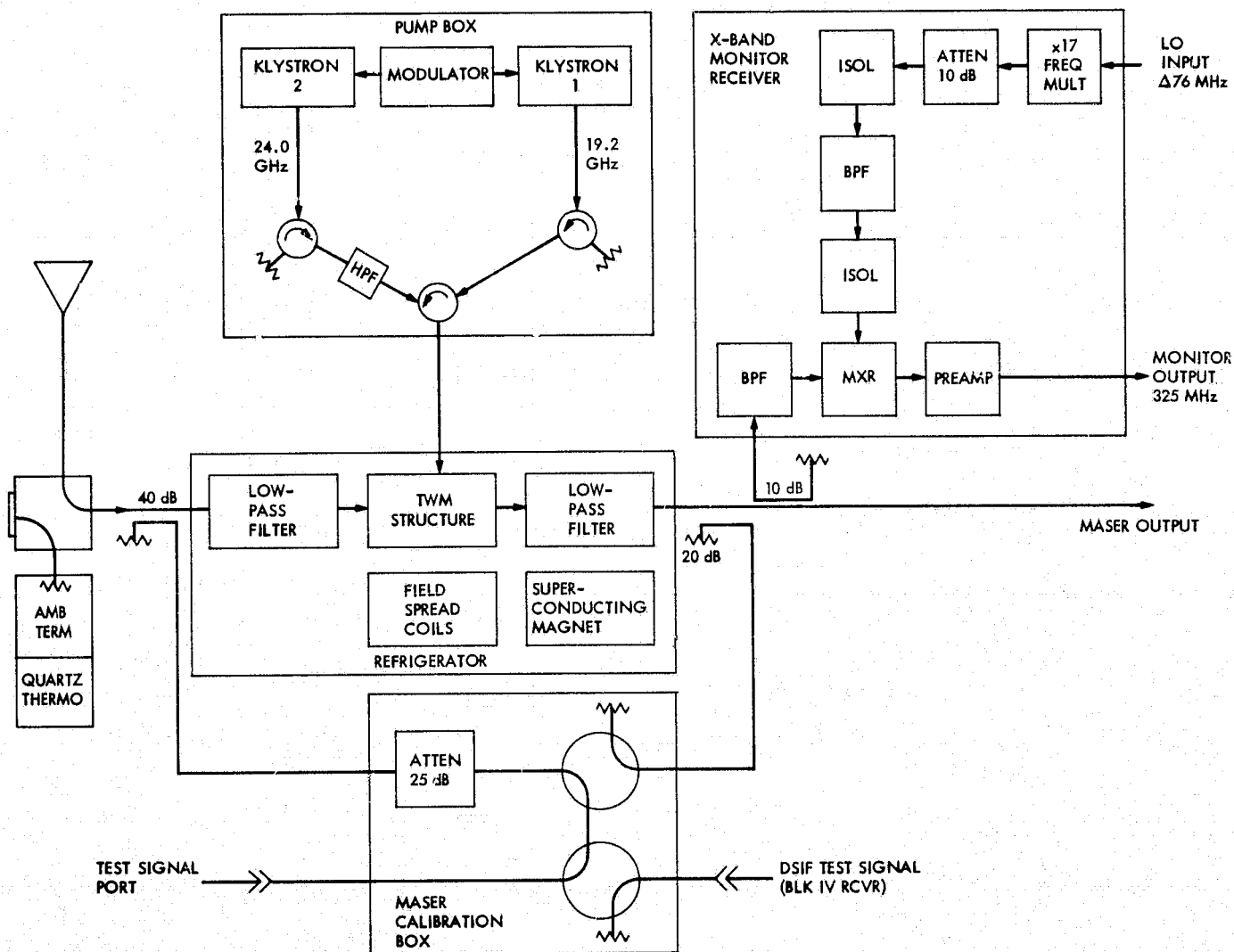
Fig. 1. X-band maser equipment: cone mounted
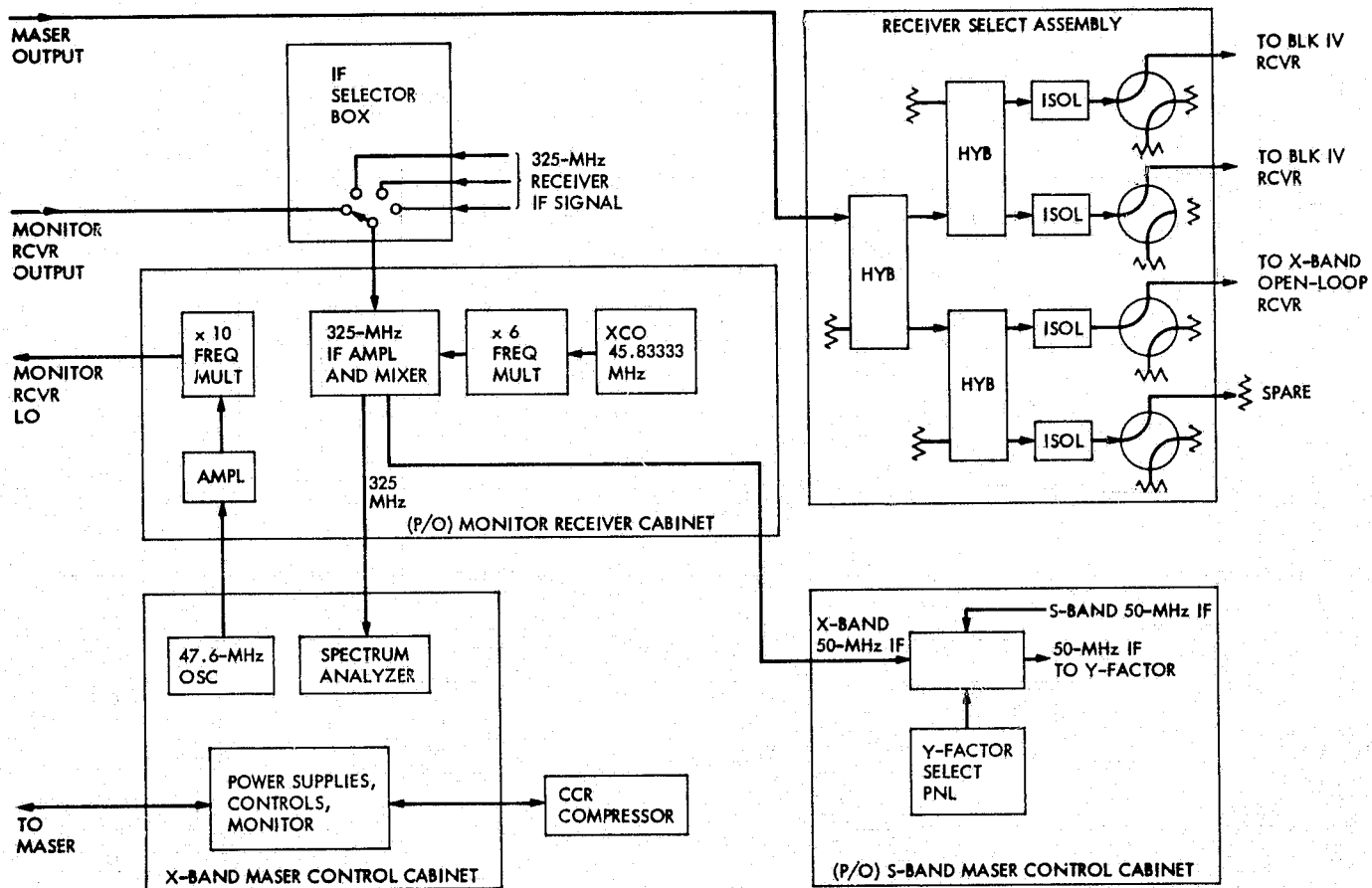
Fig. 2. X-band maser equipment: tricone, alidade, and control room
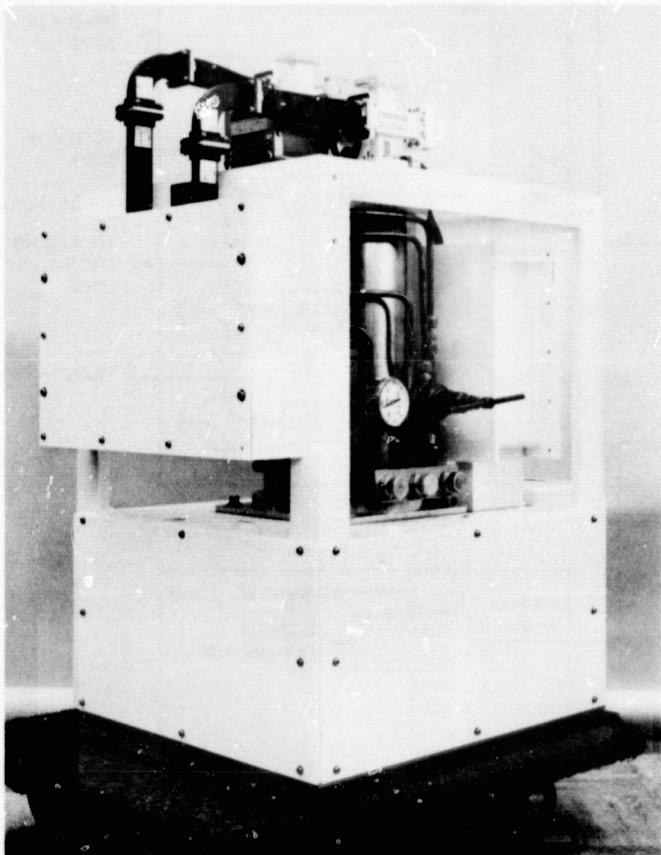
Fig. 3. TWM/CCR assembly
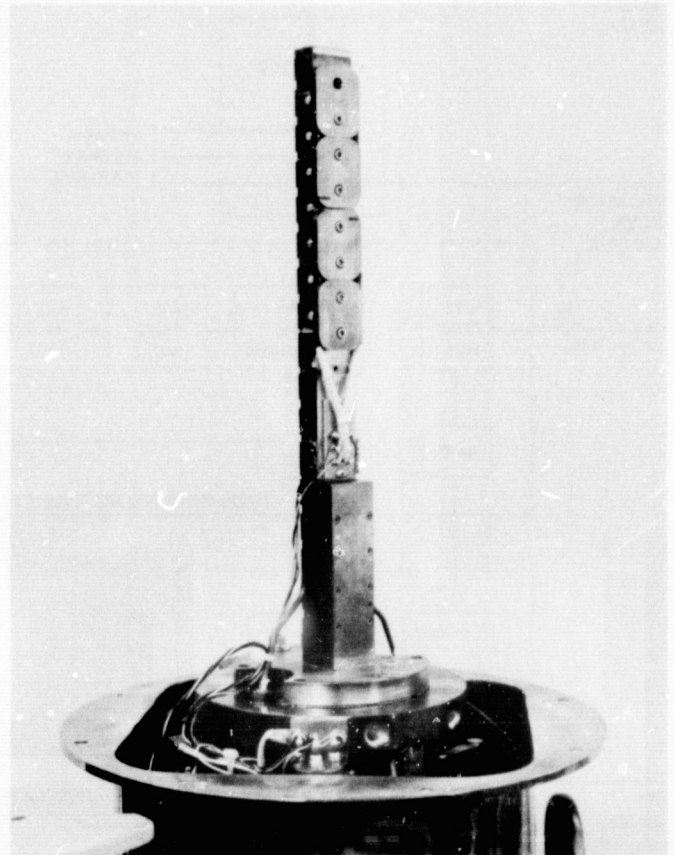
Fig. 4. Interior of refrigerator
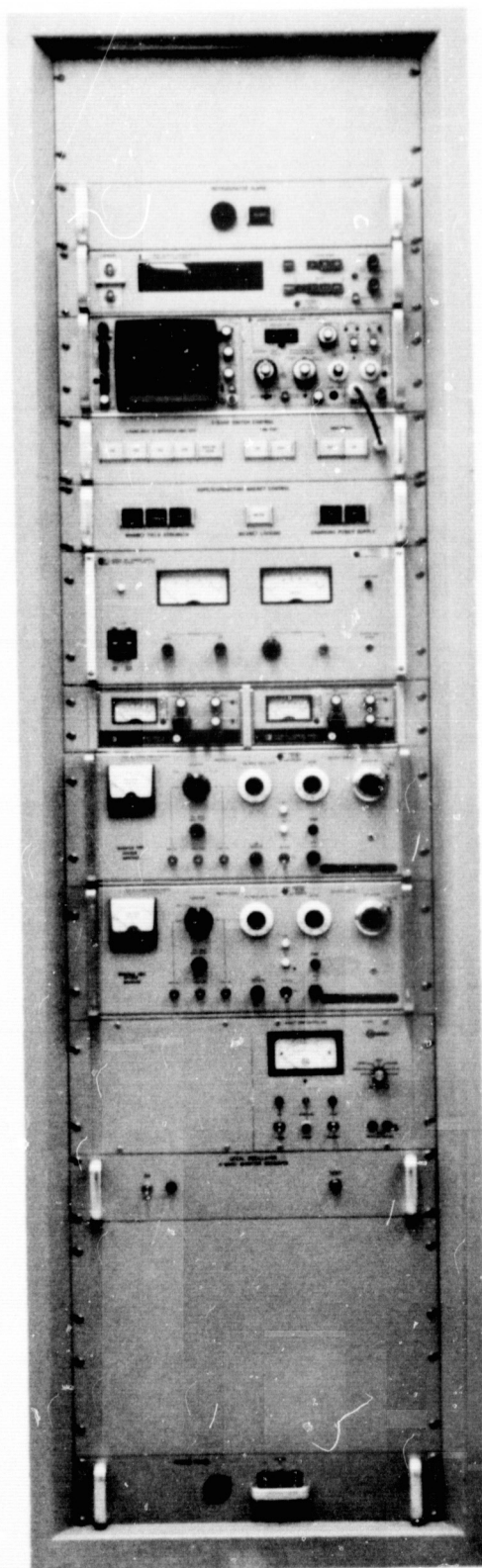
Fig. 5. Cabinet 3 controls and instrumentation
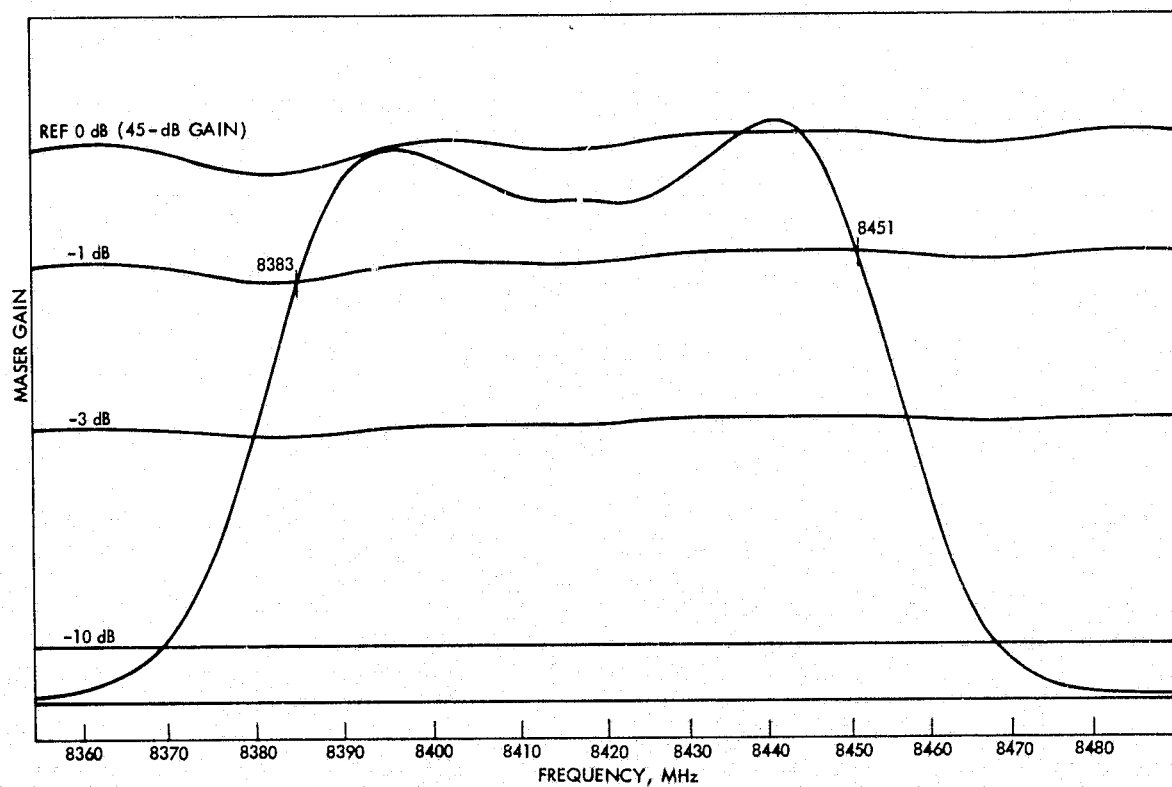
Fig. 6. X-band maser response

Implementation of DSS 43 and DSS 63 High-Power Transmitters

J. R. Paluka

R. F. Systems Development Section

Progress of installation and test of the DSS 43 and DSS 63 high-power transmitters is traced through procurement, installation, and test of the equipment at DSS 13 to overseas shipment and installation status at DSS 63 as of January 25, 1975. The schedule for this activity is to have the DSS 63 subsystem installed, tested, and transferred to operations for the Viking project by mid-July 1975, and the DSS 43 subsystem operational by mid-October 1975.

I. Introduction

In 1970 a high-power transmitter was installed, tested, and transferred to operations at DSS 14. Plans were then initiated to provide high-power transmitters at each 64-m station. In January 1974 the implementation schedule was accelerated by two years. This required a very intensive effort to complete the design and the procurement, and to provide training and test at Goldstone. Present plans are to install high-power transmitters at DSS 43 and DSS 63 during 1974 and 1975. The schedule for this activity is to have the DSS 63 subsystem installed, tested, and transferred to operations for the Viking project by mid-July 1975, and the DSS 43 subsystem transferred to operations by mid-October 1975.

Procurement of major components for these transmitters was started in late 1972. Delivery of most equipment was made in 1973 and 1974. Some of these components were shipped directly to the overseas stations from vendors; and others, as noted below, were shipped to DSS 13 for testing before overseas shipment.

The high-power transmitter is comprised of four main equipment groups: the control group, the power amplifier group, the coolant group, and the high-voltage (HV) power supply group. Figure 1 is a simplified subsystem block diagram of the control group, the power amplifier group, and the parts of HV power supply group that were tested at DSS 13. The tests for each subsystem were conducted at the assembly level, at the group level, and at the subsystem level. Major components of the DSS 13 transmitter were substituted to provide an almost complete transmitter subsystem. The main reason for not testing the motor–generator of the power supply group and the coolant group at DSS 13 was economy. Factory

testing was performed on these units before being shipped directly overseas.

II. Testing at DSS 13

Testing of the DSS 63 transmitter was started at DSS 13 in mid-February 1974. Initially the control group was tested using a test fixture to simulate other parts of the transmitter. Figure 2 is the local control console, the main part of the control group. By late March 1974 the group-level testing of the controls was completed and interface testing with the DSS 13 heat exchanger was started. In early April the transformer/rectifier, choke, and crowbar were added to the construction of the subsystem using this test configuration and the DSS 13 motor–generator and coolant group. Both the DSS 63 and the DSS 43 power groups were successfully load-tested into a dc load to a full megawatt for approximately twenty-four hours. This test assured sufficient wattage from the power supply group for either a 100-kW or a 400-kW klystron. In early June 1974 the power amplifier group containing a 100-kW klystron (Varian X-3060) was added to complete the test configuration shown in Fig. 1. During June and the first half of July, subsystem-level tests were performed on the transmitter subsystem. On July 15 dismantling and shipping of the subsystem to DSS 63, near Madrid, Spain, was started. During the testing four personnel from DSS 63 were at JPL and DSS 13 a few weeks for training.

Assembly of the DSS 43 high-power transmitter was started in the manner described above in early August 1974. Again, the same portions of the DSS 13 high-power transmitter were used to substitute for those portions of the subsystem which were shipped directly to DSS 43 from vendors. Four personnel from DSS 43 arrived at DSS 13 in July and remained until December and January to contribute to the testing and to receive intensive on-the-job training. In early December the subsystem was dismantled and shipped to DSS 43.

III. Installation and Testing at DSS 63

Construction of facilities for the high-power transmitter subsystem was started in August 1974. The new facilities at DSS 63 consist mainly of a building to contain the transformer/rectifier, the filter choke, and the control junction box, and a complex of concrete pads for the motor–generator set (1750 HP (1305 kW) and 1300 kVA), the motor control center, the auxiliary heat exchanger, the distilled water replenishing unit, underground water tanks, and miscellaneous circuit breaker housings. Figure 3 is a

view of this pad area as it appeared in late January 1975. Of the units described above, the motor–generator set, the motor control center, the auxiliary heat exchanger, one circuit breaker box for the synchronous motor, and the 2000-gallon tank for the water replenishment system are in place. Figure 4 is a view of the transformer/rectifier building construction as it appeared in late January. A portion of the pad area described above is visible in the background. The center of this entire area is approximately 70 meters north of the DSS 63 antenna.

In addition to the installation of units pictured in Figs. 3 and 4, the majority of the transmitter equipment located in the antenna pedestal and the operations building has been installed, and interconnecting control cables have been connected. These units include the local control console (Fig. 2), the remote control console, the crowbar cabinet, the motor–generator controller, the field and focus magnet power supply racks, the high-voltage junction box and high-voltage splice box and all power and control cabling from the pedestal and operations building to the tricone where the power amplifier group will ultimately be located. Prior to the arrival of JPL and Goldstone contractor personnel at DSS 63 in November and December 1974, DSS 63 station personnel had installed and partially tested the heat exchanger of the coolant group, which is located on the antenna alidade.

Interface tests were successfully conducted for the first time between the control group and the alidade heat exchanger in late December 1974. In mid-January 1975 the power amplifier cabinet was raised to the antenna tricone (Figs. 5 and 6), and the cabinet was temporarily installed in the tricone for a period of ten days. During this period water flow tests were successfully conducted between the power amplifier cabinet and the alidade heat exchanger for the first time. The purpose of these flow tests was to verify that the heat exchanger can provide sufficient coolant water to the klystron and water load at all elevation angles of the antenna. These tests ensured that a sufficient flow of cooling water is available to the power amplifier cabinet for either a 100-kW or a 400-kW klystron.

The other purpose of temporarily installing the power amplifier cabinet was to assure that the mechanical interface of the cabinet waveguide output port would properly align with the DSS 63 microwave subsystem when the cabinet was bolted in its pre-assigned location. This test was also successfully completed and the cabinet was removed from the tricone and reinstalled in the

antenna pedestal to allow continuation of assembly level and group testing when installation of the power supply group is completed. Scheduled beneficial occupancy dates (BOD) were November 1, 1974 for the pad area (Fig. 3) a..d January 15, 1975 for the transformer/rectifier building. Scheduled completion date (transfer to operations) for the DSS 63 high-power transmitter presently is July 15, 1975.

IV. Installation at DSS 43

Most of the transmitter subsystem has been shipped to DSS 43. To date the main heat exchanger has been installed on the antenna alidade, and selection of a facilities contractor has begun. October 15, 1975 is the scheduled date for transfer of the DSS 43 high-power transmitter to operations.
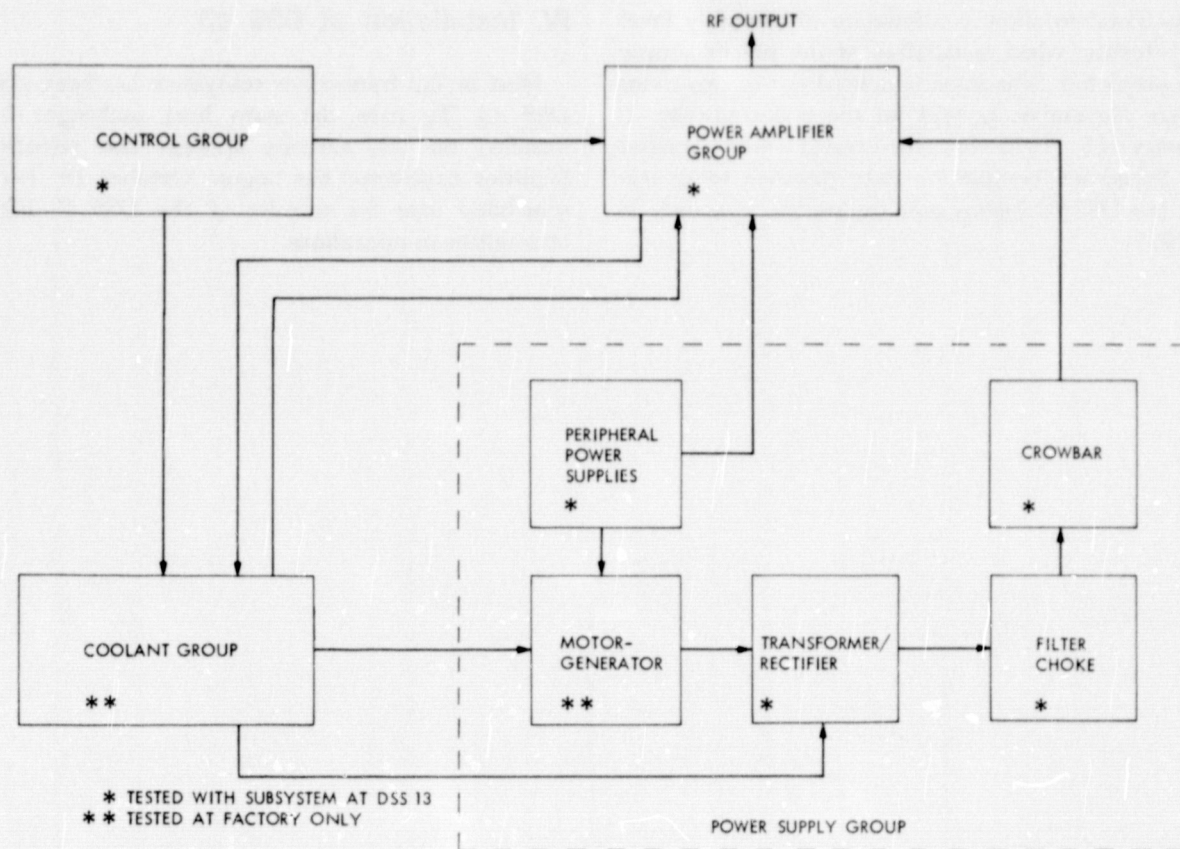
Fig. 1. Subsystem block diagram showing location of preshipment tests
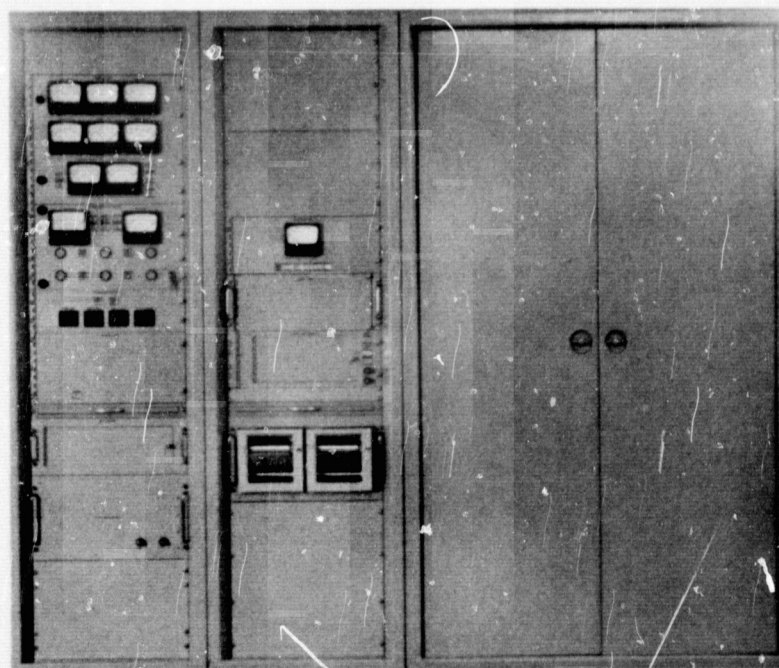
Fig. 2. Local control console
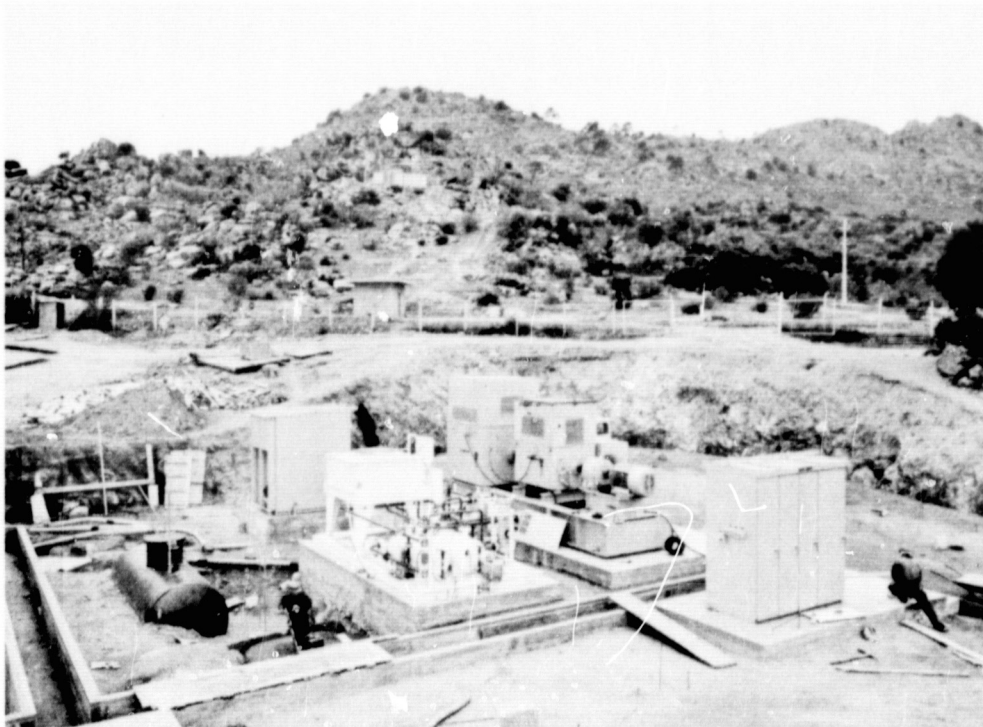
Fig. 3. Facilities status: pad area

Fig. 4. Facilities status: transformer/rectifier area
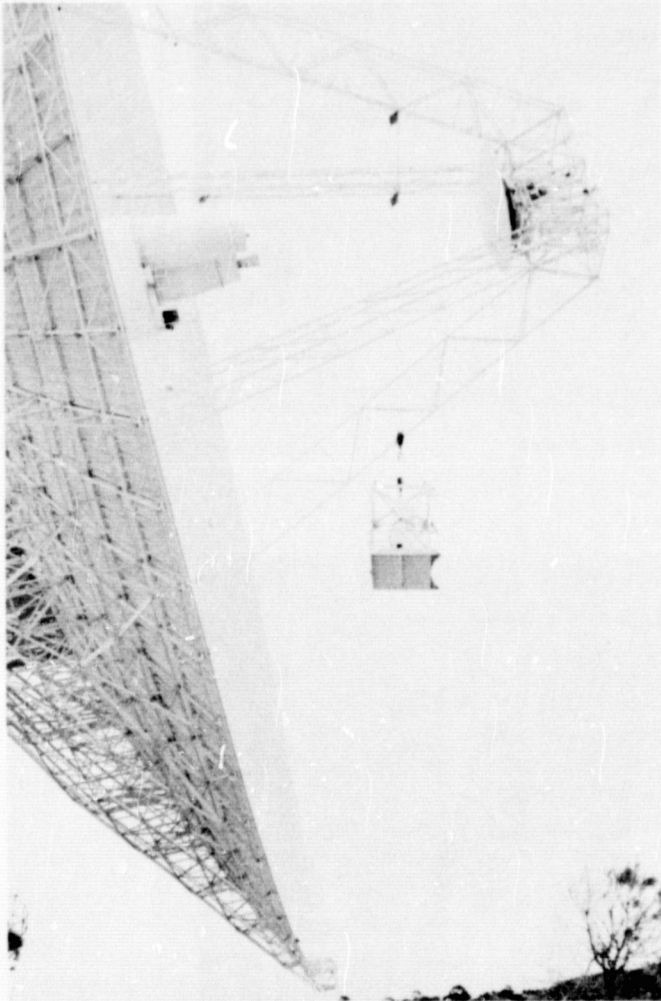
Fig. 5. Power amplifier being raised to antenna surface
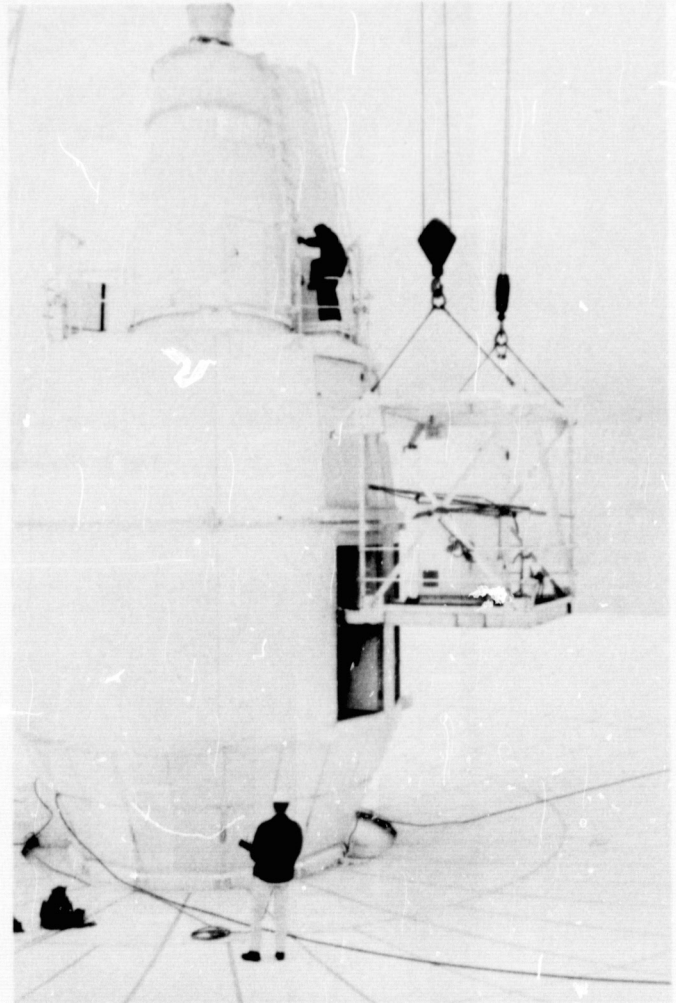
Fig. 6. Power amplifier on back porch being positioned for unloading into tricone

X-Band Tracking Operations During the Viking Orbital Phase

A. L. Berman
Network Operations Section

*X-band tracking of the Viking spacecraft in orbit around Mars will be compli-
cated due to the combination of high periapsis doppler rates and low downlink
carrier margin. This report presents methods to implement X-band tracking of the
Viking spacecraft by ramping either the ground transmitter frequency or the
ground receiver frequency. The operational impact of the two methods is assessed.*

I. Introduction

Tracking at the 64-m deep space stations with the
Block IV X-band receiver in a 10-Hz tracking loop filter
setting will be quite difficult at Viking Orbiter periapsis
because of high doppler rates. As an alternative, use of the
30-Hz tracking loop filter during Block IV X-band track-
ing is not promising because there is only marginal carrier
power above threshold (~8.7 dB) in this mode. Addi-
tionally, it had been thought (Ref. 1) that in order to
maintain a reasonably small phase error while tracking
with the Block IV X-band receiver in a 10-Hz tracking
loop filter setting, as many as 20 digital controlled oscil-
lator (DCO) ramps (frequency rates) per periapsis pass
might be required. It is therefore the intent of this report
to analyze in greater detail the operational capabilities
and constraints while tracking a Viking Orbiter with the
Block IV X-band receiver(s) in a 10-Hz tracking loop
filter setting.

II. Orbits Utilized in the Analysis

Reference 2 analyzed in great detail four separate
orbits. These consisted of permutations of periapsis alti-
tudes of 1200 and 500 km and of lines of apsides either
normal to or parallel to the Mars-Earth vector. These can
be abbreviated as 500 km/N, 500 km/P, 1200 km/N and
1200 km/P. The highest periapsis doppler rates are en-
countered with the 500 km orbits, so it was considered
adequate to limit this analysis to the 500 km/P- and
500 km/N-type orbits. The periapsis doppler rates
(X-band, two-way) for these two orbit types can be seen
in Figs. 1 and 2, respectively.

III. Consideration of Static and Dynamic Phase Error

In the initial consideration of the adequacy of a given
receiver to track a given signal, one is concerned with
both the static phase error (SPE) due to frequency dis-

placement and dynamic phase error ($\Delta\theta$) due to frequency rate. As it turns out, the pacing criterion for the worst Viking orbital case (the 500-km/P-type orbit), in terms of necessary ramping of the X-band receiver, is the dynamic phase error, and hence this study will be mostly focused on this particular parameter. Also, any receiver ramping schemes which will alleviate the dynamic phase error problem, coupled with judicious choices of starting receiver frequencies, will almost automatically keep the total frequency displacement small, and hence negate most static phase error buildup. Quite simply, if one is ramping the receiver to keep the received frequency rate within certain bounds as in Fig. 3, the cumulative frequency displacement

$$\sum_{n=1}^{i} \int_{n-1}^{n} \left\{ R_n - \frac{d}{dt}(D2) \right\} dt \sim 0$$

(where R_n is the receiver ramp rate and d/dt (D2) is the received doppler rate) is relatively small when compared to that frequency displacement which would result from no ramping of the receiver.

IV. Analysis of Receiver DCO Ramps to Maintain Dynamic Phase Error Below 13 deg

Rather arbitrarily selecting a (conservative) objective of maintaining the phase error ($\Delta\theta$) at 13 deg or less, one has the following pertinent information from the DSN/ Flight Project Interface Design Handbook (Ref. 3) and from Ref. 1:

Block IV X-band receiver carrier margin at 10 Hz tracking loop filter ≈ 13.51 dB

Downlink frequency rate required to produce $\Delta\theta = 13$ deg at a carrier margin of 13.5 dB $\approx \pm 15$ Hz/s.

The periapsis 2-way X-band doppler frequency rates versus time for the 500-km/P-type and 500-km/N-type orbits are shown in Figs. 1 and 2, respectively. Overlaying the doppler frequency rates in Figs. 1 and 2 are the required receiver ramps to keep the dynamic phase error approximately equal to or less than 13 deg, and hence from the information above, to keep the (relative) frequency rate at the receiver (= downlink frequency rate minus receiver ramp rate) approximately equal to or less than ± 15 Hz/s. As can be seen in Fig. 1, the 500-km P-type orbit is the more extreme case, requiring 11 re-

ceiver DCO ramps during the periapsis period. The 500-km/N-type orbit (see Fig. 2) is only slightly less difficult, requiring 8 receiver DCO ramps during the periapsis period.

V. Error Analysis

In the previous section the number of receiver DCO ramps required to produce a $\Delta\theta$ of 13 deg or less was analyzed; however, this (implicitly) assumed that the predictions used to generate the required ramp parameters would be perfectly matched to the actual data. At this point it would be reasonable to briefly examine the effect of using (slightly) inaccurate predictions.

Let one assume that a reasonable goal would be the generation of a ramp scheme designed to keep $\Delta\theta$ at 13 deg or less, but that one would tolerate occasional $\Delta\theta$'s of up to 17 deg because of inaccuracies in the predictions. Given this ground rule, one needs to determine what magnitude of prediction error would cause a combined $\Delta\theta$ of 17 deg, and, if one could expect prediction errors for the Viking orbital phase to be bounded by this (to-be-determined) prediction error. For a $\Delta\theta = 17$ deg, one has from Ref. 3, the following received doppler frequency rate: $\approx \pm 20$ Hz/s. Differencing this value with the ramp scheme goal of ± 15 Hz/s for the (relative) received frequency rate, one wishes to determine what size prediction error would thus cause a two-way X-band doppler frequency rate error of $\approx \pm 5$ Hz/s.

For both the 500-km N-type and 500-km P-type orbits, the maximum rate of change of frequency rate is

$$\left\{ \frac{d}{dt} \text{(frequency rate)} \right\}_{max} \gtrsim (10 \text{ Hz/s})/\text{min}$$

such that a frequency rate error would translate into an equivalent (prediction) time error of

$$\Delta t = \frac{5 \text{ Hz/s}}{(10 \text{ Hz/s})/\text{min}} \approx 30 \text{ s}$$

If recent past experience with respect to prediction accuracy at planetary encounters, etc., proves to be a reliable guide, one can indeed expect that, in general, trajectory errors during the Viking Orbital Phase will be less than 30 s (Δt), and hence expected errors in the prediction data from which ramp rates will be generated should add less than 4 deg of $\Delta\theta$.

$C - 3$

VI. Operational Considerations

Let one consider the simplest case of just one receiver —a Block IV X-band receiver in the two-way mode with a 10-Hz tracking loop filter setting. If one considers a 500-km P-type orbit, and using the criterion previously established in Section IV, 11 separate ramps will have to be programmed into the receiver DCO per periapsis pass. At the DSS the operation will be complicated because the DCO holds only 4 ramps at any given time, and, as the initial ramps are executed, subsequent ramps will have to be manually entered into the DCO in near real time. Additionally complicating the receiver operator's job is the fact that the ramps are exhausted in as little as three minutes, thus allowing little time for the operator to enter and verify new ramps.

Generation of the ramp instructions in the Network Operations Control Area (NOCA) should also prove to be difficult, and in particular, time-consuming. Receiver frequency predictions are not generated in the prediction system, and the only method by which they can be generated (now) is manual, with the aid of Hewlett-Packard Programmable Electronic Calculators. Also, the Block IV DCO receiver frequency level is quite unfamiliar to most of the Network Operations Control Team (NOCT). Finally, assuming the ramp instructions are generated by the NOCT, they will have to be transmitted manually (via teletype) to the DSS, with a greatly increased risk of transmission errors, etc.

The above considers only the difficulties in ramping one receiver. If the Block IV S-band receiver is also in a 10-Hz tracking loop filter configuration, it too will require ramping, under some circumstances. Consider a 500-km P-type orbit. The maximum frequency rate at X-band (two-way) is $\approx$ 160 Hz/s. Thus at S-band it would be $\approx$ (3/11) {160 Hz/s} $\approx$ 44 Hz/s. From Ref. 2, the Block IV S-band receiver carrier margin equals 21.3 dB, so that (from Ref. 3), a phase error equal to 13 deg results from a receiver frequency rate of $\approx \pm 30$ Hz/s. Thus, to avoid excessive phase error, the Block IV S-band receiver will also require some ramping.

Finally, if three-way X-band doppler is ever desired from another 64-m DSS during a periapsis pass, the extremely laborious and time-consuming tasks described above will be doubled.

To summarize the above, receiver ramping during Viking Orbiter periapsis passes can be accomplished; however, it will:

(1) Place additional burdens on the DSS receiver operator

(2) Consume large amounts of manpower from the NOCT, because of the semimanual mode of receiver level ramp generation

(3) Entail considerably more risk of error because of the manual mode (teletype) of transmission

VII. Use of Uplink Ramping

The idea of utilizing the DCO capability to ramp the uplink and thus reduce the total downlink frequency rate is obvious and certainly merits being investigated. For instance, considering the 500-km P-type orbit, the total periapsis 2-way doppler rate excursion is $\approx$ 170 Hz/s (-10 to $+160$). If one chooses and appropriately locates five uplink ramps at the following equivalent X-band frequency rates of $+10$, $+40$, $+70$, $+40$, and $+10$ Hz/s, then one will have modified the uplink such that the spacecraft will see a maximum frequency rate (at equivalent X-band level) of ± 15 Hz/s. More importantly one would reduce the total 2-way X-band downlink frequency rate excursion to $\approx$ 110 Hz/s (-20 to $+90$).

Instead of 11 DCO ramps in the receiver, one would now require only 7. However, 5 ramps are now required in the exciter, making a total of 12 ramps altogether. Considering the added complications of ramping the exciter and the receiver, it does not seem that ramping the uplink in the above described fashion will buy anything substantial.

A more interesting (although perhaps seemingly bizarre!) approach might be to consider over-ramping the uplink by a factor of 2. This poses no particular difficulty for the S-band spacecraft receiver, and, in any case, produces the same frequency rate at the spacecraft as if the uplink was not ramped at all. But more importantly, it should theoretically drive the downlink doppler frequency rate to some small limit such that the X-band receiver would not have to be ramped at all. As a matter of fact, this is exactly what happens. Quite simply, let one define at some time:

F_{2x} = two-way X-band downlink frequency

TSF = track synthesizer frequency (transmitted uplink frequency at DCO level, $\approx$ 44 MHz)

$\dot{r}_{up}$ = uplink range rate

$r_{\mathrm{dn}} = $ downlink range rate

$c = $ speed of light

Then one has

$$F_{2x} \text{ rate} = \frac{d}{dt}[F_{2r}]$$

$$= \frac{d}{dt}\left\{48\frac{880}{221} TSF\left[1 - \frac{(r_{\mathrm{up}} + r_{\mathrm{dn}})}{c}\right]\right\}$$

$$= -48\frac{880}{221} TSF\left\{\frac{d}{dt}\left[\frac{(r_{\mathrm{up}} + r_{\mathrm{dn}})}{c}\right]\right\}$$

Now if one assumes a ramped TSF, say TSF_R, and a corresponding F_{2x}, say $(F_{2x})_R$, one would have

$$(F_{2x})_R \text{ rate} = \frac{d}{dt}[(F_{2x})_R]$$

$$= \frac{d}{dt}\left\{48\frac{880}{221} TSF_R\left[1 - \frac{(r_{\mathrm{up}} + r_{\mathrm{dn}})}{c}\right]\right\}$$

$$= 48\frac{880}{221}\left\{\left[1 - \frac{(r_{\mathrm{up}} + r_{\mathrm{dn}})}{c}\right]\frac{d}{dt}(TSF_R)\right.$$

$$\left. - TSF_R\frac{d}{dt}\left[\frac{(r_{\mathrm{up}} + r_{\mathrm{dn}})}{c}\right]\right\}$$

To drive the downlink doppler frequency rate to zero, one requires

$$\frac{d}{dt}[(F_{2x})_R] = 0$$

or

$$\frac{d}{dt}(TSF_R) = \frac{TSF_R\left\{\frac{d}{dt}\left[\frac{(r_{\mathrm{up}} + r_{\mathrm{dn}})}{c}\right]\right\}}{\left[1 - \frac{(r_{\mathrm{up}} + r_{\mathrm{dn}})}{c}\right]}$$

since $1 \gg \dfrac{(r_{\mathrm{up}} + r_{\mathrm{dn}})}{c}$

$$\frac{d}{dt}(TSF_R) \cong TSF_R\left\{\frac{d}{dt}\left[\frac{(r_{\mathrm{up}} + r_{\mathrm{dn}})}{c}\right]\right\}$$

and since $TSF_R \approx TSF$

$$\frac{d}{dt}(TSF_R) \cong TSF\left\{\frac{d}{dt}\left[\frac{(r_{\mathrm{up}} + r_{\mathrm{dn}})}{c}\right]\right\}$$

Finally, from the previous definition of F_{2x} rate, one has

$$\frac{d}{dt}(TSF_R) \cong -\frac{221}{48(880)}\frac{d}{dt}[F_{2x}]$$

$$\cong -\frac{221}{48(880)}\{F_{2x} \text{ rate}\}$$

Following the above logic, uplink ramps corresponding to those in Fig. 1 (approximately twice the uplink frequency rate and, of course, moved backward (earlier) from the times in Fig. 1 by one round-trip light time (RTLT)) were input into the 500-km P-type orbit predictions. The results in the downlink doppler frequency rate are just as expected—the X-band downlink frequency rate is constrained to ±15 Hz/s. These results can be seen in Fig. 4. For this case no ramping of the receiver would be required. At first glance, it would not seem that anything of particular value has been achieved, since one now has 11 exciter ramps instead of 11 receiver ramps. However, on closer inspection, a number of operational benefits would appear to accrue, i.e.,

(1) The uplink frequency level is far more familiar to the NOCT.

(2) The necessary uplink ramp parameters can be obtained from prediction output quantities (XA and DD2) with far less effort than producing receiver level predictions and receiver level ramp parameters.

(3) Uplink ramping requires no individual receiver frequencies, whereas receiver predictions require fairly current individual receiver parameters (the 21-MHz free-running oscillator) measured at the DSS.

(4) Uplink ramps would routinely be transmitted within normal predictions (via high-speed data (HSD)) and would thus be virtually guaranteed free of transmission errors, in contrast to sending large amounts of receiver ramp data manually (via teletype).

(5) When one considers the possibility of Block IV S-band tracking with a 10-Hz tracking loop filter, or, far more important, the addition of X-band 3-way tracking at a separate 64 m DSS, no additional receiver ramping is required, in marked contrast to the receiver ramping case, where the number of total required ramps increases by 100% or more— one ramped uplink covers all receivers!

In consideration of the above, the possibility of using overcompensated uplink ramping might merit further investigation.

References

1. Chaney, W., *High X-Band Doppler Offsets and Rates During Viking Orbital Phase*, IOM NSE-74-155, July 8, 1974 (JPL internal document).

2. Koerner, M., *Viking RF Receiver Phase-Locked Loop Phase Errors Produced by Spacecraft Motion*, IOM 3395-74-055, June 6, 1974 (JPL internal document).

3. *Deep Space Network/Flight Project Interface Design Handbook*, Document 810-5, Revision D, Feb. 15, 1975 (JPL internal document).
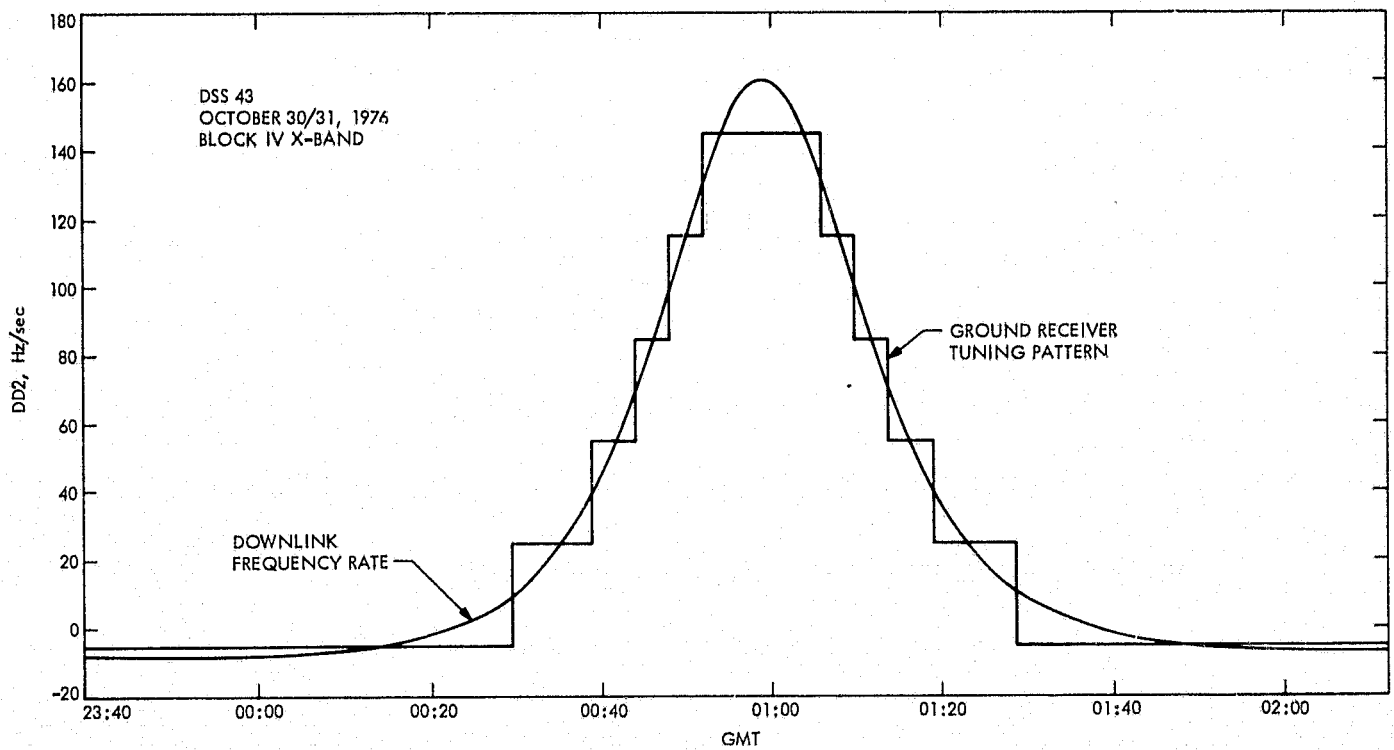
Fig. 1. Viking Orbiter 500-km/P-type orbit 2-way doppler rate versus GMT
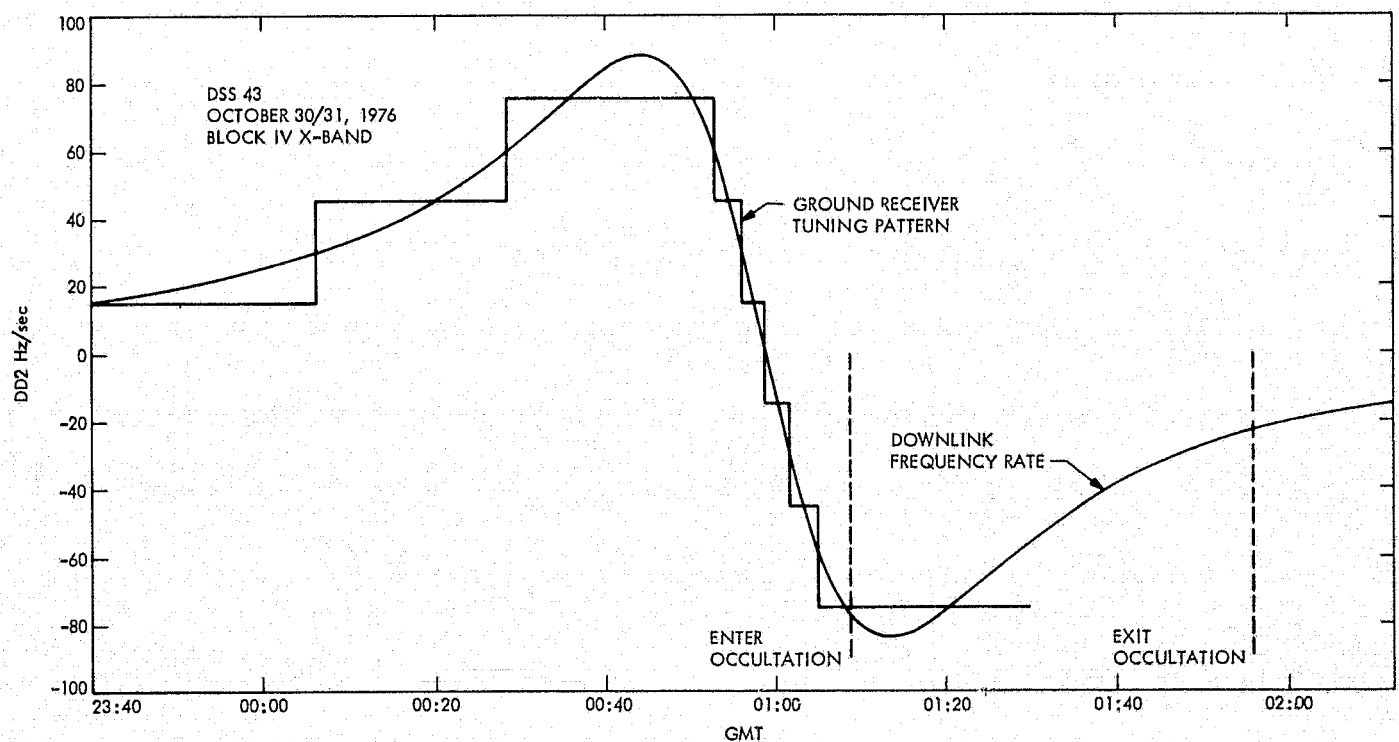
Fig. 2. Viking Orbiter 500-km/N-type orbit 2-way doppler rate versus GMT
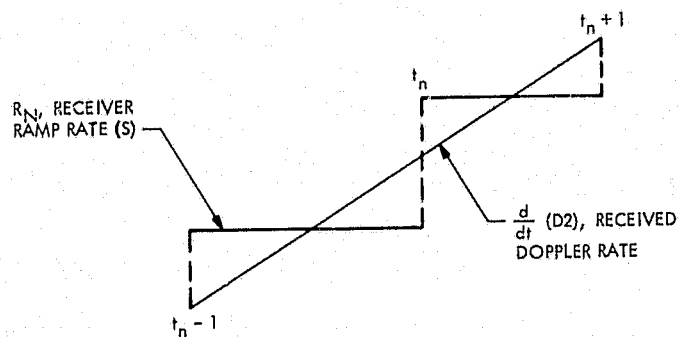
Fig. 3. Receiver ramp rates vs received doppler rate
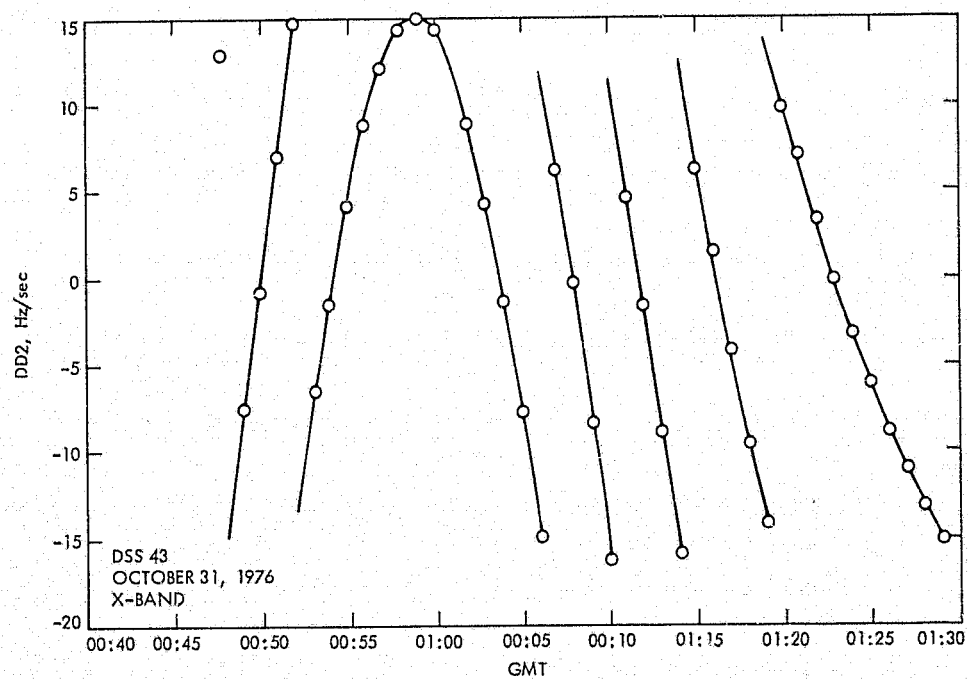
Fig. 4. D2 frequency rate with over-ramped uplink for Viking Orbiter 500-km/P-type orbit

TDA Data Management Planning: Readability of Flow Charts

E. C. Posner
TDA Planning Office

This article proposes a "global" readability standard for flow charts in DSN software implementations. The standard limits the kinds of closures and returns that can occur from decision nodes. It is proved that the standard is equivalent to permitting only those flow charts that are constructible from hierarchical expansion of the three structures BLOCK, IFTHENELSE, and LOOPREPEAT. The LOOPREPEAT structure is the simultaneous generalization of DOWHILE and DOUNTIL. Considerations of code as opposed to flow chart readability, however, may rule out the use of LOOPREPEAT in favor of allowing only its special cases DOWHILE and DOUNTIL.

I. Introduction

We propose a standard for flow charts to be used in DSN implementations. We first define a flow chart as a finite directed graph with five kinds of nodes:

(1) START nodes with no links entering the node and one link leaving.

(2) END nodes with one link entering and none leaving.

(3) FUNCTION nodes with one link entering and one leaving.

(4) DECISION nodes with one link entering and two leaving.

(5) COLLECTOR nodes with two links entering and one leaving.

We further require that there be exactly one START node and one END node. We also demand that the flow chart be *connected* in the sense that, given any node, there is a directed path from START to END going through the node. The condition on DECISION nodes that they have only two outputs is a mathematical convenience for proof purposes, and the use of multiple output decisions (cases) would be allowed in any DSN standard. A similar comment applies to COLLECTOR nodes.

More precisely, a (finite) directed graph is a collection of points called *nodes*, and directed edges, called *links*. Nodes are connected to nodes by links, where the direction is indicated by an arrowhead at the *forward* end of the link, the other end being called the *rear*. Each link must start and end at a (possibly the same) node. It starts

at its rear end and ends at its forward end. A *path* from one node n_1 to another n_2 is a sequence of nodes $n_1 = m_1$, m_2, $--$, $m_p = n_2$ and links l_1, l_2, $--$, l_{p-1}, such that link l_j starts at m_j and ends at m_{j+1}, $1 \leq j \leq p - 1$.

A flow chart then is a directed graph, where the graph nodes are the function boxes, decision boxes, and collector nodes. We will, however, draw all nodes as dots, since the definition of "flow chart graph" makes it clear whether a given graph node corresponds to a function, decision, or collection.

Given flow charts G_1 and G_2, together with a function node F of G_1, we define the *hierarchical expansion of G_1 by replacing F by G_2*, $H(G_1, F; G_2)$ as a new flow chart G_3. Specifically, let link l_1 end at F and l_2 start at F. Remove node F from the set of nodes of G_1 and add the set of nodes of G_2 other than START and END. Let l_1 end at the first node of G_2 reached from its START, and let l_2 start at the last node before the END of G_2. Then the START and END of G_2 have been removed, but all other nodes remain and are the same kind of node. The fact that G_3 is a flow chart can be readily verified.

Let G be a flow chart and F a function node of G. We can get a new flow chart G' with one less node and one less link as follows: Remove F from the set of nodes of G. Let l_1 end at F_1 and l_2 start there. Remove these two links from the set of links and add a new link l' which starts at the node from which l_1 started, and ends where l_2 ended (see Fig. 1). This operation permits us to remove a "no-op" function at a FUNCTION node.

Let A be a finite set of flow charts, called *structures*. Define $A_0 = A$, and A_1, the *one-step completion of A*, as the class of all flow charts which can be obtained from the structures in A by removing a function node, or by replacing a function node of a structure G by a structure H in A, where H may be different from G. Define A_n for $n > 1$, the *n-step completion of A*, to be the one-step completion of A_{n-1}. Define A_∞, *the completion of A*, to be

$$\bigcup_{n=1}^{\infty} A_n,$$

the flow charts obtainable from the structures in A by hierarchical expansion. Note that if G and H are in A_∞, and F is a function node of G, then replacing F in G by H leads to a flow chart still in A_∞; that is, A_∞ is *complete* under hierarchical expansion.

Finally, let us define a looping decision and a non-looping decision. A *nonlooping decision* node in a flow

chart is one for which all paths to END starting at the decision ultimately coincide at some collector node before any path from the decision again reaches that decision node. Otherwise the decision node is called a *looping decision*. A link starting at a decision node with the property that all paths to END starting with the link avoid the given decision node is a *non-looping link*; if there is a way to reach the decision node starting with the link, it is called a *looping link*.

Let us now define a set $\tilde{R}$ of structures which consists of the three structures BLOCK, IFTHENELSE, and LOOPREPEAT, as in Fig. 2. Note that LOOPREPEAT becomes DOWHILE if node G is removed and DOUNTIL if F is removed. Hence, by Mills' Theorem (Ref. 1), every algorithm can be flow charted by a flow chart in R_∞, since it can be flow charted by a flow chart in the completion of BLOCK, IFTHENELSE, and DOWHILE (or alternatively of BLOCK IFTHENELSE, and DOUNTIL).

II. Readability of Flow Charts

A nonlooping decision node is said to have the *Unique Merger Property* if the node at which all paths out of the decision first merge has the property that any two paths starting with different links out of the decision node also merge for the first time at that node. The decision node in IFTHENELSE satisfies Unique Merger.

A looping decision node is said to have the *Forced Loop Closure Property* provided the following holds. An *external input* to a loop is a collector node reachable from the decision that has an output path to the decision node. It also has an input path from START not containing the same output link of the given decision node that was on the input path to the collector node. Note that each looping decision node has at least one external input to a loop it creates. We require that the following hold for at least (it turns out exactly) one of the output links of the looping decision; such links are called *looping links*: every path starting at a looping link must return to the looping decision. We require that there be only one external input node. We also demand that every path starting with the looping link go through the external input, and go through it on only one of its two input links, before returning to the looping decision. It follows from connectivity that only one of the two outputs of a looping decision can be looping—otherwise there is no way to reach END starting from the decision. Note that the decision node of LOOPREPEAT has the Forced Loop Closure Property.

We say that a flow chart has the *Readability Property* provided every nonlooping decision satisfies Unique Merger, and every looping decision satisfies Forced Loop Closure. Observe that if G_1 and G_2 satisfy the Readability Property, or, more briefly, are *Readable*, then if F is any function node in G_1, the flow chart $H(G_1, F; G_2)$ is also Readable. Thus every flow chart in R_∞ is Readable. The next section proves the main result of this article, that every Readable flow chart is in R_∞. Hence, the Readable flow charts can be obtained by using the three structures in R together with hierarchical expansion, and every flow chart so obtained is Readable. By Mills' Theorem previously referenced, then, we also conclude that every algorithm can be flow charted by a Readable flow chart.

III. The Main Theorem on Readability

The theorem below is proved by contradiction, but the proof is actually a recursive procedure for hierarchically expanding a Readable flow chart using the three structures in R: BLOCK, IFTHENELSE, and LOOPREPEAT.

THEOREM. *R_∞ is exactly the class of Readable flow charts.*

PROOF. That every flow chart in R_∞ is Readable has already been noted in the previous section. The hard part is to prove that every Readable flow chart can be obtained from hierarchical expansion of the three structures in R.

If not, let G be an alleged counterexample with the smallest number of nodes among the counterexamples, that is, among the Readable flow charts not in R_∞. Note that G has no function nodes, for they could be removed to yield another counterexample. We will show that G has no looping decisions. Let p be such a looping decision, with external input C as in Fig. 3.

Let π_1 denote the set of paths from C to p, and π_2 the set from p to C. Can there be a path λ from a node r on a path in π_2 to a node D on a path in π_1? No, because all paths from p starting with the looping link of p go through C, by the definition of Forced Loop Closure for the loop started by p.

Can there be a path μ from a node s on a path in π_1 to a node E on a path in π_2? The answer is again No, but for a slightly more complicated reason. This time, look at the loop started by s, which must satisfy Forced Loop Closure. The node C is still an external input node, but so is E because of the path $C \rightarrow s \rightarrow p \rightarrow E$. This situation is of course ruled out, so μ does not exist either.

Then Fig. 3 can be thought of as Fig. 4, where there are no paths between the nodes in A and in B (which each might be empty sets), and where there are no entries or exits from A and B other than the ones shown. That is, the original G is a hierarchical expansion (including possibly node removal) of a graph G_1 which has a function node in place of the structure of Fig. 4. Figure 4 itself is a hierarchical expansion of IFTHENELSE, the two graphs corresponding to A and B being the graphs replacing the FUNCTION nodes of LOOPREPEAT. These two graphs are also Readable, however, and have fewer nodes; hence they are in R_∞ (or are null). The graph G_1 as we have observed can be obtained from a Graph G_2 by hierarchically expanding at a function node by IFTHENELSE. But G_2 has fewer nodes than G_1, hence fewer nodes than G, and so is in R_∞. So G itself would be in R_∞. This proves that G has no looping decision nodes.

So G has only nonlooping decisions. Let p be such a node, with merger node M. An *external input* is a node C on a path from p to M that can be reached from START without going through p, or, if it cannot be reached from START without going through p, then such paths must go through M before reaching C. If we knew that there were no external inputs, we would be done as in the LOOPREPEAT case, for Unique Merger plus the lack of external inputs would cause the nonlooping decision to look like Fig. 5. The same hierarchical expansion idea would work.

First note that if C were an external input, there is no path from M to C not going through p. For it must be possible to reach END from M, and it must therefore be possible to reach END from M without going through C. Let r be a node at which a path to END first leaves the path from M to C. This r is, of course, a decision node, but it is looping because of the path $r \rightarrow C \rightarrow M \rightarrow r$. Since G has no looping decision nodes, there is no path from M to C not going through p.

Thus, if C exists at all, the situation of Fig. 6 must prevail: there is a path from START to C not going through p.

There is of course a path to p from START also. There are two possibilities: i) there is a path from START to p not going through C; ii) every path from START to p goes through C.

In case i), there is a last node s where the paths from START to C and to p agree, as in Fig. 7. However, s

violates Unique Merger, since paths starting with both links out of s meet for the first time at C and also at M. So we are in case ii), in which every path from START to p goes through C, as in Fig. 8. In this case, there is a path from M to p, for there is no way of leaving the path from C to M without going through M, by Unique Merger. Then p is a looping decision, already ruled out. This proves the theorem.

IV. Reversing a Flow Chart

This section proves an amusing corollary to the theorem of Section III. Some people read flow charts backward in trying to understand them, so define the *reversal* of a flow chart as the flow chart with the same nodes but arrowheads reversed. Then FUNCTION nodes remain FUNCTION nodes, DECISION nodes become COLLECTOR nodes, COLLECTOR nodes become DECISION nodes, and START and END are interchanged. However, we still have a flow chart, as is easy to see. If G is a flow chart, let G^R denote its reverse. Note the commutativity of reversing and hierarchical expansion:

$$H(G_1^R, F; G_2^R) = H^R(G_1, F; G_2)$$

Likewise, note the commutativity of reversing and completion:

$$(A^R)_\infty = (A_\infty)^R$$

We then have the following Corollary to the theorem of Section III.

COROLLARY. The reverse of a readable flow chart is a readable flow chart.

PROOF. By the theorem, if G is readable, G is in R_∞, where R consists of BLOCK, IFTHENELSE, and LOOPREPEAT. Hence G^R is in $(R^R)_\infty$. But the reverse of BLOCK is BLOCK, of IFTHENELSE is IFTHENELSE, and of LOOPREPEAT is LOOPREPEAT. So $R^R = R$, and G^R is in R_∞. By the theorem again, G^R is readable, as required.

V. Readability of Code

We have seen that if one adopts the flow chart readability requirement, the only permitted structures automatically become BLOCK, IFTHENELSE, and LOOPREPEAT. Therefore, those are all we would ever propose to even consider permitting as a DSN standard set of structures. It may however be preferable to not allow the full force of LOOPREPEAT but only permit DOWHILE and DOUNTIL, for reasons of code readability. The reason would be that the code for LOOPREPEAT is less readable.

The reason is that the EXIT from the loop of Fig. 9 occurs in the middle of the code, looking like Fig. 10. On the other hand, DOWHILE and DOUNTIL have their EXITS at the end of their code, as is proper for top-down readability (Fig. 11). But the exact form of the code and the tradeoffs involved seem rather language dependent, and the problem of whether to universally ban LOOPREPEAT for DSN software implementations is still under investigation.

Acknowledgment

Reference

1. Mills, H. D., *Mathematical Foundations for Structural Programming*, IBM Federal Systems Div., Rockville, Md., February 1972.
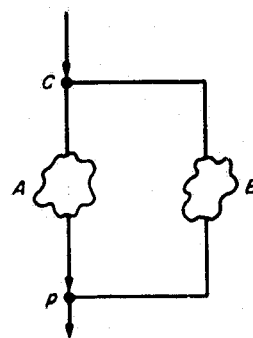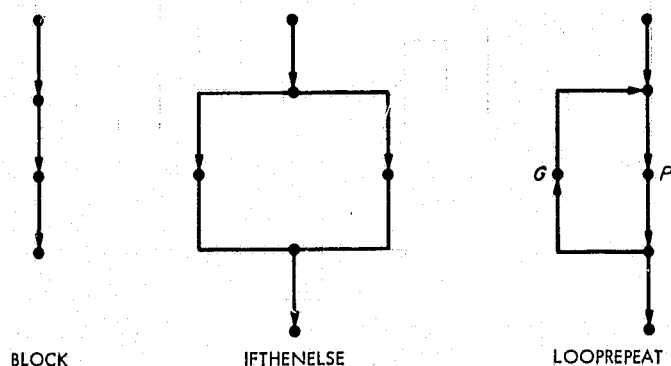
Fig. 1. Removing a FUNCTION node

BLOCK   IFTHENELSE   LOOPREPEAT
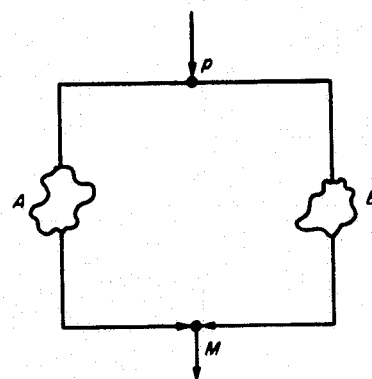
Fig. 2. The three structures of R

Fig. 3. A looping de-
cision node in G

Fig. 4. How to
view Fig. 3

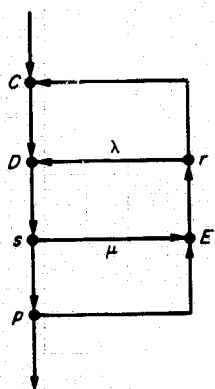Fig. 5. A nonlooping
decision
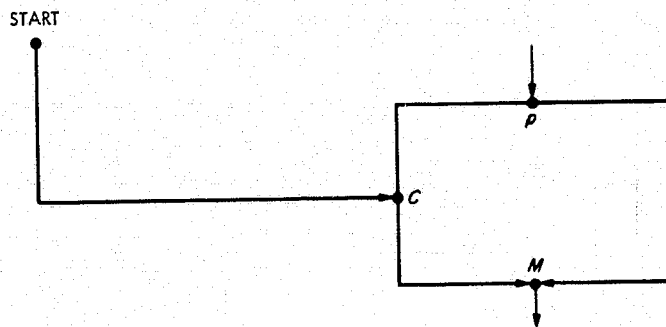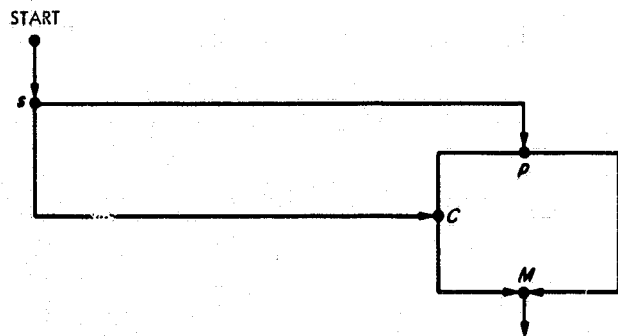

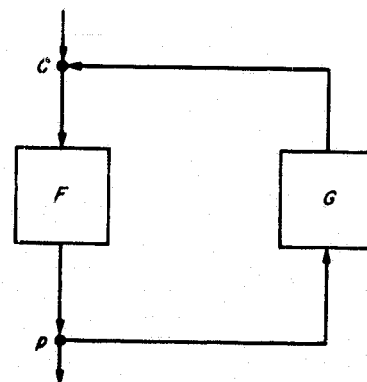Fig. 6. The external input
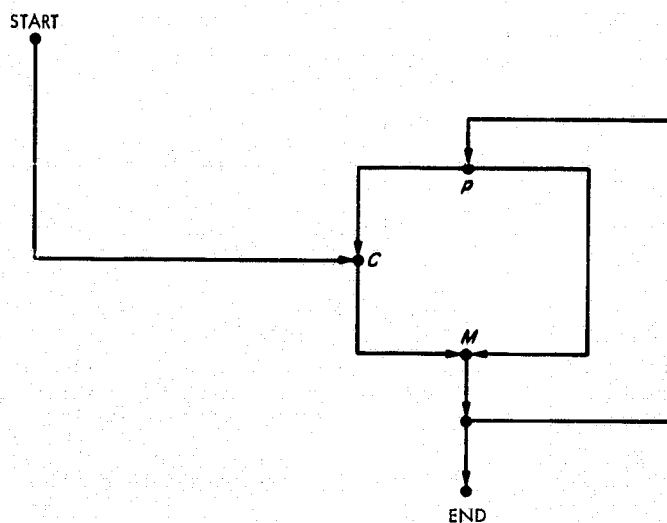
Fig. 7. The first case

Fig. 8. The second case

Fig. 9. LOOPREPEAT

```
LOOP COLLECTOR NODE
PERFORM F
EXIT LOOP IF p
PERFORM G (code for G ends with RETURN to COLLECTOR node.)
```

Fig. 10. Code for LOOPREPEAT

LOOP COLLECTOR NODE	LOOP COLLECTOR NODE
PERFORM F	PERFORM G UNLESS p
RETURN TO COLLECTOR NODE UNLESS p	(Code for G ends with RETURN to COLLECTOR node)
EXIT LOOP	EXIT LOOP
DOWHILE	DOUNTIL

Fig. 11. Code for DOWHILE and DOUNTIL

Automatic Cable Tester

W. D. Schreiner

Quality Assurance DSN and Mechanical Hardware Section

Because of problems encountered and the time required to test multiconductor cables, the Automatic Cable Tester was designed and built by JPL Quality Assurance. This instrument has significantly reduced test time and increased the reliability of the hardware.

I. Introduction

Due to the increased number of cables and the time required to test them, it was necessary for Quality Assurance to find improved methods of performing the tests. A review was conducted of all commercially available equipment that would meet our requirements. The constraints were:

(1) The need for test flexibility at low volume.

(2) Compatibility with existing equipment.

(3) The need to be more cost effective.

No equipment was available that would meet our requirements. Therefore, it was necessary for JPL Quality Assurance to design and build the Automatic Cable Tester (ACT). The use of this instrument has increased the accuracy and reliability of test results, while reducing the man-hours required to perform necessary tests.

II. Description of Equipment

The JPL Automatic Cable Test Set (Fig. 1) consists of one commercial piece of test equipment plus three JPL-designed panels. These units are:

(1) 0-1000-volt commercial power supply and 100-circuit relay scanning unit. The scanning unit accepts only pin-to-pin circuits.

(2) Multicircuit patch panel. The patch panel provides the capability to test cables that are not wired in the normal pin-to-pin configuration, thus eliminating the need for additional testing in a manual mode.

(3) Connector adapter panel. The connector adapter panel provides a full selection of connector adapters without the operator having to stop and locate specific adapters for the particular cable under test.

(4) Branch circuit switching panel. The branch circuit switching panel is designed to pre-program the test set to accept multi-pin circuits on a cable under test. Without the branch circuit panel, the unit would reject the cable as being shorted.

The test set automatically tests each circuit for proper terminal-to-terminal resistance (continuity) and simultaneously checks each circuit against all other circuits for shorts and high-resistance leakage. Cables can also be checked separately for shorts or continuity. In the "shorts only" condition, only one end of the cable needs to be connected to the tester. The operator can select high voltage for dielectric breakdown tests, or use very low voltage for testing circuitry that cannot withstand high voltage. All test parameters, such as test time, type of test, reject levels, etc., can be selected on the control unit.

III. Implementation Results of Automatic Test Equipment

The previously used method of testing multiconductor cables was limited to a continuity test with an ohmmeter or a battery/buzzer (this method is incapable of determining poor terminations such as cold solder and uncrimped pins) and a Hi-Pot and/or megohm test by hand between each pin and all adjacent pins (individually). The manual method is subject to human error (i.e., failure to test a pin) and at best was incomplete. A true dielectric strength (Hi-Pot) and insulation resistance test (Meg) should be performed between each pin (circuit) and all other pins, shields, and connector shells tied together in common.

Operation of the tester (Fig. 2) is simple and can be performed with minimum operator training. Once the cable under test is connected and test parameters have been set, it is necessary only for the operator to push the start button. The test is completely automatic with the tester stopping and identifying all faults.

A significant benefit of the new equipment is the savings in test time. For example, in testing a 100-wire, 2-connector cable, excluding setup time, the old method took two persons 30 minutes each, while the new method only required one person approximately 1 minute to perform the same task.

An additional advantage of the test equipment is safety of operation. Previous methods of testing using high voltages were hazardous in their actual use, plus the side effect of "charging" the unit under test, where electrical shock and possible injury could result. The Automatic Test Unit self-shorts all circuits after test, thus eliminating such hazards.

The significant increase in reliability was a contributing factor in the DSN Engineering decision to discontinue procurement of spare cabling for the Deep Space Network.

IV. Future Plans

All multiconductor cables are electrically inspected using the new JPL Automatic Cable Tester. Cables not meeting the required electrical parameters are separated and identified to prevent their being put into service. A program has already been initiated to identify the exact cause of failures, and steps are being taken to prevent further occurrences.
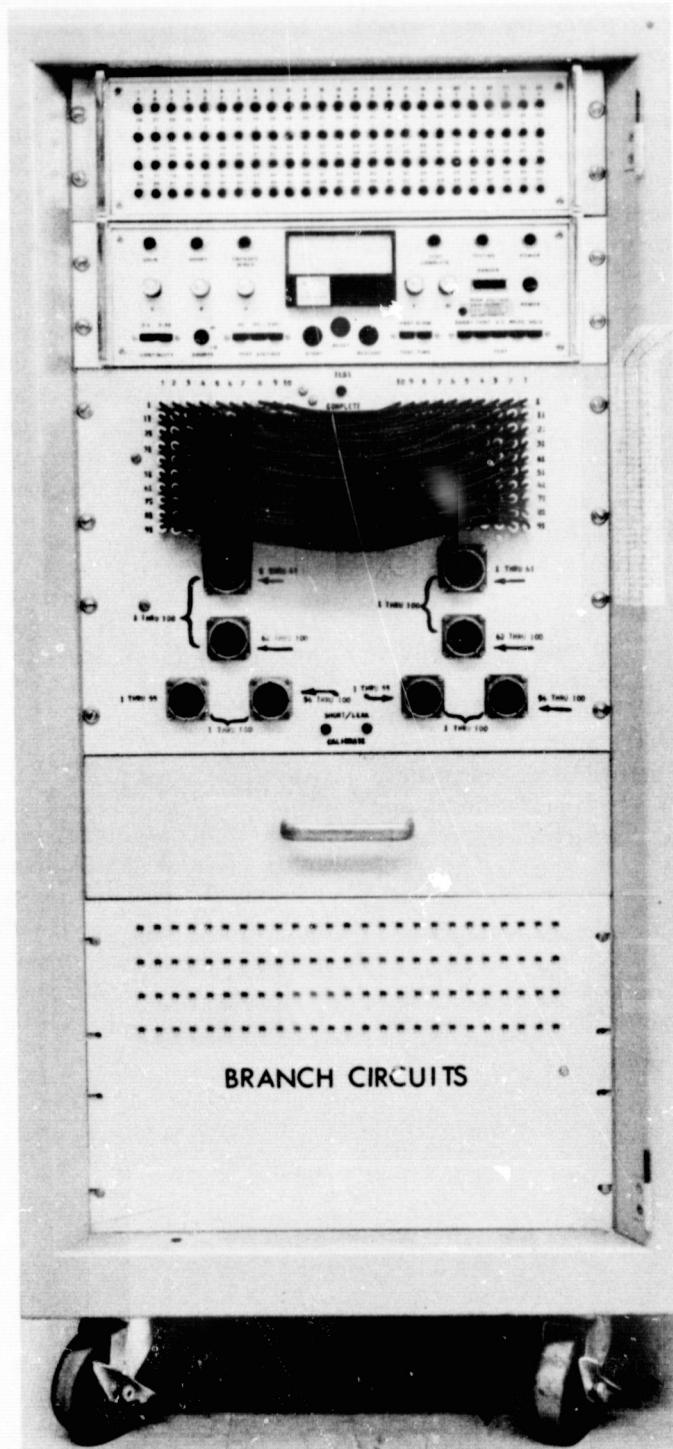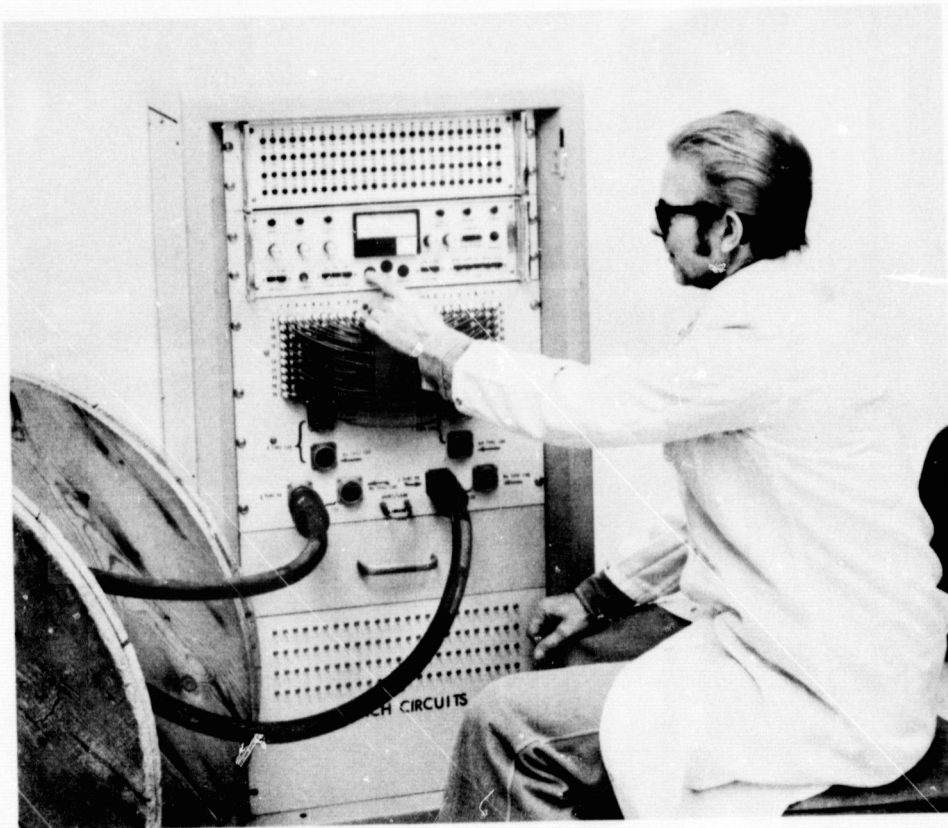
Fig. 1. JPL Automatic Cable Tester

Fig. 2. Operator using Automatic Cable Tester